AMPK regulation of myeloid inflammatory responses during acute and chronic disease

Tyler Smith

This thesis is submitted to the Faculty of Medicine in partial fulfillment of the requirements for the degree of Doctorate in Philosophy with specialization in Biochemistry.

Department of Biochemistry, Microbiology and Immunology

Faculty of Medicine

University of Ottawa

Abstract

AMPK is a heterotrimeric kinase that shifts cellular metabolism to favour catabolism once activated by changes in glucose, adenine nucleotide, fatty acid, or calcium levels. Innate immune cells such as macrophages must rewire metabolic signaling to efficiently respond to inflammatory insults. In this dissertation, we aim to link AMPK-mediated changes in metabolism to immune cell function under several inflammatory states including atherosclerosis and bacterial infection. To begin, we examine a downstream target of AMPK in the cholesterol synthesis pathway, HMG-CoA reductase, which has links to the cholesterol-driven pathology of atherosclerosis. By using a combination of mouse and cell models that lack the inhibitory AMPK phosphorylation site on HMG-CoA reductase, we establish that this signaling axis does not significantly impact atherosclerosis progression. This work highlights the importance of preclinical atherosclerosis model selection and the context-dependent roles of AMPK in atherosclerosis. Next, we investigate how AMPK activity influences macrophage function in the response to infection with *Salmonella enterica* serovar Typhimurium (*S*.Tm). We observe that pharmacological AMPK activation in macrophages suppresses a subset of NF-κB-dependent target genes during infection. Metabolomics data suggest that activating AMPK rewires nitric oxide, TCA, and pyrimidine synthesis metabolism in infected macrophages. Mice expressing overactive AMPK (β1/β2-G2A) succumb to *S*.Tm infection earlier than wild-type mice, though mice treated with the allosteric activator, MK-8722, are unaffected. These data support how AMPK plays distinct roles during gram-negative bacterial infection at the cellular and systemic levels. Finally, we interrogate the effects of AMPK β subunit myristoylation and how it affects AMPK protein stability. We measured AMPK protein levels in cells and mice lacking the AMPK myristoylation site (β1/β2-G2A) and observed a strong decrease in steady state γ subunit

levels alongside more mild decreases in α and β subunit levels. These were unaffected by proteasomal inhibition, and knockdown of proposed myristoylation-dependent E3 ubiquitin ligases ZYG11B and ZER1 had no effect on AMPK protein levels. We conclude that non-canonical regulators of protein stability must influence non-myristoylated AMPK protein levels. Collectively, this work advances our understanding of AMPK function within immune cells and during inflammatory disease progression.

Table of Contents

Acknowledgments

I would not be here without the incredible support network that has made these last six years enjoyable and enriching.

To my thesis advisory committee, Drs. Katey Rayner, Mireille Ouimet, and Subash Sad, thank you for your thoughtful guidance through the years. I feel well prepared for my next steps having been challenged every TAC meeting to rigorously defend my ideas. There are elements of each of your areas of expertise scattered throughout this thesis, and it certainly would not have become what it is without your support.

Thank you to the numerous trainees who came through the Fullerton Lab, who gave me the chance to share my love for science. Over the years, my direct mentees Casey, Lara, Rama, and Aaron, all challenged me to grow as a mentor. I learned so much from each of you, and I hope you learned something from me too. I also have to thank the countless other trainees including Alexia, Habiba, and Maya, who brought that fun, carefree attitude that only Honours students can. When times were tough, you lifted all of our spirits with plenty of Quote Board material.

Speaking of the lab, I was the beneficiary of fantastic mentors from the start of my graduate school experience.

Nick, you showed me the way of the macrophage. You taught me that science is fluid, and everyone has their way of doing it. I am still appreciative of your tricks related to surface tension in cell culture. How could I forget to mention the numerous pranks and fun your brought to the lab each day? Our Milli-Q dispenser remains monocled and moustached to this day. Thank you for guiding me in the early days.

Conor, your ability to be in five places at once will never cease to amaze me. You taught me many techniques early on, and later, we worked as an incredible team on harvest days. I might still be plating CFUs if you had not been there. Your football knowledge is always appreciated, and I must say if I had to pick a second team, hypothetically of course, it would be the Bengals.

Ciara, your western blots were the stuff of legends, and I have still never met anyone that has prompted so many “I have never seen that before” statements in the lab. Even though I had a tendency to forget much of what we talked about, I always appreciated our conversations.

Peyman, I can almost say I’ve become an immunologist from all of our discussions. You taught me flow cytometry and many other less conventional techniques that I consider to be mainstays in my repertoire today. A true innovator, you always had a Peyman type of way of doing things. I also appreciate your willingness to talk science at any time. Many lab meetings I came away with new perspectives and a sharpened sense of how to explain my ideas. You and Lucia (and Mango) were great friends along the way.

Julia, our shared experiences are a highlight of my time in the Fullerton lab. There were many long nights of strange accents and general goofiness, but we also shared a level of rigour and dedication that made it easier to push through the hard times. As I come to the end of my studies, I can confirm that I did indeed follow in your footsteps, just one and a half years behind. I will always remember our early scientific discussions about SCAP and SREBP2 and our marveling at how Goldstein and Brown somehow discovered everything. Thank you for your support to this day, and I will always cherish our time in the lab.

To the Heart Institute crew: you were my metabolic disease-based home away from home. Andrew (you still technically count as being part of the Fullerton lab), Natasha, Nayda, Cassie, Cam, and Serena (from the place with the real best pizza in Ontario). All of you have been sources of laughs and thoughtful discussions at conferences and beyond. I cherish all of our friendships.

Thank you to Red and everyone that served on the BMIGSA with me. I believe we struck a balance between social event coordination and addressing key issues that arose during our time on the council. I am grateful for the community that came out of the BMIGSA and also for the platform that it gave us to advocate for growth within the Faculty.

Thank you to all my incredible friends outside of the lab for keeping me on track.

Thank you to Carolyn. You have been a steady source of support and inspiration as I get to watch your successes from afar. I would not have thought that our small conversation in the sad BSC room one afternoon would turn into us continuing to keep in touch years later. While I will likely print 240 less copies of my thesis than you did, one of them will certainly be reserved for you.

Damian, you were an incredible roommate. Whether it was blasting hype music in the morning, or kicking off COVID with a homemade birthday cake, you always brought the good energy. Though TMM feels like a lifetime ago, I am grateful for our time together and that we have kept in touch.

To Zack and Shannon, you have been tremendous friends and a steady motivator for me throughout this time. Zack, you learned early on to stop asking me, “so do you know what your project is about now?”, because as we discovered, things are always changing. I feel like we could write an anatomy textbook at this point between all of our physio discussions, and I look forward to many more in the future.

To the volleyball crew. Stephen, Kat, Morgs, Mike, Sarah, Chase, and Dallas, I am forever grateful for that first beach season where we banded together. The weekly reprieve from science has continued to fuel me, especially towards the end. More than that, I appreciate the friendships that evolved out of our attempts at keeping a ball off the ground. Looking forward to many more spikes and laughs.

Thank you Morgan, for giving me my start in science and the space to pursue my own interests. In February 2018, as an unsuspecting and chlorinated undergrad, you gave me the opportunity to take charge of a (very small) rotation project. Despite my suboptimal, yet descriptive naming strategy for the nanoparticle formulations involved in that project ("normal", "fast", and "super fast"), it brought forth the independence that I believe is essential to complete a degree as long and as challenging as this one. It is the responsibility of the supervisor to create a lab environment that is enriching for all students, and I thank you for the environment you have continued to cultivate, one in which I learned more than I ever thought I could. The official Fullerton Lab Quote Board will travel with me in spirit, not only because I have the dubious title of most entries, but also because it represents the incredible times we had along the way. While I experienced many trials and tribulations, as any good doctoral experience should have, I can't help but think of Andy Bernard's "I wish there was a way to know you're in the good old days before you've actually left them" as I put this final chapter to rest. With 7 years spent in your lab, I truly appreciate your patience, and most importantly, your continued trust in me as a scientist. I will forever cherish our extended meetings and musings of AMPK and all things metabolism and hope they will not end with the completion of this degree.

To my parents, you have been there since day one. Early on, you supported my curiosity and cultivated my love of learning, something that has grown during my time in this degree. Our frequent calls gave me strength to continue when I struggled, and I always knew I could depend on your insight in spaces beyond the lab. To my grandparents, especially my late Papa, who represents the extra T initial in my authorship name because there are far too many TK Smiths in academia, thank you for your continued support of my endeavors.

To Claire, my partner and the person that I couldn't have done this without. There was more than one experiment that would have failed had you not jumped in to lend your support. Whether in the form of an extra lunch for a long day, or a subtle "you can do this", you knew how to give me the strength I needed in that moment. There are so many unseen moments during a PhD. Of struggle. Of weakness. Of listlessness. But also, of excitement, hope, and celebration. You were there during the lows, but you also have a gift for amplifying the highs. You were always there, by my side through it all. Thank you.

Thank you to all the other mentors and friends I have met along the way that have unquestionably shaped my experience and outlook on science and on life. Without these colourful humans, my PhD experience would have been infinitely more grey.

Abbreviations

AAV: adeno-associated virus
ABC: ATP-binding cassette transporter
ACC: acetyl-CoA carboxylase
acLDL: acetylated low-density lipoprotein
ACVD: atherosclerotic cardiovascular disease
ADaM: allosteric drug and metabolite
AICAR: 5-aminoimidazole-4-carboxyamide ribonucleoside
AMPK: AMP-activated protein kinase
AMPKAR: AMPK activity reporter
Apo: apolipoprotein
ASS1: arginosuccinate synthase 1
AUC: area under the curve
BMDM: bone marrow-derived macrophage
BMT: bone marrow transplant
CaMKK2: Calcium/calmodulin kinase kinase 2
CBS: cystathionine β-synthase
CE: cholesteryl ester
CFU: colony forming units
CRL2: cullin 2-RING E3 ubiquitin ligase
CytoD: cytochalasin D
DHAP: dihydroxyacetone phosphate
ECAR: extracellular acidification rate
FBP: fructose-1,6-bisphosphate
FRET: fluorescence resonance energy transfer
G2A: glycine-2-alanine
G6P: glucose-6 phosphate
GFP: green fluorescent protein
GI: gastrointestinal
HDL: high-density lipoproteins
HK: heat-killed
HMGCR: 3-hydroxy-3-methyl-glutaryl-coenzyme A reductase
HSC: hematopoietic stem cells
HSPC: hematopoietic stem and progenitor cells
IL: interleukin
iNOS: inducible nitric oxide synthase
INSIG1: insulin-induced gene 1
IP: intraperitoneal
KEGG: Kyoto Encyclopedia of Genes and Genomes
KI: knock-in
LDL: low-density lipoprotein
LDLR: low-density lipoprotein receptor
LK: lineage$^-$cKit$^+$Sca1$^-$ cells
LKB1: liver kinase B1
LPS: lipopolysaccharide
LSK: lineage$^-$cKit$^+$Sca1$^+$ cells

LT-HSC: long-term hematopoietic stem cell
LXR: liver X receptor
MEF: mouse embryonic fibroblast
MPP: multipotent progenitor
mTORC1: mechanistic target of rapamycin complex 1
MyD88: myeloid differentiation primary response 88
NDP: nucleotide diphosphate
NF-κB: nuclear factor kappa B
NLR: NOD-, LRR- and pyrin domain-containing
NLS: nuclear localization signal
NMP: nucleotide monophosphate
NO: nitric oxide
NOX2: NADPH oxidase 2
NTP: nucleotide triphosphate
OCR: oxygen consumption rate
OMM: outer mitochondrial membrane
PCSK9: Proprotein convertase subtilisin/kexin type 9
PKA: protein kinase A
PRKDC: DNA-dependent protein kinase
PRR: pattern recognition receptors
RNS: reactive nitrogen species
ROI: region of interest
ROS: reactive oxygen species
ST-HSC: short-term hematopoietic stem cell
S.Tm: *Salmonella enterica* subsp. *enterica* serovar Typhimurium
SCAP: SREBP cleavage-activating protein
SCV: *Salmonella*-containing vacuole
SPI: *Salmonella* pathogenicity island
SREBP: sterol regulatory element-binding protein
STAT1: signal transducer and activator of transcription 1
SUMO: small ubiquitin-related modifiers
TCA: tricarboxylic acid cycle
TLR: toll-like receptor
TNF: tumour necrosis factor
TRIF: TIR-domain-containing adaptor-inducing interferon-β
ULK1: Unc-51-like autophagy-activating kinase 1
UPS: Ubiquitin-proteasome system
VLDL: very low density lipoproteins
WD: western diet
WT: wild type
ZER1: zyg-11 homolog B-like protein
ZYG11B: zyg-11 family member B

List of Figures and Tables

Thesis Format

This thesis is written in accordance with the guidelines from the Department of Biochemistry, Microbiology and Immunology in the Faculty of Medicine at the University of Ottawa. This thesis begins with a broad introduction on the key topics involved in my thesis, centered around the metabolic kinase, AMP-activated protein kinase (AMPK), and its role in regulating atherosclerosis and bacterial infections (Chapter 1). It will continue with published work about AMPK and its regulation of a cholesterol synthesis enzyme in the context of atherosclerosis (Chapter 2). I will then share unpublished results surrounding AMPK and bacterial infection alongside a regulatory modification that affects AMPK activity and protein stability (Chapters 3 & 4). In Chapter 5, I will discuss how my collective work contributes to the AMPK field, and what the most pressing questions are moving forward.

Chapter 1: Introduction.

Chapter 2: AMPK-mediated regulation of endogenous cholesterol synthesis does not affect atherosclerosis in a murine Pcsk9-AAV model.

This article was published in *Atherosclerosis*, Vol 397, **Tyler K.T. Smith**, Peyman Ghorbani, Nicholas D. LeBlond, Julia R.C. Nunes, Conor O'Dwyer, Nia Ambursley, Claire Fong-McMaster, Lucía Minarrieta, Leah A. Burkovsky, Rama El-Hakim, Natasha A. Trzaskalski, Cassandra A.A. Locatelli, Cameron Stotts, Ciara Pember, Katey J. Rayner, Bruce E. Kemp, Kim Loh, Mary-Ellen Harper, Erin E. Mulvihill, Julie St-Pierre, Morgan D. Fullerton, **AMPK-mediated regulation of endogenous cholesterol synthesis does not affect atherosclerosis in a murine *Pcsk9*-AAV model**, 117608,

Chapter 3: Elevated AMPK activity modulates the host response to *Salmonella enterica*.

Chapter 4: AMPK myristoylation affects its protein stability.

Chapter 5: General conclusions and future perspectives

Chapter 1: Introduction

1.1 Preface

This chapter contains introductory material that was prepared for an invited review at *Nature Metabolism* (currently under revision: NATMETAB-RA241213787A).

1.2 AMP-activated protein kinase

This section explores the initial findings that led to the discovery of AMPK, as well as our current understanding of upstream inputs and downstream consequences of AMPK activation.

1.2.1 Kinases and the historical discovery of AMPK

Phosphate. A simple tetrahedral anion derived from phosphorus-containing rock or ore that shapes the biological world, its influence spanning kingdoms. From the original discovery of phosphorus by Henning Brandt in search of the Philosopher's Stone, to our current understanding of inorganic phosphate and its use in biological systems through phosphorylation, to say phosphate is ubiquitous is a profound understatement. The enzymatic attachment of phosphate onto target serine, threonine, or tyrosine residues was a key step in vastly expanding the cellular repertoire in exerting control over protein activity beyond absolute abundance.

Derived from the Greek word kineîn, which fittingly means "to move", protein kinases rapidly phosphorylate target protein residues once activated. The human kinome is comprised of at least 518 kinases that broadly segregate into seven main evolutionary families[1]. Being the orchestrators of substrate-level phosphorylation, kinases share common regulatory structural features that enable them to catalyze ATP hydrolysis and load the γ-phosphate of ATP onto target hydroxyl groups. A kinase core is comprised of an N-terminal lobe with five β strands and a helical C-lobe that provides a cleft where the adenine ring of ATP can bind[2]. In the case of

serine/threonine kinases, the residue following a conserved DFG amino acid sequence in the N-terminal lobe can dictate serine versus threonine preference[3]. Also essential is an activating segment that, when phosphorylated, leads to kinase activation[2]. This presents a key distinction from other enzyme classes such as those involved in metabolism, which are generally active but acutely inhibited by allosteric and post-translational feedback mechanisms. In contrast, kinases are typically inactive under basal conditions but become transiently activated in response to their respective stimuli.

The first evidence for protein phosphorylation came from Edwin Krebs and Edmond Fischer, who would later receive Nobel Prizes in Physiology for their discovery. Prior to their work in the 1950s, phosphoproteins such as casein were known to exist, though they were thought to be inert nutrient sources of phosphate in the diet[4]. Phosphorylase, which is the enzyme that degrades glycogen to glucose-1-P, was predicted to exist in two forms, active phosphorylase a and inactive phosphorylase b. The balance between these two forms was found to be dependent on reversible phosphorylation, where phosphorylase kinase activity dynamically regulated phosphorylase[5,6]. Thus, this began the reframing of phosphorylation from a simple dietary byproduct to a reversible regulator that can modulate protein activity.

About a decade after the phosphorylase kinase discoveries, the elucidation of a cyclic AMP-activated protein kinase, now more commonly known as protein kinase A (PKA), kickstarted the hunt for new kinases[7]. The story of AMPK thus begins in the early 1970s, where two independent groups, one from Indiana University[8], the other from Purdue University[9], coincidentally both from the state of Indiana, discovered that two metabolic enzymes in 3-hydroxy-3-methyl-glutaryl-coenzyme A reductase (HMGCR) and acetyl-CoA carboxylase

(ACC) were inhibited due to phosphorylation. However, in the case of ACC, there was no reported effect on activity with the addition of AMP[9].

These observations remained understudied, until Grahame Hardie at the University of Dundee, who initially studied carbohydrate biochemistry, became interested in phosphorylation and how it regulated fatty acid synthesis via ACC. Using lactating rabbit mammary gland tissue, he confirmed that ACC was regulated by phosphorylation, though the mechanism was thought to be dependent on PKA[10]. Follow-up studies focused on isolating additional kinases and exploring the role of cyclic AMP-mediated inhibition of ACC, particularly downstream of glucagon, where the prevailing idea was that both PKA and a second kinase, ACC kinase 2, phosphorylated and inactivated ACC on the same tryptic peptide[11–13]. During this same time, multiple groups had further characterized the role of phosphorylation in regulating HMGCR[14,15], with a particularly interesting observation that HMGCR activity is potently suppressed by AMP[16]. The distinction of ACC kinase 2, which still inhibited ACC activity in the presence of PKA and casein kinase inhibitors, was appreciated in 1986[17], and one year later, David Carling in Grahame Hardie's lab made the connection that gave rise to the AMPK field as we know it today. Several key observations laid the groundwork for our understanding of AMPK regulation, then termed "acetyl-CoA carboxylase kinase-3" or ACK3: 1) ACK3 was regulated by phosphorylation, as treatment with phosphatases inhibited its activity and its inhibition of ACC activity; 2) ACK3 activity was allosterically increased in the presence of palmitoyl-CoA; 3) ACK3 could potently inhibit HMGCR activity and on a similar timescale in relation to AMP levels[18]. Armed with this new perspective, the soon after renamed AMPK was then shown to be the main kinase for ACC, where PKA phosphorylation did not affect ACC activity[19]. Additional AMPK substrates were identified shortly afterwards including hormone sensitive lipase, phosphorylase kinase, and

glycogen synthase, with preliminary suppositions applied to the sequence preference of AMPK[20]. This was also accompanied by the development of the SAMS peptide, a 15 amino acid peptide that has the same sequence as the ACC phosphorylation site at S79, with the exception of the PKA-dependent phospho site at S77 being mutated to alanine[21]. This would prove to be an invaluable tool to measure AMPK activity against a known substrate. Further work purifying AMPK revealed that there was a 63 kDa subunit that could be phosphorylated, as well as several other polypeptides[22]. It was also discovered around this time that AMPK was allosterically activated by AMP, in addition to AMP-dependent activation of upstream kinases[23].

The impact of Krebs on the AMPK field was not only related to his initial findings regarding phosphorylase kinase; one of his postdoctoral fellows in the 1970s would also impact the AMPK field in profound ways. Though initially focusing on other kinases including PKA[24], the myosin light chain kinase[25], and PKC[26], Bruce Kemp turned to AMPK when investigating the impact of insulin regulation of ACC[27]. This study evolved into a series of others, many mirroring the findings of Hardie and Carling throughout the 1990s. For example, multiple studies identified SNF1, the glucose metabolism-related kinase as the *Saccharomyces cerevisiae* homologue to mammalian AMPK[28–31]. Additionally, mammalian AMPK was discovered to not only comprise one subunit, but three[30,32,33], where the newly identified β and γ subunits acted in a regulatory fashion[34]. Though these subunits also had homology to yeast proteins, expression of AMPK β and γ subunits in yeast could not make up for the absence of their homologues, suggesting that while AMPK α and SNF1 are conserved metabolic regulators, there are significant differences in their regulatory mechanisms[34]. A greater appreciation for tissue specific differences in expression of these subunits, and the identification of multiple isoforms of the subunits ensued, with identification of two α subunits[35–37], two β subunits, and three γ subunits.

Beyond this, post-translational modifications of the AMPK subunits were explored[38], and the main activating site was identified as T172 on AMPK α[39], setting the stage for future studies.

The work that nucleated in these two main camps, that of Grahame Hardie at the University of Dundee and Bruce Kemp at St. Vincent's Institute, laid the foundation for the AMPK field, which has expanded rapidly to encompass over 100 validated targets with differing effects on metabolism and cellular function across a range of tissues and disease states. The continued work of descendants of these scientific lineages, as well as many others, have deeply expanded our understanding of this unique kinase. The concise and systematic nature of these initial studies underscore the rigor upon which I have tried to build my own thesis. The work I present hereafter reflects my own conceptualization of the AMPK field, as well as my attempts at understanding the implications of AMPK signaling.

1.2.2 AMPK subunit expression through evolution and organ specificity

AMPK is an αβγ heterotrimer comprised of a catalytic α-subunit and two regulatory β- and γ-subunits. Mammals express multiple isoforms of each subunit that are encoded by distinct genes. *PRKAA1* and *PRKAA2* encode α1 and α2, *PRKAB1* and *PRKAB2* encode β1 and β2, and *PRKAG1*, *PRKAG2* and *PRKAG3* encode γ1, γ2 and γ3, leading to the potential for 12 unique combinations depending on tissue expression[40]. The β subunit contains binding sites for both α and γ subunits[41] and a key residue in S108 that is required for full allosteric activation at the allosteric drug and metabolite (ADaM) site[42]. Furthermore, subcellular localization is regulated by the β subunits owing to a myristoylation event at the N-terminus[43]. All three *γ* subunits possess a unique arrangement of four tandem cystathionine β-synthase (CBS) repeats. CBS domains are known to arise in pairs in other known proteins, but the presence of four is unusual

in eukaryotic cells[44]. Each of the four CBS domains produce a theoretical binding site for adenine nucleotides AMP, ADP, or ATP. However, only three of these sites bind adenine nucleotides, which have been named site 1, site 3, and site 4. As well, site 4 constitutively binds AMP in a nonexchangeable fashion. Thus, AMPK is allosterically activated by AMP through the reversible binding of AMP to sites 1 and 3[45].

From an evolutionary perspective, eukaryotes express varying homologues of AMPK to facilitate similar stress-dependent functions. In *Saccharomyces cerevisiae*, SNF1 is activated in response to low glucose and rewires glucose metabolism-related gene expression, while the *Arabidopsis thaliana* SnRK1 becomes activated through changes in upper glycolytic intermediates such as glucose-1-phosphate and glucose-6-phosphate. While these evolutionarily divergent species exhibit vastly different requirements when responding to energy stress, all express a variation of the mammalian αβγ heterotrimer with differing isoform compositions. However, SNF1 and SnRK1 differ from mammalian AMPK in that they are not allosterically activated by AMP[46], though ADP can protect SNF1 from dephosphorylation in a manner similar to mammalian AMPK[47]. Regardless, AMPK activity was required during early eukaryotic evolution to allow cells to respond to varying stressors. In fact, AMPKα may be among the oldest of the kinases alongside CaMKK1, STK11, and MAPK1/3 to first evolve from bacterial proto-kinases[48]. While the β subunits are restricted to eukaryotes, there is also evidence for the AMPKγ subunit in prokaryotic organisms, similar to AMPKα[48].

Unique mammalian AMPK complexes presumably accommodate the heterogenous metabolic profiles of distinct cells and tissues. While the α1β1γ1 heterotrimer is the most widely expressed combination of subunits, there also exist specialized expression patterns restricted to tissues with unique metabolic requirements. For example, it is widely recognized that the γ3

isoform is almost exclusively expressed in skeletal muscle, assembles solely into α2β2 complexes, and is found mainly in glycolytic fibres[49,50]. By contrast, γ2 expression is markedly elevated in the heart and thought to form AMPK complexes alongside α2 and β1[51]. Immune cells express primarily α1, β1, and γ1, though there is modest expression of β2 and γ2 as well[52]. However, the precise regulatory differences between these subunit compositions across tissues remains understudied[40].

1.2.3 Regulation by adenine nucleotides, calcium, and lysosomal damage

Activation of AMPK is universally recognized to occur by phosphorylation of the kinase domain activation loop at threonine 172 (α1-T183, α2-T172; α-T172 nomenclature commonly used). Phosphorylation of this site by upstream kinases is enough to boost AMPK activity by over 100-fold[39,53]. Adenine nucleotide-based activation of AMPK takes place via a three-pronged mechanism involving sensing of the exchange of ATP with AMP or ADP at binding sites within the CBS domains on the γ-subunit: 1) AMP and ADP both promote α-T172 phosphorylation and 2) prevent its dephosphorylation by phosphatases, and 3) AMP further allosterically activates AMPK complexes already phosphorylated on α-T172[54,55]. It is in this way that AMPK is a true adenylate charge-regulated protein, rather than solely being activated by AMP. The concept of adenylate charge was first proposed by Atkinson in the 1960s to frame how changes adenine nucleotide abundance, those being AMP, ADP, and ATP, provide direct feedback about the metabolic status of cells (Figure 1.1A,B)[56]. While this theory fell to the wayside due to a lack of enzymes that respond directly to adenylate charge, it accurately describes AMPK regulation by adenine nucleotide levels[57]. However, the sensitivity of AMPK to adenylate charges varies with heterotrimer composition, where complexes containing α2 and β2 subunits are more sensitive to

AMP levels[58]. However, α2 complexes are also more sensitive to dephosphorylation[58], suggesting that these heterotrimer assemblies are designed to quickly respond to large fluctuations in adenylate charge, such as those found in skeletal muscle.

AMPK α-T172 phosphorylation is essential for full activation of AMPK and is regulated by several upstream kinases. Of the most well characterized, liver kinase B1 (LKB1) typically phosphorylates α-T172 upon glucose starvation (described in greater detail below) or following changes in adenine nucleotide levels. Calcium/calmodulin kinase kinase 2 (CaMKK2) phosphorylates α-T172 following increases in intracellular Ca^{2+} levels[53,59], which is particularly apparent in conditions such as genotoxic stress[60,61], hypoxia[62], and hormone signaling in the brain[63,64]. Facilitating this CaMKK2-AMPK interaction is the scaffolding protein IQGAP1 that directly binds to both AMPKα and CaMKK2[65]. While initially questioned as a bonified upstream kinase[66,67], it has become clear that TAK1-mediated phosphorylation of AMPK α-T172 occurs specifically under conditions of lysosomal damage, wherein TAK1 is ubiquitinated and activated by USP9X[68]. This compartmentalized signaling cascade also explains how other TAK1-activating stimuli such as bacterial lipopolysaccharides (LPS) do not increase AMPK activity[69,70]. Beyond these validated kinases, there are a number of *in vitro* validated T172 kinases such as those from the STE20 family that will require further validation as AMPK-activators under diverse physiological states[71,72].

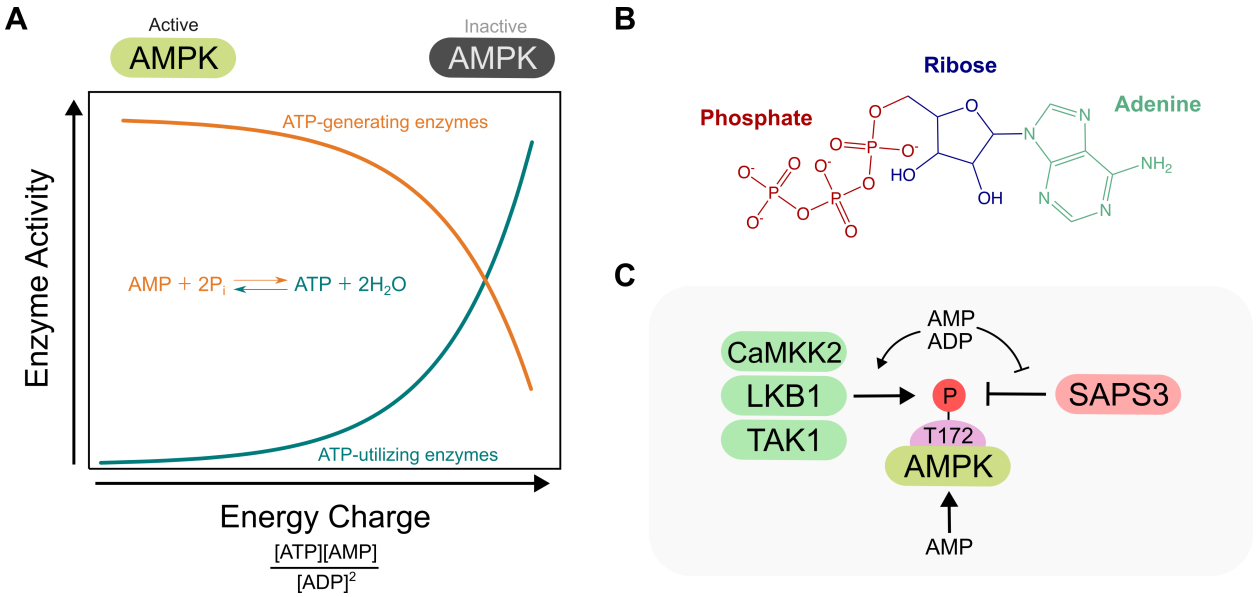

Figure 1.1: AMPK regulation by adenine nucleotides. (A) Original energy charge hypothesis with broad AMPK activation states superimposed. Adapted from D.E. Atkinson, *Biochemistry* (1968). **(B)** Structure of ATP. **(C)** Tripartite regulation of AMPK phosphorylation and activation at T172 by adenine nucleotides. Both AMP and ADP binding support phosphorylation of T172 by upstream kinases CaMKK2, LKB1, or TAK1, while simultaneously opposing dephosphorylation by phosphatases such as SAPS3. Only AMP can allosterically activate AMPK under physiological conditions.

1.2.4 AMPK subcellular localization and nutrient-dependent activation

<u>AMPK biosensors as tools to assess subcellular localization and activity</u>

AMPK activity has traditionally been assessed using phosphorylation-specific antibodies targeting downstream effectors or the AMPK heterotrimer itself. However, these readouts lack both spatial and temporal information. While subcellular fractionation or organelle enrichment techniques can provide spatial context to AMPK activity, it remains challenging to measure temporal dynamics. Therefore, molecular tools that can detect AMPK activity in real-time in various compartments are crucial for unraveling how AMPK responds to a diverse range of physiological and pharmacological stimuli.

Fluorescence resonance energy transfer (FRET) is a phenomenon where emitted energy from one fluorophore excites a nearby fluorophore[73]. Typical constructs contain a CFP and YFP

fluorescent pair that are matched with an optimal kinase substrate motif (MRRVA**T**LVDL for AMPK) and an FHA1 domain, which has a high affinity for phosphopeptides. Substrate motif phosphorylation promotes FHA1 binding, which facilitates FRET and provides immediate kinase activity visualization. Subcellular targeting of these biosensors can therefore provide real-time, organelle-specific activity measurements.

AMPK biosensors have provided fundamental knowledge on how AMPK responds to various inputs. Constructs such as AMPK activity reporter (AMPKAR)[74], AMPKAR-EV[75], AMPKAR2[76,77], and AMPK/BRSK activity reporter (ABKAR)[78,79] rely on a reporter construct, while others such as AMPfret takes advantage of conformational changes in the heterotrimer itself[80]. Despite their utility, FRET biosensors suffer from high fluorescence background that can interfere with sensitivity. To circumvent this issue, ExRai AMPKAR measures the change in emission wavelength of a single circularly permutated enhanced green fluorescent protein (GFP), rather than FRET between two different fluorophores[81]. This significantly reduced the background fluorescence observed with prior FRET sensors.

Application of these biosensors to tissues has been limited to mice globally expressing AMPKAR-EV[75]. In these mice, AMPK activity is higher in skeletal muscle in response to exercise[75] and during viral infection[82]. While many of these constructs have been applied to immortalized cell lines, several studies have interrogated AMPK subcellular localization and signaling in retinal[83], breast cancer[84], or neuronal cells[85], highlighting the value of using these tools to understand AMPK signaling in diverse cell types. Combinatory expression of multiple sensors, perhaps through pairing AMPK biosensors with prospective phosphatase biosensors could help deconstruct the cues leading to AMPK activation and deactivation[86]. With the

generation of more sensitive and widely applicable biosensors, these tools will continue to shape how we view spatiotemporal AMPK signaling.

Myristoylation and other lipid signals as regulators of AMPK function and localization

Protein N-terminal glycine myristoylation describes the lipidation of N-terminal glycine residues with a 14-carbon fatty acid chain. Canonically, myristoyl groups provide a lipid moiety for otherwise soluble proteins to associate with membranes, although they can also regulate protein function. Because the myristoyl group is shorter than other lipid modifications such as palmitoyl or prenyl groups, it does not anchor its target proteins to membranes as tightly. For this reason, secondary lipidation events or the presence of a polybasic sequence is often required for myristoylated proteins to consistently anchor to membranes[87].

AMPK is co-translationally myristoylated on both β subunits at N-terminal glycine residues (G2) by NMT1 following cleavage of the N-terminal methionine residue[38,43,88]. Myristoylation is necessary for basal association of AMPK with the lysosome[89,90] and mitochondria[91], suggesting that membrane lipid content does not appreciably affect AMPK binding. Additionally, non-myristoylated (G2A) mutants have elevated basal activity, but are unresponsive to AMP binding, suggesting that the myristoyl group exerts a gatekeeping effect on canonical AMPK activation, but is required for full allosteric activity[43,54,92]. Indeed, a myristoyl-switch mechanism has been proposed to modulate AMPK activity, wherein the myristoyl group binds within an intramolecular binding pocket on the AMPK heterotrimer until binding by AMP or ADP displaces the myristoyl group[43]. While applicable to severe nutrient stress that disrupts cellular adenylate charge, this framework falls short in addressing how inactive AMPK associates with membranes.

How does AMPK associate with membranes in the absence of an activating stimulus? Evidence from other myristoylated kinases such as Abl[93] demonstrates that a favourable environment can promote displacement of the myristoyl group from the protein and onto a membrane. Therefore, proximity of cytosolic AMPK to membrane compartments, perhaps alongside local fluctuations in AMP levels, may be sufficient to facilitate binding to membranes. While occupied on the membrane, this conformation produces a "pre-activated" state, where T172 in the kinase domain is more accessible to upstream kinases. This model could explain how lysosomal and mitochondrial pools of AMPK are activated more rapidly than cytosolic pools in response to 2-DG and ADaM site allosteric activation[81]. To disengage from membranes, a more favourable environment for binding of the myristoyl group to the intramolecular binding pocket would have to occur. As elaborated on below, these interactions are likely transient but could be prolonged through protein-protein interactions that restrain AMPK at various membrane compartments. An example of this would be the recently described "pyrimidinosome" at the mitochondrial membrane[94].

Non-myristoylated mutants of AMPK have reduced protein stability and exhibit both a diffuse and perinuclear punctate localization[43,91,92]. These puncta resemble biomolecular condensates, which have a higher likelihood of forming between proteins with intrinsically disordered regions and RNA-binding capacities[95]. Non-myristoylated AMPK satisfies both of these criteria considering the N-terminus of the β subunits has low order and the circular long non-coding RNA *circACC1* binds to the β and γ subunits[96]. Along these lines, several phosphorylation sites have been identified on the β subunit N-terminus that could contribute to the solubility of non-myristoylated AMPK[88]. However, the only evidence of non-myristoylated AMPK *in vivo* comes from rheumatoid arthritis, where authors paradoxically observed decreased

AMPK activity and no change in protein levels as a result of reduced cellular myristoylation[97]. Outside of myristoylation, palmitoylation (attachment of a 16-carbon fatty acid chain) of both α subunits at C209 and C542 by DHHC17 at least partially depends on myristoylation of the β subunits, and can also influence the association of AMPK with membranes[98]. These lipidation events ensure that AMPK is directed to the appropriate organelle in a timely and signaling-specific manner, though the molecular details underlying this association requires refinement.

AMPK activity is also linked to fatty acid levels through direct binding of long chain-fatty acyl-CoAs to the ADaM site, which is situated between the α and β subunits[42]. This effect is specific to medium and long-chain fatty acyl-CoA esters, but not their closely related unesterified derivatives. Consistent with observations of AMPK-activating small molecules, such as A-769662 and salicylate[99,100], these effects are not observed with β2-containing complexes and require S108 phosphorylation on AMPK β1. Beyond fatty acyl-CoAs, fasting can also increase levels of linoleic acid, which may bind to the AMPK γ1 subunit and promote nucleotide-independent activation and synergy with AMP[101]. Though the exact binding site will have to be verified empirically, this presents a multi-pronged fatty acid regulatory system ensuring that AMPK is activated under fasting conditions. Taken together, AMPK is regulated at multiple levels by lipid species, with myristoylation playing a key role in subcellular localization as well as activity suppression.

Lysosomal AMPK localization and responsiveness to upper glycolysis-related metabolites

Throughout evolution, cells have developed sophisticated pathways to respond to varying degrees of nutrient stress to survive. Adequate glucose is required to fuel glycolysis and generate intermediates essential for oxidative phosphorylation and other pathways. While prolonged

glucose starvation can lead to severe nutrient stress and higher AMP:ATP and ADP:ATP ratios, mild reductions in glucose availability can also induce metabolic adaptations designed to maximize survival in low glucose conditions.

AMPK is activated in response to glucose starvation by LKB1 at the lysosome following the aldolase-mediated sensing of fructose-1,6-bisphosphate (FBP). Upon FBP depletion, aldolase undergoes a conformational change that promotes its disengagement from V-ATPase in a transient receptor potential V channel-dependent manner while simultaneously displacing mechanistic target of rapamycin complex 1 (mTORC1) from the lysosome[89,90,102]. Lysosomal AMPK then interacts with LKB1-AXIN1/2, and is activated by LKB1-mediated phosphorylation of T172[103], though the involvement of AXIN in this process has been questioned[104]. In line with this, glucose starvation mimetics such as low-dose metformin[105] and aldometanib[106] also activate AMPK through this platform. All of these pathways supposedly converge on exclusive lysosomal, but not mitochondrial activation of AMPK[107].

While low glucose levels can activate AMPK via this lysosomal activation platform, there exist several additional mechanisms through which AMPK activity is regulated by flux through upper glycolysis. The product of hexokinase-mediated phosphorylation of glucose, glucose-6 phosphate (G6P), can be used to generate inositol, which directly binds to and competes with AMP at CBS3 and CBS4 to impair AMPK activity[108]. On the other hand, flow of G6P into the oxidative pentose phosphate pathway leads to elevated ribulose-5-phosphate levels that can inhibit LKB1[109]. However, the oxidative pentose phosphate pathway also produces γ-6-phosphogluconolactone as a byproduct, which decreases phosphatase activity and actually supports AMPK activity[110]. Glycogen, which is thought to inhibit AMPK activity via binding to the carbohydrate binding module on the β subunits[111], requires adequate G6P for conversion into

G1P and UDP-glucose for synthesis. G6P dehydrogenase itself has been shown to interact with AMPKα directly, though the precise implications of this interaction will have to be validated empirically[112]. Therefore, from a metabolite perspective, AMPK activity is exquisitely linked to glucose and its immediate downstream metabolites and is coordinately regulated through a combination of sensing of FBP, γ-6-phosphogluconolactone, inositol, glycogen, and ribulose-5-phosphate levels.

Beyond metabolite-level regulation, glucose-dependent phosphorylation of key residues also fine tunes AMPK activity. For example, phosphorylation at α1-S487 (commonly referred to as S485 in accordance with the rat AMPKα1 sequence) and α2-S491 are generally inhibitory and are elevated under anabolic conditions such as high glucose or insulin engagement[113]. A multitude of kinases can phosphorylate these sites, including including AKT[113–118], p70S6K[119], SGK1[120], PKC[121], PKA[122,123], and PKD1[124,125]. Additionally, mTORC1, which typically has high activity in glucose-replete conditions[104], phosphorylates AMPKα1-S347 and α2-S345[126], where the α2-S345 phosphorylation site can prevent AMPK from localizing to the lysosome[127]. This interaction of AMPK with lysosomes is transient (<30 sec), aligning with observations that ACC, a cytosolic target, is rapidly phosphorylated following glucose starvation[127]. The DNA-activated protein kinase PRKDC also regulates lysosomal AMPK activation through phosphorylation of γ1-S192/T284 and can support LKB1-mediated activation of AMPK at the lysosome downstream of glucose starvation[128]. Other potential glucose-sensitive phosphorylation sites include α1-S496 by AKT and PKA[129], α1-T490 and α2-T485 by GSK3[130], and α1-T467 by PIM2[131]**.** While some phosphatases can impact T172 phosphorylation levels during glucose replete[92,110,132–135] or starvation[136] conditions, SAPS3, as part of the highly conserved PP6

phosphatase complex, is the only phosphatase validated to target AMPK *in vivo* in response to changes in glucose levels[137,138].

Prolonged glucose starvation can also induce oxidative stress[139]. There has been some debate regarding the reactive oxygen species (ROS)-dependent[140,141] versus AMP-dependent[142–145] activation of AMPK in response to oxidative stress. However, several sites on AMPK are redox-sensitive such as α2-C130 and α2-C174[146], with others having been identified through screens[147]. Of note, AMPK α and other serine/threonine kinases share a conserved cysteine residue at the +2 position relative to the activating T-loop site, signifying the widespread sensitivity of kinases to redox regulation.

Regardless of the route of activation or modification, these data suggest that AMPK is associated with lysosomes prior to encountering any stimulus but can rapidly disengage from the lysosome to then signal to cytosolic or other organellar targets following its finely tuned activation in response to decreased glycolytic flux.

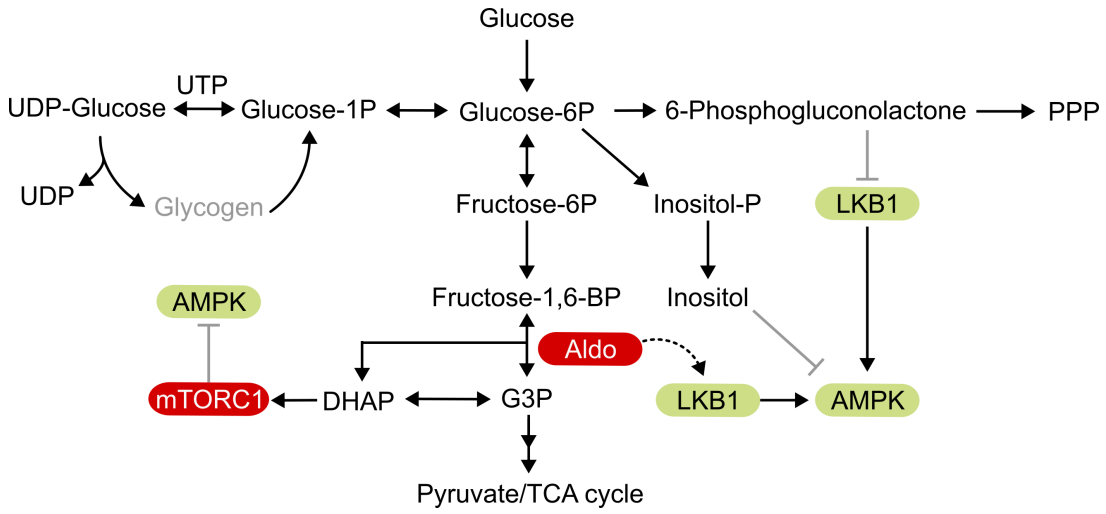

Figure 1.2: Metabolite-based regulation of AMPK activity due to reduced glycolytic flux. AMPK can be activated by decreased abundance of several upper glycolytic metabolites. Both inositol and 6-phosphogluconolactone are products of glucose-6P metabolism, resulting in derepression of AMPK activity. Decreased fructose-1,6-bisphosphate levels generate a conformational change in aldolase, leading to activation of AMPK. Additional decreases in DHAP inhibit mTORC1 activity. Prolonged starvation can lead to reduced glycogen stores, relieving potential inhibition of AMPK activity.

Mitochondrial AMPK localization

Mitochondria influence metabolism through energy transducing pathways resulting in ATP production and the release of non-ATP signaling factors[148–151]. Increasing evidence of AMPK-mediated regulation of mitochondrial dynamics speaks to a complex interplay that allows cells to rapidly respond to severe stressors such as ATP depletion or hypoxia.

AMPK associates with the outer mitochondrial membrane (OMM) because trypsin[152] or proteinase K[62,153] digestion of isolated mitochondria results in AMPK dissociating with other OMM proteins. Additionally, most mitochondrial targets, including ACC2[154,155], MFF[156], ARMC10[157], AKAP1[158] and MTFRL1[153] are OMM proteins. Several recently identified AMPK targets including MCU[159] and PDHA[160] are localized on the inner mitochondrial membrane and matrix, respectively, implying that AMPK entry into mitochondria is possible. However, more mitochondrial subfractionation studies will be required to expand on this mechanism. AMPK localization to the mitochondrial membrane does not require intrinsic activity, as dominant negative mutants accumulate equally to wild-type (WT) AMPK[152]. This and other work suggests that AMPK associates with mitochondria constitutively and is activated following a rise in AMP:ATP and ADP:ATP ratios[107]. However, in the case of mitochondrial depolarization with CCCP, AMPK content on mitochondria rapidly increases within minutes[161]. Inositol reduction downstream of glucose starvation also leads to AMPK-dependent mitochondrial fission at very early timepoints[108]. This observation is at odds with another proposed framework in which only severe energy stress induces mitochondrial AMPK activation and mitochondrial fission[107]. Regardless, the functional implications of acute AMPK activation are reflected by pro-mitochondrial fission signaling. Mitochondrial fission can generate distinct pools of daughter mitochondria depending on whether the scission initiation site is located at the midzone or

periphery[162]. This is important for propagating the mitochondrial network[163], targeting mitochondria with low membrane potential for mitophagy[162], or enhancing fatty acid oxidation[164]. Given the array of mitochondrial AMPK targets and their localization, AMPK could potentially affect affect both midzone and peripheral fission, remodeling the mitochondrial network in the process.

In the context of hypoxia, AMPK requires egl-9 family hypoxia inducible factor 1 for increased mitochondrial association and subsequent activation via CaMKK2, providing the first evidence of a widely-expressed AMPK translocation factor[62]. Inactive AMPK is also part of the OMM-localized "pyrimidinosome", which is a complex of several enzymes involved in pyrimidine synthesis[94]. However, under hypoxic conditions, AMPK activation results in dissociation from the pyrimidinosome[94]. These data also support the idea that AMPK is present at the mitochondria under non-stressed conditions. Together, AMPK is an OMM-associated protein in the non-stressed state but can accumulate in response to specific triggers such as hypoxia and mitochondrial depolarization to fuel mitochondrial fission.

Nuclear AMPK localization

Translocation of proteins through nuclear pore complexes is tightly regulated. For frequent shuttling between the nucleus and cytoplasm, cargo proteins typically require both a nuclear localization signal (NLS) and nuclear export signal (NES)[165]. To date, no definitive NLS has been identified on the AMPK heterotrimer. However, the AMPK α1 and α2 subunits both contain an NES, characterized by conserved leucine residues at their C-termini[166]. Likewise, heterotrimers containing either α1 or α2 subunits localize to the nucleus, although their regulation can differ depending on cell type and stimulus[60,167]. These NES regulate the export of

the AMPK heterotrimer to the cytoplasm in a Ran-dependent shuttling process that is also required for the import of AMPK into the nucleus[166]. Because AMPK lacking the NES still accumulates in the nucleus, it is likely that there is either 1) an unidentified NLS elsewhere on the AMPK heterotrimer to promote importin binding, or 2) a secondary cargo protein that contains a putative NLS facilitates the transit of AMPK into the nucleus. It is generally agreed upon that AMPK shuttles between the nucleus and cytosol frequently, resulting in little change in the total amount of nuclear AMPK, although some studies have detected increased AMPK content in the nucleus following activation[81,168].

There are currently two main mechanisms through which nuclear AMPK is activated. First, in the context of genotoxic stress, nuclear AMPKα1-containing heterotrimers are activated by CaMKK2 in the nucleus due to elevated nuclear $[Ca^{2+}]_i$[60,61]. Though CaMKK2 is considered a cytosolic protein, nuclear CaMKK2 localization has been reported[169]. The second mechanism posits that AMPK is activated in the cytosol and then shuttles into the nucleus in the activated state. In support of this, forced nuclear localization of AMPKα2 renders it unresponsive to 2-DG treatment[81]. Additionally, AMPK that is retained in the nucleus has low basal activity relative to shuttling AMPK[166]. Indeed, AMPK activity had no effect on the nuclear retention of AMPK lacking its NES, affirming that the AMPK nuclear import machinery functions independent of AMPK activity[166]. Recent work uncovered that nuclear UHRF1 binds to and recruits the phosphatase PP2A to dephosphorylate AMPK in the nucleus, which also affects AMPK activity in the cytosol[135]. Interestingly, this effect was observed downstream of glucose starvation, which is typically thought to be restricted to lysosomal pools of AMPK[107,135]. Of note, UHRF1 is mainly expressed in proliferative cell types and hematopoietic progenitors, so this mode of nuclear AMPK regulation is likely cell type specific.

While both AMPK α1 and α2 subunits have an NES, AMPK α1-containing heterotrimers are specifically retained within the nucleus during apoptosis[170]. This selectivity is conferred via a caspase-3 cleavage site at the C-terminus that cleaves the NES without compromising AMPK activity[170]. The AMPK α1 and α2 C-terminal 20 amino acids share about 70% similarity, with key leucine residues required for the NES being conserved[166]. This difference raises the possibility that alternate proteases could cleave the α2 NES under different, non-apoptotic stimuli.

Taken together, nuclear AMPK activation is context dependent. With genotoxic stress, characterized by increases in nuclear $[Ca^{2+}]_i$ levels, CaMKK2 phosphorylates AMPK in the nucleus. In conditions of nutrient stress such as glucose starvation or high AMP:ATP or ADP:ATP ratios, AMPK is activated in the cytosol and translocates into the nucleus in the activated state.

1.2.5 Regulation of AMPK protein turnover by ubiquitin and ubiquitin-like modifiers

Proteostasis describes the cumulative regulatory mechanisms that maintain a certain level of abundance of a specific protein. This integrates a number of cellular processes such as transcription, translation, and degradative pathways. One of the universal ways in which cells dispose of misfolded, aggregated, or nonfunctional proteins is through the ubiquitin-proteasome system (UPS). The UPS depends on ubiquitin, which is an 8.6 kDa protein that can be attached to target lysine residues either singularly or in chains through an elaborate system featuring ubiquitin-activating (E1), ubiquitin-conjugating (E2), and ubiquitin-ligating enzymes (E3), the latter of which number nearly 700. E3 ubiquitin ligases provide the specificity of the UPS, where substrate receptor proteins within the E3 complex bind to target residues and facilitate ATP-

dependent ubiquitination of target lysine residues. Depending on ubiquitin chain composition, ubiquitination can result in signaling changes as is typical of K63-linked chains, or it can target proteins for degradation in the proteasome if they are K48-linked chains.

Several AMPK-specific E3 ubiquitin ligases target AMPK for degradation. AMPK α1 is ubiquitinated by the testis and cancer-specific MAGE-A3/A6-TRIM28 complex[171], while α2 is ubiquitinated by the E2 enzyme UBE2O in both cancer[172] and skeletal muscle contexts[173]. The E3 ubiquitin ligase WWP1 can also ubiquitinate α2, although its involvement in α1 regulation was not investigated[174]. Complexes that can ubiquitinate both α subunits are MG53[175], which targets AMPK during hyperglycemia alongside AMPK α1-491 phosphorylation, MKRN1[176], and cereblon-CRL4A[177]. Interestingly, cereblon-CRL4A can also ubiquitinate the γ1 subunit[178], while there remains no validated E3 ubiquitin ligase complexes specific for γ2 or γ3. The β1 subunit is ubiquitinated and targeted for degradation by the adipose-restricted CIDEA[179], while the Laforin-Malin complex polyubiquitinates both β1 and β2 subunits with K63-linked chains[180]. The latter ubiquitination events may increase AMPK protein levels by sequestering it in inclusion bodies[180].

Similar to how MG53 requires a phosphorylation motif prior to ubiquitinating AMPK, both the GID complex[181] and Fbxo48[182] recognize phosphorylated AMPK α-T172 under glucose starvation conditions. However, given the complexity of measuring long-lived, phosphoregulated proteins such as AMPK, more work is required to fully understand the dynamics of α-T172 recognition as a regulator of AMPK. AMPK may also be ubiquitinated with linear M1-linked chains via LUBAC[183]. As with phosphorylation, ubiquitination is reversible through the action of deubiquitinase enzymes. AMPK can be deubiquitinated by USP9X[184], which was initially observed with AMPK-related kinases[185], and by USP10[186], which is responsible for removing

K63-linked polyubiquitin chains from four lysine residues on both α1 and α2 subunits. Modulation of target-specific ubiquitination using deubiquitinase-targeting chimeras, referred to as DUBTACs, is being explored therapeutically to increase target protein expression[187]. Of note, a DUBTAC based on USP7 exhibited promising results in increasing AMPK β protein levels *in vitro*[188].

SUMOylation, which involves the attachment of small ubiquitin-related modifiers (SUMO) onto lysine residues, often competes with ubiquitination. AMPK is SUMOylated by PIAS4 on both the β2[189] and α1 subunits, the latter of which inhibits its activity[190]. Additionally, SENP2 deSUMOylates AMPKα and renders it more susceptible to ubiquitination and subsequent degradation[191]. Thus, ubiquitination and SUMOylation are multifaceted regulators of AMPK protein stability and activity.

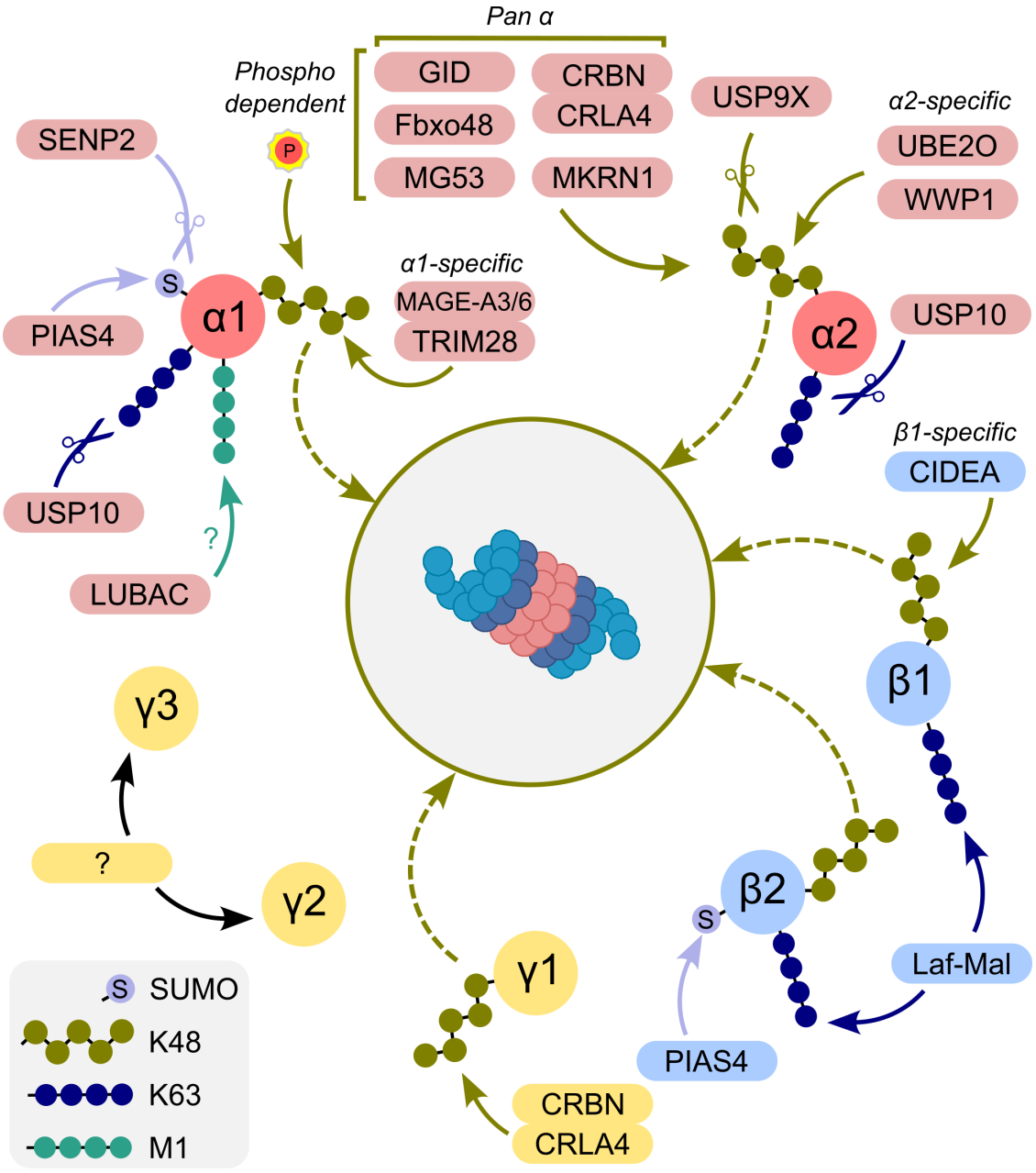

Figure 1.3: Regulation of AMPK subunits by ubiquitin and ubiquitin-like modifiers. Validated regulators of ubiquitination and SUMOylation of individual AMPK subunits. K48-linked chains result in degradation in the 26S proteasome, while linear K63- and M1-linked chains can affect AMPK signaling and localization.

1.2.6 Pharmacological activators and inhibitors of AMPK activity

Given that AMPK generally supports catabolic signaling, pharmacological activation of AMPK has been pursued in the context of metabolic disease. While this is not an exhaustive list of small molecule activators and inhibitors of AMPK, it will highlight some of the key pharmacological tools used in this thesis (Figure 1.4). The first widely used AMPK activator was AICAR, which is a prodrug for ZMP[192]. Acting as an AMP mimetic, AICAR results in potent AMPK activation, though it can cause significant off-target effects[193]. In a similar way, the first-line type 2 diabetes mellitus treatment, metformin, activates AMPK by inhibiting mitochondrial electron transport chain function, or through lysosomal activation, depending on the dose[105,194]. More severe mitochondrial electron transport chain inhibitors such as rotenone can also activate AMPK indirectly in an adenylate charge-dependent manner[195]. Targeting of the lysosomal activation pathway has led to the development of an aldolase inhibitor called aldometanib that blocks FBP binding, resulting in AMPK activation[106].

While AICAR took advantage of AMP-mediated allosteric activation, a selective activator in A-769662 targeted the ADaM site[99,196,197]. This interaction was specific to β1-containing heterotrimers and depended on phosphorylation at S108 on the β1 subunit[197]. Though it is now appreciated that long chain fatty acyl-CoAs can bind the ADaM site[42], A-769662 was the first synthetic small molecule to take advantage of this mode of activation. Salicylate, which is the active component of aspirin, can also bind to the ADaM site directly to increase AMPK activity[100]. With a significant deviation from the A-769662 backbone, the development of 991 led to significantly higher potency[198]. However, 991 still favoured β1-containing heterotrimers[198]. It was the development of MK-8722[199] and similar small molecules like PF-739[200] that ushered in pan-β activation, though MK-8722 still activated β1 complexes to a greater

extent[199]. The ability to activate β2 complexes meant that skeletal muscle AMPK, which exclusively expresses β2, could now be pharmacologically targeted. These activators led to significantly improved glucose sensitivity in mice and non-human primates in models of type 2 diabetes mellitus[199,200]. However, it also generated non-pathological cardiac hypertrophy and increased glycogen content. Even though cardiac hypertrophy can result from elite athletic training[201], regulatory agencies did not want to risk these off-target cardiac effects and the drug did not advance through clinical trials. Subsequent iterations on this structure have yielded ADaM site activators like SC4[202] with improved activation of β2 complexes. Interestingly, recent press releases from Nimbus Therapeutics have suggested that a newly developed compound may achieve highly-selective β2 activation, although this will have to be verified empirically.

While much of the focus on drug development has centered on AMPK-activating small molecules, AMPK inhibition may be beneficial in treating certain types of cancer[203]. The original, and most dubious, inhibitor of AMPK activity is compound C or dorsomorphin[204,205]. While it does inhibit AMPK activity, it also inhibits a host of other kinases to an equal or greater extent[206]. More recent developments include SBI-0206965[207], though this displays similar potency in inhibiting ULK1 activity[208], and BAY-3827, which is 5-10 times more potent than SBI-0206965; however, it suffers from poor bioavailability *in vivo*[209]. Regardless, these two inhibitors can serve as useful tools *in vitro*.

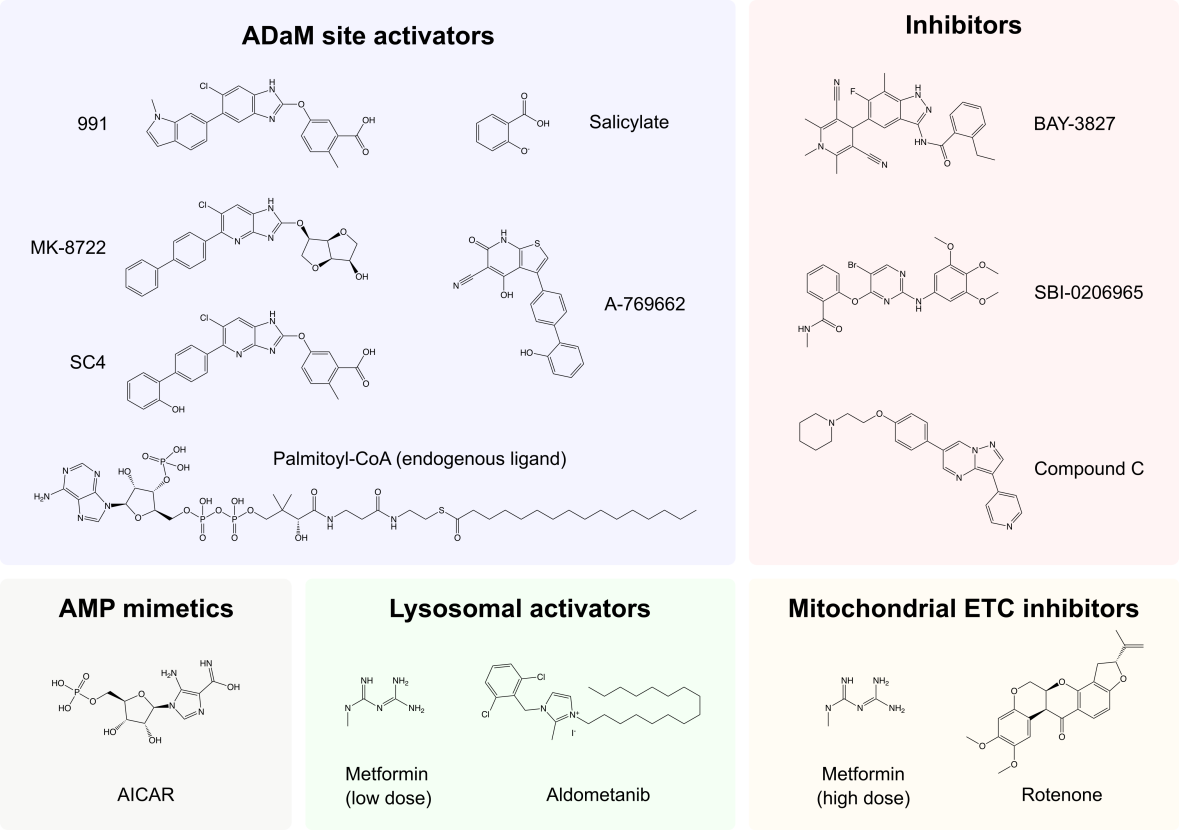

Figure 1.4: Chemical structures of common AMPK activators and inhibitors. Structures of direct activators and inhibitors (ADaM site, AMP mimetics, inhibitors) and indirect activators (lysosomal, mitochondrial electron transport chain inhibitors) of AMPK.

1.2.7 AMPK: conclusions

In the simplest of terms, AMPK is a stress-activated kinase, becoming activated due to changes in intracellular calcium, varying nutrient levels, or adenylate charge. The duration of activity, as well as the tissue type and nature of the stimulus, will dictate how and when AMPK becomes activated alongside its corresponding effects on cellular metabolism. Much of this introduction has focused on upstream inputs and specific regulation of AMPK in various nutrient-based contexts. Considering downstream AMPK targets now number well over 100, I will only discuss targets that have direct relevance to the disease states discussed in this thesis, those being atherosclerosis and *Salmonella enterica* infection, in their respective sections.

1.3 Atherosclerosis

The following section describes the major contributors to atherosclerotic cardiovascular disease with a particular focus on how myeloid cells derived from the hematopoietic system such as monocytes and macrophages drive initiation and accumulation of atherosclerotic plaque. The role of hypercholesterolemia and hematopoiesis in driving atherosclerosis, intracellular regulation of cholesterol homeostasis in macrophages, as well as common murine atherosclerosis models will also be discussed.

1.3.1 Atherosclerosis initiation and progression: a hematopoietic-driven pathology

Atherosclerotic cardiovascular disease (ACVD) continues to be one of the leading causes of death worldwide, contributing to stroke, myocardial infarction, and a variety of other clinical manifestations[210]. Atherosclerosis describes the accumulation of lipid and cells in the vasculature, leading to arterial stiffening and increased risk of thrombosis. Key to the initiation and progression of atherosclerosis is elevated circulating cholesterol levels. Early studies led by Russian pathologist Nikolai Anitschkow demonstrated that feeding rabbits cholesterol was sufficient to mimic atherosclerosis development, and also suggested that removal of cholesterol from the diet could lead to plaque regression[211]. The transport of cholesterol was later determined to reside within lipoproteins, particularly low-density lipoproteins (LDL)[212]. Seminal studies based on patients with familial hypercholesterolemia from Goldstein and Brown elucidated the core processing pathway of LDL via the LDL receptor (LDLR) in the liver[213]. However, the overabundance of circulating cholesterol is only one side of the atherosclerosis equation. Initial predictions of the inflammatory nature of atherosclerosis development came from Rudolf Virchow in the mid-19th century, although this wasn't widely supported until the

turn of the 21st century[214]. Regardless, it is now appreciated that atherosclerosis does not result from the passive accumulation of lipid within artery walls, but rather, the active, complex inflammatory response to lipid accumulation[215].

As alluded to above, LDL particles transport cholesterol through the circulatory system and act as the initiators of lesion development. Apolipoprotein B (ApoB) 100 forms the protein backbone of the LDL particle[216]. This becomes problematic upon entry into the subendothelial space of the vasculature, where basic residues on ApoB100 can interact with negatively charged proteoglycans in the extracellular matrix[217]. The retention of LDL particles can lead to their oxidation or enzymatic cleavage, producing modified LDL that can trigger inflammatory signaling[218,219]. The proteoglycans that trap LDL particles are produced by smooth muscle cells, which can also act as some of the earliest initiators of inflammatory signaling. Upon exposure to modified lipoproteins, these smooth muscle cells generate chemokines that attract monocytes to the point of inflammation[220–222]. Subsequent differentiation of monocytes to macrophages represents a key step in atherogenesis because they functionally differ from tissue resident adventitial macrophages that regulate vascular collagen deposition[223] and replicate locally within the intima[224,225]. Proliferation of monocyte-derived macrophages can overtake this resident macrophage population and fuel the inflammatory tone of the plaque[226]. Just as modified lipoproteins can trigger activation of smooth muscle cells, the same process applies to lesional macrophages. Cholesterol crystals[227], oxidized LDL[228], and dysregulation of cholesterol efflux[229], can prime and activate the NOD-, LRR- and pyrin domain-containing protein 3 (NLRP3) inflammasome, leading to processing and secretion of IL-1β. Furthermore, mTORC1 activity, which can support inflammatory signaling, is increased under high cholesterol conditions[230], and has been connected to worsened atherosclerosis following high protein diet

feeding due to elevated plasma leucine levels[231,232]. Additional inflammatory regulators such as receptor-interacting serine/threonine-protein kinase 1 can support atherosclerotic lesion development[233]. If circulating cholesterol levels are not restrained, macrophages and smooth muscle cells eventually become lipid laden and develop a foam cell phenotype. Foam cells in advanced plaques are made up of macrophages and smooth muscle cells that acquire macrophage markers[234–236]. Even though foam cells themselves display generally anti-inflammatory macrophage gene signatures[237], they are prone to undergoing cell death, which can itself be an inflammatory event[238]. Eventually, without adequate efferocytosis of dead cells, a necrotic core can form within the plaque that is secured by a fibrous cap produced by smooth muscle cells[239]. Should this fibrous cap thin, it can lead to thrombosis, clotting, and potential stroke or heart attack[240].

Given that monocytes and macrophages are some of the earliest initiators of atherosclerotic lesions, it is no surprise that hematopoiesis, or the production of circulating immune cells from a small subset of restricted stem cells, plays a key role in atherosclerosis progression. The hematopoietic system under homeostatic conditions is housed in the bone marrow. Here, hematopoietic stem and progenitor cells (HSPCs) respond to cues from the surrounding microenvironment that can bias their differentiation towards either myeloid or lymphoid lineages. In the context of atherosclerosis, hypercholesterolemia has been shown to bias HSPCs towards the myeloid lineage, resulting in overproduction of cells such as monocytes and neutrophils[241–243]. This can also result from endothelial cell dysfunction under hypercholesterolemic conditions as well[244]. Additionally, accumulation of HSPCs in the spleen can support extramedullary hematopoiesis, further supplying a pool of myeloid cells into circulation[245–247]. Together, these two reservoirs overproduce monocytes, but there is also

evidence that the cells are epigenetically wired to be more proinflammatory. The concept of trained immunity refers to the incorporation of epigenetic marks following exposure to an acute stimulus that generates a magnified response when cells are stimulated a second time[248]. Mice fed a western diet have been shown to develop trained immunity in HSPCs that leads to long term proinflammatory potentiation[249]. This phenomenon has also been observed following exposure to oxidized LDL[250] and hyperglycemia[251], stimuli that are highly relevant to hypercholesterolemic conditions. These long term effects can pass through generations, considering offspring display epigenetic hematopoietic rewiring and worsened atherosclerosis if their mothers consumed a western-type diet[252,253]. Beyond hypercholesterolemia-induced bias in progenitors, outgrowth of mutated hematopoietic stem cells (HSCs) can also contribute to myeloid bias. This is termed clonal hematopoiesis and is officially described as the expansion of HSC clones in the absence of other hematopoietic abnormalities. Mutations in epigenetic and signaling regulators such as *DNMT3A*, *TET2*, *ASXL1*, and *JAK2* are significantly associated with greater risk of developing coronary artery disease[254], though *DNMT3a* and *TET2* seem to be the most common by a wide margin[255]. While there is significant data suggesting that clonal hematopoiesis is a symptom, rather than a driver of atherosclerosis due to elevated HSC proliferation under hypercholesterolemic conditions[256], newer evidence from a longitudinal study in human patients[255] and in mice[257] demonstrates that it is more likely a driver of atherosclerosis. However, it is probable that greater hypercholesterolemia-dependent HSC proliferation, in addition to the accumulation of somatic mutations, contributes to the negative role of hematopoietic rewiring during atherosclerosis. All together, these immune-mediated mechanisms within and beyond the plaque microenvironment fuel the long term growth of atherosclerotic lesions in hypercholesterolemic settings.

1.3.2 AMPK as a regulator of cholesterol metabolism and its potential contribution to atherosclerosis

The dysregulation of circulating and intracellular cholesterol metabolism drives atherosclerosis. High levels of free cholesterol within the cell can be acutely toxic owing to its disruption of membrane composition, as well as potent modulation of metabolism downstream of oxidation by either enzymatic or ROS-generated oxysterol species[258]. As such, intracellular cholesterol levels are tightly regulated through coordinated uptake, esterification, storage, lipolysis, efflux, and *de novo* production of cholesterol species. AMPK has been implicated in a number of the regulatory steps in cholesterol metabolism, each potentially contributing to its role in exerting anti-atherosclerosis activity.

The main exogenous source of unmodified cholesterol in macrophages is LDL and is taken up through the LDLR system. Following binding of LDL to LDLR, the receptor and its ligand are internalized via the endomembrane system, whereby LDLR is returned to the plasma membrane in the recycling endosome[259]. Alternatively, modified forms of LDL such as oxidized or aggregated LDL can also be internalized, though this is facilitated by scavenger receptors that do not respond to LDLR feedback mechanisms[260,261]. One such feedback mechanism is through proprotein convertase subtilisin/kexin type 9 (PCSK9)[262,263], which can bind LDLR and prevent recycling to the cell surface; however, this is less relevant in macrophages due to low PCSK9 expression. Endosomes containing LDL can fuse with the lysosome, leading to the generation of free cholesterol from cholesteryl esters (CE) via the action of lysosomal acid lipase[264]. Lysosomal export of free cholesterol depends on the Niemann-Pick type C proteins, where Niemann-Pick type C2 is a soluble lysosomal protein that transfers free cholesterol to Niemann-

Pick type C1, a transmembrane protein, for release into the cytosol[265]. From there, cholesterol can be trafficked to either the plasma membrane, ER, or lipid droplets. In the ER, acyl-CoA:cholesterol acyltransferase 1 catalyzes the esterification of free cholesterol to CE[266], which given sufficient CE to phospholipid ratio, can bud and form nascent lipid droplets[267]. This pool of stored cholesterol in the form of CE can be liberated upon lipid droplet fusion with lysosomes in a selective form of autophagy referred to as lipophagy[268]. Alternatively, lipolysis initiated at the lipid droplet by any lipolysis regulators such as adipose triglyceride lipase can contribute to release of free cholesterol, as well as lipid droplet size reduction for more efficient lipophagy[269].

Beyond uptake, free cholesterol can also be synthesized *de novo* in an energetically costly pathway that converts acetyl-CoA into various downstream sterol and isoprenoid species, the latter of which are important for membrane localization of proteins[270]. The rate limiting step in *de novo* cholesterol synthesis, otherwise known as the mevalonate pathway, is catalyzed by HMGCR, which reduces HMG-CoA to mevalonate, consuming NADPH in the process. HMGCR is also the target of the majority of statin classes, which remain some of the most highly prescribed drugs in the world for treating reducing hypercholesterolemia[271,272]. HMGCR is an ER transmembrane protein that is exquisitely responsive to changes in cholesterol and oxysterol levels, leading to transcriptional, post-transcriptional, translational, and degradative regulatory mechanisms[273,274]. From a protein stability perspective, high sterol conditions lead to insulin-induced gene 1 (INSIG1) stabilization and binding to HMGCR[275]. This brings one of three E3 ubiquitin ligases into close proximity to HMGCR, gp78[276], TRC8[277], or RNF145[278], to facilitate ubiquitination and subsequent ER-associated degradation in the 26S proteasome. These interactions do not occur under sterol-depleted conditions, allowing for stabilization of HMGCR protein levels and elevated cholesterol synthesis. Additionally, HMGCR is regulated at the

transcriptional level by the ER-bound transcription factor sterol regulatory element-binding protein 2 (SREBP2), which is itself highly sensitive to sterol levels. Here, an adaptor protein called SREBP cleavage-activating protein (SCAP) binds to COPII vesicles and SREBP2 within the ER membrane[279,280]. Under high sterol conditions, INSIG1 binds to SCAP and retains SREBP2 in the membrane, opposing transcription of cholesterol synthetic genes[281]. When sterols are depleted, SCAP undergoes a conformational change, supporting an interaction with COPII vesicles that facilitate the transfer of SREBP2 to the Golgi, where it is cleaved and activated by Golgi-specific proteases[282]. The cleaved N-terminus of SREBP2 then translocates to the nucleus, where it stimulates transcription of cholesterologenic genes such as *HMGCR*[283]. Notably, fatostatin represents a statin-family drug that retains SREBPs in the ER, contrasting with other statins that target HMGCR activity[284].

As cholesterol cannot be enzymatically degraded in mammalian cells, it is essential to export excess cholesterol to avoid intracellular accumulation, as is a hallmark in atherosclerotic macrophages. There are two main cholesterol efflux transporters in macrophages, those being ATP-binding cassette transporter (ABC) A1 and ABCG1, which facilitate the transfer of intracellular free cholesterol to extracellular acceptors ApoA1 and HDL, respectively[285]. The control over this process is governed by the oxysterol-sensitive transcription factors, the liver X receptors (LXR)[286]. Upon oxysterol binding to LXRs, they heterodimerize with retinoid X receptors and bind to LXR-responsive elements, triggering transcription of target genes such as *Abca1* and *Abcg1* and ultimately increasing cholesterol efflux[287,288]. This is part of a larger process termed reverse cholesterol transport, wherein HDL cholesterol is transported back to the liver to facilitate bile acid production and excretion via the intestines[289].

This combination of cholesterol uptake, esterification, storage, lipolysis, *de novo* synthesis, and efflux coordinately ensures that cellular cholesterol levels do not fall out of an acceptable range. AMPK foreseeably impacts intracellular cholesterol homeostasis across a broad range of regulators that affect these processes, although how these work in concert during atherosclerosis remains obscure. First, AMPK has been shown to associate with C-terminus of LDLR itself[290]. However, this AMPK-LDLR interaction were not explored further. AMPK can also regulate lipid droplet dynamics in several ways. AMPK regulates the release of free cholesterol and fatty acids by phosphorylating the lipolysis regulators hormone sensitive lipase and adipose triglyceride lipase[291]; however, only the latter is activated by AMPK. It is worth noting that, in spite of its nomenclature, hormone sensitive lipase and adipose triglyceride lipase are both readily expressed in macrophages[52]. Furthermore, AMPK-mediated phosphorylation of perilipin 2 and 3 has been shown to support lipolysis of lipid droplets[292,293], where additional phosphorylation of CHK2α leads to perilipin 2/3 degradation[294]. In response to starvation conditions, AMPK has also been shown to redistribute lipid droplets along microtubules with implications on β oxidation[295]. AMPK phosphorylation of ORP8 was recently shown to be supportive of lipophagy initiation[296]. Considering lipolysis often works in concert with lipophagy[269], AMPK may exert synergistic functions in supporting lipid droplet catabolism.

Beyond regulating cholesterol storage and lipolysis, perhaps the most well characterized interaction between AMPK and cholesterol metabolism is its direct phosphorylation of HMGCR, which occludes binding of HMG-CoA within the active site, preventing mevalonate production[297]. However, AMPK regulation of HMGCR may not be limited to activity suppression. AMPK phosphorylation of INSIG1 leads to elevated INSIG1 stability, potentially increasing HMGCR ubiquitination and targeting for degradation[298]. While this was not

experimentally demonstrated, AMPK phosphorylation of INSIG1 did have a marked effect on SREBP processing[298]. Considering INSIG1 regulates SREBPs through binding to SCAP, as well as HMGCR by facilitating contact with E3 ubiquitin ligases that target it for degradation, AMPK may exert multiple layers of regulation on *de novo* cholesterol synthesis. There is also evidence for AMPK phosphorylating nuclear SREBP2, even though an exact site was not identified and this remains somewhat speculative[299]. The final link between AMPK and cholesterol homeostasis relates to cholesterol efflux. AMPK activation has been shown to increase LXR protein levels, potentially in a BRCA1/BRD4-dependent mechanism that remains poorly defined[300,301]. However, this does align with functional improvements observed in cholesterol efflux following AMPK activation[300,302]. Collectively, AMPK is likely involved in many aspects of cholesterol regulation, making it imperative that specific models are applied to determine the physiological role for these phosphorylation sites *in vivo* (Figure 1.5).

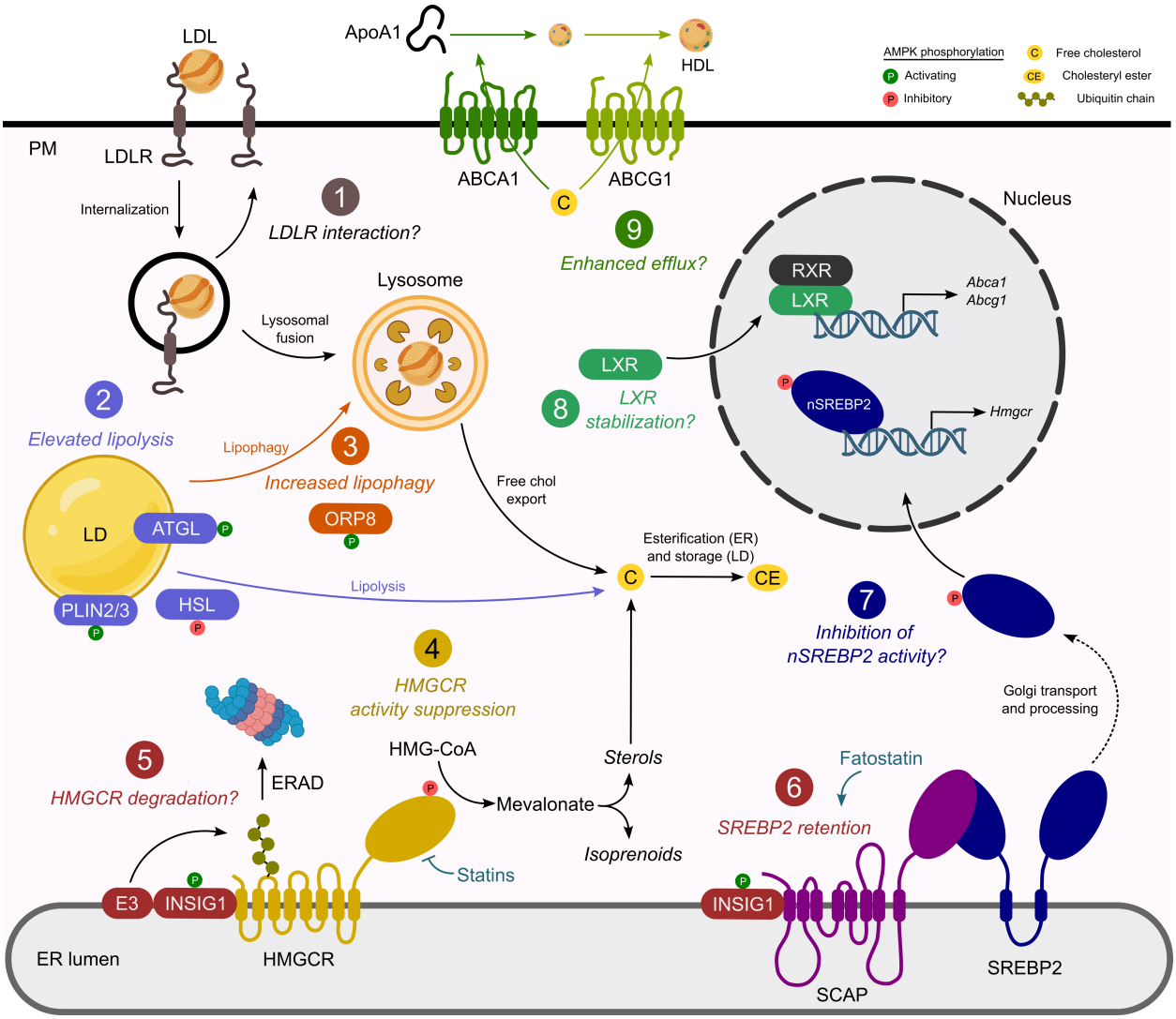

Figure 1.5: AMPK regulates cholesterol metabolism at multiple steps. Cholesterol is taken up into cells via LDL binding to LDLR and internalization into the endosomal compartment. AMPK interacts directly with the LDLR C-terminus (1). Following lysosomal fusion, CE is broken down into free cholesterol and is exported into the cytosol. This cholesterol can be re-esterified in the ER and stored in lipid droplets (LD). CE stored in lipid droplets can be released through either elevated lipolysis, which is regulated by AMPK targets such as ATGL, HSL, or perilipin 2/3 (2), or through autophagic breakdown of lipid droplets via lipophagy, of which the AMPK target ORP8 is a positive regulator (3). *De novo* cholesterol and isoprenoid synthesis is fueled by HMGCR-mediated reduction of HMG-CoA to mevalonate, where AMPK can directly inhibit this process through phosphorylation (4). INSIG1 directly regulates HMGCR protein stability, as well as SREBP2 retainment in the ER. AMPK increases INSIG1 protein stability through phosphorylation, potentially increasing HMGCR degradation (5) or SREBP2 retention (6). Under low sterol conditions, SCAP-SREBP2 translocates to the Golgi, is cleaved to its active nuclear form (nSREBP2), then triggers transcription of cholesterologenic genes such as *HMGCR*. AMPK has been implicated in directly phosphorylating and inhibiting nSREBP2 (7). AMPK activation can also result in stabilization of LXR, leading to enhanced transcription of *Abca1* and *Abcg1* (8), which may have functional implications in the export of intracellular free cholesterol to acceptors ApoA1 and HDL (9). Only canonical LDLR-mediated cholesterol uptake depicted.

1.3.3 Mouse models of atherosclerosis and our current understanding of AMPK regulating disease

As human atherosclerosis development takes place over decades, it is difficult to physiologically model the disease in animals. Diets rich in cholesterol and lipid such as a western diet (WD) do not increase circulating cholesterol levels sufficiently to induce rapid atherosclerosis in mice, unless employing a supraphysiological 1.25% cholesterol diet[303]. For reference, most chow diets contain no added cholesterol, and the recommendation for human consumption is below 0.1%[304]. Mouse susceptibility to developing atherosclerosis depends on the strain, where C57BL/6J mice were more prone to develop atherosclerotic lesions[303]. Additionally, matching the lipoprotein profile from mice to humans remains a challenge. At baseline, mice transport cholesterol primarily in high-density lipoproteins (HDL), whereas humans transport a majority in LDL[305]. This is due in part to human expression of cholesterol ester transfer protein, which can facilitate the transport of CE from HDL to LDL[306]. Additionally, human plasma cholesterol concentrations are approximately twice that of mice[305].

Thus, there was a need for genetic models to both accelerate disease and more accurately model the lipoprotein profile relevant to human atherosclerosis. The first widespread murine atherosclerosis model was the *Apoe*$^{-/-}$ model, where ApoE is an integral component of most lipoproteins except for LDL[307,308]. Mice lacking ApoE develop atherosclerosis spontaneously, even in the absence a high cholesterol diet, due to sizable increases in very low-density lipoproteins (VLDL). An alternative model discovered shortly thereafter was the *Ldlr*$^{-/-}$ model [309]. Considering hepatic LDL clearance is principally responsible for controlling systemic LDL levels, its deletion leads to strong increases in circulating LDL[309]. In contrast to the *Apoe*$^{-/-}$ mice, *Ldlr*$^{-/-}$ mice require a high-fat, high-cholesterol diet to develop advanced atherosclerosis,

representing a severe, but less drastic model than *Apoe*$^{-/-}$ mice[309]. However, the lipoprotein profile is more similar to that of humans, where LDL drives atherosclerosis, rather than VLDL in the case of *Apoe*$^{-/-}$ mice. ApoE is also involved in HDL formation, which when absent, leads to dysfunctional HDL and therefore reduced reverse cholesterol transport[310]. Furthermore, ApoE is highly expressed in myeloid cells and contributes to hematopoietic regulation[311]. Strikingly, a bone marrow transplant (BMT) of WT bone marrow into *Apoe*$^{-/-}$ mice shields *Apoe*$^{-/-}$ mice from atherosclerosis development[312]. Due to these additional confounding factors observed in *Apoe*$^{-/-}$ mice, subsequent attempts at mouse model generation have focused on mimicking the *Ldlr*$^{-/-}$ lipoprotein phenotype due to its similarity to human disease.

LDLR recycling in hepatocytes is regulated by PCSK9, which when absent causes autosomal dominant familial hypercholesterolemia[313]. Observations that PCSK9 overexpression recapitulated the phenotype of the *Ldlr*$^{-/-}$ mouse[314] eventually led to the development of a reliable adeno-associated virus (AAV)-based gain of function PCSK9 variant (*Pcsk9*-AAV) that similarly mimics the *Ldlr*$^{-/-}$ background[315]. This model avoids the need to cross mice onto an *Ldlr*$^{-/-}$ background and also does not affect germline expression of LDLR. However, PCSK9 can be proinflammatory on its own, as patients administered PCSK9 inhibitors have reduced proinflammatory cytokines within carotid plaques[316]. Additional methods to increase circulating cholesterol levels include administration of antisense oligonucleotides targeted against LDLR[317], as well as CRISPR-AAV approaches to generate liver-specific deletion of LDLR[318]. In general, these models induced hypercholesterolemia, though to a lesser extent than in *Ldlr*$^{-/-}$ mice. Despite the differences between mice and humans, this collection of mouse models can generally replicate the most relevant pathological signatures observed in human coronary artery disease[319].

The role of AMPK in regulating atherosclerosis is somewhat conflicting. Pharmacological activation of AMPK using direct and indirect activators from the initiation of atherosclerosis strongly supports an anti-atherogenic effect of AMPK activity [299,320–323]. However, targeted approaches using tissue-specific and knock-in models have yielded contrasting results.

Myeloid AMPK α1 deletion led to increased atherosclerosis on an *Ldlr*$^{-/-}$ background, though the effect was subtle, and traced to changes in inflammatory gene transcription[324], of which AMPK is an established regulator[325]. In contrast, AMPK α1 deletion on an *Apoe*$^{-/-}$ background attenuated atherosclerosis, in part due to an apparent increase in monocyte to macrophage differentiation[326]. This was supported by an additional *Apoe*$^{-/-}$ study[327]. Surprisingly, even myeloid AMPK α2 deletion, despite α2 being lowly expressed in myeloid cells, led to reduced atherosclerosis burden on an *Apoe*$^{-/-}$ background[328]. Thus, there appears to be distinct differences in how AMPK affects atherosclerosis depending on the model of hypercholesterolemia. In line with this, work from our lab has demonstrated that combinatory myeloid deletion of α1 and α2 subunits has no effect on *Pcsk9*-AAV-induced atherosclerosis[329]. This study also did not observe significant atheroprotective effects following administration of an ADaM site activator six weeks after inducing hypercholesterolemia[329]. More studies will be required to determine if AMPK activation can feasibly reduce lesion sizes if started after the initiation of atherosclerosis.

Beyond the myeloid compartment, endothelial AMPK has been shown to be atheroprotective due to AMPK activation following laminar flow disruption. This was mechanistically tied to an increase in glycolysis that ensured proper endothelial barrier integrity in atheroprone regions of the vasculature[330]. However, smooth muscle cell deletion of AMPK α2

reduced atherosclerotic burden in *Apoe*$^{-/-}$ mice, an effect mapped to increased plaque stability[331]. Again contrasting with these results, AMPK α2 knockout mice, which would theoretically affect endothelial cells and smooth muscle cells to a greater extent than myeloid cells, developed worsened atherosclerosis on an *Ldlr*$^{-/-}$ background due to elevated ER stress[332]. A link between *Prkaa1* expression and miR-33 has also been made, where miR-33-induced suppression of *Prkaa1* alters macrophage polarization and atherosclerosis in an *Ldlr*$^{-/-}$ model. However, the effect on protein level regulation was less clear[333]. Therefore, despite systemic administration of pharmacological activators leading to reduced atherosclerosis, tissue specific knockouts on an *Apoe*$^{-/-}$ background are generally supportive of a pro-atherogenic role for AMPK. This contrasts with most studies based on *Ldlr*$^{-/-}$ or *Pcsk9*-AAV backgrounds, where the opposite is observed. Future studies must be directed towards comparing these models in the context of tissue-specific AMPK disruption to clarify these inconsistencies.

1.4 Host defense against *Salmonella enterica* infection

The following section departs from the chronic inflammatory state induced by hypercholesterolemia, and ventures into the tactical triggering of acute inflammation by the gram-negative bacteria *Salmonella enterica*. Topics will include *Salmonella enterica* virulence mechanisms *in vivo*, as well as macrophage defenses employed to fight intracellular *Salmonella enterica* replication alongside what is known about AMPK and regulating bacterial infection.

1.4.1 Historical discovery of salmonellosis and classification

Salmonella is a genus of gram-negative bacilli in the *Enterobacteriaceae* family that typically causes gastroenteritis in humans, or in the case of some serovars, typhoid fever. *Salmonella* was first discovered in 1855 and subsequently named after an American pathologist Daniel Elmer Salmon. The *Salmonella* genus is divided into two main species, *Salmonella enterica* and *Salmonella bongori*, of which *Salmonella enterica* can be further subdivided into six subspecies including *S. enterica* subsp. *enterica*, *S. enterica* subsp. *salamae*, *S. enterica* subsp. *arizonae*, *S. enterica* subsp. *diarizonae*, *S. enterica* subsp. *houtenae*, and *S. enterica* subsp. *indica*. Of these, *Salmonella enterica* subsp. *enterica* is responsible for over 99% of the infections in mammals and humans[334]. Serovars, which are based on antigenicity of the O antigen (somatic antigen; a component of lipolysaccharide), and H antigens (flagella antigen), define individual subtypes of *Salmonella*, and currently number at over 2600, 1600 of which belonging to *Salmonella enterica*[335].

The serovars of greatest concern to human health are *Salmonella enterica* subsp. *enterica* serovar Typhi, *Salmonella enterica* subsp. *enterica* serovar Enteritidis, and *Salmonella enterica* subsp. *enterica* serovar Typhimurium (*S.*Tm). These pathogens account for over 150,000 global

deaths annually, while the number of cases in Canada numbers close to 90,000[336]. For the purposes of this thesis, though distinct serovars exhibit different virulence mechanisms, the following sections will focus on *S*.Tm.

1.4.2 Salmonella infection dynamics in vivo

Initial infection in the gastrointestinal tract

S.Tm and related non-typhoidal *Salmonella enterica* species are food-borne pathogens, and as such have developed sophisticated virulence mechanisms to outcompete intestinal microbiota and invade the epithelium and immune cells in the gut. Intestinal microbiota diversity can oppose outgrowth of *S*.Tm by competing for nutrient resources[337], prompting the need for prior antibiotic administration in some mouse models of *S*.Tm infection[338]. To circumvent this colonization resistance, *S*.Tm relies on host inflammatory responses to facilitate a successful infection. Inflammation in this case is a tissue-specific response to infection, resulting in cytokine production that attracts immune cells to the point of infection[339]. *S*.Tm invasion is initiated in the Peyer's Patches, where it employs a type three secretion system to inject *Salmonella* pathogenicity island (SPI)-1 effector proteins into M cells to facilitate infection[340]. Through activation of Wnt/β-catenin signaling, *S*.Tm can also enhance epithelial-to-mesenchymal transition of gut epithelial cells and increase the number of susceptible M cells[341]. Within one hour of invasion, M cells lyse, resulting in a gap in the follicle-associated epithelium that allows *S*.Tm to invade adjacent enterocytes. This generates SPI-1-dependent inflammation, triggering myeloid differentiation primary response 88 (MyD88)-related inflammatory signaling[342]. Inflammation serves *S*.Tm in several ways. First, increased infiltration of neutrophils into the gut lumen results in ROS that generates tetrathionate, which can serve as a

terminal electron acceptor in *S*.Tm respiration[343]. Additionally, mucins are upregulated during intestinal inflammation and provide amino acids that *S*.Tm seeks out for survival[344]. This occurs in a chemotaxis-dependent manner, in which nutrient ligands transmit signals to flagellar machinery and trigger movement towards these nutrients. *S*.Tm expresses eight established chemosensory receptors, of which three have been demonstrated to affect fitness during intestinal colonization[345,346]. Among amino acids, aspartate is particularly important for *S*.Tm-induced inflammation and is imported alongside malate[347]. Aspartate can then be used as a fuel source for fumarate-dependent anaerobic respiration downstream of commensal bacterial lysis[348]. One of the most strongly induced proteins by epithelial cells during the inflammatory response is the antimicrobial lipocalin-2, which is secreted into the intestinal lumen to limit bacterial iron uptake[349]. To counter this, *S*.Tm expresses an enzyme that can oppose lipocalin-2, providing a competitive advantage[350]. Emerging evidence also supports a role for galvanotaxis, or the influence of electrical potentials around certain cells, to direct invasion[351,352]. In this model, certain areas of the gut such as the follicle associated epithelium, which contains M cells, exhibit differing electrical potential relative to other villi-covered areas[352]. Therefore, *S*.Tm is well equipped to deal with host antibacterial responses in the gut, and employs a combination of energy taxis, chemotaxis, and galvanotaxis-based strategies to outcompete intestinal microbiota to invade the intestinal epithelium.

Systemic infection and long-term persistence

Once *S*.Tm escapes through the gut, it enters systemic circulation through a still unclear mechanism. However, the mesenteric lymph nodes, which serve as a transition point between the gut and systemic circulation, can harbour *S*.Tm for over a year in mouse models of persistent

infection[353]. Other work has also pointed to the hepatobiliary system as a niche for persisting *S*.Tm due to a lack of bacterial killing mechanisms[354]. Regardless, macrophages represent a primary reservoir for *S*.Tm, in which non-replicating *S*.Tm can establish long-term persistence and protection from antibiotics[355]. Macrophage subtypes *in vivo* are complex but can be approximated to align with well-established *in vitro* polarization states. M1-like macrophages are canonically induced through exposure to lipopolysaccharide (LPS) and represent a classical antibacterial response. This is accompanied by aerobic glycolysis and production of proinflammatory cytokines. M2-like macrophages, on the other hand, are generated through IL-4 exposure and resemble macrophage populations specialized in wound healing[356]. Of note, most tissue-resident macrophages exhibit more M2-like characteristics at baseline, potentially due to close association with resident B cells[357]. Granulomas are microstructures comprised of macrophages and other immune cells and can serve as a protection zone for *S*.Tm. Interestingly, their long-term persistence can be traced to residence within macrophages expressing inducible nitric oxide synthase (iNOS), and are physically distant from Th1 cells that may be required for efficient bacterial killing[358]. Despite expression of iNOS, which is typically an M1-related marker, M2 gene programs are more closely associated with permissiveness over the long term[359,360]. *S*.Tm enforces this state through SPI-2-dependent metabolic rewiring to make macrophages more permissive to infection and help *S*.Tm survive antibiotic administration[361]. It is worth noting that only certain mouse models can develop persistent infection. Expression of *Nramp1*, which is an iron transporter essential for bacterial killing, can dictate whether a mouse strain is susceptible to *S*.Tm infection[362,363]. The commonly used C57BL/6J mouse line does not express *Nramp1*, and therefore succumbs quickly to even low amounts of bacteria[364]. Altogether,

S.Tm uses a combination of virulence mechanisms to invade the gut and establish long-term reservoirs in macrophages.

1.4.3 Macrophage killing mechanisms downstream of Salmonella infection

As established above, macrophages are the primary reservoir for *S*.Tm *in vivo*. The give and take of macrophage killing mechanisms versus *S*.Tm evasion dictates whether a successful cellular, and ultimately, systemic infection will ensue[365]. Macrophages attempt to phagocytose and kill *S*.Tm or undergo cell death themselves in order to transmit signals to nearby immune and non-immune cells. The following section details how *S*.Tm affects these processes and how it generates a protective niche that allows it to survive intracellularly.

<u>*S*.Tm and PRR signaling</u>

Pattern recognition receptors (PRRs) become activated upon engagement of their cognate pathogen-specific ligands. In the case of *S*.Tm, it triggers signaling through several toll-like receptors (TLRs), NOD-like receptors (NLRs), and cytosolic nucleic acid sensors. Upon binding to TLRs, signals are either transduced through MyD88, which is associated with classical induction of nuclear factor kappa B (NF-κB)-mediated transcription, or TIR-domain-containing adaptor-inducing interferon-β (TRIF), which stimulates an antiviral type I interferon response. *S*.Tm flagellin, lipoproteins, and genomic DNA triggers TLR5, TLR2, and TLR9 activation, respectively, all of which lead to MyD88 activation[366–368]. *S*.Tm LPS activates TLR4/CD14, leading to both MyD88 and TRIF-dependent signaling[342,368–370]. These overlapping TLRs trigger robust induction of NF-κB-mediated transcription that increases protein levels of antimicrobial proteins such as NADPH oxidase 2 (NOX2) and iNOS, inflammasome components,

proinflammatory cytokines, and metabolic regulators[371]. However, TLR-dependent phagosomal acidification is also required for *S.*Tm expression of SPI-2 genes that support intracellular survival[368]. Outside of TLRs, NLRs include a family of cytosolic PRRs, of which *S.*Tm can activate the NLRP3 and NLRC4 inflammasomes due to sensing of bacterial mRNA[372,373], flagellin[374,375], as well as the SPI-1 needle and inner rod proteins[376–378]. Inflammasome activation leads to caspase-1 activation and cleavage of the proinflammatory cytokines pro-IL-1β and pro-IL-18 to their active forms, as well as gasdermin D, which creates pores through which IL-1β and IL-18 can be secreted[379,380]. Caspase-1 in particular is important in the early stages of infection, while caspase-4 is more relevant as the infection progresses[381]. Additionally, cGAS-STING-mediated sensing of mitochondrial and degraded bacterial DNA contributes to the full type I interferon response following *S.*Tm infection[382].

One of the outputs of PRR signaling is cytokine production designed to alert other cell types to the presence of *S.*Tm. Unlike neutrophils or some T cells, which can store cytokines in granules that are released upon an intracellular trigger, macrophages rely on constitutive secretion of cytokines following their *de novo* synthesis and subsequent endosomal trafficking. Canonical constitutively secreted cytokines include IL-6 and tumour necrosis factor alpha (TNF-α). IL-6 is an example of a soluble cytokine that is generated and processed through the recycling endosome before fusing with the plasma membrane and releasing into the extracellular space[383]. TNF-α, in contrast, is trafficked as a membrane protein, which is then cleaved by matrix metalloproteinase 9 to trigger its release[383]. However, to increase secretion of either of these cytokines, there must be a corresponding increase in transcription and translation. This is accomplished via activation of NF-κB and Janus Kinase-signal transducer and activator of transcription (STAT)-mediated transcription[384]. AMPK activation has been associated with

suppression of both of these pathways, thereby exerting general anti-inflammatory effects, though the precise mechanisms remain unclear. AMPK activation negatively regulates NF-κB transcriptional activity for select inflammatory targets such as *Il6* and *Il12b*, while sometimes being observed to increase IL-10 secretion in innate immune cells[325,385]. Additionally, AMPK can inhibit STAT1 nuclear localization, potentially explaining reductions in proinflammatory transcript expression[386]. Work from adipocytes supports a model in which AMPK inhibits STAT3 phosphorylation downstream of IL-6 receptor signaling, as well as preventing NF-κB nuclear translocation[387]. Collectively, macrophages sense *S*.Tm through a multitude of inputs, leading to complex downstream signaling that integrates *S*.Tm invasion with gene expression changes, though the relevance of AMPK in this process requires further investigation.

S.Tm phagocytosis and the role of autophagy in bacterial killing

Macrophage phagocytosis of gram-negative bacteria occurs through several distinct receptors depending on whether the bacterium has been modified. Both antibody-mediated opsonization and complement-mediated coating of bacteria can render *S*.Tm an easier phagocytosis target. The Fc receptors, of which FcγRI, FcγRII, and FcγRIII are expressed in macrophages, mediate antibody-dependent uptake of pathogens[388]. Meanwhile, β2 integrins such as CD11b and CD11c can serve as complement receptors[389]. TLR4, described above for its role in sensing LPS and transmitting pathogenic signals, also plays a direct role in the uptake of gram-negative bacteria through one of its adaptors[390].

Following uptake into macrophages, *S*.Tm forms what is called the *Salmonella*-containing vacuole (SCV) that depends on cues from phagosome acidification[368]. This is unique

to *S*.Tm when compared with other intracellular bacterial pathogens such as *Shigella* spp, which instead opt to lyse the phagosome to escape into the cytosol[391]. The timeline for SCV development typically includes an initial phase within 30 min of uptake, wherein the membrane is enriched in early endosomal markers such as Rab5. Within another 30 min, late endosome or lysosomal markers such as V-ATPase are enriched on the SCV, which functions to reduce the luminal pH while the SCV translocates to a juxtanuclear position[368,392]. However, hundreds of host proteins in the endomembrane system have been identified as targets of *S*.Tm effectors during the uptake of *S*.Tm and establishment of the SCV, the majority of which remain uncharacterized[393]. During phagosomal acidification, one survival mechanism *S*.Tm employs is to decrease its cytosolic pH to handle acid stress[394]. Additional contact points with V-ATPase exist, where SopF expression and modulation of V-ATPase ADP-ribosylation leads to inhibition of xenophagy[395]. Also present in the mature phagosome are numerous antibacterial peptides such as defensins[396].

Autophagic degradation of internalized bacteria represents a key antibacterial defense pathway[397,398]. Termed xenophagy, this specialized form of autophagy exhibits several key differences from macroautophagy in the context of *S*.Tm infection. To replicate and spread, *S*.Tm must escape the SCV niche and enter the cytosol. Mammalian cells can sense cytosolic *S*.Tm through galectin family proteins, which specialize in binding carbohydrates[399]. SCV-induced damage to the endomembrane system often occurs while it is being established, resulting in recognition by host galectin-8[400]. This leads to an association with the autophagy receptors NDP52, optineurin, and p62, fueling autophagosome engulfment[400–402]. This is also accompanied by mTORC1 inactivation[403], as well as potential galectin-9-mediated activation of AMPK through TAK1, though this was not explicitly tested with *S*.Tm[68]. Changes in host ubiquitin

signaling is another hallmark of *S*.Tm infection, and is required for coating of cytosolic bacteria prior to xenophagy[404,405]. This is accomplished by a variety of E3 ubiquitin ligases that either recognize and ubiquitinate *S*.Tm directly or indirectly[406]. Beyond xenophagic degradation, there is also evidence that ubiquitin chains can be physically removed in an ATP-dependent process that causes bacterial cell lysis[407]. Linear chains in particular are also important for activating NF-κB signaling, fueling the inflammatory response to *S*.Tm[408,409].

The role of AMPK in macroautophagy, and by extension, xenophagy, requires revision given recent findings. Macroautophagy consumes large amounts of ATP, and while it is activated under prolonged starvation conditions and can help restore cellular energy balance, it is not an energy-efficient process in the short term. Acute glucose starvation activates AMPK and inhibits mTORC1, which were long presumed to exert opposing effects on autophagy induction through AMPK activation and mTORC1 inhibition of their shared target, unc-51-like autophagy-activating kinase 1 (ULK1)[410]. However, in recent years it has become clear that glucose starvation, rather than inducing autophagy as is observed in amino acid starvation, inhibits autophagic flux[411–415]. AMPK drives this process by inhibiting autophagosome maturation, which is observable downstream of glucose starvation and allosteric AMPK activation, though AMPK likely exerts some inhibitory effect during amino acid withdrawal as well[415–417]. This is due to AMPK phosphorylation of ULK1 S556 and T660, but only in the presence of the mTORC1 phosphorylation site S758, leading to the stabilization of the AMPK-ULK1 interaction and inhibition of ULK1 activity[417,418]. This inhibition is likely the result of ULK1 sequestration by scaffolding protein 14-3-3, which also depends on AMPK-mediated S694 phosphorylation[419,420]. Though AMPK has generally been considered to have pro-xenophagy activity[421], it is important to contextualize these findings within the framework that AMPK

acutely inhibits ULK1 activity. Since ULK1 is required for xenophagy induction[422], there may be some anti-xenophagic effects of AMPK activation. From another angle, AMPK was recently shown to directly phosphorylate parkin to induce selective mitophagic degradation[420]. Parkin is an E3 ubiquitin ligase responsible for coating *S*.Tm in ubiquitin to fuel the host xenophagy response[423], which could positively link AMPK and xenophagy. Regardless, more work will be required to determine the role of AMPK in bacterial-related autophagy.

Immunometabolic changes downstream of *S*.Tm

Engagement of various PRRs can trigger signaling downstream of *S*.Tm engagement that drastically rewires macrophage metabolism to fulfill various antibacterial functions. Downstream of TLR4, induction of aerobic glycolysis leads to increased glycolytic flux without a corresponding increase in oxidative phosphorylation, despite oxygen being readily available. This accomplishes several aims. First, it increases flux through the tricarboxylic acid (TCA) cycle, which leads to increased abundance of key antimicrobial metabolites in succinate, fumarate, and the product of *cis*-aconitate decarboxylation, itaconate. The latter is the most highly induced metabolite in macrophages following LPS treatment[424,425], where itaconate can influence metabolism through electrophilic modification of proteins[426,427] and direct inhibition of succinate dehydrogenase[428]. Part of this increase in itaconate following *S*.Tm infection is dependent on transcription factor EB (TFEB)[429]. Interestingly, AMPK directly phosphorylates an upstream regulator of TFEB to increase its activity[195]. Given the importance of itaconate for generating anti-bacterial responses, diverse bacterial species including *S*.Tm have developed itaconate degrading pathways to combat itaconate production[430,431]. Additionally, one of the consequences of increasing itaconate is succinate accumulation[428]. This has been shown to be a

key signal for *S*.Tm pathogenesis, since strains lacking a succinate transporter exhibit impaired survival[432]. It also plays an essential role in augmenting IL-1β production via HIF-1α[433]. Furthermore, the SPI-1 effector SopE2 inhibits serine synthesis while supporting glycolysis [434]. Another consequence of elevated flux through glycolysis is increased lactate production. Exactly how glycolysis is induced by *S*.Tm is still somewhat obscure, though glycolytic flux is primarily governed by upper glycolysis and lactate excretion[435]. In line with this, phosphorylation and activation of the glycolytic enzyme PFKL following LPS treatment has been shown to increase production of FBP[436]. During *S*.Tm infection, lactate can independently activate SPI-2 genes, notably increasing SteE expression and promoting M1-like macrophage polarization[437]. These observations suggest that macrophage glycolytic rewiring is not only a byproduct of TLR engagement, but rather, an intentional consequence of *S*.Tm virulence mechanisms.

Another metabolic pathway strongly induced during infection is arginine metabolism. Arginine is a multifaceted amino acid that, in the context of bacterial infection, is taken up into cells and processed by iNOS to generate nitric oxide (NO) and citrulline[438]. NO can be converted into reactive nitrogen species (RNS) that have both antibacterial and direct effects on metabolism. Accumulated NO can directly inhibit mitochondrial aconitase 2 and inhibit the electron transport chain[439,440]. With an increase in NO, there is a corresponding increase in iNOS-generated citrulline that is metabolized in two ways. The first is through elevated expression of the enzyme laccase domain containing 1, which catalyzes the conversion of citrulline to ornithine and isocyanate [441,442]. This step links the early proinflammatory increase in NO and citrulline to the immunosuppressive effects of polyamine accumulation later in the inflammatory response [443,444]. The second route for citrulline metabolism is through the arginosuccinate shunt, wherein arginosuccinate synthase 1 (ASS1) is induced to generate

arginosuccinate from citrulline [445]. Processing of arginosuccinate also leads to fumarate production, a pathway that is important for inducing the interferon response [446]. Collectively, *S*.Tm infection in macrophages leads to drastic rewiring of glycolytic, TCA cycle, and arginine metabolism.

ROS and RNS generation in response to *S*.Tm

ROS and RNS play key roles in the antibacterial response within macrophages. ROS refers to any oxygen species that is more reactive than molecular oxygen, and includes superoxide, hydroxyl and peroxy radicals, as well as non-radical H_2O_2, which unlike other ROS forms, can diffuse across membranes[447]. Though ROS are produced constantly at low levels as a byproduct of mitochondrial respiration or β oxidation, TLR engagement can augment mitochondrially-produced ROS[448] and directly modulate NF-κB signaling[449]. The main targeted producer of superoxide in phagocyte is NOX2, which when mutated causes severe persistent bacterial and fungal infections[450]. Additional superoxide may be produced by xanthine oxidase, which can support proinflammatory cytokine production[451]. The manner in which NOX2-derived ROS kills *S*.Tm is somewhat contentious, but it is likely a combination of affecting *S*.Tm ΔpH, as well as inducing DNA and protein damage[452–454]. However, *S*.Tm counters this respiratory burst by shifting metabolism to favour glycolysis[453]. Regardless, real-time measurements of oxidative and nitrosative stress support the view that when *S*.Tm resides within the SCV, it experiences minimal redox stress owing to a subset of SPI-2-dependent effectors[455]. Therefore, *S*.Tm exhibits several defense mechanisms against the antibacterial effects of host-derived ROS and RNS.

Macrophage cell death in response to *S*.Tm

Induction of cell death is a host strategy designed to amplify the inflammatory response and prevent persistent infection. In response to *S*.Tm, caspase-1 and caspase-11 fuel the induction of pyroptotic cell death[456,457]. Pyroptosis requires gasdermins and ninjurin-1 to form pores for the release of cell contents as well as the proinflammatory cytokines IL-1β and IL-18[380,458]. This aligns with *in vivo* data where during acute orogastric infection, gasdermin D is the only gasdermin family member that provides protection against *S*.Tm infection[459]. *S*.Tm also causes apoptosis[460], which is in part due to TLR4-mediated activation of protein kinase R[461]. Necroptosis, which is a regulated form of necrosis depending on receptor-interacting protein kinases 1 and 3[462], is also induced by *S*.Tm in an interferon-dependent manner[463].

1.4.4 AMPK regulation during S.Tm infection

Physiological sources of AMPK activation during infection

Which physiological conditions could lead to AMPK activation during infection *in vivo*? A conserved sickness behaviour during a subset of viral and bacterial infections is anorexia, which is described as a concerted suppression of appetite that results in hypoglycemia[464]. Considering AMPK is sensitive to decreased circulating glucose levels, it is likely that low glucose could be an activating signal. This is observed following infection by the gram-negative bacterium *Yersinia pseudotuberculosis*, which causes a rapid drop in blood glucose levels without a corresponding drop in food intake[465]. Glucose injections designed to increase circulating glucose levels suppressed infection in mice, while fasting worsened infection[465]. This study also linked AMPK activity to worsened bacterial burden[465]. However, during viral infection, AMPK activation was shown to support viral clearance, despite there being similar

acute drops in blood glucose levels[82]. Regardless, activation of AMPK was detected in both instances. This may not be the case during *S*.Tm infection. Inflammatory cytokines such as IL-1β and TNF-α can produce fever and anorexia symptoms, relaying information to brainstem neurons to promote sickness behaviour[466,467]. *S*.Tm exploits this by inhibiting the anorexic response through expression of SlrP[468]. This effector inhibits caspase-1 cleavage and reduces the secretion of IL-1β and communication with the central nervous system through the vagus nerve[468]. Therefore, endogenous AMPK activity during infection will depend in part on the host glycemic response to different pathogens.

Evidence for altered AMPK activity during *S*.Tm infection

Though studies are limited, there is significant evidence for the activation of AMPK during *S*.Tm infection, though this depends on the cell type. There are two main studies investigating AMPK activity following *S*.Tm infection in macrophages. Ganesan et al. reported that *S*.Tm infection transiently decreases ATP levels and increases the ratio of NAD+/NADH, resulting in AMPK activation one hour post-infection[469]. However, ATP levels were also low at four hours, raising the question of why AMPK would be active at one hour and not four hours post-infection in their model. This also contrasts with other studies reporting that *S*.Tm has only a mild effect on AMP:ATP ratios during macrophage infection[465]. This study attempted to link AMPK activation during infection to improved xenophagy, which, as detailed above is a tenuous link. In another study, Ma et al. identified FLT4 as an upstream tyrosine kinase responsible for AMPK activation during *S*.Tm infection[470]. This work formed a strong link between FLT4 and AMPK; however, tyrosine phosphorylation is not a canonical regulator of AMPK activity. This group made the same conclusion as the previous study, that AMPK activation supports

autophagic signaling and *S*.Tm clearance. Though these studies support a role for macrophage AMPK in the cellular response to *S*.Tm, they lack key details regarding the precise mechanisms and consequences of AMPK activation. A final study from Losier et al. focused primarily on AMPK in the context of epithelial cell invasion, where they reported strong induction of AMPK activity[421]. Interestingly, epithelial cells, in contrast with macrophages, do not exhibit elevated mTORC1 activity upon infection, an effect traced to amino acid depletion[471]. Given that AMPK and mTORC1 activity typically oppose each other[472], it is curious that in macrophages both AMPK and mTORC1 have been reported as active in response to *S*.Tm[421,469,470]. Another contributor to AMPK activation could be TLR9, which is stimulated by *S*.Tm infection[368] and has been shown to activate AMPK alongside Beclin-1[473]. However, this was only measured in skeletal muscle, and would have to be verified in macrophages[473]. Taken together, the role of AMPK during macrophage *S*.Tm infection is still largely understudied and requires further refinement.

Rationale and objectives

Given the multitude of downstream targets of AMPK, as well as upstream inputs on activity, it remains of utmost importance to contextualize how a central metabolic regulator such as AMPK influences inflammatory disease progression across a range of pathologies. It is well established that AMPK broadly supports anti-inflammatory signaling, though its precise role in both sterile and pathogen-induced inflammation requires further interrogation. Many AMPK studies have relied on knockout models, which, while effective, lack the specificity to interrogate AMPK signaling with granular detail. Because AMPK has many roles beyond phosphorylation by means of forming multi-protein complexes, and is present at nearly every subcellular organelle, wholesale disruption of these signals could skew interpretations of downstream readouts.

With this in mind, this dissertation aims to explore the role of myeloid AMPK to better understand how AMPK regulates and is regulated by inflammatory conditions. The work presented herein spans both chronic and acute inflammatory pathologies in atherosclerosis and *Salmonella enterica* infection while highlighting important considerations in preclinical model selection, immune cell metabolism, and phosphoregulation of disease.

Given that AMPK signaling to HMGCR was presumed to be protective against atherosclerosis, we **hypothesized** that disrupting the AMPK-HMGCR signaling axis would exacerbate atherosclerosis. We addressed this hypothesis in Chapter 2 using a point mutant mouse model at the AMPK phosphorylation site on HMGCR and a *Pcsk9*-AAV-based model of murine hypercholesterolemia.

Additionally, though it is established that AMPK supports anti-inflammatory signaling, it has remained unclear how this affects cell intrinsic and systemic responses to live bacteria. We

hypothesized that increasing AMPK activity in macrophages and mice would worsen the response to the gram-negative bacterial pathogen *S*.Tm. We addressed this hypothesis in Chapter 3 using both genetic and pharmacological AMPK activation models alongside oral and intraperitoneal (IP) *S*.Tm infection routes.

Finally, given that AMPK myristoylation regulates not only AMPK activity, but also its protein levels without a clear regulator, we **hypothesized** that myristoylation-dependent machinery targeted non-myristoylated AMPK for degradation. We addressed this hypothesis using a range of proteostasis inhibitors and a genetic model expressing a non-myristoylated AMPK mutant.

Chapter 2: AMPK-mediated regulation of endogenous cholesterol synthesis does not affect atherosclerosis in a murine *Pcsk9*-AAV model

2.1 Preface

This chapter has been published as a research article[474]. It was also highlighted in an editorial (attached in Appendix I).

Tyler K.T. Smith[1,2,4], Peyman Ghorbani[1,2,4], Nicholas D. LeBlond[1], Julia R.C. Nunes[1,2,4], Conor O'Dwyer[1,2,4], Nia Ambursley[1], Claire Fong-McMaster[1,4], Lucía Minarrieta[1,2,4], Leah A. Burkovsky[1], Rama El-Hakim[1], Natasha A. Trzaskalski[1,5], Cassandra A.A. Locatelli[1,5], Cameron Stotts[1,5], Ciara Pember[1], Katey J. Rayner[1,2,5], Bruce E. Kemp[6,8,9], Kim Loh[7,8,9], Mary-Ellen Harper[1,2,4], Erin E. Mulvihill[1,2,4,5], Julie St-Pierre[1,2,4], Morgan D. Fullerton[#1,2,3,4]. AMPK-mediated regulation of endogenous cholesterol synthesis does not affect atherosclerosis in a murine *Pcsk9*-AAV model. *Atheroscler.* 397: 117608, 2024. 10.1016/j.atherosclerosis.2024.117608.

Affiliations

[1]Department of Biochemistry, Microbiology and Immunology, Faculty of Medicine, University of Ottawa, Ottawa, ON, Canada

[2]Centre for Infection, Immunity and Inflammation, Ottawa ON, Canada

[3]Centre for Catalysis Research and Innovation, Ottawa ON, Canada

[4]Ottawa Institute of Systems Biology, Ottawa, ON, Canada

[5]University of Ottawa Heart Institute, Ottawa, ON, Canada

[6]Protein Chemistry and Metabolism, St. Vincent's Institute of Medical Research; Fitzroy, Australia

[7]Diabetes and Metabolic Disease, St. Vincent's Institute of Medical Research; Fitzroy, Australia.

[8]Mary MacKillop Institute for Health Research, Australian Catholic University; Melbourne, Australia

[9]Department of Medicine, University of Melbourne; Melbourne, Australia.

[#]Correspondence: Dr. Morgan Fullerton, Department of Biochemistry, Microbiology and Immunology, Faculty of Medicine, University of Ottawa, 4109A Roger Guindon Hall, 451 Smyth Rd, Ottawa, Ontario, Canada, K1H 8M5

CEediT Authorship Statement

Tyler K.T. Smith: Conceptualization, Methodology, Validation, Formal analysis, Investigation, Writing – original draft, Writing – review & editing, Visualization. **Peyman Ghorbani:** Conceptualization, Investigation, Validation, Writing – review & editing. **Nicholas D. LeBlond:** Conceptualization, Methodology, Investigation. **Julia R.C. Nunes:** Investigation, Writing – review & editing. **Conor O'Dwyer:** Investigation. **Nia Ambursley:** Investigation. **Claire Fong-McMaster:** Investigation, Writing – review & editing. **Lucía Minarrieta:** Investigation. **Leah A. Burkovsky:** Investigation. **Rama El-Hakim:** Investigation. **Natasha A. Trzaskalski:** Investigation. **Cassandra A.A. Locatelli:** Investigation, Writing – review & editing. **Cameron Stotts:** Investigation, Writing – review & editing. **Ciara Pember:** Investigation. **Katey J. Rayner:** Resources. **Bruce E. Kemp:** Methodology, Resources. **Kim Loh:** Methodology, Resources. **Mary-Ellen Harper:** Resources. **Erin E. Mulvihill:** Resources, Writing – review &

editing. **Julie St-Pierre:** Resources. **Morgan D. Fullerton:** Conceptualization, Resources, Writing – review & editing, Supervision, Funding acquisition.

2.2 Abstract

Background and Aims

Dysregulated cholesterol metabolism is a hallmark of atherosclerotic cardiovascular diseases, yet our understanding of how endogenous cholesterol synthesis affects atherosclerosis is not clear. The energy sensor AMPK phosphorylates and inhibits the rate-limiting enzyme in the mevalonate pathway HMG-CoA reductase (HMGCR). Recent work demonstrated that when AMPK-HMGCR signaling was compromised in an *Apoe*$^{-/-}$ model of hypercholesterolemia, atherosclerosis was exacerbated due to elevated hematopoietic stem and progenitor cell mobilization and myelopoiesis. We sought to validate the significance of the AMPK-HMGCR signaling axis in atherosclerosis using a non-germline hypercholesterolemia model with functional ApoE.

Methods

Male and female HMGCR S871A knock-in (KI) mice and WT littermate controls were made atherosclerotic by intravenous injection of a gain-of-function *Pcsk9*^{D374Y}-adeno-associated virus (AAV) followed by high-fat and high-cholesterol atherogenic western diet feeding for 16 weeks.

Results

AMPK activation suppressed endogenous cholesterol synthesis in primary BMDM from WT but not HMGCR KI mice, without changing other parameters of cholesterol regulation. Atherosclerotic plaque area was unchanged between WT and HMGCR KI mice, independent of sex. Correspondingly, there were no phenotypic differences observed in hematopoietic

progenitors or differentiated immune cells in the bone marrow, blood, or spleen, and no significant changes in systemic markers of inflammation. When lethally irradiated female mice were transplanted with KI bone marrow, there was similar plaque content relative to WT.

Conclusions

Given previous work, our study demonstrates the importance of preclinical atherosclerosis model comparison and brings into question the importance of AMPK-mediated control of cholesterol synthesis in atherosclerosis.

2.3 Introduction

Atherosclerotic cardiovascular diseases (ACVD) remain among the leading causes of mortality worldwide[210]. Atherosclerotic plaque development is driven by hypercholesterolemia and the retention of cholesterol-rich LDL within subendothelial spaces, leading to immune cell recruitment and maladaptive inflammatory responses. Despite the appreciated importance of reducing circulating LDL to minimize ACVD, our understanding of how cell-intrinsic cholesterol metabolism influences atherosclerosis remains underdeveloped.

AMPK is a heterotrimeric energy sensor that is activated by changes in adenine nucleotide ratios[54] and concentrations of metabolites such as FBP[90] or saturated long-chain fatty acyl-CoAs[42]. Once activated, AMPK signals to downstream targets to suppress anabolic pathways and activate catabolic signaling to restore cellular energy balance[475]. *De novo* cholesterol synthesis is an energy-demanding process that occurs through the mevalonate pathway, which produces both sterol and isoprenoid intermediates[476]. Within the mevalonate pathway, HMGCR is the rate-limiting enzyme and is highly regulated[477]. HMGCR activity is suppressed when S871 (S872 in humans) is phosphorylated by AMPK, forming a link between energy sensing and mevalonate pathway flux[8,18,297].

The role of AMPK in atherosclerosis, while well studied, lacks clarity. A majority of studies indicate that AMPK activity is protective against murine atherosclerosis[324,331–333,478], particularly when pharmacologically activated from the onset of hypercholesterolemia[299,320–323]; however, others have demonstrated the opposite[326,328,479] or found no effect[329]. The discrepancies observed in various AMPK atherosclerosis studies could be a result of differing hypercholesterolemia models, of which there are three main approaches to induce murine atherosclerosis: ApoE knockout mice[307], LDLR knockout mice[309], and injection of a PCSK9 AAV containing a gain-of-function PCSK9 variant (*Pcsk9*-AAV), which generates a hypercholesterolemic lipoprotein profile similar to *Ldlr*$^{-/-}$ mice[315]. Both *Ldlr*$^{-/-}$ and *Pcsk9*-AAV models are typically accompanied by administration of a high-fat, high-cholesterol Western diet (WD), which is representative of the fast food-based diet that originated in Western society, while *Apoe*$^{-/-}$ mice develop hypercholesterolemia on a chow diet alone.

Systemic pharmacological activation, as well as global and cell type-specific knockout models broadly affect AMPK signaling and make it challenging to decipher the significance of individual downstream outputs. Targeted knock-in (KI) mouse models have made it possible to test the physiological significance of select metabolic axes. To this end, recent work on the AMPK-HMGCR signaling axis employed an HMGCR S871A KI point mutant mouse model that renders HMGCR insensitive to AMPK-mediated regulation[480]. These mice developed more hepatic steatosis on a high-fat, high-carbohydrate diet, hinting at the relevance of this signaling axis *in vivo*. In a subsequent study, these mice were crossed onto an atherogenic *Apoe*$^{-/-}$ background and it was found that they developed more atherosclerotic plaque in a hematopoiesis-dependent manner[478].

Given that ApoE is known to regulate hematopoiesis and cholesterol homeostasis[311], we sought to clarify whether atherosclerosis is affected in a non-*Apoe*$^{-/-}$ model of hypercholesterolemia. In this study, we used the same HMGCR S871A KI mice, but induced atherosclerosis through the use of a *Pcsk9*-AAV coupled with WD feeding to circumvent potential non-AMPK-related hematopoietic effects of *Apoe* deletion[315]. Importantly, this model generates hypercholesterolemia mainly by enhancing degradation of LDLR in the liver, and does not have any known direct effects on hematopoiesis[315].

In contrast with what was observed on an *Apoe*$^{-/-}$ background, *Pcsk9*-AAV HMGCR KI mice did not accumulate more atherosclerotic plaque than their WT counterparts. We investigated other parameters of the plaque microenvironment and also performed extensive immune phenotyping and similarly observed no genotype changes. These data were supported by *ex vivo* models using bone marrow-derived macrophages (BMDM). Collectively, our work emphasizes the importance of murine atherosclerosis model selection and highlights the context-dependent role of AMPK signaling in atherosclerosis.

2.4 Materials and Methods

Generation of bone marrow derived macrophages

WT and HMGCR KI C57BL/6J mice were anesthetized and euthanized by cervical dislocation. The tibias and femurs of both legs were isolated, cleaned, then placed in ice cold 1% FBS/PBS until further processing. The ends of the bones were cut, and one femur and one tibia were placed into a 0.5 ml tube that was punctured with a 27-gauge needle and contained within a 1.5 ml Eppendorf tube. The bones were then centrifuged at 10,000 *x g* for 1 min into 100 µl of high glucose DMEM (Wisent #319-005-CL) supplemented with 10% FBS (Wisent #080-150) and 1% penicillin streptomycin (Thermo Fisher Scientific #SV30010), referred to hereafter as complete DMEM. The resulting bone marrow pellet was resuspended in complete DMEM and passed through a 40 µm filter (Corning #352340). The cell suspension was diluted in complete DMEM before adding L929-conditioned media (M-CSF-enriched; in complete DMEM) to a final concentration of 20% L929-conditioned media and 100 ml total. The cell suspension was then distributed evenly into five 15 cm dishes and incubated at 37 °C and 5% CO_2. After 4 days, each plate received an additional 5 ml of 20% L929-conditioned media. At day 6, the differentiated BMDM were washed once with PBS, then incubated on ice with 8 ml of cold 10 mM EDTA/PBS for 10 min. The plates were struck to dislodge the cells, and the remaining cells were gently scraped and transferred to 50 ml conical tubes before being centrifuged at 500 *x* g for 5 min and resuspended in complete DMEM. The cells were then counted using Trypan blue (Thermo Fisher Scientific #15250061) (average yield 100 x 10^6 BMDM per mouse) and seeded into respective plates at a density of 0.156 x 10^6 BMDM/cm^2.

BMDM generation and treatment paradigm

Unless otherwise specified, all treatments for BMDM were performed in high glucose DMEM containing 10% FBS and 1% penicillin/streptomycin. Cells were left to adhere overnight following initial seeding, after which the media was aspirated, cells were washed once with warm PBS, and treatment media was added. Any subsequent treatments were spiked in at a small volume. The following concentrations were used: MK-8722 (2 μM; a gift from Merck), A-769662 (100 μM; AdooQ Bioscience #A11071), LPS from *Escherichia coli* O111:B4 (100 ng/ml; MilliporeSigma #L3024).

Aggregated LDL formation

Native human LDL (Kalen Biomedical; #770200) was diluted to 1 mg/ml in sterile PBS and vortexed at maximum speed for 4 min. The suspension was then centrifuged at 10,000 *x g* for 10 min. The resulting pellet (aggregated LDL; agLDL) was resuspended to a final concentration of 3 mg/ml determined by bicinchoninic acid (BCA) assay (Thermo Fisher Scientific #PI23225) according to the manufacturer's protocol. agLDL was added to culture media at a final concentration of 50 μg/ml. BMDM were considered lipid loaded following overnight incubation in agLDL-supplemented media. Subsequent treatments, if performed with a full media change, were additionally supplemented with 50 μg/ml agLDL.

Cholesterol efflux

Acetylated LDL (acLDL; 50 μg/ml; Thermo Fisher Scientific #AAJ650298PL) was pre-equilibrated with 0.5 μCi/ml [^{3}H]cholesterol (PerkinElmer #NET139001MC) in complete DMEM. BMDM were incubated with radiolabeled acLDL for 24 h. Radioactive medium was removed and cells were washed twice with PBS. Cells were then equilibrated in high glucose DMEM supplemented with 2% lipoprotein deficient serum (LPDS) and 0.2% fatty acid-free

BSA (MilliporeSigma #A8806) for 2 h in the presence or absence of A-769662 (100 μM) or equivalent DMSO (0.2%) (Thermo Fisher Scientific #BP231100). Fresh medium was then replenished in the presence or absence of 0.2% BSA, recombinant human Apo-AI (5 μg/ml; Thermo Fisher Scientific #J64506), or human HDL (50 μg/ml; Thermo Fisher Scientific #J64903), with or without A-769662. After 24 h, medium was collected and adherent cells were washed twice with PBS, then lysed with 0.1M NaOH (BioShop #SHY777.500) and added to Ultima Gold liquid scintillation fluid (PerkinElmer #6013159). Radioactivity was determined by liquid scintillation counting (LSC) on a Tri-Carb 4910TR Beta Liquid Scintillation Analyzer (PerkinElmer). Efflux is expressed as a percentage of disintegrations per minute (DPM) for [([^{3}H]cholesterol in medium)/([^{3}H]cholesterol in medium + [^{3}H]cholesterol in cells)] x 100%. Efflux to either Apo-AI or HDL was calculated by subtracting the effluxes of the wells containing only BSA without Apo-AI or HDL from those containing it.

***de novo* lipogenesis**

BMDM were either cotreated with A-769662 (100 μM) or pretreated for 1 h with MK-8722 (2 μM) or equivalent DMSO (0.05%) before spiking in [^{3}H]acetate (1 μCi/ml; PerkinElmer #NET003005MC) and 500 μM "cold" acetate for 4 h. To measure [^{3}H]acetate incorporation into cholesterol, cells were washed twice with PBS, scraped in PBS, and then lipids were extracted using a Bligh and Dyer extraction[481]. A cholesterol standard was loaded along with each lane and lipids were separated by thin layer chromatography using a solvent system of heptane:isopropyl ether:glacial acetic acid (60:40:3)[482]. Following exposure to iodine vapours, silica was scraped and bands corresponding to cholesterol were collected into scintillation vials before determining radioactivity by LSC. The molar amount of [^{3}H]acetate incorporation into cholesterol was determined using the specific activity of the labeled media. To measure acetate incorporation

into fatty acids (i.e., saponifiable lipids), cells were washed twice with PBS, scraped in PBS, and added to a mixture of 1 ml 40% potassium hydroxide (MilliporeSigma #484016) and 2 ml methanol (Thermo Fisher Scientific #A412P-4) then boiled at 80°C for 1 h to lyse cells. 3 ml petroleum ether (Thermo Fisher Scientific #E139-4) was added and samples were vortexed to mix phases. The organic phase was transferred to scintillation vials (Ultident #17-S207) and a second extraction was performed. 700 µl of 12N hydrochloric acid (Thermo Fisher Scientific #A144500) was added to acidify the solution and two more extractions were performed. Organic phases were left overnight to dry, then resuspended scintillation fluid and radioactivity measured. A limitation to these methods is not knowing the amount of endogenous acetate in each condition, which could affect the interpretation of fold changes between groups.

Cholesterol uptake

acLDL (50 µg/ml) was pre-equilibrated with 0.5 µCi/ml [^{3}H]cholesterol in DMEM supplemented with 10% FBS overnight. BMDM were treated with A-769662 (100 µM) or DMSO (0.2%) for 1 h prior to the addition of radioactive media for 30 min. The radioactive media was removed and cells were washed twice with PBS. Cells were lysed with 0.1M NaOH, with a small aliquot used for protein quantification by BCA. Cell lysates were added to Ultima Gold liquid scintillation fluid and radioactivity was quantified by LSC and made relative to DMSO controls.

ELISA

Cell culture supernatants were collected and transferred to 96 well U-bottom plates (Thermo Fisher Scientific #7000165) and stored at -80 °C. ELISAs for murine TNF-α (Bio-Techne #DY410), IL-6 (Bio-Techne #DY406), and IL-1β (Bio-Techne #DY401) were performed according to manufacturers' instructions. Briefly, ELISA plates (Bio-Techne #DY990) were

coated with 100 µl of capture antibodies diluted in PBS, covered with an adhesive strip, and left to incubate at room temperature (RT) overnight. The plates were washed three times with wash buffer (0.05% Tween-20/PBS) before adding 300 µl of reagent diluent (1% BSA/PBS) and incubating for 1 h at RT. Cell culture supernatants (diluted in reagent diluent at 1/4 - 1/16 dilutions for 100 µl final volume), or a two-fold serial dilution of recombinant murine TNF-α, IL-6, or IL-1β was added to each well and incubated for 2 h at RT. The plates were again washed and 100 µl of biotinylated detection antibodies in reagent diluent was then added to each well and incubated for 2 h at RT. Following another wash step, 100 µl of streptavidin-HRP (1:40 in reagent diluent) was added for 20 min at RT. The plates were washed again before adding 100 µl of substrate solution (1:1 mixture of H_2O_2 and tetramethylbenzidine) and incubating at RT. After 15-20 min, 50 µl of 2N H_2SO_4 was then added and optical density of each well read at both 450 nm (primary) and 540 nm (optical impurities). Following subtraction of absorbance at 540 nm from 450 nm, the wells were blanked and standard absorbances fitted with a four-parameter logistic curve-fit.

Extracellular flux analysis

BMDM were plated in 96-well culture plates (Agilent #103794) at $7.5x10^4$ cells/well in complete DMEM. Cells were incubated for 18 h with LPS (100 ng/ml) prior to initiating the mitochondrial stress test. Oxygen consumption rate (OCR) and extracellular acidification rate (ECAR) by live cells, with ECAR indicating mostly glycolysis, was measured on a Seahorse XFe96 Analyzer (Agilent). Cartridge ports were loaded with 10X concentrations of drugs: 15 µM oligomycin (Cayman Chemical #11341), 15 µM FCCP (Cayman Chemical #15218), and 10 µM rotenone (Cayman Chemical #13995)/10 µM antimycin A (MilliporeSigma #A8674)/20 µM Hoechst 33342 (Thermo Fisher Scientific #62249) following the Mito Stress Test protocol (Agilent). Data

were normalized by relative DNA fluorescence intensity quantification on an EVOS FL Auto 2 (Thermo Fisher Scientific) microscope and Qupath 0.4.2 (University of Edinburgh).

RNA isolation, cDNA synthesis, and RT-qPCR.

Cells were treated as described and washed once with PBS before adding 115 µl/cm^2 TriPure RNA isolation reagent (Roche #11667165001). RNA isolation was carried out according to the manufacturer's instructions with all centrifugation steps at 4°C. Chloroform (0.2 ml/ml TriPure) was added to tubes and mixed thoroughly before centrifuging at 12,000 *x g* for 15 min. The upper aqueous phase was collected and transferred to new tubes where 0.5 ml isopropanol/ml TriPure was added. Samples were centrifuged at 12,000 *x g* for 10 min and the supernatant was discarded. A volume of 1 ml of 70% ethanol/ml of TriPure was added and samples centrifuged at 7,500 x g for 5 min. The supernatant was discarded and samples were air dried for 30 min before resuspending in DNase/RNase free H_2O (Wisent #809-115-CL) and incubating at 55 ºC for 10 min. RNA concentration and quality (A260/280) was measured using the Take3 Plate (Agilent #TAKE3-SN) on the Synergy H1 Plate Reader (BioTek). RNA concentration was equalized using DNase/RNase free H_2O, after which 300-400 ng of RNA was transferred to 8-strip PCR tubes (Diamed #DIATEC420-1378). All-in-One 5X RT Master Mix (Applied Biological Materials #G592) was added and reverse transcription initiated by cycling at 37 °C for 15 min, followed by 60 °C for 10 min and finally 95 °C for 3 min on a T100 thermal cycler (Bio-Rad). Synthesized cDNA was diluted to a final concentration of ~2.5 ng/µl in DNase/RNase free H_2O such that each qPCR reaction contained ~10-12 ng of cDNA. For Taqman probes, primary pairs were diluted 1:20 in 2X QuantiNova Probe PCR Master Mix (Qiagen #208254) and 5.25 µl was added per reaction. For non-Taqman probes, forward and reverse primers were diluted to 250 nM in BlasTaq 2X qPCR MasterMix (Applied Biological Materials #G891) and 5.6 µl was added per

reaction. Either 4.75 µl or 4.4 µl of diluted cDNA was added for a 10 µl total reaction volume. Samples were transferred to the Rotor-Gene Q (Qiagen) and subjected to an initial 3 min incubation at 95 °C before 40 cycles of 1 sec at 95°C then 10 sec at 60°C. Relative expression was calculated with the $^{\Delta\Delta}$Ct method[483] using a combination of *Actb* and *Tbp* genes as housekeepers. Primer sequences are listed in Supplemental Table 2.1.

Mitochondrial to nuclear DNA ratio

DNA isolation was carried out as previously described[484]. Briefly, macrophages were homogenized in 500 µl DNA lysis buffer (5 mM EDTA, 0.2% SDS, 200 mM NaCl, 100 mM Tris, pH 8.0) and 5 µl of 20 mg/ml proteinase K (Thermo Fisher Scientific #25530049) was added and the lysate was incubated overnight at 55°C. 500 µl of phenol/chloroform/isoamyl alcohol (25:24:1) was added to each lysate and mixed thoroughly before centrifuging at 16,000 *x g* for 10 min at 4°C. The upper aqueous phase was transferred to new tubes, and 600 µl cold isopropanol was added to precipitate DNA overnight at -20°C. Samples were then centrifuged at 16,000 *x g* for 10 min to pellet DNA. DNA pellets were washed in 1 ml 70% ethanol and left to air dry before resuspending in 200 µl DNase/RNase free H_2O (Wisent #809-115-CL) and incubated at 55 °C for 10 min. DNA concentration and purity were measured using a NanoDrop 2000 spectrophotometer (Thermo Fisher Scientific). Mitochondrial to nuclear DNA ratios were measured using qPCR for the mitochondrial DNA-encoded gene *Mtco1* and nuclear DNA-encoded gene *Ndufv1*. Each 10 µl qPCR reaction contained 1 ng DNA (DNA equalized to 0.5 ng/µl), 5 µL SsoAdvanced™ Universal SYBR® Green Supermix (Bio-Rad #1725271), and 1.5 µl of forward and reverse primers diluted to 3.33 µM. Samples were loaded into the CFX96 Touch Real-Time PCR Detection System (Bio-Rad) and subject to an initial 3 min incubation at

98 °C before 40 cycles of 15 sec at 95°C then 60 sec at 59°C. Mitochondrial to nuclear DNA ratios were calculated using the $^{\Delta\Delta}$Ct method.

In vivo *Methods*

Mouse models

C57BL/6J mice were purchased from The Jackson Laboratory (#00664) and bred in house. HMGCR S871A KI mice were generated as previously described[480]. All mice were housed in ventilated cages at ~23 °C and maintained on a 12 h/12 h light-dark cycle with *ad libitum* access to a standard rodent chow (58% kcal from carbohydrates, 18% kcal from fat, and 24% kcal from crude protein; Harlan Teklad #2018) and water. All experiments conducted were in accordance with the Canadian Council of Animal Care and approved by the Animal Care Committee at the University of Ottawa (BMI3549/3644).

***Pcsk9*-AAV-induced hypercholesterolemia and tissue collection**

Male and female WT and HMGCR KI mice were aged 8-12 weeks before being intravenously injected with 2.5 x10^{10} genome copies of a human gain-of-function *Pcks9^{D374Y}* mutant packaged in an AAV8 vector by the Penn Vector Core at the University of Pennsylvania. Immediately following viral infection, mice were placed on a WD (43% kcal from carbohydrates, 40% kcal from fat, 17% kcal from protein, with 0.15% cholesterol; Research Diets #D12079) to exacerbate hypercholesterolemia. After 16 or 26 weeks of WD feeding (mice aged between 24-28 weeks or 36 weeks at endpoint), mice were fasted for 4 h before being anaesthetized with a ketamine and xylazine mixture (150 mg/kg ketamine and 10 mg/kg xylazine), exsanguinated by cardiac puncture, and perfused with PBS through the left ventricle. Tissues of interest were removed and either snap frozen in liquid nitrogen, fixed in 10% neutral-buffered formalin (MilliporeSigma #HT501128), or processed for downstream analysis by flow cytometry.

Bone marrow transplant

Bone marrow from four WT and four HMGCR KI female donor mice was isolated and pooled by genotype. WT recipient mice were lethally irradiated with two doses of 4.5 Gy (9 Gy total) 1-2 h prior to transplantation. Following successful transplantation, mice were monitored for 4 weeks for recovery, after which they were subjected to the same *Pcsk9*-AAV experimental paradigm as described above.

***In vivo* EdU labeling**

After 16 weeks on a WD following *Pcsk9*-AAV injection, WT and HMGCR KI mice were injected IP with 750 µg of warm 5-ethynyl-2'-deoxyuridine (EdU; Click Chemistry Tools #1149) in PBS. Mice were fasted post-injection for 4 h until lethal anaesthetization with ketamine and xylazine and tissue collection as described above.

Single cell suspension preparation

For various downstream readouts, single cell suspensions were prepared for the spleen, bone marrow, and blood. Spleens were placed in ice cold 1% FBS/PBS and then mashed through a 100 µm cell strainer (Thermo Fisher Scientific #22363549) that was pre-wetted with 1 ml of 1% FBS/PBS into a 50 ml conical tube. A further 9 ml of 1% FBS/PBS was passed through the strainer before centrifuging at 500 *x* g for 5 min at 4°C. The supernatant was decanted and the pellet was resuspended in 2 ml of RT RBC lysis buffer (155 mM NH_4Cl (MilliporeSigma #A9434), 10 mM $NaHCO_3$ (BioShop #SOB308), 10 mM EDTA) to selectively lyse erythrocytes and incubated for 5 min at RT. 10 ml of ice cold 1% FBS/PBS was then added and the samples were centrifuged and then resuspended in 5 ml of ice cold 1% FBS/PBS. The tibia and femur from the right leg were removed and placed in ice cold 1% FBS/PBS. Bone marrow was isolated and pelleted as described above. Pellets were resuspended in 1 ml of RT RBC lysis buffer and

incubated at RT for 2 min. The suspension was passed through a pre-wetted 100 µm filter followed by 10 ml of ice cold 1% FBS/PBS. The cells were centrifuged and resuspended in 2 ml of 1% FBS/PBS. Whole blood was collected by cardiac puncture, transferred to a 1.5 ml Eppendorf tube with 10 µl of 0.5 M EDTA, and shaken thoroughly before placing on ice. Blood volumes were then recorded and transferred to a 15 ml tube containing 9 ml of RT RBC lysis buffer and incubated for 10 min at RT. The cells were centrifuged and subjected to another round of RBC lysis for 10 min. The cells were centrifuged again and resuspended in 1 ml of ice cold 1% FBS/PBS. Single cell suspensions of bone marrow and spleen were enumerated using Trypan blue and a hemocytometer before continuing to downstream applications.

Flow Cytometry

Single cell suspensions from bone marrow, spleen, blood, or BMDM were transferred to 1.2 ml cluster tubes (Corning #4401). Cells were centrifuged at 400 *x* g for 5 min, and then simultaneously blocked with CD16/32 (1:250; BioLegend #101302) and stained with Zombie Aqua (1:500; BioLegend #423102) for live/dead discrimination in 50 µl PBS for 30 min on ice. Progenitor panels that required CD16/32 for gating were only stained with Zombie Aqua. Cells were washed with PBS, centrifuged, and stained with primary antibodies diluted in PBAE (1% BSA, 2 mM EDTA, 0.05% sodium azide (Ricca #7144.8-16) in PBS) for 20 min on ice protected from light. The cells were washed with PBS and secondary antibodies added as required for another 20 min on ice. Cells were washed in PBS, centrifuged, and fixed with 2% paraformaldehyde (PFA) in PBS (BioShop #PAR070.500) for 15 min on ice. The cells were washed with PBS and finally resuspended in PBAE for analysis on the LSR Fortessa (BD). Complete information regarding antibodies and stains can be found in Supplemental Table 2.2.

Serum Cholesterol measurements

Blood was collected from mice by cardiac puncture at experimental end point. Blood was left to clot on ice for 4 h, then centrifuged at 3000 RPM for 10 min at RT. The upper phase containing serum was collected, aliquoted, and stored at -20 °C. Serum was submitted to the Centre for Phenogenomics, where total cholesterol, HDL cholesterol, triglycerides, direct LDL cholesterol, and glucose were measured using the Beckman Coulter AU480 clinical chemistry analyzer in combination with appropriate reagents, calibrators, and quality control materials.

Liver cholesterol measurements

Approximately 30 mg of liver was homogenized in 500 µl PBS and then snap frozen and thawed on ice twice. Liver lysates were centrifuged at 14,000 RPM for 5 min at 4 °C and supernatants were transferred to new microfuge tubes and the pellets discarded. A Bligh and Dyer lipid extraction was then performed using 200 µl of lysate. Isolated lipids within the chloroform phase were then evaporated under nitrogen gas and re-suspended in 50 µl of isopropanol. Cholesterol was measured using the commercially available Infinity cholesterol kit as per manufacturer's instructions and normalized to tissue weight.

Colony forming unit (CFU) assays

Semi-solid methocult media (Stemcell Technologies #03434) was thawed overnight at 4°C and 1 ml was distributed to 1.5 ml tubes using an 18G blunt-ended needle. Single cell suspensions of whole BM cells were prepared as described and diluted to a concentration of 135k cells/ml or 270k cells/ml in sterile 1% FBS/PBS to plate at two cell densities per sample. These cell suspensions were diluted 1/10 in methocult media, vortexed, then transferred to 6 well plates using an 18G blunt-ended needle such that each well contained either 15 k or 30 k whole BM cells. Interwell space was filled with 3 ml of sterile water to minimize evaporation. Plates were

incubated at 37°C for 12 days, then imaged at 4X magnification on the EVOS FL Auto 2 imaging system (Thermo Fisher Scientific), followed by image tiling. The number of colonies and their classifications were then manually counted by an individual blinded to experimental group.

Atherosclerosis quantification methods

Cardiac tissue embedding and sectioning

Hearts were fixed in 10 ml of 10% neutral-buffered formalin for at least 48 h at 4°C. Hearts were then transferred into a sterile 20% sucrose (BioShop #SUC700.1)/PBS solution until tissue sinking (~1 h), after which they were transferred to a sterile 30% sucrose/PBS solution and incubated overnight at 4°C. Prior to embedding, hearts were removed and dried gently to remove excess sucrose solution. A razor blade was used to cut the apical two-thirds of the heart on a 20° transverse angle. The top third (containing the aortic root) was embedded within a tissue standard sized cryomold (VWR #25608-916) with optimal cutting temperature medium (Thermo Fisher Scientific #23-730-571), which was flash frozen with an isopentane-dry ice slurry and stored at -80°C. The aortic root was sectioned using a Leica CM 1850 cryostat at 10 µm serial sections at -16°C. Each slide (Thermo Fisher Scientific #15-188-48) contained nine serial sections collected at 100 µm intervals, spanning at least 800 µm on a total of 10 slides.

H&E lesion and necrotic core quantification

Frozen slides containing aortic root cross sections were equilibrated at RT for 2 h, followed by fixation in 10% neutral-buffered formalin for 10 min at RT. Slides were then subjected to standard H&E staining procedures on the Leica Bond III Immunostainer. Images were acquired on the Axio Scan Z1 Slide Scanner at 20X magnification. The aortic root and all lesions were outlined manually on ImageJ[485], with each selection saved as a region of interest (ROI). Two

main forms of measurement were calculated. The first was percentage aortic root, in which all plaque measurements were scaled against the size of the aortic root on each section, which can help reduce variation due to different orientations. The second was mm^2, where plaque was calculated as area alone. ROIs were converted to area and summed to calculate total plaque area per section, or as a fraction of aortic root per section. From these values, summed area, average area of 3-5 sections, and area-under-the-curve (AUC) of plaque histograms were quantified across sections, corresponding to the 800 μm traveled through the aortic root. Folded or poor-quality sections were excluded from the AUC calculation. Necrotic core area was calculated using the lesion area ROIs detailed above. The original image was first duplicated before thresholding with the "Triangle" autothreshold setting[486]. This area was then converted to a mask, after which ROIs were pasted back into the ROI manager. Total thresholded area within each ROI was then exported to a .csv file. The area was summed to calculate necrotic core area per section, and then summed with other sections and expressed as either percentage of lesion area or total necrotic core area in mm^2.

Immunofluorescent labeling

Slides containing aortic root cross-sections were equilibrated at RT at least 1 h and a hydrophobic pen (Millipore) was used to draw barriers around all sections. Subsequent steps were performed in a dark, humidified chamber. Sections were fixed in 4% PFA for 15 min and washed with PBS. Slides were permeabilized with PBS containing 1% BSA, 0.1% saponin (MilliporeSigma #84510). Slides were then incubated in permeabilization buffer with 1 mM copper(II) sulfate pentahydrate (MilliporeSigma #C8027), 2 mM tris-hydroxypropyltriazolylmethylamine (THPTA) (Click Chemistry Tools #1010), 10 mM sodium ascorbate (Sigma #A7631), and 5 μM AFDye 594 Azide Plus (Click Chemistry Tools #1481) for

30 min at RT. Slides were washed and incubated with anti-Mac-2-biotin (Tebubio #CL8942B) overnight at 4°C. Slides were washed and incubated with streptavidin iFluor647 (AAT Bioquest #16966), 20 μM BODIPY 493/503 (Cayman Chemical #25892), and 2.8 μM DAPI (MilliporeSigma #D1306) for 1-2 h at RT. Slides were then washed and mounted with Fluoromount G (Thermo Fisher Scientific #00-4958-02) and #1.5 coverslips and imaged after curing on an Axio Scan Z1 microscope (Zeiss) using a 20X objective. Images were processed using Qupath 0.4.2. Aortic root and plaque areas were defined manually and quantified for cells by nuclei (DAPI) detection. Total $BODIPY^+$ and $Mac2^+$ area was quantified and expressed as a percentage of total plaque area. EdU puncta either colocalized or not with $Mac2^+$ were enumerated and expressed as the number of EdU^+ cells per section.

Statistical Analysis

Data are represented as violin plots truncated at maximum and minimum values. The first and fourth quartiles are denoted by ½ pt lines, while the median is distinguished by a 1 pt line. Histograms are represented as mean ± SD, unless otherwise specified. Statistical analyses were performed using GraphPad Prism Software version 10.0.2. Normality of data was assessed using the Shapiro-Wilk test ($\alpha = 0.05$). For normally distributed data, differences between groups which involved a single variable were analyzed using an unpaired, two-tailed Student's t test. In groups with two or more factors, a two-way analysis of variance (ANOVA) test was performed with Tukey's post-hoc test for multiple comparisons. For non-normally distributed data, differences between groups with a single variable were analyzed using an unpaired Mann-Whitney U test. P values are reported for all meaningful comparisons to the fourth decimal, where $P<0.05$ was described as "statistically significant".

2.5 Results

Cholesterol synthesis is unresponsive to AMPK activation in HMGCR S871A KI macrophages.

Within the mevalonate pathway, HMGCR catalyzes the rate-limiting reduction of HMG-CoA to mevalonate, which is converted downstream into sterol and isoprenoid metabolites[476] (Figure 2.1A). Given the importance of macrophages to atherosclerosis progression[487], we assessed various aspects of cholesterol metabolism in BMDM from WT and KI mice (Supplemental Figure 2.1A). We first measured the sensitivity of *de novo* cholesterol synthesis to AMPK activation, which is typically suppressed following acute treatment with AMPK activators[300,480]. After treating macrophages with A-769662, an allosteric activator of AMPK[196], we observed a significant reduction in the amount of radiolabeled acetate incorporated into cholesterol in WT BMDM, but not in KI cells (Figure 2.1B). Conversely, activating AMPK with MK-8722, an alternative allosteric AMPK activator[199], suppressed *de novo* fatty acid synthesis in both WT and KI cells (Supplemental Figure 2.1B). These data validate that in BMDM, our KI model is refractory to this suppressive effect of AMPK activation on cholesterol synthesis, but retains its sensitivity to AMPK-mediated inhibition of fatty acid synthesis via phosphorylation of ACC[18]. Cellular free cholesterol levels are tightly regulated and, in addition to *de novo* synthesis, are subject to rates of lipoprotein uptake via the LDL and scavenger receptors, as well as efflux to cholesterol acceptors Apo-A1 and HDL[477]. We found that total cholesterol levels in a non-lipid loaded state were equivalent between genotypes (Figure 2.1C). Similarly, cholesterol efflux to either Apo-A1 or HDL was unchanged between genotypes regardless of AMPK activation by A-769662 (Figure 2.1D,E). Maximal efflux, determined by incubation with T0901317, an LXR agonist that increases ABCA1 expression[488], was also unchanged. Finally, there were no

genotypic differences in cholesterol uptake from media containing radiolabeled acetylated LDL (acLDL), regardless of AMPK activation (Figure 2.1F). Collectively, these data suggest that macrophage AMPK regulates cholesterol metabolism primarily through inhibition of HMGCR-mediated mevalonate flux.

***Pcsk9*-AAV-injected HMGCR KI mice do not have increased atherosclerosis.**

Given the importance of cholesterol homeostasis in atherosclerosis alongside previous work showing increased atherosclerotic plaque in HMGCR KI mice on an *Apoe*$^{-/-}$ background, we investigated whether AMPK-mediated regulation of the mevalonate pathway was important for atherosclerotic plaque progression. We intravenously injected 8-10 week-old male and female WT and KI mice with a *Pcsk9*-AAV to degrade LDLR and increase circulating LDL-cholesterol [315]. Female mice were then fed a WD (40% kcal fat, 0.15% cholesterol) for 16 weeks before sectioning the aortic root and quantifying plaque content to assess atherosclerotic lesion burden (Figure 2.2A; Supplemental Figure 2.2). Male mice developed aortic root plaque more slowly than females (Supplemental Figure 2.3), despite experiencing similar weight gain (Supplemental Figure 2.4A,B). Therefore, a subsequent cohort of male mice was infected with the *Pcsk9*-AAV and fed a WD for 26 weeks, which produced lesions comparable to 16-week WD-fed females (Supplemental Figure 2.3B-G). At study endpoints, we measured atherosclerotic lesion area in the aortic root where, surprisingly, we observed no genotypic differences in lesion area for female mice (Figure 2.2B-D; Supplemental Figure 2.4C-H). Male mice even exhibited a trending decrease in lesion size (Supplemental Figure 2.3I-P). It is worth noting that lesion size was unchanged irrespective of quantification method, which, in addition to plaque histogram area-under-the-curve (AUC) measurements, also included total lesion area

across nine sections, and average lesion area across three to five sections where all three leaflets were visible (expressed as mm^2 and as a percentage of aortic root (Supplemental Figures 2.2-2.4)). In line with these observations, there was no change in necrotic core area (Figure 2.2E). Circulating cholesterol levels are closely linked to ACVD, where higher LDL-cholesterol strongly correlates with ACVD risk[489]. In our model, there were no changes in circulating total cholesterol, LDL and HDL-cholesterol, triacylglycerols, nor in blood glucose between genotypes in female (Figure 2.2F-J) or male (Supplemental Figure 2.4Q-T) mice. Hepatic cholesterol content was similarly unchanged (Figure 2.2K), which was interesting considering the established role of AMPK in regulating cholesterol metabolism in the liver [478,480].

Atherosclerotic lesion progression is complex and occurs over several months after initiating *Pcsk9*-AAV-induced LDLR degradation. To interrogate the dynamics of local cell turnover within the plaque microenvironment at our study endpoint[226], we injected female mice with 5-ethynyl-2'-deoxyuridine (EdU) four hours before harvest to label proliferative cells within the plaque after 16 weeks of hypercholesterolemia (Figure 2.3A). Following click chemistry and staining with neutral lipid (BODIPY) and macrophage-like (Mac2/Galectin-3) markers, we assessed immune cell content, as well as proliferation and lipid content (Figure 2.3B). Lipid content and $Mac2^+$ staining area as a percentage of lesion area was unchanged between WT and KI female mice (Figure 2.3C,D). Lesional proliferating cells (cells with nuclear EdU stain) were also unchanged between genotypes, and we observed a similar amount of $Mac2^+EdU^+$ and $Mac2^-EdU^+$ cells (Figure 2.3E-G). Collectively, these data suggest that AMPK signaling to HMGCR is not a prominent regulator of atherosclerosis in *Pcks9*-AAV-generated mice.

Bone marrow and splenic hematopoiesis is unchanged between WT and KI mice.

Bone marrow and extramedullary hematopoiesis are well-established upstream drivers of atherosclerosis through the hypercholesterolemia-dependent overproduction of myeloid lineage progenitors and their progeny[241–243,246]. Moreover, *Apoe*$^{-/-}$ mice lacking AMPK-HMGCR signaling had elevated myelopoiesis in the bone marrow and in the spleen, resulting in extramedullary hematopoiesis[478]. Given this previous observation, we wondered how the regulation of endogenous cholesterol synthesis may affect the hematopoietic system in our model. To address this, we performed comprehensive immune phenotyping using flow cytometry on bone marrow and splenic HSPCs (Supplemental Figure 2.5).

HSPCs can be divided into two main classes. Lineage^{-}cKit^{+}Sca1^{-} (LK) cells are more differentiated and have less self-renewal potential, while Lineage^{-}cKit^{+}Sca1^{+} (LSK) cells, which includes populations of multipotent progenitors (MPP) and HSC, have greater self-renewal capacity [490]. Following persistent *Pcsk9*-AAV-induced hypercholesterolemia for 16 weeks in WT and KI mice, we measured progenitor populations in the bone marrow and spleen (Figure 2.4A,B). In the bone marrow, we observed no genotypic changes in the frequency of LK (Figure 2.4C) or LSK (Figure 2.4D) progenitor populations. This trend was also evident for total LK cells (Supplemental Figure 2.6A), although the downstream granulocyte-monocyte progenitors (GMPs) were unchanged in frequency (Figure 2.4D) and total counts (Supplemental Figure 2.6B) in females. To further interrogate the LSK population, we used CD135, CD150, and CD48 markers to separate short-term (ST)-HSC and long-term (LT)-HSC, as well as lymphoid-biased MPP4, myeloid-biased MPP3, and erythroid-biased MPP2 cells (Figure 2.4B). We observed no differences in any of these progenitor subsets in frequency (Figure 4F-J) or total counts (Supplemental Figure 2.6D-H). The ratios of these populations were also unchanged between

genotypes (Figure 2.4K). While *Pcsk9*-AAV-injected male mice developed less plaque than females at 16 weeks (Supplemental Figure 2.3), they had equivalent or greater circulating LDL-cholesterol compared to female mice Supplemental Figure 2.4Q-T; Figure 2.2F-J). Therefore, hypercholesterolemia-induced hematopoietic perturbations were still expected, even with reduced plaque burden. Of note in males, ST-HSCs were elevated in frequency in KI mice relative WT (Supplemental Figure 2.7G); however, all other populations were equivalent between genotypes (Supplemental Figure 2.7).

We next interrogated the potential for increased progenitors in the spleen, which was observed in the *Apoe*-deficient model and taken as evidence of sustained extramedullary hematopoiesis and a potential by-product of HSPC mobilization from the bone marrow[478]. However, we did not observe any changes in splenic progenitor frequency or total count in female (Figure 2.4L,M; Supplemental Figure 2.6I,J) or male (Supplemental Figure 2.7I,J,S,T) mice in our *Pcsk9*-AAV model. While steady-state levels of progenitors can indicate hematopoietic skewing, it does not capture the functional differentiation potential of progenitors. To address this, we performed CFU assays where we plated whole bone marrow in growth factor-rich media sufficient to induce the differentiation of progenitors into major myeloid lineages including granulocytes (CFU-G), monocytes/macrophages (CFU-M), or a combination of the two representing greater self-renewal potential (CFU-GM). We observed no genotypic changes in the total amount of colonies (Figure 2.4N), as well as the amount of CFU-M (Figure 2.4O), CFU-G (Figure 2.4P), and CFU-GM (Figure 2.4Q) colonies. When expressed as a percentage of total colonies there were similarly no changes (Figure 2.4R). These data support the notion that systemic, as well as cell-intrinsic AMPK signaling to HMGCR has little role in

regulating bone marrow and extramedullary hematopoiesis under *Pcsk9*-AAV-induced hypercholesterolemic conditions.

Circulating immune cell populations do not contribute to plaque size in whole-body KI mice.

Circulating Ly6C^{hi} monocytes are major immune drivers of atherosclerosis [241]. Although there were no changes in hematopoietic progenitor populations, we next profiled mature myeloid cells from the bone marrow (Figure 2.5A-D), spleen (Figure 2.5E-H), and blood (Figure 2.5I-L). Aligning with our progenitor data, there were no genotypic differences in frequency or the total amount of Ly6C^{hi} or Ly6C^{lo} monocytes in the bone marrow of female (Figure 2.5B,C; Supplemental Figure 2.8A,B) or male (Supplemental Figure 2.9A,B,J,K) mice. This trend held true for monocytes in the spleens of female (Figure 2.5F,G; Supplemental Figure 2.8D,E) and male (Supplemental Figure 2.9D,E,M,N) mice, as well as circulatory monocytes in female (Figure 2.5J,K; Supplemental Figure 2.8G,H) and male (Supplemental Figure 2.9G,H,P,Q) mice. Interestingly, bone marrow neutrophil frequency was significantly higher in female KI mice (Figure 2.5D). However, this effect size was small and did not carry through to neutrophils in the spleen (Figure 2.5H) or in circulation (Figure 2.5L). There were no genotypic changes in neutrophils in any tissue in male mice (Supplemental Figure 2.9C,F,I,L,O,R). These data demonstrate that mature myeloid cells in HMGCR KI mice are proportionally equivalent to WT mice. Between the myeloid and progenitor immune phenotyping, these data suggest that there are minimal hematopoietic perturbations when AMPK signaling to HMGCR is disrupted in a whole-body context.

Inflammatory signaling is unaltered in mice and cells without AMPK-HMGCR signaling.

Under hypercholesterolemic conditions, cells are exposed to a variety of inflammatory signals that promote signaling through NF-κB[491]. Metabolic intermediates of the mevalonate pathway such as mevalonate itself[492] and isoprenoid species[493] have been shown to influence the cellular responses to inflammation. To test how macrophages lacking AMPK-HMGCR signaling would react to a lipid-rich environment, we lipid-loaded BMDM from non-hypercholesterolemic mice with vortex-aggregated LDL (agLDL) overnight before measuring lipid content and gene expression (Figure 2.6A). BODIPY staining, as a proxy for neutral lipid content, was equivalent between genotypes in the basal and lipid-loaded states (Figure 2.6B,C). Cells similarly responded to short-term lipid loading for six hours with acLDL (Figure 2.6D). Under lipid-loaded conditions, we measured several lipid-sensitive and insensitive genes in the mevalonate pathway and others. By comparing the mRNA fold change in response to agLDL within each biological replicate, we found that HMGCR KI BMDM had lower transcript expression in mevalonate pathway genes *Hmgcs1*, *Hmgcr*, and *Fdft1*, while others such as *Mvk*, *Dhcr7*, and *Dhcr24* were unchanged between genotypes (Figure 2.6E). Genes involved in isoprenoid regulation such as *Pggt1b* and *Fntb* were largely unaffected by lipid-loading, although there was a trend towards lower *Ggpps1* in KI cells. Interestingly, KI BMDM had lower expression of two G1/S regulators in *Rrm1* and *Slbp* following lipid-loading, while other cell cycle markers for G2/M such as *Top2a* and *Mki67* were unchanged between genotypes but suppressed with lipid-loading[494]. *Msr1*, which encodes several scavenger receptors, was suppressed, while *Fabp4*, which generates a lipid-binding protein, was elevated, with no genotypic differences (Figure 2.6E).

To assess whether these differing responses to agLDL loading affected inflammatory cytokine production downstream of NFκB signaling, we lipid-loaded BMDM before stimulating the cells with the TLR4 agonist, LPS, for a further two, six, or twenty-four hours (Figure 2.6F). Secreted amounts of TNF-α and IL-6 were unchanged between genotype (Figure 2.6G,H), although TNF-α secretion was significantly higher in the lipid-loaded condition than the basal state (Figure 2.6G). At the mRNA level, *Il1b* transcript followed the opposite trend, with it being much lower in the lipid-loaded state with no genotypic changes (Figure 2.6I). IL-1β secretion, induced via exposure to ATP after four hours of LPS stimulation also showed no genotypic differences (Figure 2.6J).

Responses to inflammation are tightly linked to available ATP stores. To interrogate bioenergetics under activated conditions, we performed extracellular flux analyses with a mitochondrial stress test on basal and LPS-stimulated WT and KI BMDM. LPS stimulation decreased the oxygen consumption rate (OCR) both basally and at maximal respiration (Supplemental Figure 2.10A) while increasing the extracellular acidification rate (ECAR) basally and following the addition of all injections (Supplemental Figure 2.10B). While there were no genotype differences in basal respiration, maximal respiration, and proton leak, ATP-linked respiration was higher in LPS-stimulated KI cells (Supplemental Figure 2.10C-F). BMDM were respiring maximally at baseline and therefore had minimal reserve capacity, although this was higher in KI cells (Supplemental Figure 2.10G). To assess mitochondrial content, we measured the ratio of mitochondrial DNA to nuclear DNA and observed no differences between WT and KI cells (Supplemental Figure 2.10H). Collectively, these data suggest that mitochondrial biology is largely unaffected in HMGCR KI BMDM under pro-inflammatory conditions.

While these data demonstrate the minimal role of AMPK signaling to HMGCR in macrophage acute inflammatory responses, we wondered if this translated to *in vivo* conditions. Following our *Pcsk9*-AAV-induced hypercholesterolemia paradigm (Figure 2.6K), we measured circulating cytokines using a multiplex cytokine array. Similar to our *in vitro* results, we observed no changes in circulating NF-κB-dependent TNF-α, IL-6, or IL-1β, nor in IL-10, which generally exerts anti-inflammatory effects (Figure 2.6K-N). Collectively, these data support that AMPK signaling to HMGCR has little role in the response to inflammatory stimuli whether in the basal or lipid-loaded state.

Bone marrow transplanted HMGCR KI mice develop equivalent atherosclerosis to WT-transplanted mice.

In primary macrophages, we validated the importance of energy metabolism in the regulation of endogenous cholesterol synthesis (Figure 2.1). To directly test whether the hematopoietic AMPK-HMGCR signaling axis contributes to *Pcsk9*-AAV-induced atherosclerosis, we transplanted bone marrow from female WT or KI mice into lethally irradiated WT mice. Following immune reconstitution, we injected the mice with the *Pcsk9*-AAV and fed them a WD for 16 weeks (Figure 2.7A). Aligning with our whole-body KI data, aortic root lesion area in female KI BMT mice was not different from mice reconstituted with WT bone marrow when expressed as a percentage of aortic root (Figure 2.7C,D; Supplemental Figure 2.11A-C). Aortic lesion area in KI BMT mice was slightly higher than in WT when measured in mm^2 instead of aortic root percentage (Supplemental Figure 2.11D-G). There was also a trend towards increased necrotic core area in the KI BMT mice, although this was not statistically significant (Figure 2.7D). Within the BMT cohorts, changes in aortic root lesion area were relatively small

and were driven by several high responders in the KI group, suggesting that the biological relevance of hematopoietic AMPK-HMGCR signaling is minimal in our model (Supplemental Figure 2.11D-G). Circulating total cholesterol levels were significantly higher in the KI BMT mice (Figure 2.7E), which may have contributed to the trends observed in this BMT cohort relative to our prior whole-body cohorts. Despite the elevation in circulating cholesterol, serum levels of TNF-α, IL-6, and IL-1β were all unchanged between genotypes, as was IL-10 (Figure 2.7F-I). Together, our data demonstrate that while the AMPK-HMGCR signaling axis regulates cell-intrinsic cholesterol synthesis, its involvement in the development and progression of atherosclerosis is subtle in the *Pcsk9*-AAV hypercholesterolemic model.

2.6 Discussion

We used a non-germline *Pcsk9*-AAV-induced hypercholesterolemia approach to promote atherosclerosis in mice with or without a functional AMPK-HMGCR signaling axis. We observed no changes in total plaque burden, necrotic core area, or in plaque lipid content in the aortic root of both male and female mice. Moreover, BMT experiments confirmed that AMPK signaling to HMGCR in immune cells contributes little to the overall plaque burden in *Pcsk9*-AAV-induced atherosclerosis.

In the previous study using HMGCR S871A KI mice on an *Apoe*$^{-/-}$ background, dysregulated hematopoiesis in the bone marrow and spleen led to increased plaque burden downstream[478]. This work was the first to interrogate a specific target of AMPK in the context of atherosclerosis and examine the link between endogenous cholesterol synthesis and myelopoiesis. Given the differences between atherosclerosis models, it is important to compare key readouts between studies, which both harboured the identical S871A point mutation on HMGCR. Firstly, the two models yielded differential effects of the KI mutation on lesion size: here we observed no change in plaque area in our *Pcsk9*-AAV model while an increase was seen in *Apoe*$^{-/-}$ mice. When comparing average plaque area, we report lesions approximately twice the size (~0.4-0.6 mm^2 vs ~0.15-0.3 mm^2), which could be due to the elevated circulating cholesterol levels in our model, which were ~1.5 fold higher. It is possible this elevated hypercholesterolemia may have masked an effect that would have otherwise been observable at lower circulating cholesterol levels. Additionally, AMPK-HMGCR signaling in plaque resident cells may be important at earlier phases of atherosclerosis, and we failed to capture this change at 16 weeks of hypercholesterolemia. However, we did not observe any genotypic changes in male mice at 16 weeks, which, owing to their slower plaque development than females, provided a

proxy for an earlier stage of lesion progression (Supplemental Figure 2.3). Moreover, our circulating total cholesterol levels are in line with other *Pcsk9*-AAV studies[315], as well as AMPK studies on *Ldlr*$^{-/-}$[324] and *Apoe*$^{-/-}$ backgrounds[479].

Nonetheless, we explored the role of AMPK-HMGCR signaling on hypercholesterolemia-induced hematopoietic perturbations in our *Pcsk9*-AAV model to compare with our *Apoe*$^{-/-}$ study. Here, we observed no changes in any major immune cell populations, suggesting that AMPK-HMGCR signaling is not a critical regulator of hypercholesterolemia-induced hematopoiesis. The cell-autonomous role of ApoE in regulating HSPC expansion and monocytosis is well described[311], and evidenced by a BMT of WT bone marrow into *Apoe*$^{-/-}$ mice protecting the *Apoe*$^{-/-}$ mice from atherosclerosis[312]. We propose that our lack of hematopoietic phenotype indicates that combined deficiency of AMPK-HMGCR signaling *and* ApoE is required to observe hematopoietic dysregulation under hypercholesterolemic conditions. Such discrepancies have been observed recently in a study regarding the glucose-dependent insulinotropic polypeptide receptor during atherosclerosis, where significant increases in plaque area were observed in *Apoe*$^{-/-}$ but not in a *Pcsk9*-AAV model[495]. Future work in *Pcks9*-AAV models could consider employing antisense oligonucleotides targeted to ApoE to tease out ApoE-dependent effects and compare between models. When viewing the AMPK-HMGCR signaling axis through the lens of our study and the *Apoe*$^{-/-}$ study, it is likely that AMPK-HMGCR signaling plays a subtle role in atherosclerosis, but the major downstream effectors of AMPK signaling and its atheroprotective role remain unknown.

Given the importance of environmental variables when considering murine cardiometabolic studies, it is possible that differences in housing conditions and microbiome composition may have affected results between our studies[496]. Moreover, while the

atherosclerotic models (*Apoe*$^{-/-}$ vs. *Pcsk9*-AAV) are major drivers of dysregulated lipoprotein homeostasis, dietary composition (chow vs WD) and the resulting impact on gut homeostasis and systemic lipid regulation may have differential effects in both models as well[497]. Finally, while ApoE deficiency affects hematopoiesis directly, *Pcsk9*-AAV overexpression results not only in liver LDLR degradation, but also in supraphysiological concentrations of circulating PCSK9. PCSK9 has been implicated as a positive regulator of NF-κB-dependent signaling[498,499], and appears to itself be regulated downstream of TLR4 signaling[500]. In atherosclerotic plaques of *Apoe*$^{-/-}$ mice, PCSK9 expression increases as lesions develop while inhibiting PCSK9 slows plaque progression[501], pointing to the potential confounding effects of elevated circulating PCSK9 in our *Pcsk9*-AAV model.

To circumvent these confounders in the future, it may be beneficial to consider alternative hypercholesterolemia models. Coupling WD-feeding with *Ldlr* antisense oligonucleotides is a promising avenue and has been shown to induce atherosclerosis[502], although this may not be as effective as using *Ldlr*$^{-/-}$ mice[317]. With the potential of liver-targeting antisense oligonucleotides[503], optimally designed *Ldlr* antisense oligonucleotides could generate fewer off-target effects than *Pcsk9*-AAV models while also not requiring whole-body germline deletion of key cholesterol regulators like LDLR and ApoE. Alternatively, use of an *Alb*-Cre-ERT2 model with floxed *Ldlr* alleles would theoretically delete *Ldlr* specifically in the liver following tamoxifen injection, though to our knowledge this technique has not been explored in murine atherosclerosis research.

Cholesterol was one of the first identified drivers of atherosclerosis[504], and its excess in circulation can exacerbate lesion development. While this has been long appreciated, the role for intracellular cholesterol synthesis, particularly within the atherosclerotic lesion

microenvironment, has garnered much less attention. Genetic deletion of *Hmgcr* is lethal during embryonic development[505]; however, myeloid-specific *Hmgcr* knockout leads to increased plaque formation on an *Ldlr*$^{-/-}$ background[506]. This was shown indirectly to be a result of prenylation-dependent pathways downstream of HMGCR, and not of *de novo* sterol synthesis. It will be interesting to probe the importance of metabolic regulation of the various mevalonate pathway outputs, both sterol and non-sterol, in the context of atherosclerosis and other models of chronic inflammation.

Mevalonate pathway flux is intimately linked to macrophage inflammatory responses to pathogen-associated molecular patterns. Within the sterol branch of the mevalonate pathway, both lanosterol and desmosterol have been shown to suppress TLR4-mediated inflammatory signaling[507,508]. Macrophages co-stimulated with LPS and interferon γ downregulate lanosterol 14-α demethylase following type I interferon signaling and accumulate lanosterol, which both suppresses further activation and increases membrane fluidity[507]. Within the isoprenoid branch, several studies have implicated isoprenoids as key mediators of the statin-induced suppression of inflammatory signaling in response to LPS[509]. Indeed, defective protein geranylgeranylation hyperactivates the cellular response to LPS[493], an effect mapped to altered PI(3)K activity[510].

AMPK activity has been established as having anti-inflammatory effects in the context of macrophage activation[325,385], yet surprisingly little is understood mechanistically. Our extensive LPS stimulation experiments, which included both lipid-loaded and lipid-deprived states, show that AMPK-mediated suppression of cholesterol synthesis through phosphorylation of HMGCR does not affect the acute, nor prolonged response to LPS. These observations, though in cultured macrophages, suggest that AMPK suppression of cholesterol synthesis does not contribute to its overall anti-inflammatory effect, despite the involvement of mevalonate pathway intermediates

in regulating inflammatory signaling. A recent study using BMDM generated from a myeloid-specific knockdown of ACC 1 and 2 showed a suppressed production of inflammatory cytokines in response to LPS[511]. Our acetate incorporation experiments highlight that AMPK activation in macrophages has a stronger suppressive effect on *de novo* fatty acid synthesis than it does on cholesterol synthesis (Figure 2.1B, Supplemental Figure 2.1B). Therefore, it would be interesting to probe whether AMPK regulation of fatty acid metabolism influences inflammatory responses and if this would have a significant effect on a chronic inflammatory pathology such as atherosclerosis.

Murine models of atherosclerosis only partially mimic human pathology, with several key differences in plaque development having been identified between mice and humans. The relative contribution of smooth muscle cell-derived foam cells is higher in human atherosclerosis compared to mice[234] and there are important discrepancies in lipoprotein homeostasis[512]. While direct investigation into AMPK signaling in human atherosclerosis progression is minimal, metformin, which is an indirect activator of AMPK, has been shown to generally reduce all-cause mortality in patients with myocardial infarction and heart failure[513]. In the future, clinical implementation of direct AMPK activators that circumvent inducing cardiac hypertrophy[199] will be necessary to assess whether AMPK activation is a viable therapeutic strategy for reducing ACVD risk.

Mouse models that target specific phosphoregulatory nodes remain the best way to dissect the physiological significance of individual signaling axes. Here, we confirm that AMPK-dependent phosphorylation of HMGCR is important for regulating cholesterol synthesis in macrophages. However, loss of this signaling axis in a *Pcsk9*-AAV-driven model of hypercholesterolemia does not significantly influence markers of atherosclerosis, hematopoiesis,

or inflammation in male or female mice. This study highlights the importance of murine atherosclerosis model validation and contextualizes the complex role of AMPK in regulating atherosclerosis.

2.7 Figures

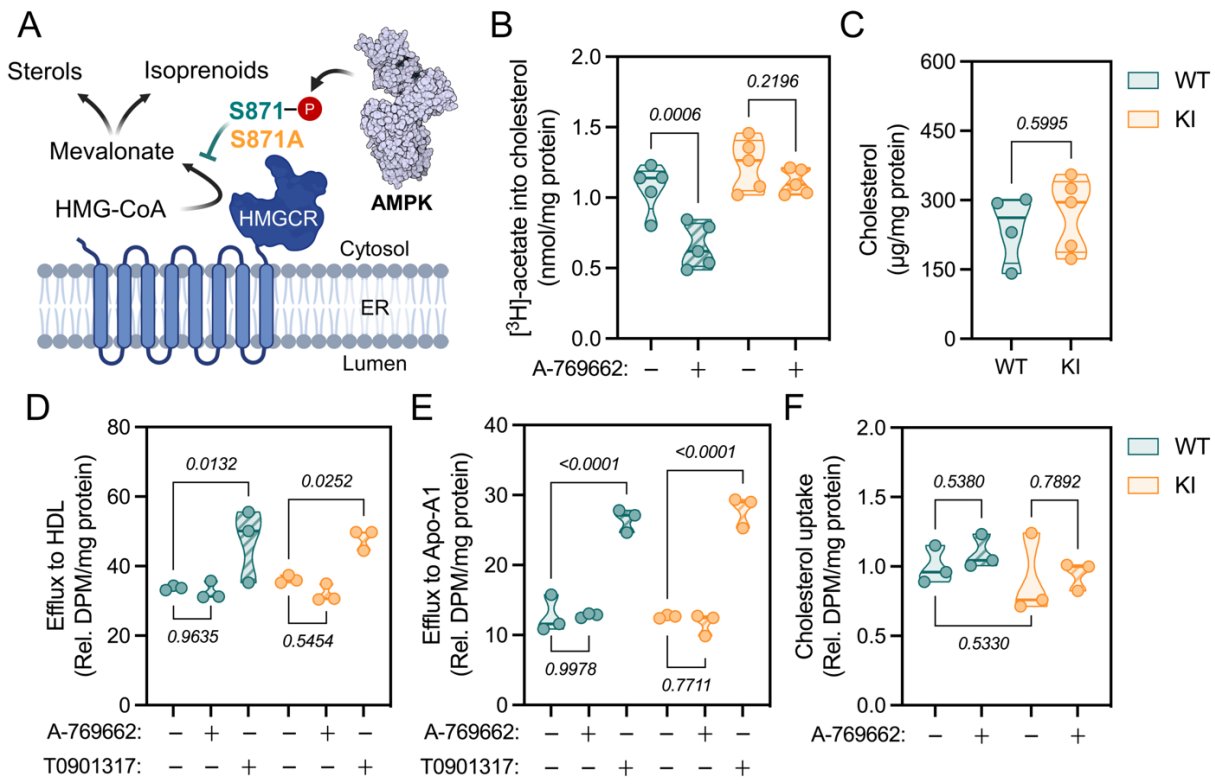

Figure 2.1: Cholesterol synthesis is unresponsive to AMPK activation in HMGCR S871A KI macrophages. (A) Schematic of model: AMPK phosphorylates S871 on WT HMGCR and reduces its activity, whereas S871A KI cells are not responsive to AMPK-mediated phosphorylation. **(B)** BMDM were labeled for 4 h with [^{3}H]-acetate (1 μCi/ml) with or without cotreatment of A-769662 (100 μM) and incorporation into *de novo*-synthesized cholesterol was measured by thin layer chromatography (n=4 WT and KI). **(C)** Total cholesterol levels (BMDM; n=4 WT and n=5 KI). **(D,E)** Cholesterol efflux to HDL **(D)** and Apo-A1 **(E)** cholesterol acceptors 24 h post lipid-loading with [^{3}H]-cholesterol-labeled acLDL (50 μg/ml) with A-769662 (100 μM) or T0901317 (10 μM) cotreatments. **(F)** BMDM cholesterol uptake from media containing [^{3}H]-cholesterol-labeled acLDL (50 μg/ml) for 15 min with or without 30 min A-769662 (100 μM) pretreatment. Data represented as violin plots truncated at maxima and minima with median and first and fourth quartiles outlined. *P* values calculated using two-way ANOVA with Tukey's post-hoc analysis for (B,D,E,F) and an unpaired, two-tailed Student's t-test for (C).

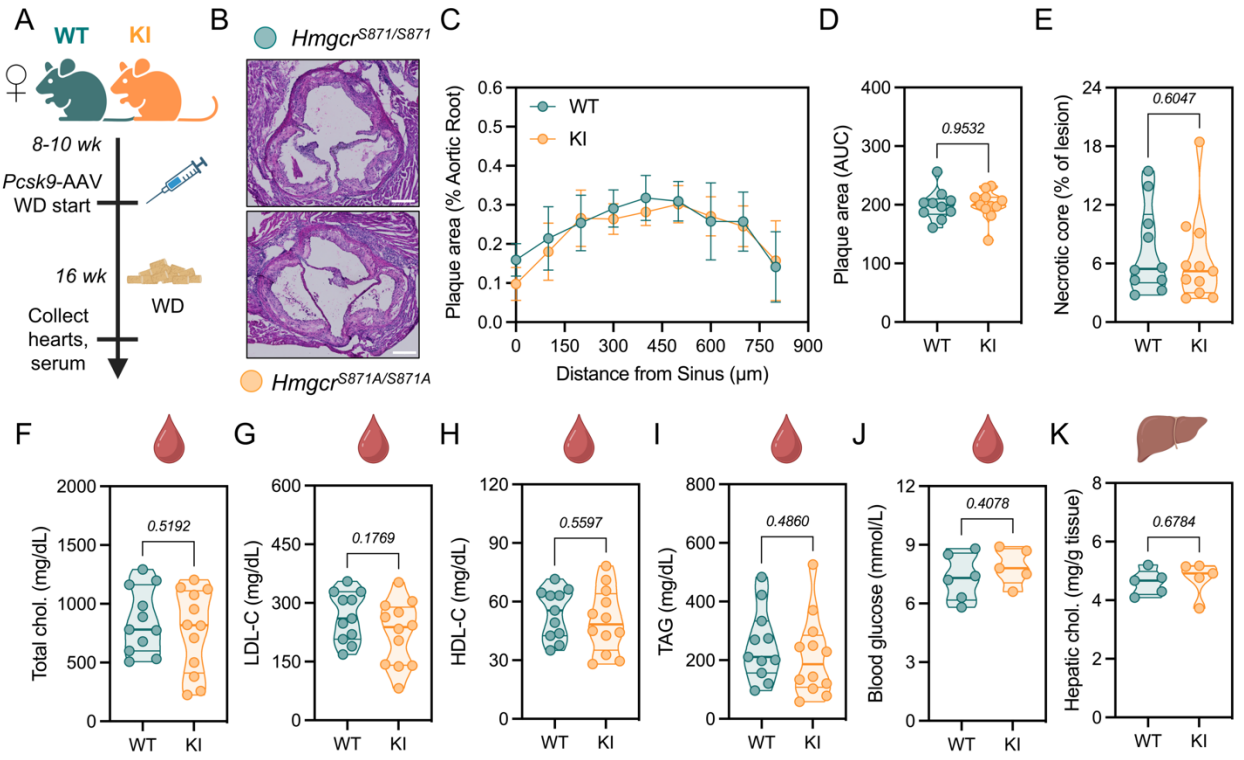

Figure 2.2: HMGCR S871A KI mice do not develop more aortic root plaque than WT mice in a *Pcsk9*-AAV-induced hypercholesterolemia atherosclerosis model. (A) Schematic of model: 8-10 wk old female mice were injected i.v. with *Pcsk9*-AAV8 (2.5 x 10^{10} genome copies) and fed a western diet (40% kcal fat, 0.15% cholesterol) for 16 wk. **(B)** Representative H&E image of the aortic root (scale bar = 200 μm). **(C,D)** Aortic root plaque area expressed as a percentage of aortic root in a histogram spanning 800 μm **(C)** and the resulting area under the curve **(D)** (n=10 WT and n=11 KI mice). **(E)** Necrotic core expressed as a percentage of lesion area (n=10 WT and n=11 KI mice). **(F-I)** Serum measurements of total cholesterol **(F)**, LDL-cholesterol **(G)**, HDL-cholesterol **(H)**, triacylglycerols **(I)**, and blood glucose **(J)** (n=6-11 WT and n=5-12 KI mice). **(K)** Hepatic cholesterol content (n=5 WT and KI). Data represented as violin plots truncated at maxima and minima with median and first and fourth quartiles outlined or as a histogram with mean ± SD. *P* values calculated using an unpaired, two-tailed Student's t-test for (D; F-K), or an unpaired, two-tailed Mann-Whitney U test for (E).

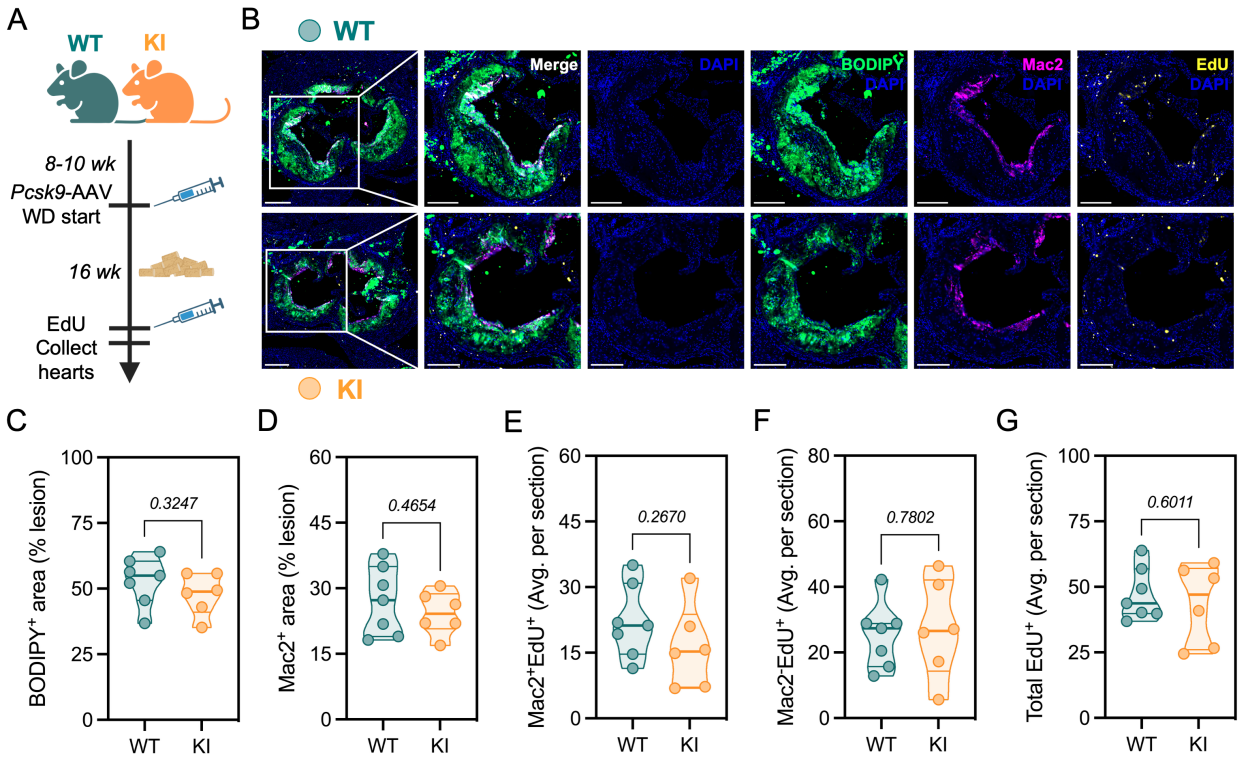

Figure 2.3: Plaque lipid content and macrophage proliferation is equivalent between WT and HMGCR S871A KI mice. (A) Schematic of experiment: female WT and KI mice were made atherogenic as in Figure 2. 4 h before harvest, mice were injected with EdU to label plaque proliferative cells. **(B)** Representative panel of immunofluorescent staining with BODIPY 493/503 staining in green, Mac2 in pink, EdU in yellow, and DAPI in blue (overview scale bar = 300 μm; inset scale bars = 200 μm). **(C,D)** BODIPY 493/503$^+$ area **(C)** and Mac2$^+$ area **(D)** expressed as a percentage of lesion area (n=7 WT and n=6 KI). **(E-F)** EdU$^+$ nuclei for Mac2$^+$ **(E)**, Mac2$^-$ **(F)**, and total plaque cells **(G)** expressed as average cells per section (n=7 WT and n=6 KI). Data represented as violin plots truncated at maxima and minima with median and first and fourth quartiles outlined. *P* values calculated using an unpaired, two-tailed Student's t-test.

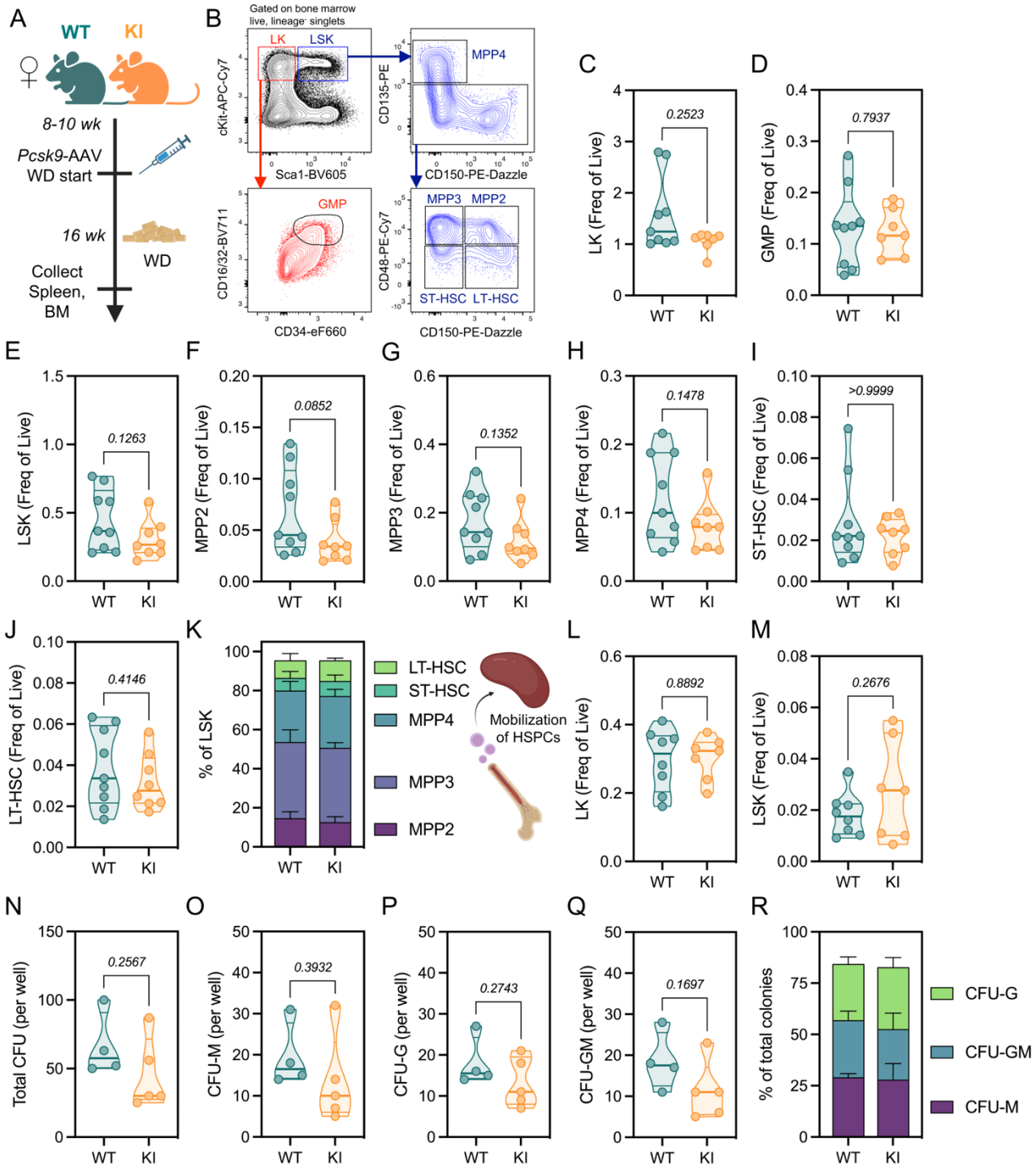
A
WT
KI
8-10 wk
Pcsk9-AAV
WD start
16 wk
WD
Collect
Spleen,
BM
B
Gated on bone marrow
live, lineage- singlets
LK
LSK
cKit-APC-Cy7
Sca1-BV605
CD135-PE
CD150-PE-Dazzle
MPP4
GMP
CD16/32-BV711
CD34-eF660
CD48-PE-Cy7
MPP3
MPP2
ST-HSC
LT-HSC
C
LK (Freq of Live)
0.2523
D
GMP (Freq of Live)
0.7937
E
LSK (Freq of Live)
0.1263
F
MPP2 (Freq of Live)
0.0852
G
MPP3 (Freq of Live)
0.1352
H
MPP4 (Freq of Live)
0.1478
I
ST-HSC (Freq of Live)
>0.9999
J
LT-HSC (Freq of Live)
0.4146
K
% of LSK
LT-HSC
ST-HSC
MPP4
MPP3
MPP2
Mobilization
of HSPCs
L
LK (Freq of Live)
0.8892
M
LSK (Freq of Live)
0.2676
N
Total CFU (per well)
0.2567
O
CFU-M (per well)
0.3932
P
CFU-G (per well)
0.2743
Q
CFU-GM (per well)
0.1697
R
% of total colonies
CFU-G
CFU-GM
CFU-M
WT
KI

Figure 2.4: Hematopoietic progenitor populations are unchanged in HMGCR S871A KI mice. (A) Atherosclerosis was induced in WT and KI female mice as in Figure 2.2. **(B)** Representative gating strategy in bone marrow to identify LK (red) and LSK (blue) populations. (**C-J)** Frequency of live, single cells for LK **(C)**, GMP **(D)**, LSK **(E)**, MPP2 **(F)**, MPP3 **(G)**, MPP4 **(H)**, ST-HSC **(I)**, and LT-HSC **(J)** populations in bone marrow (n=9 WT and n=8 KI). **(K)** Frequency of LSK populations (n=9 WT and n=8 KI). **(L,M)** Frequency of live, single cells for LK **(L)** and LSK **(M)** splenic progenitors (n=8 WT and n=7 KI). **(N-R)** 15,000 whole bone marrow cells were plated in methocult media and colony forming units (CFU) counted after 14 days of differentiation. Total CFUs **(N)**, CFU-M **(O)**, CFU-G **(P)**, and CFU-GM **(Q)** (n=4 WT and n=5 KI). **(R)** CFU-M, CFU-G, and CFU-GM colonies as a percentage of total colonies. Data represented as violin plots truncated at maxima and minima with median and first and fourth quartiles outlined or as stacked bar graphs representing mean ± SD. *P* values calculated using an unpaired, two-tailed Student's t-test for (D-H,J,L-Q), or an unpaired, two-tailed Mann-Whitney U test for (C,I).

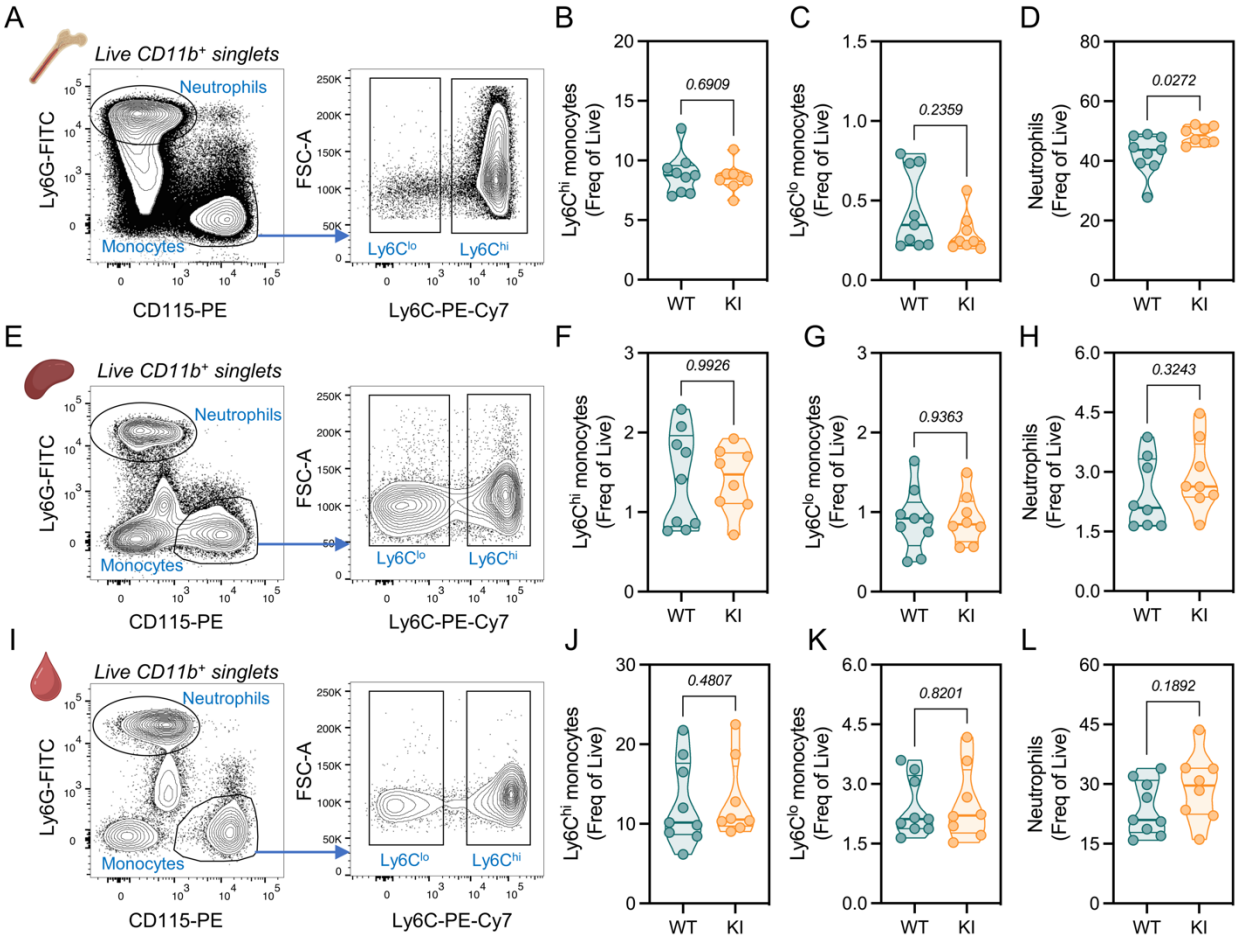

Figure 2.5: Mature myeloid populations are unchanged in HMGCR S871A KI mice. Atherosclerosis was induced in WT and KI female mice as in Figure 2. **(A)** Representative gating strategy for bone marrow myeloid cells. **(B-D)** Frequency of live, single cells for Ly6C^{hi} monocytes **(B)**, Ly6C^{lo} monocytes **(C)**, and neutrophils **(D)** in bone marrow (n=9 WT and n=8 KI). **(E)** Representative gating strategy for splenic myeloid cells. **(F-H)** Frequency of live, single cells for Ly6C^{hi} monocytes **(F)**, Ly6C^{lo} monocytes **(G)**, and neutrophils **(H)** in spleen (n=9 WT and n=8 KI). **(I)** Representative gating strategy for circulating myeloid cells. **(J-L)** Frequency of live, single cells for Ly6C^{hi} monocytes **(J)**, Ly6C^{lo} monocytes **(K)**, and neutrophils **(L)** in circulation (n=9 WT and n=8 KI). Data represented as violin plots truncated at maxima and minima with median and first and fourth quartiles outlined. *P* values calculated using an unpaired, two-tailed Student's t-test for (B,D-H,K-L), or an unpaired, two-tailed Mann-Whitney U test for (C,J).

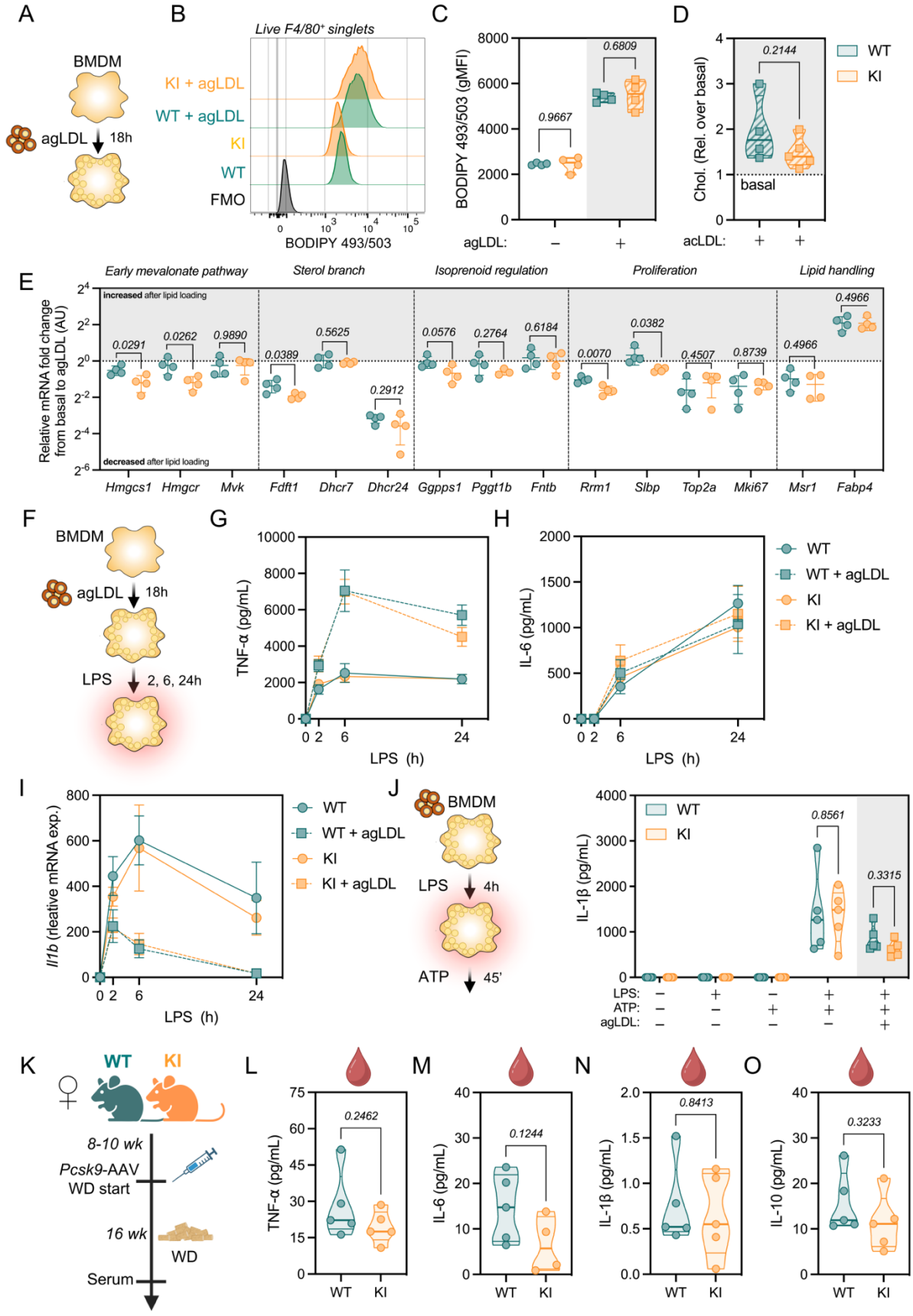
A
BMDM
agLDL
18h
B
Live F4/80+ singlets
KI + agLDL
WT + agLDL
KI
WT
FMO
BODIPY 493/503
C
BODIPY 493/503 (gMFI)
0.9667
0.6809
agLDL:
D
Chol. (Rel. over basal)
0.2144
basal
acLDL:
WT
KI
E
Early mevalonate pathway
Sterol branch
Isoprenoid regulation
Proliferation
Lipid handling
Relative mRNA fold change from basal to agLDL (AU)
increased after lipid loading
decreased after lipid loading
0.0291
0.0262
0.9890
0.0389
0.5625
0.2912
0.0576
0.2764
0.6184
0.0070
0.0382
0.4507
0.8739
0.4966
0.4966
Hmgcs1
Hmgcr
Mvk
Fdft1
Dhcr7
Dhcr24
Ggpps1
Pggt1b
Fntb
Rrm1
Slbp
Top2a
Mki67
Msr1
Fabp4
F
BMDM
agLDL
18h
LPS
2, 6, 24h
G
TNF-α (pg/mL)
LPS (h)
H
IL-6 (pg/mL)
LPS (h)
WT
WT + agLDL
KI
KI + agLDL
I
Il1b (reative mRNA exp.)
LPS (h)
J
BMDM
LPS
4h
ATP
45'
IL-1β (pg/mL)
0.8561
0.3315
LPS:
ATP:
agLDL:
K
WT
KI
8-10 wk
Pcsk9-AAV
WD start
16 wk
WD
Serum
L
TNF-α (pg/mL)
0.2462
M
IL-6 (pg/mL)
0.1244
N
IL-1β (pg/mL)
0.8413
O
IL-10 (pg/mL)
0.3233

Figure 2.6: S871A KI HMGCR macrophages respond similarly to inflammatory stimuli. (A) Lipid loading schematic: BMDM from non-hypercholesterolemic mice were lipid-loaded overnight with vortex-aggregated LDL (agLDL; 50 μg/ml) for 18 hours. **(B-C)** Representative BODIPY493/503 staining **(B)** and gMFI quantification **(C)** (n=4 WT and KI). **(D)** BMDM were lipid-loaded for 6 h with acLDL (50 μg/ml) and relative fold increase over non-lipid loaded state plotted. **(E)** BMDM were lipid loaded overnight with agLDL (50 μg/ml) and gene expression was measured by RT-qPCR. Values are represented as the fold change with lipid-loading within each biological replicate (n=4 WT and KI). **(F-I)** Schematic of inflammatory activation. BMDM were lipid loaded overnight with agLDL (50 μg/ml) before being stimulated with LPS (100 ng/ml) for 2, 6, and 24 h. Concentration of TNF-α **(G)** and IL-6 **(H)** in culture supernatants (n=4 WT and KI). **(I)** Relative fold change in *Il1b* mRNA transcript. **(J)** BMDM were lipid loaded for 24 h with agLDL (50 μg/ml) and stimulated with LPS (100 ng/ml) for 4 h before spiking in ATP (2 mM) for 45 min. Concentration of IL-1β in culture supernatants (n=5 WT and KI). **(K-O)** Female mice were fed a WD for 16 wk following *Pcsk9*-AAV injection. Circulating TNF-α **(L)**, IL-6 **(M)**, IL-1β **(N)**, and IL-10 **(O)**. Data represented as violin plots truncated at maxima and minima with median and first and fourth quartiles outlined, or as histograms with mean ± SD. *P* values were calculated using a two-way ANOVA with Tukey's post-hoc analysis in (C,J), an unpaired, two-tailed Student's t-test for (D,E,L,M,O), or a two-tailed, unpaired Mann-Whitney U test for (N).

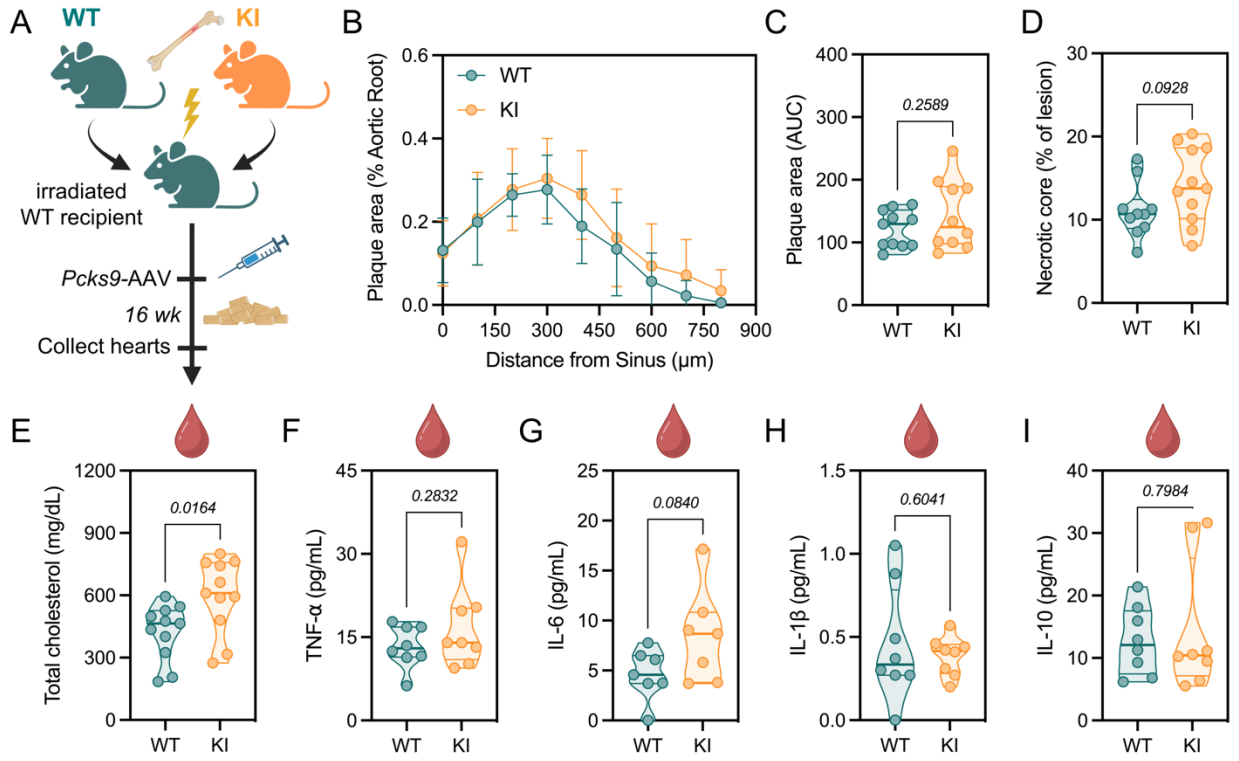

Figure 2.7: HMGCR S871A KI bone marrow transplanted mice do not have elevated plaque. (A) Schematic of experiment: bone marrow from female WT and KI mice were transplanted into lethally irradiated WT mice. Following a 4 wk recovery period, mice were injected i.v. with *Pcsk9*-AAV8 (2.5×10^{10} genome copies) and fed a western diet (40% kcal fat, 0.15% cholesterol) for 16 wk. **(B,C)** Aortic root plaque area expressed as a percentage of aortic root in a histogram spanning 800 μm **(B)** and the resulting area under the curve **(C)** (n=11 WT and n=10 KI mice). **(D)** Necrotic core expressed as a percentage of lesion area (n=10 WT and n=11 KI mice). **(E)** Serum total cholesterol. **(F-I)** Serum cytokine concentration for TNF-α **(F)**, IL-6 **(G)**, IL-1β **(H)**, and IL-10 **(I)**. Data represented as violin plots truncated at maxima and minima with median and first and fourth quartiles outlined, or as histograms with mean ± SD. *P* values were calculated using an unpaired, two-tailed Student's t-test for (C-H), or a two-tailed, unpaired Mann-Whitney U test for (I).

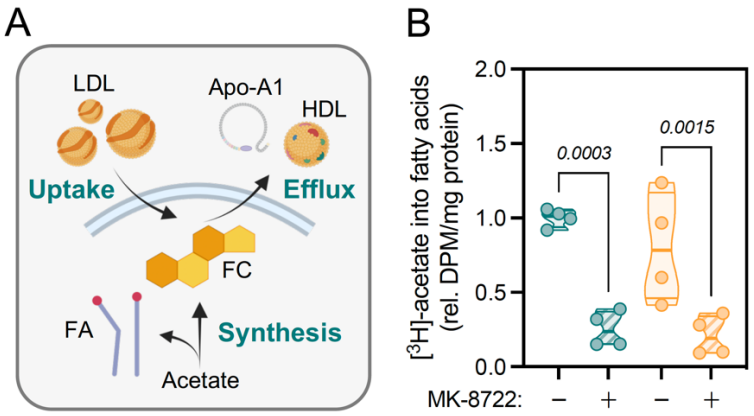

Supplemental Figure 2.1: Allosteric activation of AMPK suppresses fatty acid but not cholesterol synthesis in HMGCR S871A KI macrophages. (A) Schematic of cholesterol regulation: free cholesterol (FC) levels are regulated by rates of synthesis, uptake, and efflux. **(B)** BMDM were labeled for 4 h with [^{3}H]-acetate (1 µCi/ml) and incorporation into *de novo* fatty acid synthesis was measured with or without a 1 h MK-8722 (2 µM) pretreatment (n=4 WT and KI). *P* values calculated using two-way ANOVA with Tukey's post-hoc analysis.

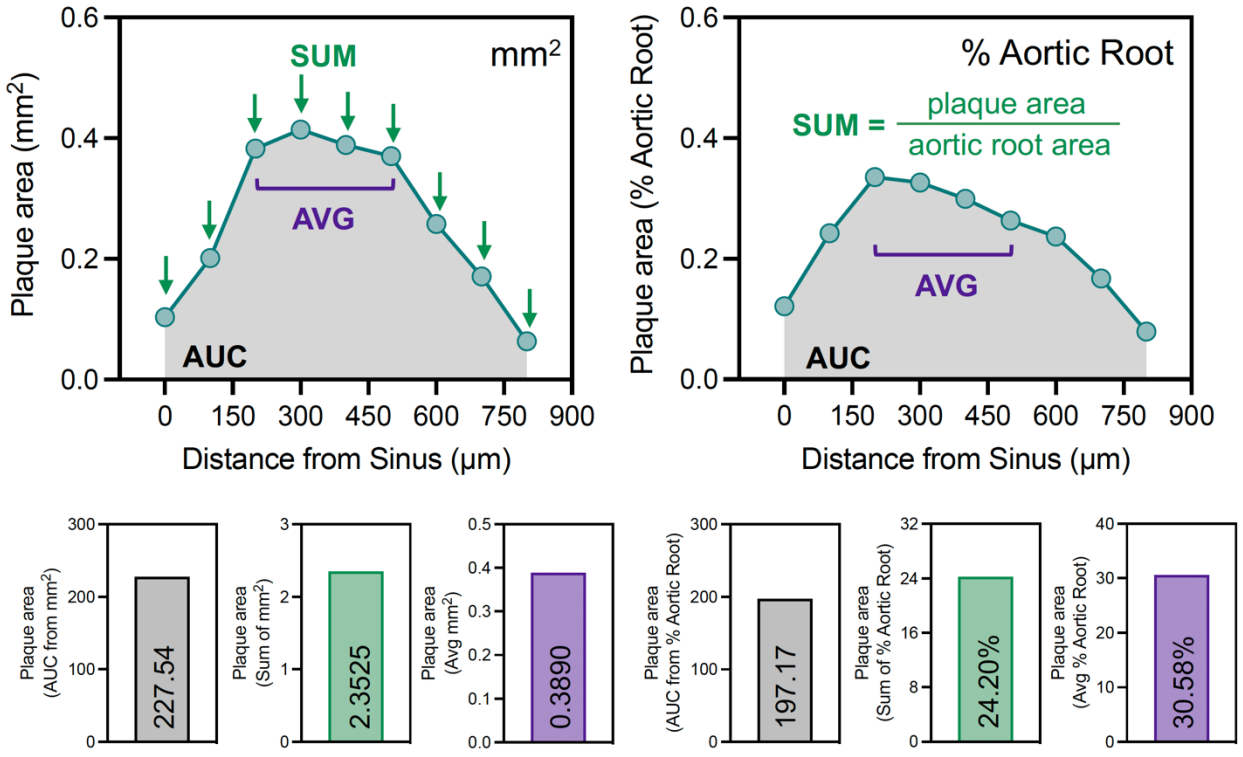

Supplemental Figure 2.2: Atherosclerosis quantification workflow. Frozen aortic sinuses were sectioned at 10 μm serially across 10 slides such that each slide contained 9 sections spaced 100 μm apart and spanning 800 μm in total. Plaque was manually outlined in H&E-stained sections on ImageJ. **Left:** Plaque histogram representing the plaque on each section expressed in mm^2 or **Right:** as a percentage of aortic root. AUC measurements are derived from the histograms, while sum is the total plaque amount in mm^2 or the total plaque area divided by the total aortic root area. Average lesion area is the average of 3-5 sections starting from when three leaflets are clearly identifiable.

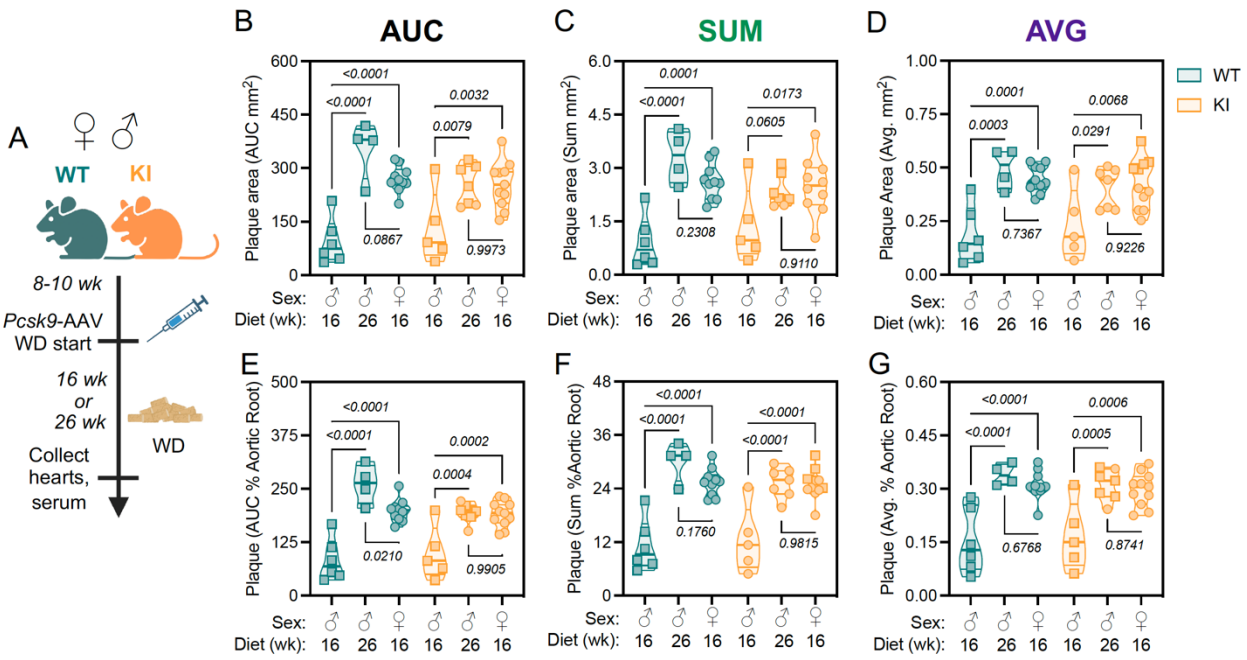

Supplemental Figure 2.3: *Pcsk9*-AAV-induced hypercholesterolemia affects male and female mice differently. (A) Schematic of model: 8-10 wk old male and female mice were injected i.v. with *Pcsk9*-AAV8 (2.5 x 10^{10} genome copies) and fed a western diet (40% kcal fat, 0.15% cholesterol) for 16 or 26 wk. **(B-D)** Atherosclerotic plaque expressed in mm^2 for AUC **(B)**, sum **(C)**, and average lesion size **(D)**. **(E-G)** Atherosclerotic plaque expressed as a percentage of aortic root for AUC **(E)**, sum **(F)**, and average lesion size **(G)**. Data represented as violin plots truncated at maxima and minima with median and first and fourth quartiles outlined. *P* values calculated using two-way ANOVA with Tukey's post-hoc analysis.

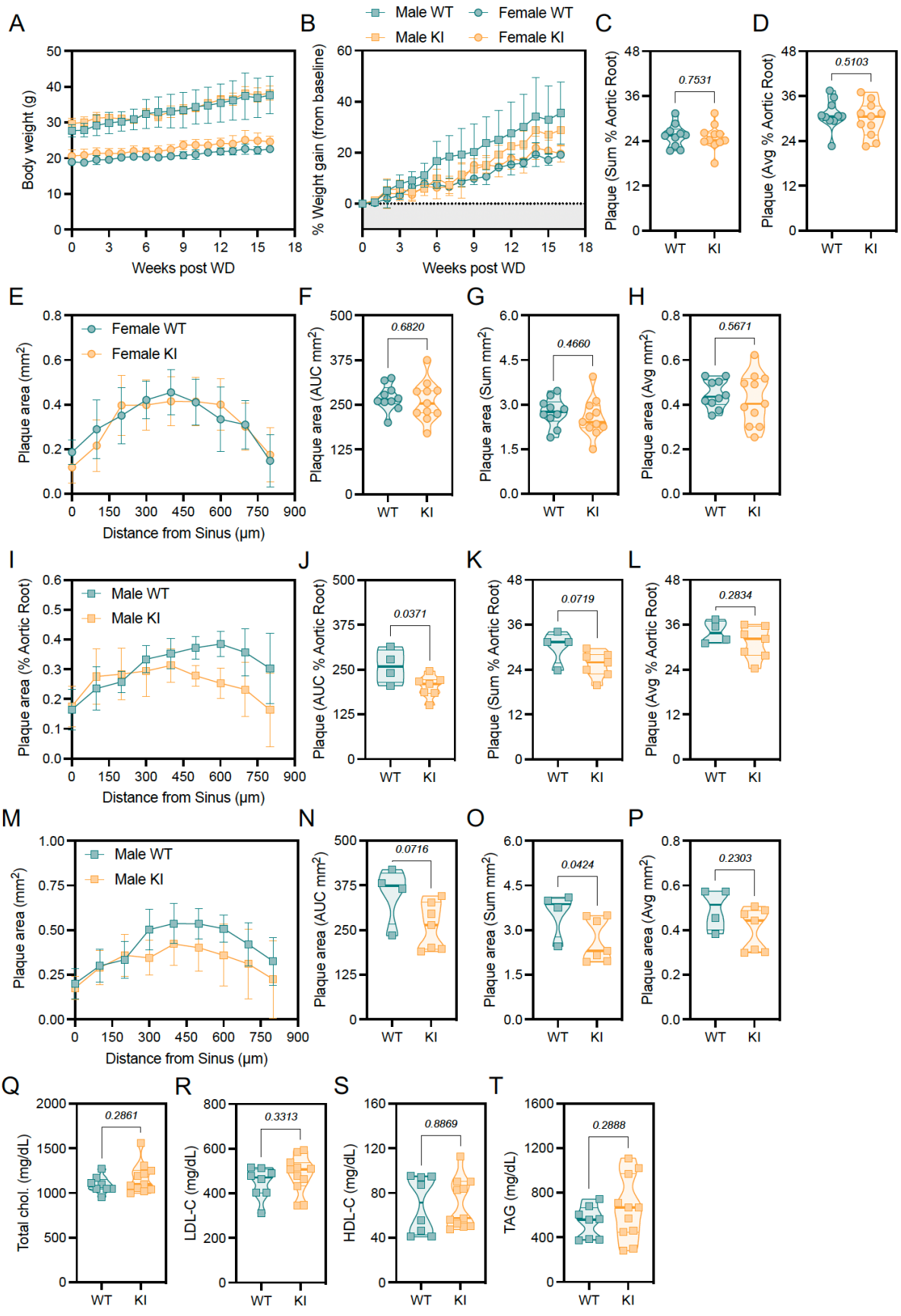
A
Body weight (g)
Weeks post WD
B
Male WT
Female WT
Male KI
Female KI
% Weight gain (from baseline)
Weeks post WD
C
Plaque (Sum % Aortic Root)
0.7531
WT
KI
D
Plaque (Avg % Aortic Root)
0.5103
WT
KI
E
Female WT
Female KI
Plaque area (mm²)
Distance from Sinus (μm)
F
Plaque area (AUC mm²)
0.6820
WT
KI
G
Plaque area (Sum mm²)
0.4660
WT
KI
H
Plaque area (Avg mm²)
0.5671
WT
KI
I
Male WT
Male KI
Plaque area (% Aortic Root)
Distance from Sinus (μm)
J
Plaque (AUC % Aortic Root)
0.0371
WT
KI
K
Plaque (Sum % Aortic Root)
0.0719
WT
KI
L
Plaque (Avg % Aortic Root)
0.2834
WT
KI
M
Male WT
Male KI
Plaque area (mm²)
Distance from Sinus (μm)
N
Plaque area (AUC mm²)
0.0716
WT
KI
O
Plaque area (Sum mm²)
0.0424
WT
KI
P
Plaque area (Avg mm²)
0.2303
WT
KI
Q
Total chol. (mg/dL)
0.2861
WT
KI
R
LDL-C (mg/dL)
0.3313
WT
KI
S
HDL-C (mg/dL)
0.8869
WT
KI
T
TAG (mg/dL)
0.2888
WT
KI

Supplemental Figure 2.4: Aortic root atherosclerosis is unchanged between WT and KI male and female mice. (A,B) Atherosclerosis was induced in male and female mice using *Pcsk9*-AAV followed by 16 wk of WD feeding. Body weight **(A)** and percentage weight gain **(B)** (n=5 WT and KI). **(C-H)** Female aortic sinus plaque measurements: summed plaque area **(C)** and average plaque area **(D)** expressed as a percentage of aortic root; plaque area histogram **(E)**, AUC **(F)**, summed plaque area **(G)** and average plaque area **(H)** expressed in mm^2 (n=10 WT and n=11 KI). **(I-P)** Atherosclerosis was induced in male mice using *Pcsk9*-AAV followed by 26 wk of WD feeding. Aortic sinus plaque histogram **(I)**, AUC **(J)**, summed plaque area **(K)**, and average plaque area **(L)** expressed as a percentage of aortic root; plaque histogram **(M)**, AUC **(N)**, summed plaque area **(O)**, and average plaque area **(P)** expressed in mm^2 (n=4 WT and n=7 KI). **(Q-T)** Serum lipid measurements from 16 wk WD-fed male mice: total cholesterol **(Q)**, LDL-C **(R)**, HDL-C **(S)**, TAG **(T)** (n=8 WT and n=11 KI). Data represented as violin plots truncated at maxima and minima with median and first and fourth quartiles outlined, or as histograms with mean ± SD. *P* values were calculated using an unpaired, two-tailed Student's t-test (C,D,F-H,J-L,N,Q,R,T) or an unpaired, two-tailed Mann-Whitney U test (O,P,S).

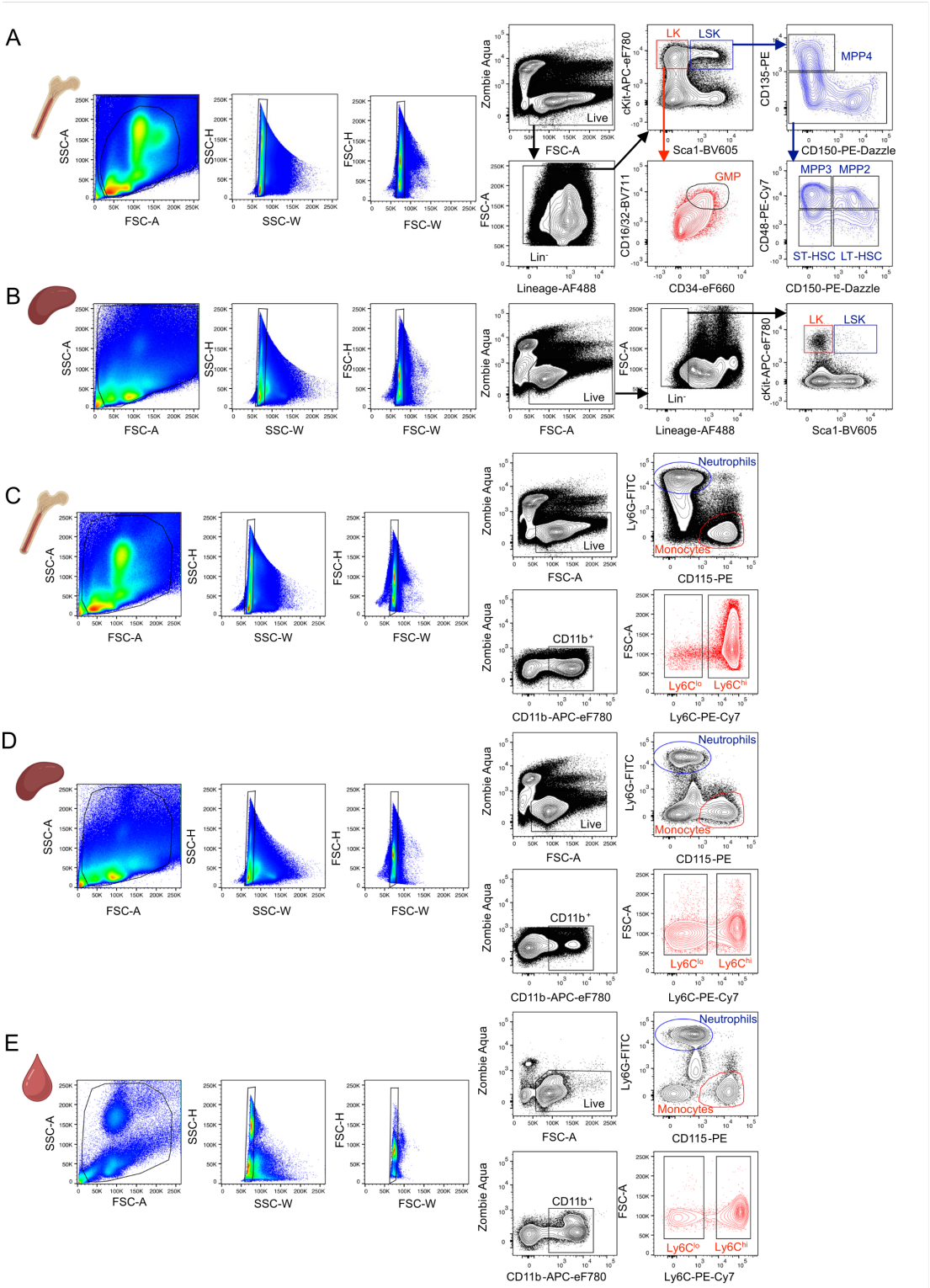

Supplemental Figure 2.5: Representative hematopoietic and myeloid gating strategies. (A,B) Progenitor gating strategy for bone marrow **(A)** and spleen **(B)**. **(C-E)** Myeloid gating strategy for bone marrow **(C)**, spleen **(D)**, and blood **(E)**.

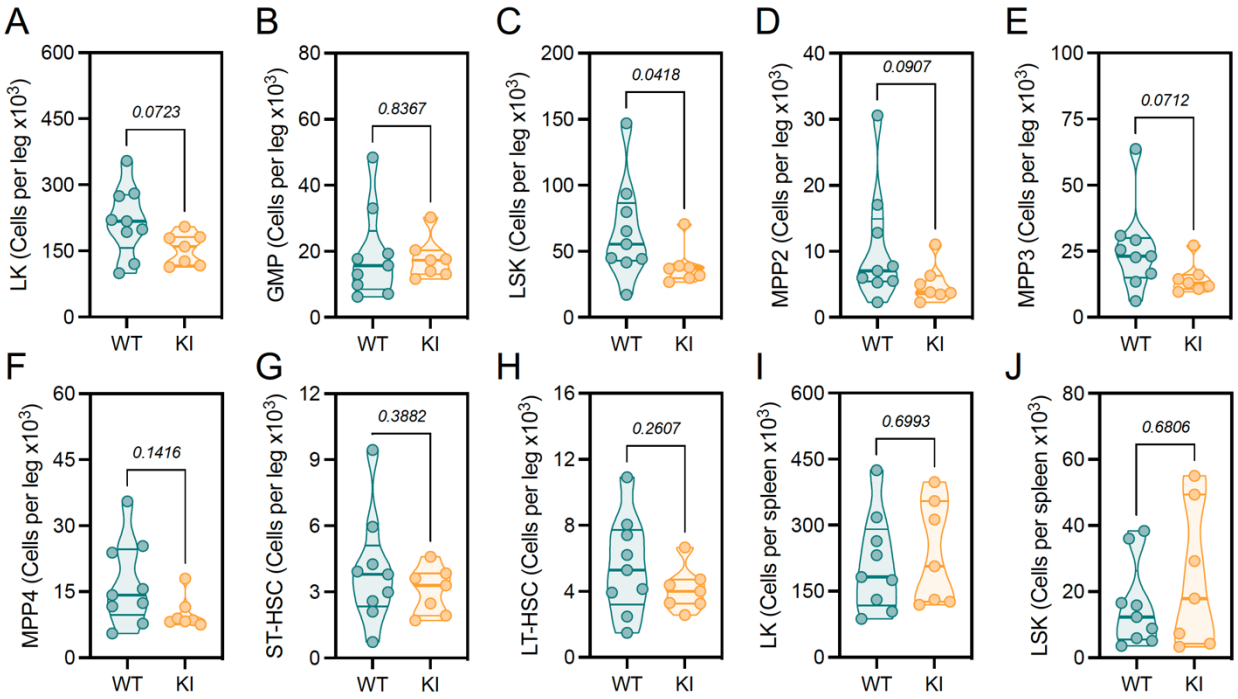

Supplemental Figure 2.6: Total hematopoietic progenitor populations are unchanged in female HMGCR S871A KI mice. Atherosclerosis was induced in WT and KI female mice as in Figure 4. **(A-H)** Total cells per leg for LK **(A)**, GMP **(B)**, LSK **(C)**, MPP2 **(D)**, MPP3 **(E)**, MPP4 **(F)**, ST-HSC **(G)**, and LT-HSC **(H)** populations in bone marrow (n=9 WT and n=7 KI). **(I,J)** Total cells per spleen for LK **(I)** and LSK **(J)** populations (n=9 WT and n=7 KI). Data represented as violin plots truncated at maxima and minima with median and first and fourth quartiles outlined. *P* values were calculated using an unpaired, two-tailed Student's t-test (A,B,G-I) or an unpaired, two-tailed Mann-Whitney U test (C-F,J).

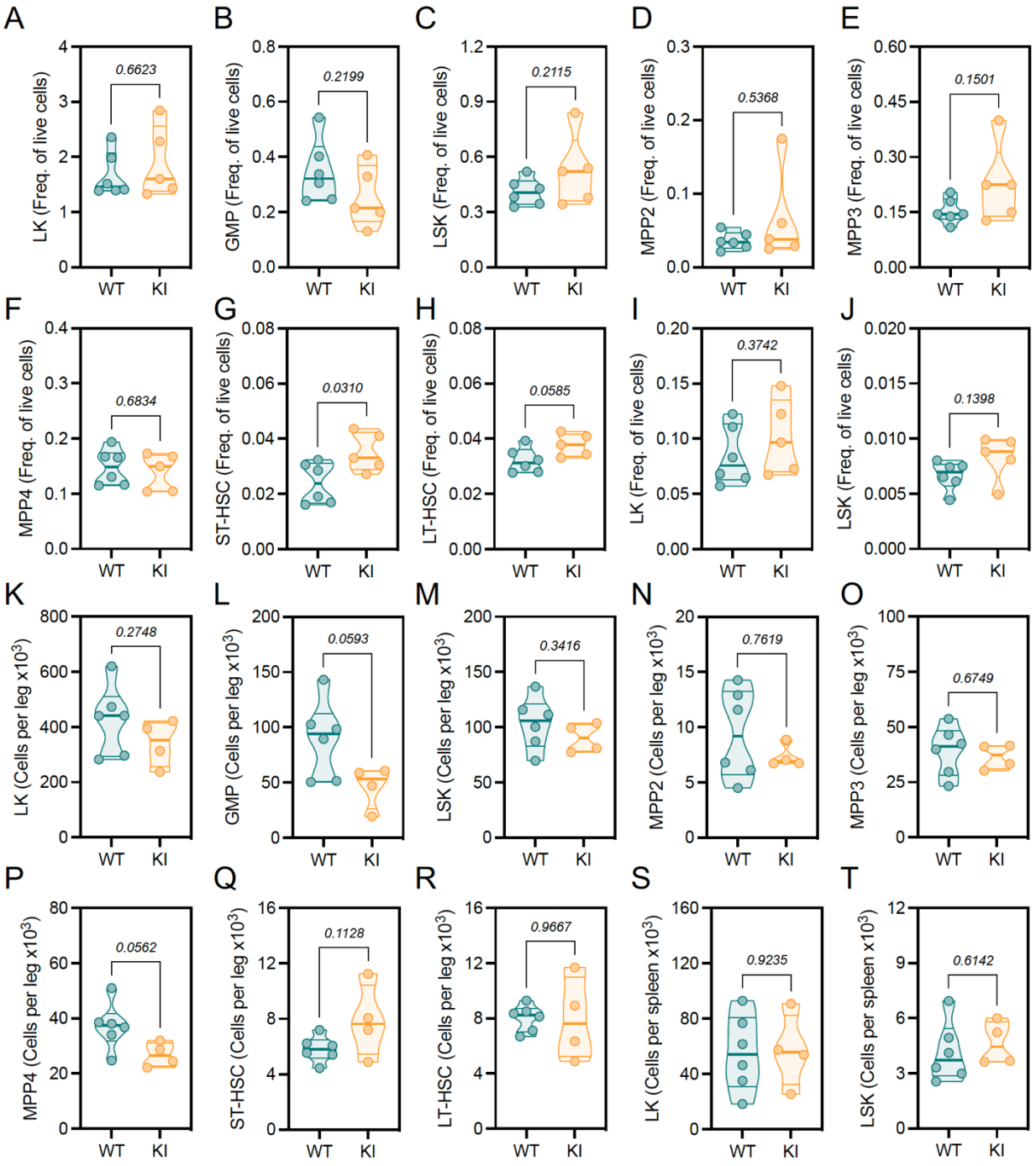

Supplemental Figure 2.7: Total hematopoietic progenitor populations are largely unchanged in male HMGCR S871A KI mice. Atherosclerosis was induced in WT and KI male mice as in Figure 4. **(A-H)** Frequency of live, single cells for LK **(A)**, GMP **(B)**, LSK **(C)**, MPP2 **(D)**, MPP3 **(E)**, MPP4 **(F)**, ST-HSC **(G)**, and LT-HSC **(H)** populations in bone marrow (n=6 WT and n=5 KI). **(I,J)** Frequency of live, single cells for LK **(I)** and LSK **(J)** populations in spleen (n=6 WT and n=5 KI). **(K-R)** Total cells per leg for LK **(K)**, GMP **(L)**, LSK **(M)**, MPP2 **(N)**, MPP3 **(O)**, MPP4 **(P)**, ST-HSC **(Q)**, and LT-HSC **(R)** populations in bone marrow (n=6 WT and n=4 KI). **(S,T)** Total cells per spleen for LK **(S)** and LSK **(T)** populations (n=9 WT and n=7 KI). Data represented as violin plots truncated at maxima and minima with median and first and fourth quartiles outlined. *P* values were calculated using an unpaired, two-tailed Student's t-test (B,C,E-M,O-T) or an unpaired, two-tailed Mann-Whitney U test (A,D,N).

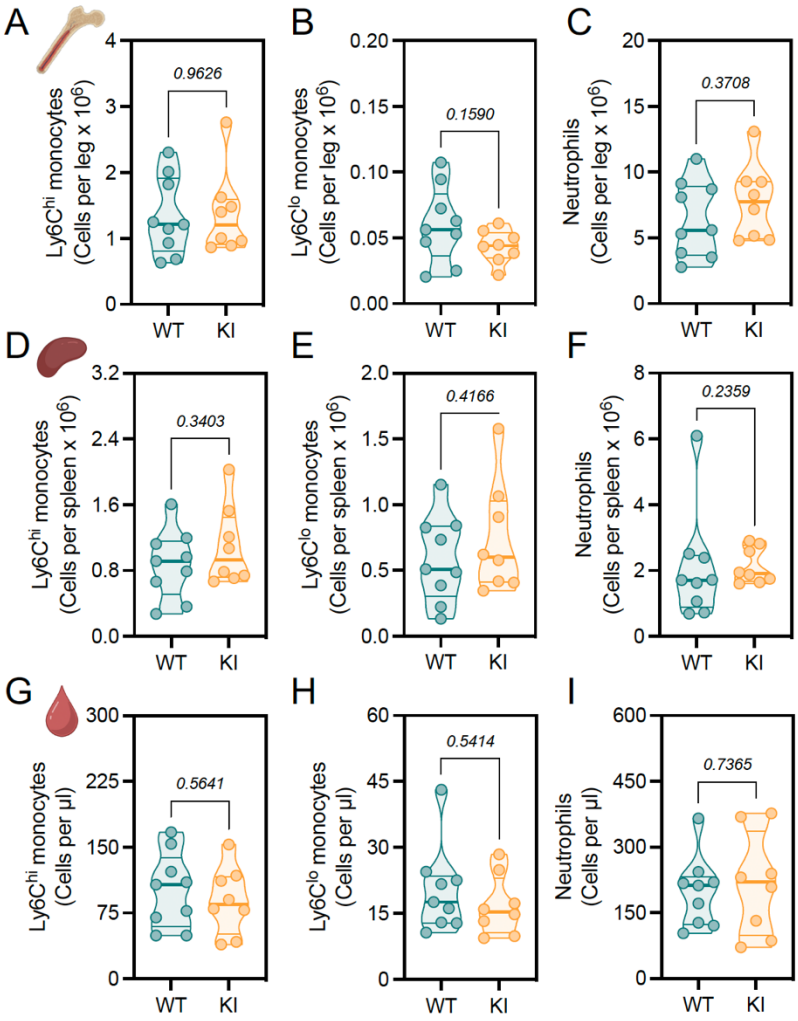

Supplemental Figure 2.8: Total myeloid populations are unchanged in female HMGCR S871A KI mice. Atherosclerosis was induced in WT and KI female mice as in Figure 4. **(A-C)** Total cells per leg for Ly6C^{hi} monocyte **(A)**, Ly6C^{lo} monocyte **(B)**, and neutrophil **(C)** bone marrow populations. **(D-F)** Total cells per spleen for Ly6C^{hi} monocyte **(D)**, Ly6C^{lo} monocyte **(E)**, and neutrophil **(F)** populations. **(G-I)** Total cells per µl of whole blood for circulating Ly6C^{hi} monocyte **(G)**, Ly6C^{lo} monocyte **(H)**, and neutrophil **(I)** populations (n=9 WT and n=8 KI). Data represented as violin plots truncated at maxima and minima with median and first and fourth quartiles outlined. *P* values were calculated using an unpaired, two-tailed Student's t-test (B-E,G,O) or an unpaired, two-tailed Mann-Whitney U test (A,F,H).

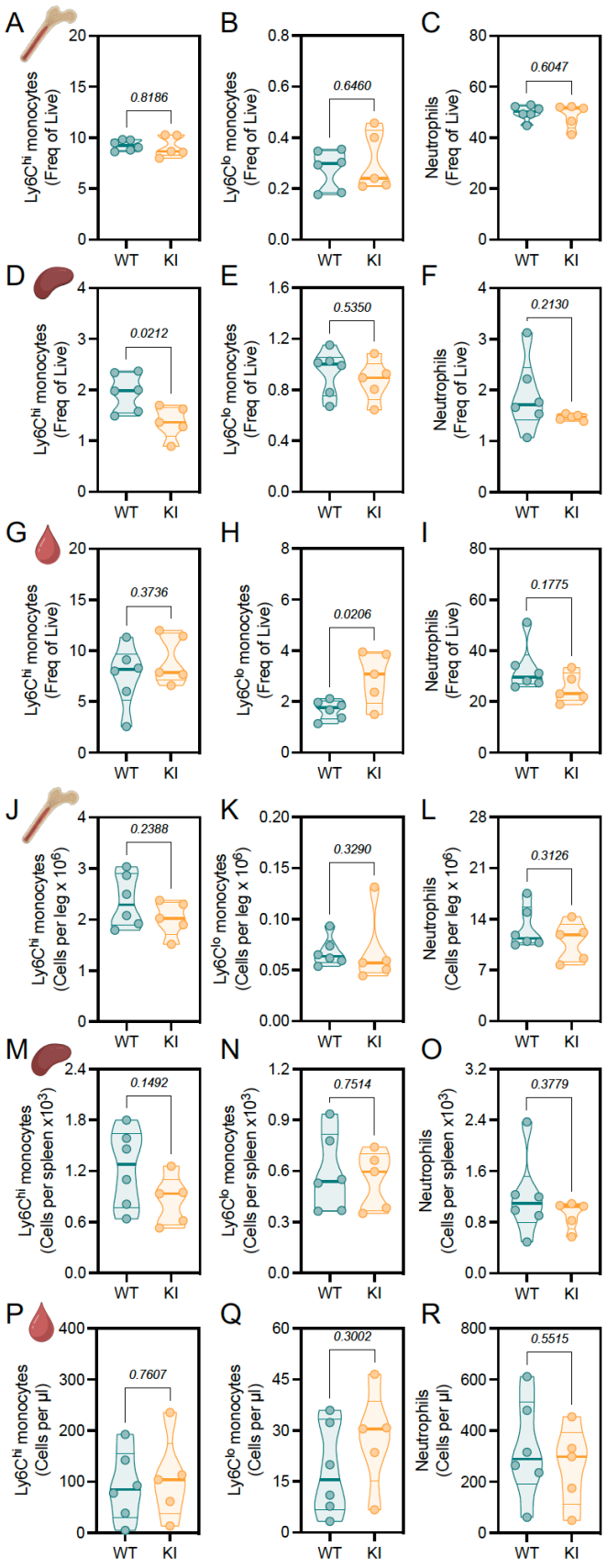

Supplemental Figure 2.9 Total myeloid populations are unchanged in male HMGCR S871A KI mice. Atherosclerosis was induced in WT and KI male mice as in Figure 4. **(A-C)** Frequency of live cells for Ly6C^{hi} monocyte **(A)**, Ly6C^{lo} monocyte **(B)**, and neutrophil **(C)** bone marrow populations. **(D-F)** Frequency of live cells for splenic Ly6C^{hi} monocyte **(D)**, Ly6C^{lo} monocyte **(E)**, and neutrophil **(F)** populations. **(G-I)** Frequency of live cells for circulating Ly6C^{hi} monocyte **(G)**, Ly6C^{lo} monocyte **(H)**, and neutrophil **(I)** populations. **(J-L)** Total cells per leg for Ly6C^{hi} monocyte **(J)**, Ly6C^{lo} monocyte **(K)**, and neutrophil **(L)** bone marrow populations. **(M-O)** Total cells per spleen for Ly6C^{hi} monocyte **(M)**, Ly6C^{lo} monocyte **(N)**, and neutrophil **(O)** populations. **(P-R)** Total cells per µl of whole blood for circulating Ly6C^{hi} monocyte **(P)**, Ly6C^{lo} monocyte **(Q)**, and neutrophil **(R)** populations (n=6 WT and n=5 KI). Data represented as violin plots truncated at maxima and minima with median and first and fourth quartiles outlined. *P* values were calculated using an unpaired, two-tailed Student's t-test (A-H,J,L-R) or an unpaired, two-tailed Mann-Whitney U test (I,K).

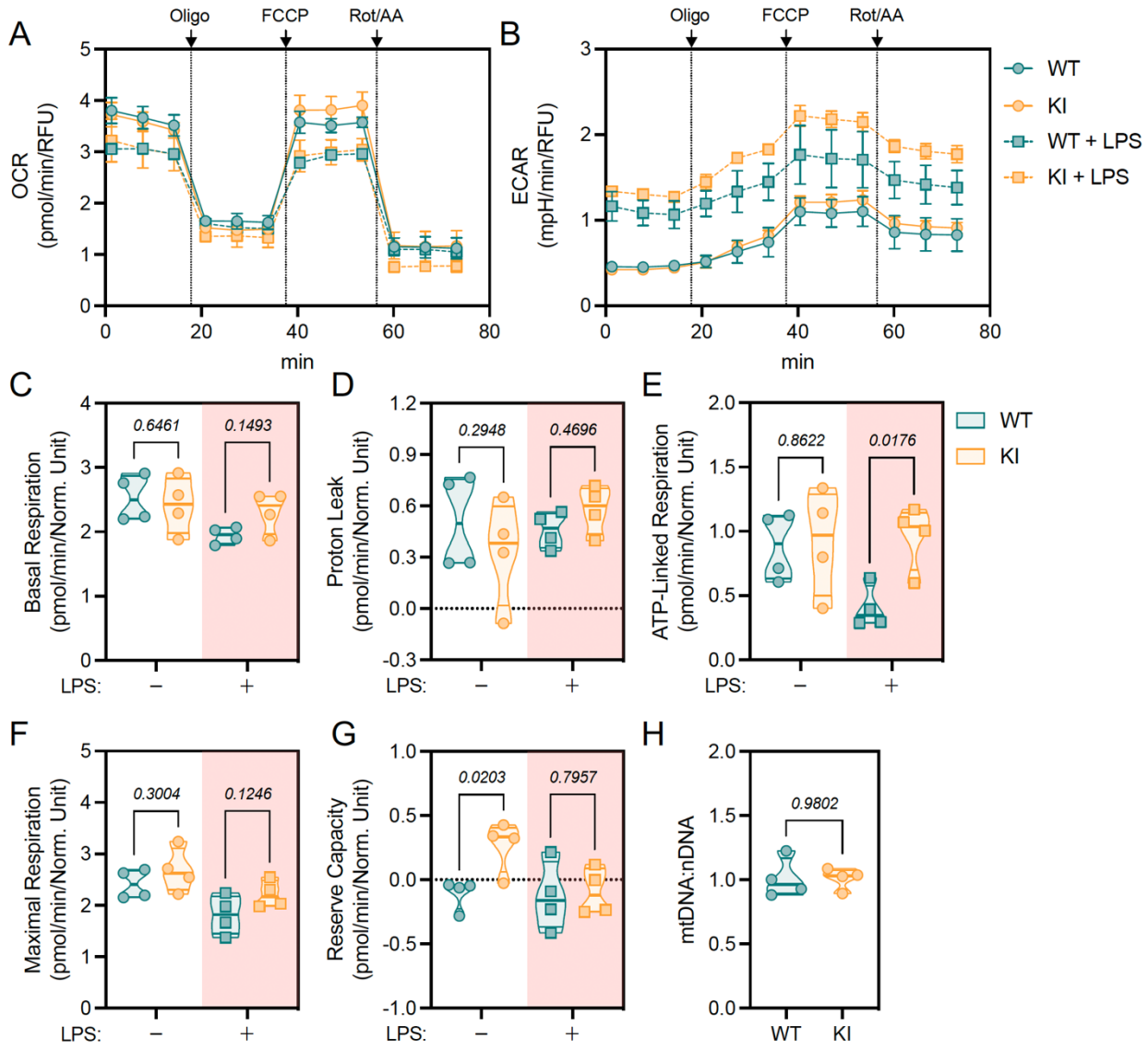

Supplemental Figure 2.10: AMPK signaling to Hmgcr in macrophages is not required for the bioenergetic response to inflammatory stimuli. BMDM were stimulated with or without LPS (100 ng/ml) for 24 h before initiating mitochondrial stress test using oligomycin (1.5 μM), FCCP (1.5 μM), and rotenone (1 μM)/antimycin A (1 μM). Data normalized to nuclei count following Hoechst staining. **(A)** Oxygen consumption rate (OCR) and **(B)** Extracellular acidification rate (ECAR) expressed as pmol/min/normalization unit. **(C-G)** Bioenergetic parameters derived from OCR: basal respiration **(C)**, proton leak **(D)**, ATP-linked respiration **(E)**, maximal respiration **(F)**, reserve capacity **(G)** (n=4 WT and KI). **(H)** Mitochondrial DNA:nuclear DNA ratio (n=4 WT and KI). Data represented as violin plots truncated at maxima and minima with median and first and fourth quartiles outlined, or as histograms with mean ± SD *P* values were calculated using a two-way ANOVA for (C-G) and a Student's t-test for (H).

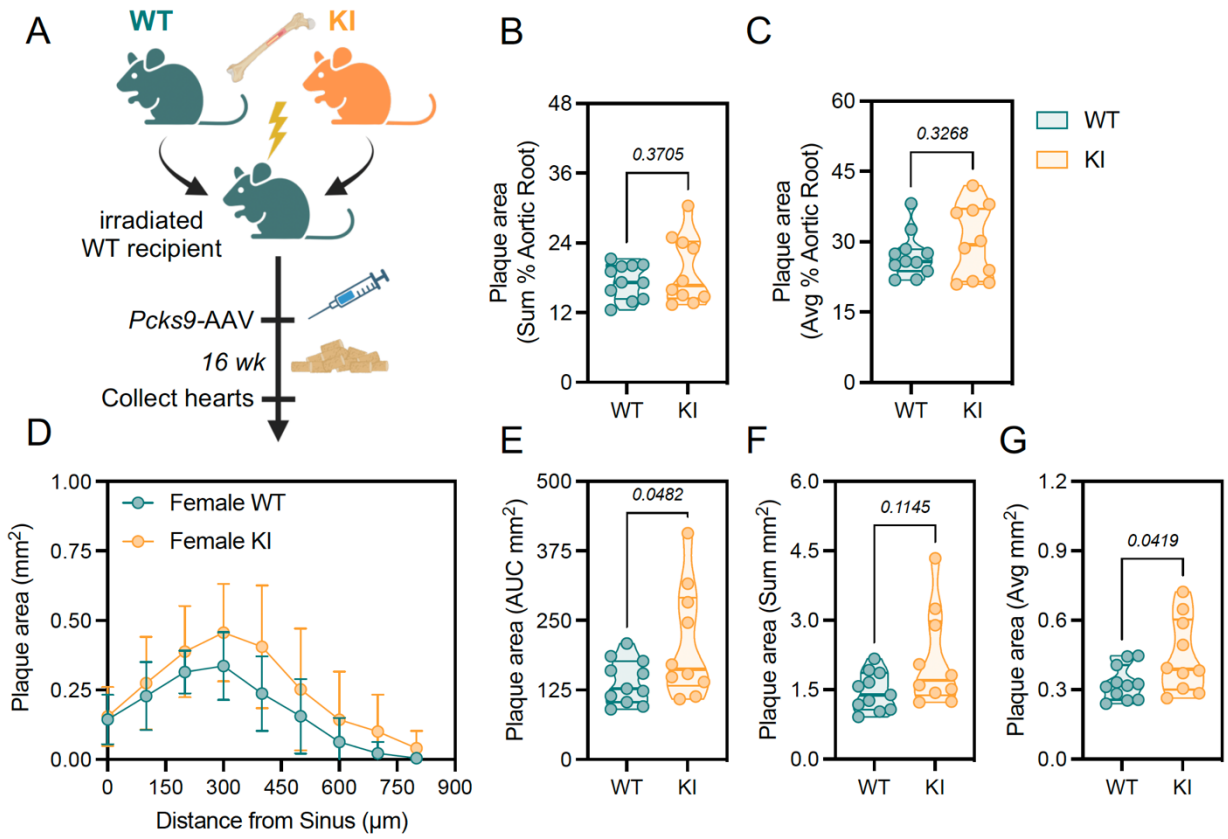

Supplemental Figure 2.11: HMGCR S871A KI bone marrow transplanted mice do not have elevated plaque. (A) Schematic of experiment: bone marrow from female WT and KI mice were transplanted into lethally irradiated WT mice. Following a 4 wk recovery period, mice were injected i.v. with *Pcsk9*-AAV8 (2.5 x 10^{10} genome copies) and fed a western diet (40% kcal fat, 0.15% cholesterol) for 16 wk. **(B,C)** Aortic root plaque area expressed as a percentage of aortic root for summed plaque across all nine sections **(B)** and average plaque size **(C)** (n=11 WT and n=10 KI). **(D)** Aortic root plaque area expressed in mm^2 in a histogram spanning 800 μm and the resulting AUC **(D)**, summed plaque **(E)**, and average plaque size **(F)** (n=11 WT and n=10 KI mice). Data represented as violin plots truncated at maxima and minima with median and first and fourth quartiles outlined, or as histograms with mean ± SD. *P* values were calculated using an unpaired, two-tailed Student's t-test (B,C,E,G) or an unpaired, two-tailed Mann-Whitney U test (F).

Supplemental Table 2.1: Primers used in RT-qPCR.

TaqMan Probes

Target (mouse)	Assay ID (Invitrogen)
Hmgcs1	Mm01304569_m1
Hmgcr	Mm01304569_m1
Mvk	Mm01304569_m1
Fdft1	Mm01304569_m1
Dhcr7	Mm00514571_m1
Dhcr24	Mm00519071_m1
Ggpps1	Mm00656129_mH
Pggt1b	Mm00553955_m1
Fntb	Mm04213852_s1
Il6	Mm00446190_m1
Il1b	Mm00434228_m1
Actb	Mm00607939_s1
Tbp	Mm00446973_m1

Oligos for use with SYBR Green

Target (mouse)	Forward (5'-3')	Reverse (5'-3')
Actb	GGCTGTATTCCCCTCCATGG	CCAGTTGGTAACAATGCCATGT
Tbp	GCTCTGGAATTGTACCGCAG	CTGGCTCATAGCTCTTGGCTC
Rrm1	GCCGCCAAGAGCGAGTTAT	TCATGGTGATCTGAGCAGGAT
Slbp	CCCACCCGGTTATGGGAGT	GGCCTTCAGGAGTTGTAAAGC
Top2a	ACCATTGCAGCCTGTAAATGA	GGGCGGAGCAAAATATGTTCC
Mki67	AGCACAAAGAGACGGTCTAAGA	CTCTGCCTCGTGACTGTGTT
Msr1	AGTGCTGTCTTCTTTACCAGC	GTGAGGAAGGGATGCTGTA
Fabp4	AAGGTGAAGAGCATCATAACCCT	TCACGCCTTTCATAACACATTCC
Mtco1	TGCTAGCCGCAGGCATTAC	GGGTGCCCAAAGAATCAGAAC
Ndufv1	CTTCCCCACTGGCCTCAAG	CCAAAACCCAGTGATCCAGC

Supplemental Table 2.2: Antibodies and dyes used for flow cytometry.

Target	Fluorochrome	Clone	Dilution	Supplier	CAT
Ly-6G	FITC	1A8	200	BioLegend	127605
CD115	PE	AFS98	200	BioLegend	135505
Ly-6C	PE-Cy7	HK1.4	400	BioLegend	128017
CD11b	APC-eF780	M1/70	200	eBioscience	47-0112-82
Sca1	BV605	D7	200	BioLegend	108134
CD16/32	BV711	93	200	BioLegend	101337
CD3e	Biotin	145-2C11	100	BioLegend	133307
Gr-1	Biotin	RB6-8C5	100	BioLegend	133307
CD45R/B220	Biotin	RA3-6B2	100	BioLegend	133307
TER-119	Biotin	TER-119	100	BioLegend	133307
CD11b	Biotin	M1/70	100	BioLegend	133307
Streptavidin	AF488	N/A	200	BioLegend	405235
CD135	PE	A2F10	200	BioLegend	135306
CD150	PE-Dazzle	TC15-12F12.2	200	BioLegend	115936
CD48	PE-Cy7	HM48-1	200	BioLegend	103424
CD34	eF660	RAM34	100	Thermo Fisher	50-0341-82
cKit	APC-eF780	2B8	200	Thermo Fisher	47-1171-82
Zombie aqua	N/A	N/A	500	BioLegend	423102

2.8 Acknowledgments

We gratefully acknowledge the support and services provided by the University of Ottawa Flow Cytometry and Virometry Core (RRID:SCR_023306), the Cell Biology and Image Acquisition Core Facility (RRID: SCR_021845), the Louise Pelletier Histology Core as well as the Animal Care and Veterinary Services at the University of Ottawa. Figures were created in part using BioRender.com (publication license: *MK25W5SDKG*). The authors would like to apologize to colleagues whose significant work could not be included due to length, citation limitations, or author oversight.

Funding: This research was funded by project grants from the Canadian Institutes of Health Research (CIHR) (PJT148634 to MDF), a uOttawa Faculty of Medicine Translational Research Grant (MDF), and a Heart and Stroke Foundation of Canada New Investigator award to EEM. MDF holds a Camille Villeneuve Chair in Cardiovascular Immunometabolism and was supported by a CIHR New Investigator Award (MSH-141981). JSP holds a Canada Research Chair in Cancer Metabolism (Tier 1). TKTS was supported by a CIHR Vanier Scholarship; NDL, JRCN and CP were supported by Ontario Graduate Scholarships; CS and CFM were supported by a CIHR Doctoral Scholarship and REH was supported by a uOttawa Centre for Infection, Inflammation and Immunity Summer Studentship Award.

Conflicts of Interest: The authors declare no competing interests.

Chapter 3: Elevated AMPK activity modulates the host response to *Salmonella enterica*

3.1 Preface

This chapter is in preparation for submission as a research article to the *Journal of Immunology* that will include pertinent data from Chapter 4.

Tyler K.T. Smith, Conor O'Dwyer, Peyman Ghorbani, Julia R.C. Nunes, Jianfan Nie, Madison Girouard, Victoria Robert-Gostlin, Aaron Reyes, Rayan El Hamra, Subash Sad, Bruce E. Kemp, Sandra Galic, Morgan D. Fullerton

Author Contributions: T.K.T.S. Conceptualization, Methodology, Validation, Formal analysis, Investigation, Writing – original draft, Writing – review and editing, Visualization. **C.O.D., P.G., J.R.C., J.N., V.R.G., M.G., A.R.,** Investigation. **R.E.H.** Conceptualization. **S.S., B.E.K., K.L., S.G.** Resources. **M.D.F.** Conceptualization, Resources, Writing – review and editing, Supervision, Funding acquisition.

3.2 Abstract

Salmonella enterica causes a range of diseases in humans; however, our understanding of how host metabolism modulates the systemic response to infection requires further investigation. AMPK is a central regulator of metabolism that, when activated, generally suppresses NF-*κ*B-mediated proinflammatory cytokine production. In this work, we interrogate the role of AMPK in the context of gram-negative bacterial infection. We report that activation of macrophage AMPK using the allosteric activator, MK-8722 during *S*.Tm infection suppresses secondary NF-

κB response target genes such as *Il6* and *Il12b*, while having minimal effect on others like *Edn1*. LC-MS-based metabolomics of infected macrophages revealed that acute AMPK activation decreased TCA cycle metabolites and increased citrulline accumulation, which could be traced to a trending elevation in *Nos2* mRNA levels and NO production. We also present preliminary evidence that AMPK α is transiently modified early during phagocytosis of *S*.Tm and other phagocytic material. In a mouse model of *S*.Tm infection, mice expressing an overactive form of AMPK exhibited greater *S*.Tm burden, while acute systemic administration of MK-8722 had no effect on bacterial pathogenesis. Reciprocal BMTs from mice with overactive AMPK revealed that elevated AMPK activity in circulating immune cells does not contribute to *S*.Tm infection. Our results suggest that AMPK activity opposes several host antibacterial mechanisms, though the relevance of these *in vivo* are likely pathogen and context specific.

3.3 Introduction

Salmonella enterica can cause severe disease in humans. Host cells undergo significant changes in metabolism to respond to invading pathogens such as *S*.Tm. AMPK is a heterotrimeric energy sensor comprised of α, β, and γ subunits that is activated by changes in adenine nucleotide ratios[54] and concentrations of metabolites such as FBP[90] or saturated long-chain fatty acyl-CoAs[514]. Once activated, AMPK signals to downstream targets to suppress anabolic pathways and activate catabolic signaling to restore cellular energy balance[475]. Adequate subcellular localization and activity is conferred by a co-translational myristoylation event on the β subunits at glycine 2, which when lost, results in elevated activity[43,92].

AMPK has been shown to negatively regulate NF-κB transcriptional activity for select inflammatory targets such as *Il6* and *Il12b*, while increasing IL-10 secretion in innate immune

cells[325,385]. Though this inhibitory effect of AMPK activation has been suggested to occur at the level of IκB and AKT[325], this would imply that AMPK globally restricts NF-κB signaling for early response genes such as *Tnf*, as well as secondary response genes like *Il6* and *Il12b*. However, the mechanisms underlying these observations, and whether this transcriptional effect modulates the systemic response to a live bacterial infection requires further refinement. Furthermore, much of our understanding has been derived from either non-specific activators such as AICAR[386,515], or knockout models in which the entire AMPK signaling network is disrupted[516], albeit in a tissue-restricted manner.

In vitro results from *S*.Tm-infected macrophages has suggested that AMPK becomes activated following *S*.Tm infection in either a TAK1[517], LKB1[421,469], or even a VEGFC-dependent manner[470]. However, recent work was unable to detect changes in AMPK signaling following infection with *S*.Tm in comparison to another gram-negative pathogen, *Yersinia pseudotuberculosis*[465]. Considering macrophage AMPK activity is reduced downstream of TLR4 engagement[69], which is also triggered during *S*.Tm infection alongside an array of other PRRs[368], it remains unclear how AMPK would be become activated during *S*.Tm infection.

We sought to determine whether AMPK is activated by *S*.Tm infection in macrophages, as well as investigate how elevated AMPK activity influences infection *in vitro* and *in vivo* using specific pharmacological activators and a genetic chronic overactivity model expressing a non-myristoylated AMPK mutant (G2A). We observe modulation of select NF-κB and signal transducer and activator of transcription 1 (STAT1)-dependent transcriptional targets downstream of *S*.Tm infection in macrophages alongside AMPK-dependent metabolic changes in arginine and TCA cycle metabolism. Bacterial burden *in vivo* was significantly elevated in our

genetic, but not pharmacological activation model, suggesting a complex regulation of the host antibacterial response depending on chronic versus acute AMPK activation.

3.4 Materials and Methods

Bone marrow-derived macrophage generation

BMDM were generated as previously described[474]. Briefly, tibias and femurs of both legs were isolated, the ends of the bones were cut and centrifuged at 10,000 *x g* for 1 min into 100 µl of RPMI 1640 (Wisent #350-000-CL) supplemented with 10% FBS (Wisent #080-150) and 1% penicillin streptomycin (Thermo Fisher Scientific #SV30010), referred to hereafter as complete RPMI. The bone marrow pellet was resuspended and cultured in 15 cm dishes containing 20% L929 conditioned medium. Media was topped up with 5 ml of 20% L929 conditioned medium on day 4, and BMDM were collected on day 6 by addition of 10 mM EDTA/PBS and gentle scraping. Cells were resuspended in 10% FBS/RPMI without antibiotics. BMDM were seeded at a density of 0.156 x 10^6 BMDM/cm^2.

Bacterial preparation

*S.*Tm SL1344, or a GFP-expressing SL1344 strain, kind gifts from Drs. Subash Sad and Ryan Russell, respectively, were grown overnight in LB media supplemented with 50 µg/ml streptomycin sulfate (MilliporeSigma #S6501) shaking at 250 RPM at 37°C. The following morning, 100 µl was transferred to a 14 ml bacterial culture tube containing 6 ml of LB media without antibiotics (1:60), and the bacteria were subcultured for 2.5 h until late log phase. An aliquot of the inoculum was transferred to a 96 well plate and the OD_{600} was measured and fit to a pre-determined standard curve, typically yielding ~3.0x10^8 CFU/ml. The bacterial suspension was centrifuged at 4500 *x g* for 5 min at 4°C, then washed once or twice with PBS depending on

final resuspension concentration. Following a final centrifugation step, the pellet was resuspended in PBS to a desired concentration and stored on ice until initiating infection. To verify MOI, *S*.Tm was diluted tenfold in 96 well plates and plated in 10 µl drops in quadruplicate. Following overnight incubation at RT, colonies were counted with a dissection microscope.

Cell culture treatments and *S*.Tm infection

Unless otherwise specified, BMDM experiments were carried out in 10% FBS/RPMI. Cells were left to adhere overnight following initial seeding, unless the cells were polarized, in which case LPS from *Escherichia coli* O111:B4 (100 ng/ml; MilliporeSigma #L3024) was spiked into plating media 4 hours after initial plating for 18 hours. Prior to infection, cells were washed once with warm PBS before adding treatment media containing MK-8722 (2 µM; a gift from Merck), aldometanib (5 µM), AICAR (200 µM), rotenone (5 µM), BI-9774 (10 µM), ionomycin (10 µM), or cytochalasin D (10 µM) for 15 or 30 min, depending on the experiment. *S*.Tm was then spiked in at the indicated MOI, typically 2 or 10. For assays involving 12, 24, or 96 well plates, plates were centrifuged after spiking in *S*.Tm at RT at 400 *x g* for 5 min before incubating the plates at 37°C for 15 min. For 6 well plates, which could not be centrifuged due to the uneven exposure of cells to air, *S*.Tm was spiked in and the infection was carried out for 20 min at 37°C. Following infection, media was aspirated and cells were washed three times with warm gentamicin/PBS (50 µg/ml; Thermo Fisher #15750060). Treatment media supplemented with 50 µg/ml gentamicin was then added back and the plates were incubated at 37°C for a further 1.5 h. Media was again aspirated and cells were washed once with gentamicin/PBS (50 µg/ml) before adding back treatment media supplemented with 10 µg/ml gentamicin and incubating at 37°C until endpoint.

SDS-PAGE and western blotting

Total cellular lysates were collected by adding 8.33 µl/cm^2 western lysis buffer (0.5% Triton X-100; 0.5% NP-40; 50 mM Tris-HCl, pH 7.5; 150 mM NaCl; 1 mM EDTA; protease inhibitor cocktail, EDTA-free (Roche #11697498001)) and transferring lysate to pre-chilled 1.5 ml tubes. Lysates were then clarified at 14,000 *x g* for 20 minutes at 4°C. After transferring supernatants to new tubes, lysate protein concentrations were determined by bicinchoninic acid (BCA) assay (Thermo Fisher #23225) according to the manufacturer's protocol. Lysate protein concentration was then equalized using western lysis buffer before adding 6X SDS loading buffer (300 mM Tris-HCl, pH 6.8; 600 mM DTT; 12% SDS; 0.6% bromophenol blue; 60% glycerol). The samples were then boiled at 95 ºC for 5 minutes and stored at -20 ºC. For SDS-PAGE, 8 – 15% polyacrylamide resolving (375 mM Tris-HCl, pH 8.8; 0.1% SDS; 0.05% TCE) and 5% stacking (130 mM Tris-HCl, pH 6.8; 0.1% SDS) gels were made in-house the day before sample running. Samples in 1X SDS loading buffer or Protein Ladder (Bio-Rad #1610374) were loaded into 10- or 15-well gels and run at 110V. The proteins were transferred to methanol-activated PVDF (Bio-Rad #1620177) using the TransBlot system (BioRad) in Turbo Buffer (48 mM Tris; 39 mM glycine; 20% methanol) for 20 minutes at 25V. Membranes were then blocked in 5% BSA (BioShop #ALB001) in TBS-T (20 mM Tris; 150 mM NaCl; 0.1% volume fraction Tween-20) for 1 hour, before distributing membranes into appropriate primary antibody dishes for overnight incubation at 4 ºC with gentle rocking (all antibodies diluted 1:1000 in 5% BSA in TBS-T; listed in Supplemental Table 3.1). The next day, membranes were washed 4X with TBS-T and then incubated with HRP-conjugated rabbit IgG secondary antibody (Cell Signaling Technology #7074S; 1:10000 in 5% BSA in TBS-T) for 1 hour at RT. The membranes were again washed

4X with TBS-T and then blots were activated with Clarity Western ECL substrate (Bio-Rad #1705061) before being imaged on the LAS ImageQuant 4000.

Metabolomics sample preparation

BMDM derived from four WT and four G2A mice were seeded at $1x10^7$ cells per 10 cm dish and were mock infected or infected with *S*.Tm-GFP (MOI 10) for 6 hours. After 6 hours of infection, media was aspirated and cells were washed three times with 5 ml of ice-cold 150 mM ammonium formate. After residual ammonium formate was removed, cells were then scraped in 230 µl of 50% MeOH/50% LC/MS-grade water equilibrated at -20°C. Scraped samples were transferred to pre-chilled 2 ml screw cap tubes with 3 ceramic beads. Another 150 µl of MeOH/H_2O was added to collect residual metabolites, then the combined 380 µl was stored at -80°C. Duplicate 10 cm dishes were prepared and infected identically for protein normalization. Treatment media was aspirated after 6h and western lysis buffer was added before flash freezing plates on liquid nitrogen and storing at -80°C. To quantify protein, samples were scraped on ice and transferred to 1.5 ml Eppendorf tubes before centrifuging at 16,000 *x g* for 20 min at 4°C. The supernatant was transferred to new tubes, and protein concentration measured by BCA to determine the total amount of protein per dish. To approximate contribution of bacterial metabolites, $2x10^7$ *S*.Tm cells were added to a 10 cm dish and incubated for 20 min at 37°C after which 10% of the volume ($2x10^6$ *S*.Tm; expected amount of intracellular bacteria assuming 20% of the surviving BMDM have at least 1 bacterium) was transferred to Eppendorf tubes. These cells were centrifuged at 5000 *x g* for 5 min, then resuspended in 150 mM ammonium formate. Following another centrifugation step, the cells were resuspended in 380 µl of 50% MeOH/H_2O and stored at -80°C. For extraction of metabolites, samples were thawed on ice and vortexed at maximum speed for 10 s before added 220 µl of ice-cold acetonitrile and vortexed again.

Samples were then bead beaten in a MagNA lyzer (Roche) for 2 x 30s at 5000 RPM, cooling on ice in between rounds. To the suspension, 600 µl of dichloromethane and 300 µl of ice cold H_2O were added, the samples vortexed, then allowed to partition on ice for 10 min. The samples were then centrifuged for 10 min at 4000 RPM at 1°C. From the upper aqueous phase, 400 µl was transferred to new tubes and stored at -80°C.

LC/MS-based mass spectrometry for metabolite identification

Samples were resuspended in water and run on an Agilent 6470A tandem quadruple mass spectrometer equipped with a 1290 Infinity II ultra-high performance LC (Agilent Technologies) utilizing the Metabolomics Dynamic Multiple Reaction Monitoring Database and Method (Agilent), which uses an ion-pairing reverse phase chromatography. This method was further optimized for phosphate-containing metabolites with the addition of 5 µM InfinityLab deactivator (Agilent) to mobile phases A and B, which requires decreasing the backflush acetonitrile to 90%. Reversed phase separation was obtained using the ZORBAX RRHD Extend-C18 column (2.1 × 150 mm, 1.8 micron, Agilent technologies) coupled to a guard column, ZORBAX Extend Fast Guards for UHPLC, Extend-C18, (2.1 mm, 1.8 micron). The mobile phase A and B are water and methanol respectively and both contain 10 mM tributylamine and 5 µM Agilent's InfinityLab deactivator solution. The auto-sampler and column compartment temperatures were maintained at 4°C and 35°C respectively. Samples were analyzed using 250 µL/min flow rate with following gradient: 0-2.5 min 100% A, 2.5-7.5 min 100%-80% A; 7.5-13 min 80%-55% A, 13-20 min 55%-1% A, 20-24 min holding at 1% A, 24.05-31.5 min backflushing the column with 90% Acetonitrile using clannel C and then 32.25-40 min equilibrating the column with 100% A. Mass spectrometry detection settings included: N_2 drying gas temperature 150°C; N_2 drying gas flow 13 L/min; nebulizer pressure 45 psig, sheath gas

temperature 325°C, sheath gas flow 12L/min, capillary voltage 2000 V, and Nozzle voltage of 500 V. Samples were injected in negative ESI mode. Dynamic multiple reaction monitoring (dMRM) transitions were optimized using authentic standards and quality control samples. Metabolites were quantified by integrating the area under the curve of each compound using external standard calibration curves with Mass Hunter Quant software (Agilent). No corrections for ion suppression or enhancement were performed, as such, uncorrected metabolite concentrations are presented.

Metabolomics data analysis

Raw concentrations for detected metabolites (μM) were converted to total nmol and normalized to protein content from duplicate 10 cm dishes (nmol/mg protein). The metabolite amounts in nmol/mg protein were then separated into groups and analyzed in R Studio. Missing values were imputed as 1/5 of the lowest value within a group, and metabolites detected in less than 50% of samples were removed. For each metabolite in paired data sets (mock vs infected, mock DMSO vs MK-8722, and *S.*Tm DMSO vs MK-8722), fold change was calculated within each biological replicate from uninfected or untreated conditions to the treated condition, resulting in a mean of 1 in the control samples. These values were then $\log_2$-transformed and were analyzed using a one-sample paired Welch's t-test to assess whether the mean $\log_2$ fold change significantly differed from zero. For unpaired data sets (WT vs G2A in infected and uninfected conditions), values were normalized to WT groups and then log2-transformed for analysis using a one-sample unpaired Welch's t-test. Kyoto Encyclopedia of Genes and Genomes (KEGG) [518] pathway enrichment analysis was performed using MetaboAnalyst 6.0 [519]. Raw P-values are reported without multiple testing correction, as the analysis was hypothesis-driven and focused on a predefined subset of metabolites with established biological relevance.

ELISA

Cell culture supernatants were collected and transferred to 96 well U-bottom plates (Thermo Fisher Scientific #7000165) and stored at -80 °C. ELISAs for murine TNF-α (Bio-Techne #DY410), IL-6 (Bio-Techne #DY406), IL-10 (Bio-Techne #DY417) and IL-1β (Bio-Techne #DY401) were performed according to manufacturers' instructions.

RNA isolation, cDNA synthesis, and RT-qPCR.

Cells were treated as described and washed once with PBS before adding 115 µl/cm^2 TriPure RNA isolation reagent (Roche #11667165001). RNA isolation was carried out according to the manufacturer's instructions with all centrifugation steps at 4°C. RNA concentration and quality (A260/280) was measured using the Take3 Plate (Agilent #TAKE3-SN) on the Synergy H1 Plate Reader (BioTek). RNA concentration was equalized using DNase/RNase free H_2O, after which 300-400 ng of RNA was transferred to 8-strip PCR tubes (Diamed #DIATEC420-1378) and reverse transcribed into cDNA using the All-in-One 5X RT Master Mix (Applied Biological Materials #G592) in a T100 thermal cycler (Bio-Rad). Synthesized cDNA was diluted to a final concentration of ~2.5 ng/µl in DNase/RNase free H_2O such that each qPCR reaction contained ~10 ng of cDNA. qPCR was performed using the BlasTaq 2X qPCR MasterMix (Applied Biological Materials #G891) according to manufacturers instructions. Relative expression was calculated with the $^{\Delta\Delta}$Ct method[483] using *Hprt1* as a housekeeping gene. Primer sequences are listed in Supplementary Table 3.2.

Flow cytometric quantification of infected cells

Following specified treatments, BMDM in 24 well plates were washed once with PBS before adding 200 µl of warm trypsin-EDTA (Wisent #325-542 CL) and incubating at 37°C for 5 min. Cells were then transferred to 1.2 ml cluster tubes (Corning #4401) containing 300 µl of cold 1%

FBS/PBS. Cells were centrifuged at 400 *x* g for 5 min and then stained with Zombie Aqua (1:500; BioLegend #423102) for live/dead discrimination in 50 µl PBS for 30 min on ice. Cells were washed with PBS, centrifuged, and fixed with 2% paraformaldehyde (PFA) in PBS (BioShop #PAR070) for 15 min on ice. The cells were washed with PBS and finally resuspended in PBAE for analysis on the LSR Fortessa (BD).

Mouse models and methods

Mouse models

C57BL/6J mice were purchased from The Jackson Laboratory (#000664) and bred in house. AMPK β1/β2 G2A mice were generated as previously described[92]. *Prkaa1*$^{fl/fl}$ and *Prkaa2*$^{fl/fl}$ mice were generated as previously described[520,521], then crossed to generate double *Prkaa1*$^{fl/fl}$/*Prkaa2*$^{fl/fl}$ mice. These were then bred with mice expressing Cre under the lysozyme M promoter (*Cre*^{LysM})[522]. All mice were housed in ventilated cages at ~23 °C and maintained on a 12/12 h light-dark cycle with *ad libitum* access to a standard rodent chow (58% kcal from carbohydrates, 18% kcal from fat, and 24% kcal from crude protein; Harlan Teklad #2018) and water. All experiments conducted were in accordance with the Canadian Council of Animal Care and approved by the Animal Care Committee at the University of Ottawa (BMIe-3742).

***S*.Tm infection models**

Male and female C57BL/6J mice, aged 6-12 weeks old were inoculated according to the intended route of infection. For orogastric infection, mice were fasted on day -1 for 3 hours before being gavaged with streptomycin sulfate in PBS (20 mg/mouse). Food was returned to cages before repeating fasting 24 hours later. Overnight culture of *S*.Tm was initiated in 6 ml of LB media containing 50 µg/ml streptomycin. After fasting the mice on day 0, *S*.Tm was grown to mid-log phase following 2.5 hours of subculture in antibiotic free LB at 37°C shaking at 250

RPM. Bacteria were transferred to new tubes, spun at 5000 x g for 5 min at 4°C, then washed twice with PBS before resuspending to $5x10^8$ CFU/ml in PBS. After 3 hours of fasting, mice were gavaged with 4-$6x10^7$ CFU of GFP *S*.Tm (bacterial burden cohorts) or WT *S*.Tm (survival cohorts) before returning food to cages. Mice were weighed and feces collected daily and processed for CFU counts before harvesting on day 5. For IP infection, mice were injected with $1x10^4$ CFU of *S*.Tm prepared as described above. For MK-8722 cohorts, mice were fasted for 3 hours before administering MK-8722 (10 mg/kg) or vehicle (0.25% (w/v) methylcellulose, 5% (v/v) Polysorbate 80, and 0.02% (w/v) sodium lauryl sulfate in sterile H_2O) by oral gavage on day 0. After another 3 hours, mice were inoculated by oral gavage with $5x10^7$ CFU/mouse

Survival Studies

Mice were infected with *S*.Tm via either orogastric or IP routes as described above. Mice were monitored twice daily (morning and evening) for bodyweight changes and signs of stress, with a disease severity score assigned following monitoring. The disease severity score was on a scale of 0-12 and was the sum of "Appearance" (0-4), "Activity" (0-4), and "Response to Stimulus" (0-4), where humane endpoint was considered a score of 8/12, or a 20% reduction in bodyweight. At endpoint, mice were injected with a lethal dose of ketamine and xylazine (150 mg/kg ketamine and 10 mg/kg xylazine) and cervically dislocated.

Bone marrow transplant

Bone marrow from one WT and one G2A donor per cohort was isolated and stored on ice in DMEM without FBS or antibiotics. Recipient mice were lethally irradiated with two doses of 4.5 Gy (9 Gy total) of X-ray radiation over a period of 5 min, with the doses administered 3 hours apart. Following the second dose, mice were injected intravenously via tail vein with $5x10^6$ whole bone marrow cells in 100 µl of DMEM and transferred into sterile cages. Following

transplantation, mice were weighed and monitored daily for 7 days and then twice weekly for a further for 4 weeks during recovery. Mice with unsuccessful transplantation were sacrificed if bodyweights dropped below 20% of their starting weight and exhibited significant distress. After 8 weeks of recovery, mice were subjected to a survival study with WT *S*.Tm as described above.

CFU quantification

Following left ventricular perfusion, tissues were isolated under aseptic conditions, weighed, then transferred to 1.8 ml homogenization vials containing three 2.8 mm ceramic beads and 0.5 ml ice cold PBS for most tissues, and 1 ml for the liver. For the distal ileum, cecum, colon, liver, and spleen, tissues were homogenized at 6000 RPM for 3x20s bursts in a MagNa Lyser (Roche). Homogenates were then centrifuged at 400 *x g* for 5 minutes before performing serial dilutions in PBS. For bone marrow and blood samples, cell pellets corresponding to either one leg or 50 µl of whole blood, were resuspended in 0.3 ml of 0.3% TX-100/PBS before being serially diluted in PBS. All preparations were plated in 10 µl drops in quadruplicate on LB agar supplemented with 50 µg/ml streptomycin at multiple dilutions. Colonies were grown overnight at room temperature and counted the following day under a dissection microscope. Counted colonies were averaged, converted to CFU/ml (blood), then to CFU/g tissue (distal ileum, cecum, colon, liver, and spleen) or CFU/leg (bone marrow).

Data Availability

All raw data is available upon reasonable request.

Statistical Analysis

Data are represented as individual points with medians and means denoted by lines for log or linear displayed data, respectively. Histograms are represented as mean ± SD, unless otherwise specified. Statistical analyses were performed using GraphPad Prism Software version 10.0.2.

Normality was assessed using the Shapiro-Wilk test with a cutoff of P>0.05 for normally distributed data. Differences between groups that involved a single dependent variable were analyzed using the parametric Welch's t test for normally distributed data, or the nonparametric Mann-Whitney U test for non-normally distributed data. In groups with two or more factors, a two-way analysis of variance (ANOVA) test was performed with Tukey's or Sidak's post hoc test for multiple comparisons, as described. *P* values are reported for all meaningful comparisons to the fourth decimal.

3.5 Results

The anti-inflammatory nature of AMPK activation has long been appreciated[325], where elevated AMPK activity is associated with suppressed transcription of classic inflammatory transcripts. However, these observations have been primarily based on experiments using purified TLR agonists and not live bacterial infections that can stimulate multiple TLRs. Proinflammatory cytokine production following TLR agonism and activation of the TLR adaptor MyD88 leads to NF-κB activation and induction of transcription in several phases (Figure 3.1A). Early response genes such as *Tnf* are transcribed as part of the first wave of NF-κB signaling and are appreciably increased following 2 hours of TLR activation. Meanwhile, transcription of second wave genes such as *Il6* and *Il10* are induced later, peaking around 6-12 hours[384]. To compare how increasing AMPK activity affects the response to pro-inflammatory stimuli, we treated bone marrow derived macrophages (BMDM) with the potent and selective AMPK activator MK-8722 during incubation with LPS or *S*.Tm. Both *S*.Tm and LPS induced expression of the early response gene *Tnf* to a similar extent (Figure 3.1B). In agreement with prior literature[325,523], we observed minimal effect of AMPK activation on *Tnf* transcript levels in either LPS or *S*.Tm-infected BMDM at 2 hours or 6 hours post-infection, though there may have been a potentiating effect of AMPK activation at longer timepoints in the LPS condition (Figure 3.1B). In contrast, the second wave target *Il6* was suppressed by ~50% at the transcript level in both LPS and *S*.Tm-infected conditions by 6 hours, with minimal effects at 2 hours or 24 hours post-stimulation (Figure 3.1C). While *Il10* has been shown to increase at the protein level following AMPK activation[325], we detected no change at the mRNA level (Figure 3.1C), raising the question of how AMPK differentially regulates targets of NF-κB signaling. Secreted TNF-α and IL-6 mirrored their induction at the mRNA level, though AMPK activation during LPS

stimulation led to higher TNF-α at 2 hours (Figure 3.2A,B). IL-10 secretion differed from its mRNA induction under AMPK activated conditions, which was especially apparent at 2 hours post-stimulation with LPS (Figure 3.2C). This effect was detectable in *S*.Tm-infected conditions by 6 hours. This lends support to a post-transcriptional mode of regulation of IL-10. Altogether, AMPK activation modulates transcription and secretion of cytokines during *S*.Tm infection in a similar manner to the more commonly used LPS as a purified TLR4 agonist.

To probe deeper into AMPK-mediated influence of gene expression during *S*.Tm infection, we again activated AMPK with MK-8722 and measured a larger set of NF-κB-dependent transcriptional targets (Figure 3.3). The early response gene *Tnf* was completely unaffected by AMPK activation at 2 hours, with minimal changes at 6 hours and later (Figure 3.3B). On the other hand, *Il1b*, which is essential for the inflammasome response to *S*.Tm, was strongly suppressed throughout the timecourse beginning at 2 hours post-infection (Figure 3.3C). When looking at secondary response genes, *Il6* was significantly lower following 6 hours of AMPK activation, aligning with the trend in *Il12b* transcript levels (Figure 3.3E). Interestingly, *Edn1*, which is another secondary response gene, was unaffected by AMPK activation (Figure 3.3F). Furthermore, *Nfkbiz*, which encodes IkBζ and is an important link between the primary and secondary NF-κB response[426], was similarly unchanged until 24 hours post-infection (Figure 3.3G). As observed previously, *Il10* mRNA levels were unchanged at any timepoint (Figure 3.3H). *Acod1* encodes the enzyme that produces the antibacterial metabolite itaconate and was also largely unaltered by AMPK activity (Figure 3.3I). When viewed together (Figure 3.3J), it is apparent that despite second wave genes sharing common upstream regulators, acute AMPK activation affects a core subset of *Il1b*, *Il6*, and *Il12b* by 6 hours post-infection. Collectively, this

suggests that AMPK activation does not uniformly suppress NF-κB signaling, as more standard kinetics would be expected to occur in other second wave response genes such as *Edn1*.

Beyond MK-8722, AICAR activates AMPK following its conversion to ZMP[192], and has been used in several studies investigating AMPK under inflammatory conditions[524]. Though a potent activator of AMPK, it has also been shown to affect a wide array of other AMP-sensitive enzymes[193], leaving its specificity to AMPK in question. When we stimulated AMPK activity via AICAR during *S*.Tm infection, it potently suppressed multiple genes, including *Il10*, and does not align with other studies using more specific AMPK activation strategies[325,385] (Supplemental Figure 3.1A-F). Therefore, inflammatory studies incorporating AICAR should be interpreted with caution.

AMPK activation induces significant metabolic changes in TCA cycle and arginine metabolism during *S*.Tm infection

As early as 2 hours after LPS stimulation, changes in metabolism can affect histone acetylation and subsequent gene transcription[525]. To identify whether there was a link between AMPK-mediated metabolic and transcriptional changes, we turned to metabolite levels during infection. Since we measured the most divergence in second wave gene expression at 6 hours (Figure 3.3), we chose to ascertain the metabolic status of the cell at this timepoint. To do so, we pretreated cells with MK-8722 or DMSO before infecting WT BMDM with *S*.Tm for 6 hours to then measure metabolite levels using LC-MS-based metabolomics (Figure 3.4A). In total, we detected 123 metabolites with good coverage of glycolytic, TCA cycle, pentose phosphate, and nucleotide synthetic pathways. Bacterial metabolites were not detected in any significant amount, as has been observed previously[434]. Expectedly, we observed drastic rewiring in infected

cells relative to mock-infected cells, including a strong increase in TCA cycle metabolites such as succinate, fumarate, malate, and the product of *cis*-aconitate decarboxylation, itaconate (Supplemental Figure 3.2A; Table 3.1). These were accompanied by elevated arginine and citrulline levels, which are required for NO production, as well as glycolytic metabolites like dihydroxyacetone phosphate (DHAP), FBP, and BPG (Supplemental Figure 3.2A), all of which are in line with other published work[434]. KEGG pathway enrichment analysis pointed to glycolysis, pyruvate metabolism, TCA cycle, and arginine and proline metabolism being among the most enriched metabolite sets (Supplemental Figure 3.2B).

When comparing the effects of AMPK activation in infected cells, several metabolic pathways were altered including the TCA cycle and arginine metabolism (Figure 3.4B). For example, TCA cycle metabolite abundance of citrate, fumarate, malate, and succinate were all significantly decreased by approximately 30-40% compared to non-AMPK-activated conditions (Figure 3.4C,D; Table 3.3). This also occurred without a significant change in pyruvate or lactate levels (Figure 3.4D), suggesting that it is not tied to a comparable drop in glycolysis, though flux analysis would be required to verify this observation. Interestingly, AMPK activation in the absence of *S*.Tm leads to increased glycolytic metabolites such as FBP and DHAP, as well as TCA cycle metabolites such as malate (Supplemental Figure 3.2C-F; Table 3.2).

The macrophage antibacterial response relies iNOS-dependent NO to generate RNS. iNOS catalyzes the conversion of arginine to citrulline, yielding NO in the process (Figure 3.4E). We detected a two-fold increase in citrulline levels with AMPK activation, which, when paired with mildly reduced arginine, aspartate, and fumarate, is suggestive of either elevated iNOS activity, or disrupted processing of citrulline to arginosuccinate via downstream ASS1 (Figure 3.4F). Notably, metabolites related to citrulline including proline, glutamate, and creatine, were

unaltered by AMPK activation during infection (Figure 3.4F). To further explore this potential link between AMPK and citrulline levels, we measured supernatant nitrite as an indirect readout of NO production following *S*.Tm infection. Though the assay lacked sensitivity to detect nitrite in non-AMPK-activated conditions, we measured a time dependent increase in nitrite levels with MK-8722 treatment (Figure 3.4G). This suggests that AMPK activity increases NO production during infection, though this must be validated using a more sensitive assay. Furthermore, we measured mRNA levels of the main metabolic enzymes influencing citrulline concentration including *Nos2*, which encodes iNOS, and *Ass1*. There was a trend towards increased *Nos2* mRNA levels at 6 hours with AMPK activation, that due to the extent of gene induction was not statistically significant (Figure 3.4H). This contrasted with *Ass1*, which was not changed by AMPK activation at 6 hours, and was even suppressed at later timepoints (Figure 3.4I). This imbalance in the enzymes that produce (iNOS) and process (ASS1) citrulline could potentially explain our observed increase at the metabolite level. To interrogate the mechanism by which *Nos2* transcript levels are paradoxically increased while other NF-κB target genes such as *Il6* and *Il12b* are decreased, we sought alternative regulators of its transcription. Signal transducer and activator of transcription 1 (STAT1) is an upstream regulator of *Nos2* transcription, as well as *Ass1* and other chemokines such as *Cxcl9*[445,526]. When we measured *Cxcl9* transcript levels in response to AMPK activation, it followed a similar trend to *Ass1* (Figure 3.4I), which is more clearly illustrated viewing the fold change in *Nos2*, *Ass1*, and *Cxcl9* relative to their paired controls (Figure 3.4K). This indicates that an AMPK-STAT1 axis is unlikely to affect *Nos2* transcript levels in our model. Regardless, in the non-infected state, in which citrulline was undetectable in our dataset, we did observe a small increase in creatine levels, highlighting that AMPK may be affecting arginine metabolism through multiple avenues (Supplemental Figure

3.4G). Collectively, acute AMPK activation in macrophages induces metabolic rewiring centered around the TCA cycle, arginine metabolism, and glycolysis during *S*.Tm infection, which may have roles in regulating gene transcription.

Acute AMPK activation has minimal effect on macrophage *S*.Tm infection

Having established that AMPK induces significant changes in a subset of inflammatory cytokines, as well as NO metabolism, we wondered if these effects would influence the antibacterial killing mechanisms of BMDM. To test this, we measured uptake of GFP-expressing *S*.Tm in either naïve (M[0]) or LPS-polarized (M[LPS]) BMDM, which exhibit greater phagocytic capacity, in the presence of MK-8722 or the phagocytosis inhibitor, cytochalasin D (CytoD). Immediately following infection, CytoD expectedly reduced the number of GFP^+ BMDM to ~10% compared to the 75% observed in non-inhibited cells (Figure 3.5A,B). AMPK activation had a small effect on bacterial uptake, increasing the number of *S*.Tm^+ cells by 5% (Figure 3.5B). In contrast, M[LPS] cells exhibited unchanged or lower bacterial burden with AMPK activation (Figure 3.4B). Following 6 hours of infection, there was still a slight AMPK-dependent increase in GFP^+ macrophages in M[0], accompanied by a decrease in M[LPS] (Figure 3.5C). By 24 hours, the trend was marginal in M[0] cells, but there was a significant 5% decrease in GFP^+ M[LPS] cells (Figure 3.5D). These data suggest that naïve and LPS-polarized macrophages respond differently to AMPK activation, though the effect of activating AMPK on bacterial burden is minimal overall. We also assessed bacterial burden by intracellular CFU at 6 hours post-infection, which revealed no changes in macrophages acutely activated with MK-8722 (Figure 3.5E). This held true for other AMPK activators including an alternative ADaM site activator in BI-9774, as well as the AMP-mimetic AICAR (Figure 3.5E). These results

signify that AMPK-induced transcriptional and metabolic changes in several key inflammatory genes have minimal combinatory effect on the immediate infectivity of BMDM. All together, acute AMPK activation, despite suppressing some NF-κB target genes important for defense against intracellular pathogens such as IL-1β, does not overtly affect the initial response to *S*.Tm in macrophages.

Infection with *S*.Tm induces a higher molecular weight AMPKα band.

AMPK and mTORC1 signaling balances catabolic and anabolic metabolism. mTORC1 is activated in the presence of LPS[527], and during the response to *S*.Tm[528]. Alternatively, AMPK activity is known to be suppressed following TLR engagement[69,325], yet multiple reports have detected paradoxical AMPK activation during *S*.Tm infection[421,469,470,517]. Given these discrepancies, we sought to validate if AMPK is indeed activated in BMDM following acute exposure to *S*.Tm. To do so, we infected BMDM with *S*.Tm and monitored for AMPK activity (Figure 3.6A). We detected a robust induction of mTORC1-related signaling as measured by phosphorylation of S6, which is a general mTORC1 activity readout (Figure 3.6B). This was induced at 1h post-infection and persisted to 6 hours before decreasing 24 hours post-infection. In contrast, when measured by phosphorylation of the downstream AMPK target, ACC, or by phosphorylation of T172 on AMPKα itself, we observed no increase in AMPK activity following infection. While this observation contrasts with prior literature, it aligns more closely with what is known about AMPK and mTORC1 activity, where it is unlikely that both kinases would be maximally activated at the same time. Nonetheless, we detected a higher molecular weight band only on the pAMPKα-T172 blot around 70 kDa. Wondering if this was merely an antibody artefact, we performed another infection experiment, this time adding MK-8722 prior to

infection to maximally activate AMPK and increase the amount of pAMPKα-T172 (Figure 3.6C). To our surprise, the MK-8722-activated conditions generated a distinct banding pattern detectable as early as 15 min post-infection that completely disappeared by 2 hours (Figure 3.6D). Moving forward, we selected the 1h timepoint to capture the potential pAMPKα T172 band we observed in the absence of MK-8722 (Figure 3.6B,D). Though MK-8722 is a potent allosteric activator of AMPK, there are many upstream inputs leading to increased AMPK activity including rises in AMP:ATP ratios, low glucose, and increased calcium levels. To determine whether this band shift was dependent on a certain mode of activation, 15 min prior to infection we pretreated BMDM with compounds designed to increase or mimic AMP levels (AICAR[192], rotenone[195]), mimic low glucose (aldometanib[106]), stimulate calcium-dependent AMPK activation (ionomycin[529]), or allosterically activate AMPK at the ADaM site (MK-8722, BI-9774[530]) (Figure 3.6E). In mock-infected conditions, we observed a strong increase in pAMPKα T172 signal with all activators. In contrast, *S*.Tm-infected cells exhibited a clear shift in banding pattern that was similar amongst the activators. This was also accompanied by a relatively clear decrease in total AMPKα at its typical migration point at 63 kDa, suggesting that the higher molecular weight protein generated may be inaccessible to the total AMPKα antibody. This appears to be specific to AMPKα1, considering there were no significant differences in either β1 or γ1 banding within these same samples (Supplemental Figure 3.3A). When BMDM were exposed to an equivalent amount of heat-killed (HK) *S*.Tm, we observed the same pattern as with live bacteria (Figure 3.6E). This becomes clearer when comparing multiple biological replicates side by side, wherein all conditions were activated with MK-8722 (Figure 3.6F). Both live and HK bacteria produced a similar pAMPKα T172 banding pattern and diverged significantly from mock-infected conditions. Again, this was accompanied by a decrease in the

total AMPKα banding pattern, and an increase in pS6 signal (Figure 3.6F). Additionally, when comparing live, HK, and a mutant *S*.Tm strain lacking the SPI-1 virulence gene *invA*, the banding pattern was very similar (Supplemental Figure 3.3B), further supporting that this potential modification does not depend on live *S*.Tm virulence.

Given that phagocytosis represents the main route through which *S*.Tm is taken up into the macrophage, we wondered if the banding shift was phagocytosis-dependent. To test this, we pretreated BMDM with either MK-8722 or the actin polymerization inhibitor CytoD prior to infection with live *S*.Tm, or exposure to HK *S*.Tm (Figure 3.6G). We again observed the band shift in *S*.Tm-infected cells, though there appeared to be multiple bands in AMPK activated conditions (Figure 3.6H). With CytoD treatment, the banding intensity lessened, but did not completely disappear, suggesting that this process may be at least partially phagocytosis-dependent (Figure 3.6H). When comparing live versus HK *S*.Tm, there was again an equivalent increase in the higher molecular weight banding that was reduced slightly with CytoD (Figure 3.6I). It is worth noting that CytoD increased mTORC1 activity in the absence of bacterial exposure (Figure 3.6H,I). These data prompted us to question whether this increase in observed molecular weight requires *S*.Tm at all, or if it is solely dependent on phagocytosis-dependent signaling. To answer this, we again pretreated BMDM with MK-8722 and CytoD before spiking phagocytic cargo including HK *S*.Tm, zymosan A particles from the yeast *Saccharomyces cerevisiae*, and particles from the gram-positive *Staphylococcus aureus* (Figure 3.6J). All three types of particles triggered the same pAMPKα T172 banding shift, which was more apparent in AMPK-activated conditions (Figure 3.6K). CytoD treatment decreased the intensity of the banding caused by all three types, linking the shift at least partially to phagocytosis (Figure 3.6K). Undoubtedly, stringent validation using alternative antibodies, as well as AMPK KO

models will be required to further interrogate this phenomenon. However, the consistent modulation of this band shift using a spectrum of AMPK activators is supportive of the specificity of this modification for AMPKα. Collectively, these data suggest that AMPKα is rapidly modulated by a transient post translational modification in macrophages during phagocytosis (Figure 3.6L).

Mice expressing a myristoylation-deficient AMPK succumb to *S*.Tm more rapidly than WT mice.

Though the primary route of *S*.Tm infection is through the gut, macrophages and the production of inflammatory cytokines play an essential role in regulating *S*.Tm pathogenesis[365]. Knowing that elevated AMPK activity reduces select production of proinflammatory cytokines in macrophages, we asked whether this was relevant in the context of whole-body infection. To address this, we used a genetic model in which mice express a glycine-2-alanine (G2A) mutation on both β1 and β2 subunits, rendering AMPK non-myristoylated and chronically overactive since myristoylation restricts AMPK activity and regulates its subcellular localization[43,92].

To understand how chronic AMPK overactivity affects *S*.Tm pathogenesis, we first pretreated WT and G2A mice with an oral gavage of streptomycin to reduce colonization resistance conferred by intestinal microbiota[338]. We then inoculated the mice 24 hours later by gavage using the same GFP-expressing SL1344 *S*.Tm strain that we used in our *in vitro* experiments (Figure 3.7A). Following this, we measured bodyweights daily, which, despite G2A mice being lighter (Supplemental Figure 3.4A), did not differ significantly over the first three days of infection when made relative to starting bodyweight (Figure 3.7B). By day four and five, there was a trend towards greater bodyweight loss in the G2A mice (Figure 3.7B). At the time of

harvest, five days post-infection, we measured colon length and observed cecum morphology, both of which exhibited minimal genotypic changes, particularly when colon length was normalized to bodyweight (Supplemental Figure 3.4B-D). Infection did not induce a prominent colon shortening phenotype when compared with naïve mice, though the cecum was expectedly shrunken and more translucent (Supplemental Figure 3.4B-D). This tracked with a high fecal burden that fluctuated by day, though did not differ between WT and G2A mice (Supplemental Figure 3.4E). To assess whether certain tissues were more susceptible to *S*.Tm infection, we measured bacterial load in gastrointestinal (GI) and systemic tissues. GI tissues such as the cecum, colon, and distal ileum, did not display any genotypic differences in *S*.Tm burden (Figure 3.7C), aligning with our colon length and fecal burden data. However, there was a clear increase in liver, spleen, and bone marrow CFU, suggesting either greater dissemination to tissues beyond the GI tract or enhanced replication within those tissues (Figure 3.7C). Our measurements of elevated bacterial burden in G2A mice was supported by increased expression of proinflammatory transcripts including *Tnf*, *Il1b*, *Il6*, *Ifng*, and *Il17a* in the spleen (Supplemental Figure 3.4F). Surprisingly, these transcript levels were unchanged in the liver, where the only significant genotypic difference was in *Il10* expression (Supplemental Figure 3.4F), highlighting tissue-specific regulation during the response to infection.

To determine whether this elevated burden translated to mortality, we subjected WT and G2A mice to oral infection and measured survival. Humane endpoint was assigned to mice reaching 20% bodyweight loss, or combined wellness measures exceeding a predetermined threshold based on activity, appearance, and response to stimulus. Initial attempts using the *S*.Tm-GFP strain from our burden experiments resulted in minimal mortality, where only 3/5 G2A mice and 0/6 WT mice succumbed to infection by day 16 before apparently clearing the

infection (Supplemental Figure 3.5A-D). However, these data were supportive of G2A mice being more susceptible to infection. To circumvent this, we infected the mice with WT *S*.Tm, which resulted in a survival time of 5-8 days in WT mice following oral infection, in line with published values[463] (Figure 3.7D). Repeating the experimental paradigm, we observed that orally-infected G2A mice succumbed significantly earlier than their WT counterparts, reaching 50% mortality about two days before WT mice (Figure 3.7E). This was especially apparent by wellness measures, where G2A mice displayed sickness behaviour earlier than WT mice (Supplemental Figure S3.4C,D). This correlated with sharper, albeit less striking, differences in bodyweight loss (Figure S3.4E), and a mild elevation in fecal *S*.Tm one day post-infection in G2A mice (Figure S3.4F). To determine whether this susceptibility depended on conditions beyond GI invasion, we infected mice via IP injection (Figure 3.6F). In line with the oral route, IP infection caused G2A mice to succumb more rapidly than WT mice (Figure 3.6G). This was also accompanied by more severe sickness behaviour and more rapid bodyweight loss (Figure S3.4G-H). When viewed in line with our bacterial burden results, these data provide strong evidence that AMPK myristoylation, and the chronic activation that results from its absence, plays a key role in the systemic response to *S*.Tm infection.

Systemic activation and modulation of AMPK activity in circulating immune cells does not affect *S*.Tm pathogenesis.

Seeing as the G2A mice displayed consistently more severe infections, we wondered if this was due to elevated AMPK activity, or some other myristoylation-dependent effect. To address this, we allosterically activated AMPK by gavage of MK-8722 three hours before initial *S*.Tm-GFP infection on day 0, and then again on days 1, 2, and 3 (Figure 3.8A). Surprisingly,

there was no trend towards greater bodyweight loss in the MK-8722-treated mice (Figure 3.8B). There were no changes in bacterial burden in GI tissues such as the mesenteric lymph nodes, cecum, and colon; however, in contrast with the G2A mice, there was also no change in systemic burden in the liver, spleen, and bone marrow (Figure 3.8C). We observed similar bacterial burden results in an IP infection model accompanied by daily IP dosing with MK-8722 (Supplemental Figure 3.6A-C). There were also no genotypic differences in endpoint blood glucose levels, which is another indicator of disease severity [531] (Supplemental Figure 3.6D). To confirm these results, we subjected mice to an oral survival experiment using WT *S*.Tm alongside oral MK-8722 administration on days 0, 1, and 2 (Figure 3.8D). Aligning with our bacterial burden data, there was no effect of MK-8722 treatment on survival (Figure 3.8E). This was also supported by mouse behavioural assessments, bodyweight changes, and fecal burden (Supplemental Figure 3.7A-D). These data demonstrate that the chronic basal elevation in AMPK activity in G2A mice differs from acute systemic activation with the allosteric activator, MK-8722.

Since we observed elevated burden only in systemic tissues in G2A mice following oral infection, we wondered if disrupting AMPK activity in circulating myeloid cells would affect pathogenesis. Using a Cre-loxP system wherein we deleted *Prkaa1/2* (AMPK α1 and α2, respectively) in *LysM*-expressing cells, which include monocytes, macrophages, and other innate immune cells, we again subjected mice to an oral infection where survival was assessed (Figure 3.8F). Similar to the MK-8722 cohorts, we observed no changes in survival when mice lacked AMPK activity in myeloid cells (Figure 3.8G). This tracked with wellness measures, bodyweight loss, and fecal *S*.Tm burden (Supplemental Figure 3.7E-H). These data support a minimal role for myeloid AMPK in regulating the systemic response to *S*.Tm infection.

To understand potential differences between the chronic AMPK activation observed in the G2A model and acute activation via MK-8722, we metabolites in G2A BMDM in the uninfected and infected state. In the absence of infection, G2A BMDM exhibited comparable increases to MK-8722-treated BMDM in the glycolytic metabolite DHAP in relation to WT untreated cells (Table 3.4). This aligned with several other metabolites such as hypoxanthine and creatine, suggesting that chronic and acute AMPK activation leads to similar metabolic phenotypes in some pathways (Table 3.4). However, G2A cells exhibited clear changes in nucleotide abundance, where most were part of purine or pyrimidine synthesis pathways (Figure 3.9C,D). Strikingly, nucleobases such as adenine and guanine were significantly lower in G2A cells than WT, while there was a stepwise increase in relative metabolite levels going from nucleotide monophosphate (NMPs) species to nucleotide diphosphate (NDPs), and finally to nucleotide triphosphates (NTPs) (Figure 3.9E). This pattern aligns with nucleotide salvage pathway induction, resulting in increased NTPs at the expense of salvageable bases such as guanine and adenine. We also observed no changes in uracil, which was the only base detected amongst the three bases that cannot be used in nucleotide salvage, those being uracil, cytosine, and thymine[532,533]. While these data are convincing, only uracil was significantly increased in infected conditions relative to mock-infected cells, indicating that, at 6 hours post-infection, the nucleotide pool as a whole is not changing significantly due to *S*.Tm (Table 3.1). This potentially explains why there were fewer significantly changed metabolites in infected G2A macrophages (Supplemental Figure 3.7A,B; Table 3.5). However, pyrimidine and purine metabolism remained among the top enriched metabolite sets (Supplemental Figure 3.7C), aligning with mock-infected cells (Supplemental Figure 3.7D,E).

G2A mice developed infections more rapidly than WT mice, though this could have been due to a combination of cell types *in vivo*. Therefore, we tested whether circulating immune cells, and potentially their dysregulated nucleotide levels, played a role in our G2A phenotype by performing reciprocal BMT experiments. We irradiated mice before transplanting either WT or G2A bone marrow into G2A recipients, or WT or G2A bone marrow in WT recipients (Figure 3.9F). Aligning with our myeloid AMPK knockout experiment, we observed no change in survival in G2A mice receiving WT bone marrow, or WT mice receiving G2A bone marrow (Figure 3.9G,H). There were also no differences in bodyweight, wellness, and fecal *S*.Tm measurements between the BMT groups (Supplemental Figure 3.8A-G). It is worth noting that while the two groups of BMT mice reached endpoint at similar times according to bodyweight loss, the G2A recipient mice exhibited stronger sickness behaviour earlier in the infection, aligning with prior cohorts (Supplemental Figure 3.8JB,E). Taken together, AMPK signaling in the circulating immune component does not appear to play a meaningful role in the response to *S*.Tm during oral infection.

3.6 Discussion

In this study, we sought to better understand how AMPK activity shapes the innate immune response to *S*.Tm. We observed that AMPK selectively suppresses *Il1b*, *Il6*, and *Il12b* at the transcriptional level and IL-10 at the post-transcriptional level during *S*.Tm infection (Figures 1-3). These changes may be linked to the metabolic status of the cell, which exhibited lower TCA cycle and elevated citrulline metabolite abundance (Figure 4). Ultimately, these changes had little effect on pathogenesis within macrophages (Figure 5), though AMPK itself may be post-translationally regulated early in the infection process or during phagocytosis (Figure 6). During *S*.Tm infection in mice, chronic (Figure 7), but not acute (Figure 8) activation of AMPK resulted in increased bacterial burden, though this was not dependent on myeloid cells but could be related to changes in nucleotide metabolism (Figure 9).

The mechanism through which AMPK inhibits select inflammatory cytokine production has remained unclear. The main differences we observed in our targeted assessment of core inflammatory genes was decreased *Il1b*, *Il6*, and *Il12b* transcription, of which *Il1b* transcription is strongly inhibited by 2 hours post-infection, alongside elevated IL-10 protein levels. These changes may be connected, as interferon signaling can inhibit *Il1b* transcription in an IL-10-dependent manner[534]. Other IL-10-related cytokines such as IL-19/20/24 can also inhibitory *Il1b* transcription[535], though we did not measure these cytokines directly. Despite the effect being more obvious in LPS-stimulated conditions, AMPK activation seemed to increase early secretion of TNF-α in addition to IL-10, independent of transcription. AMPK activity can trigger rapid Golgi disassembly through phosphorylation of GBF1[536–538]. However, this has been proposed to slow anterograde trafficking[537,539], though this was not tested in macrophages. Considering how the kinetics of cytokine transport through the trans-Golgi network can be a rate limiting step in

cytokine secretion[540], our data suggest that there may be a connection between AMPK-mediated Golgi disassembly and the resulting changes in cytokine secretion. Additionally, HIF-1α augments *Il1b* transcription following succinate accumulation[433], and we measured a significant decrease in succinate levels following AMPK activation. While this could provide some link between AMPK activity and *Il1b*, it unlikely to entirely account for the strong suppressive effect on *Il1b* levels at 2 hours post-infection. *Il6* and *Il12b* transcript induction is highly dependent on histone acetylation derived from increased glycolysis during LPS stimulation[525]. Mechanistically, ATP-citrate lyase-dependent acetyl-CoA generation from citrate in the cytosol provides acetyl-CoA needed for histone acetylation[525]. While we did not measure acetyl-CoA species directly, citrate was significantly lower in AMPK activated conditions, potentially providing a metabolic link to *Il6* and *Il12b* transcript levels.

One of the most striking AMPK-dependent metabolic changes during *S*.Tm infection was increased citrulline, which was accompanied a trending increase in NO production. Interestingly, in contrast to our observations that *Nos2* transcript levels increase with AMPK activation, AMPK has been shown to prevent nuclear translocation of STAT1[386], which is a positive regulator of *Nos2* transcription. Additionally, treatment of macrophages with the non-specific activators AICAR and metformin led to reduced nitrite levels and iNOS expression, further supporting an inhibitory AMPK-iNOS axis[541], though the opposite was observed in hepatocytes[542]. AMPK knockout models in both vascular smooth muscle cells[515] and in macrophages exposed to LPS[385] exhibit elevated STAT1 activity and increased iNOS protein levels, again suggestive of a suppressive effect on STAT1. Why then might we be observing an increase in *Nos2* and nitrite levels following AMPK activation? Given that we did not observe changes in *Nos2* levels at 2 h post-infection, it suggests that the effect of AMPK on *Nos2*

transcription is not direct, and would rule out rapid phosphorylation and prevention of STAT1 nuclear translocation[386]. Furthermore, our data demonstrates that *Ass1* and *Cxcl9*, which are also under STAT1 control, displays distinct kinetics relative to *Nos2*. Though the main regulators of *Nos2* transcription are NF-κB and STAT1[543], it is also induced in part through NRF2, which can bind to a *Nos2* enhancer region and maintain an open chromatin conformation[544]. AMPK directly phosphorylates NRF2 at S550, potentially leading to increased nuclear accumulation[545]. However, whether AMPK activation affects *Nos2* transcript levels via NRF2 will have to be determined experimentally.

Beyond potential *Nos2* regulation, there are several other links between AMPK and arginine metabolism. For one, AMPKα is *S*-Nitrosylated at C131, impairing sensitivity to AMP[546]. This presents a scenario where elevated cellular RNS suppresses AMPK activity, generating a negative feedback loop to prevent overproduction of NO. Additionally, AMPK knockout macrophages display not only dysregulated protein levels of iNOS, but also numerous other arginine metabolism proteins and transporters[385]. Furthermore, citrulline is also one of the most depleted endogenous metabolites during aging and has been traced, at least in part, due to reduced *Nos2* levels[547]. Given that AMPK activators have well established roles in supporting longevity[548,549], perhaps potentiation of citrulline levels could contribute to the anti-aging effect of AMPK activity.

Phagocytosis is a dynamic, energetically costly process for macrophages. AMPK activation downstream of *E. coli* or apoptotic thymocyte ingestion has been shown to increase phagocytosis, though this work relied on AICAR and other non-specific AMPK activators[550]. However, experiments using myeloid AMPK knockout cells detected no differences in uptake of phagocytic beads[326]. Nonetheless, a pro-phagocytic role would align with the mild increase in

*S.*Tm+ macrophages we observed following allosteric AMPK activation. However, we did not detect an increase in AMPK activity at any stage during *S.*Tm infection. On the other hand, the observed shift in molecular weight was only detected when probing for pAMPKα-T172, potentially due to steric hindrance preventing the total antibody from detecting the higher molecular weight band. This could signify that AMPKα is phosphorylated at T172 early following phagocytosis, but it is simultaneously modified to prevent downstream signaling.

Autophagic degradation of internalized cargo such as bacteria is an important host defense mechanism, and is linked with autophagy through phagolysosomal fusion. AMPK is now recognized to inhibit generalized autophagic and mitophagic induction under certain circumstances including glucose starvation[417] and exposure to mitophagic stimuli[420] due to inhibitory phosphorylation on ULK1. Since ULK1-mediated phosphorylation of ATG16L1 is required for xenophagy[422], it may be beneficial for macrophages to suppress AMPK activity to enable xenophagy to progress uninterrupted. Our data using cross-kingdom phagocytic cargo suggests that this could be a feature of xenophagy, regardless of origin, though whether other phagocytic cargo also triggers this phenomenon remains to be seen.

The band shift was approximately 10 kDa, where a monoubiquitination or SUMOylation event could potentially account for this shift. AMPKα is SUMOylated, which has an inhibitory effect on its activity[190]. Furthermore, macrophages express SUMO E3 ligase enzyme that targets AMPK, PIAS4, alongside several other PIAS enzymes. Physiologically, this scenario could be relevant if AMPK is active at the time of infection, for example if the host is in the fasted state. Ultimately, further experiments will be required to ascertain the relevance of this modification on AMPK function, though it could represent a general mechanism to suppress AMPK activity during phagocytosis.

It remains challenging to activate AMPK *in vivo* in physiological manner. We have demonstrated that chronic AMPK overactivity led to increased *S*.Tm burden that was not recapitulated by acute pharmacological activation. Other models have employed overexpression of a truncated, constitutively active AMPKα[551], or modulation of AMP binding to AMPK, rendering it less sensitive to dephosphorylation and increasing AMPK activity[552]. The latter model has since been used in studies of pancreatic cancer[553] and diet induced obesity[554], wherein application of an acute activator mimicked effects of the genetic overactivity modes. Our G2A model represents a germline, whole body overactivity model that may have differing effects on long term metabolism that cannot be replicated by cotreatment of an AMPK activator. While an infinitely simpler system, our macrophage metabolomics data demonstrated that, compared to allosterically activated macrophages, G2A cells exhibited a strong tendency towards elevated nucleotide salvage. This may be due to RRM1 phosphorylation by AMPK, which has been shown to support DNA repair mechanisms and prevent cell death[555]. Considering NO can cause DNA damage including double stranded breaks[556], G2A cells may be more resistant to antibacterial cell death initiation owing to elevated NTP availability *in vivo*. Further experimentation testing long term allosteric activator administration will be required to determine if the effects observed in G2A mice are specific to reduced myristoylation or the chronic overactivity.

Collectively, this work highlights several important regulatory nodes through which forced activation of AMPK leads to altered abundance of metabolic intermediates in the TCA cycle and arginine metabolism pathways during *S*.Tm infection, with implications on transcriptional regulation of proinflammatory cytokines as well as pathogenesis at the organismal level.

3.7 Figures

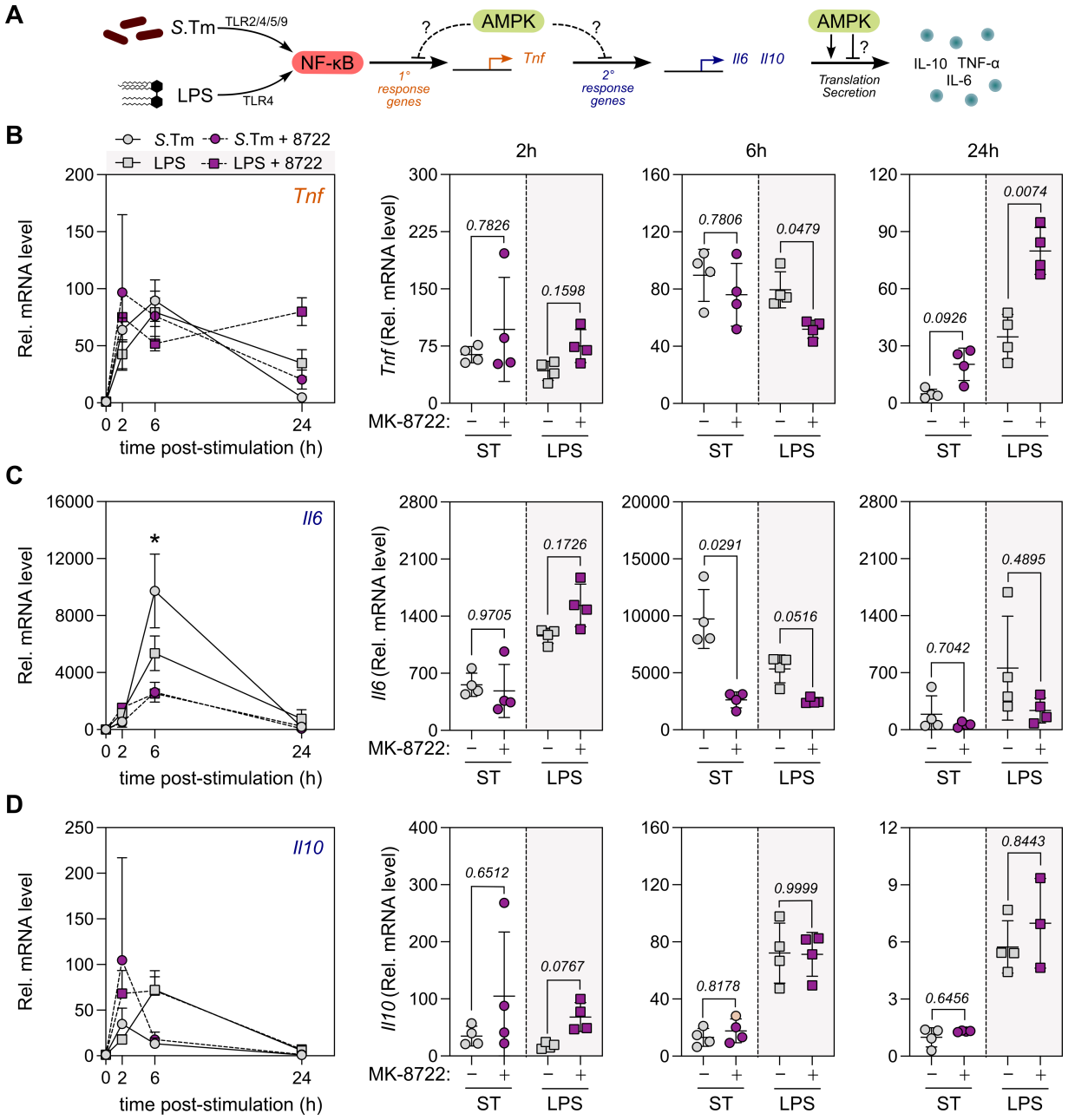

Figure 3.1: AMPK activation affects *S*.Tm-induced gene expression similar to LPS. (A) Schematic of NF-κB-mediated inflammatory transcription. LPS triggers TLR4 while *S*.Tm activates TLR2/4/5/9 to stimulate NK-κB activation, leading to primary and secondary response genes. **(B)** BMDM were treated with the AMPK activator MK-8722 (2 μM) for 15 min before spiking in either LPS (100 ng/ml) or live *S*.Tm (MOI 2) and centrifuging the plate, then incubating for a further 15 min. Cells were washed three times with gentamicin-PBS (50 μg/ml) and media supplemented with high gentamicin (50 μg/ml) was added for 1.5h before washing the cells again and replacing with low gentamicin media (10 μg/ml) for the indicated times. Relative mRNA expression of **(B)** *Tnf*, **(C)** *Il6*, and **(D)** *Il10* at 2, 6, and 24h post infection. Data represented as mean ± SD. *P* values calculated using a repeated measures two-way ANOVA with Tukey's post hoc test and reported to the fourth decimal. Conditions with $P<0.05$ for both LPS and *S*.Tm indicated with an asterisk. Data are representative of two independent experiments (n=4 per group).

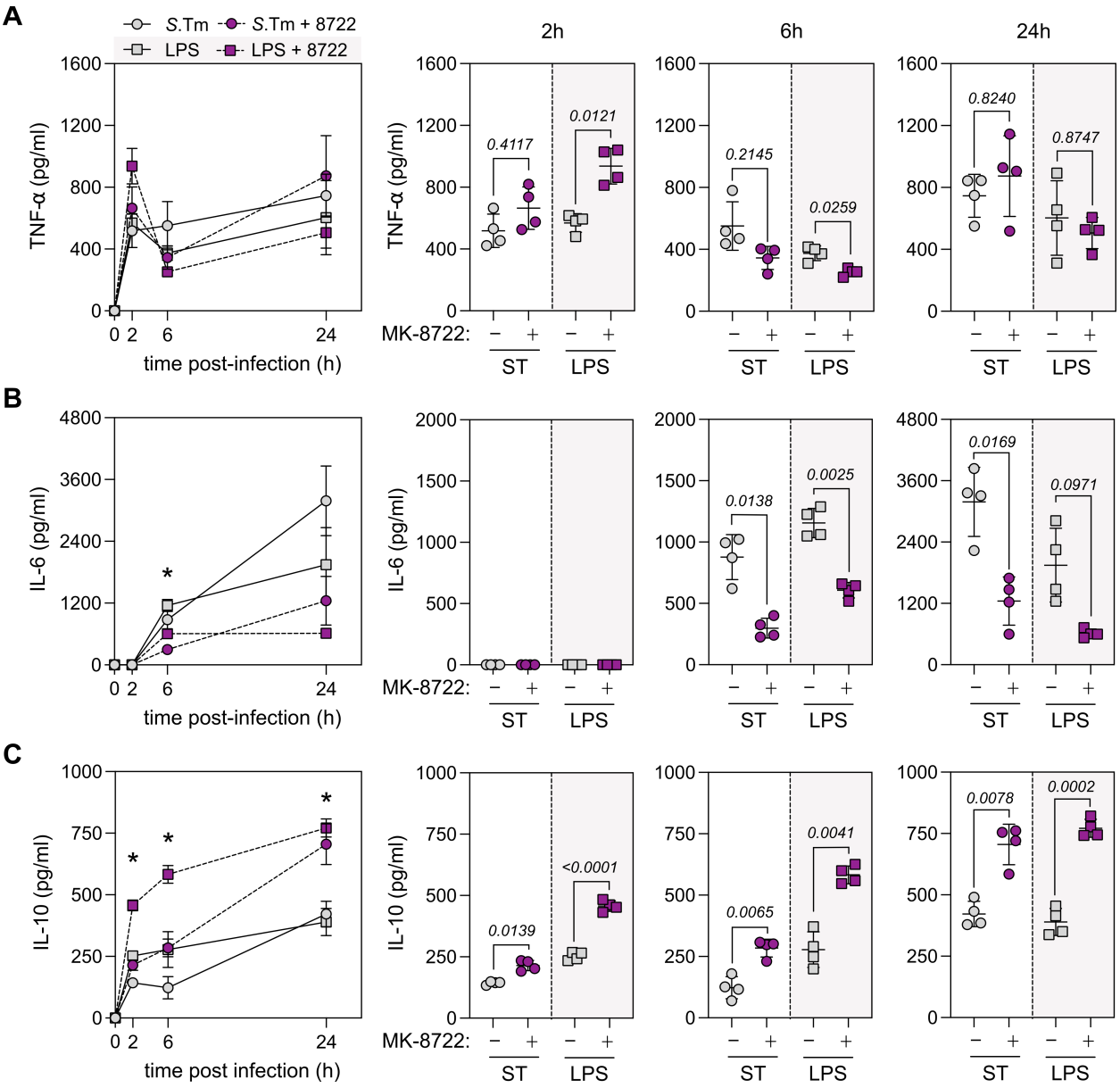

Figure 3.2: AMPK activation modulates *S*.Tm-induced cytokine secretion similar to LPS. (A) BMDM were treated with the AMPK activator MK-8722 (2 μM) for 15 min before spiking in either LPS (100 ng/ml) or live *S*.Tm (MOI 2) and centrifuging the plate, then incubating for a further 15 min. Cells were washed three times with gentamicin-PBS (50 μg/ml) and media containing MK-8722 or DMSO supplemented with high gentamicin (50 μg/ml) was added for 1.5h before washing the cells again and replacing with low gentamicin media (10 μg/ml) for the indicated times. Supernatant cytokine concentrations of **(A)** TNF-α, **(B)** IL-6, and **(C)** IL-10 at 2, 6, and 24h post infection. Data represented as mean ± SD. *P* values calculated using a repeated measures two-way ANOVA with Sidak's post hoc test and reported to the fourth decimal. Conditions with *P<0.05* for both LPS and *S*.Tm indicated with an asterisk. Data are representative of two independent experiments (n=4 per group).

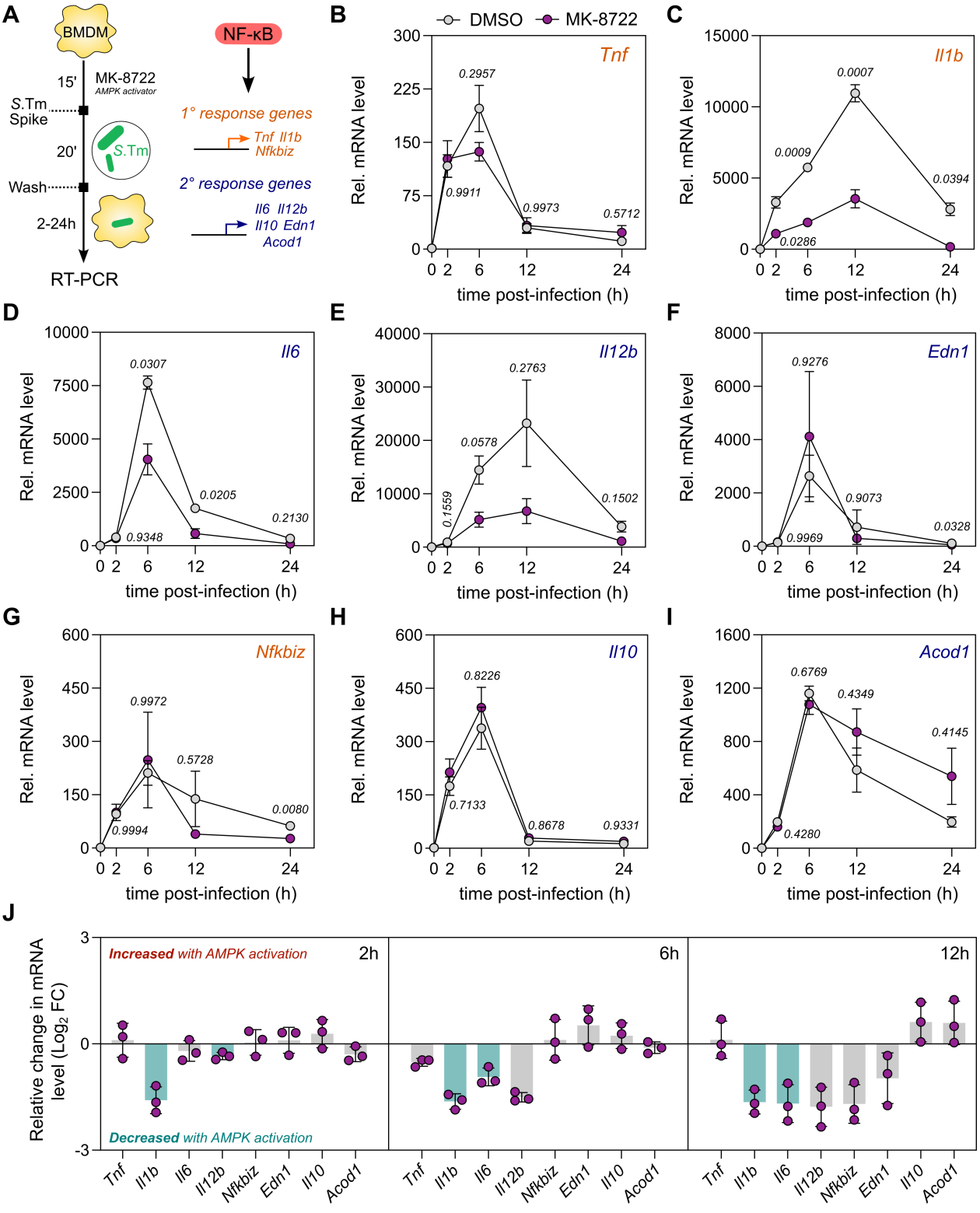

Figure 3.3: AMPK activation in macrophages suppresses select proinflammatory cytokines at early and late stages of infection. (A) Schematic of experiment: BMDM were activated with MK-8722 (2 μM) or equivalent DMSO (0.05%) for 15 min prior to spiking in S.TM-GFP (MOI 10), centrifuging the plate, then incubating for 15 min. Cells were washed three times with gentamicin-PBS (50 μg/ml) and media containing

MK-8722 or DMSO supplemented with high gentamicin (50 μg/ml) was added for 1.5h before washing the cells again and replacing with low gentamicin media (10 μg/ml) for the indicated times. Relative mRNA expression of **(B)** *Tnf*, **(C)** *Il1b*, **(D)** *Il6*, **(E)** *Il12b*, **(F)** *Edn1*, **(G)** *Nfkbiz*, **(H)** *Il10*, and **(I)** *Acod1* at 2, 6, 12, and 24h post infection. **(J)** Relative Log_2 fold change in mRNA levels due to MK-8722 treatment for data shown in (B-I). Data represented as mean ± SD. *P* values calculated using a two-way repeated measures ANOVA with Sidak's post hoc test and reported to the fourth decimal. Conditions with $P<0.05$ are coloured in green in (J). Data are representative of two independent experiments for (B-D,H) and one independent experiment for (E-G,I) with n=3 per group.

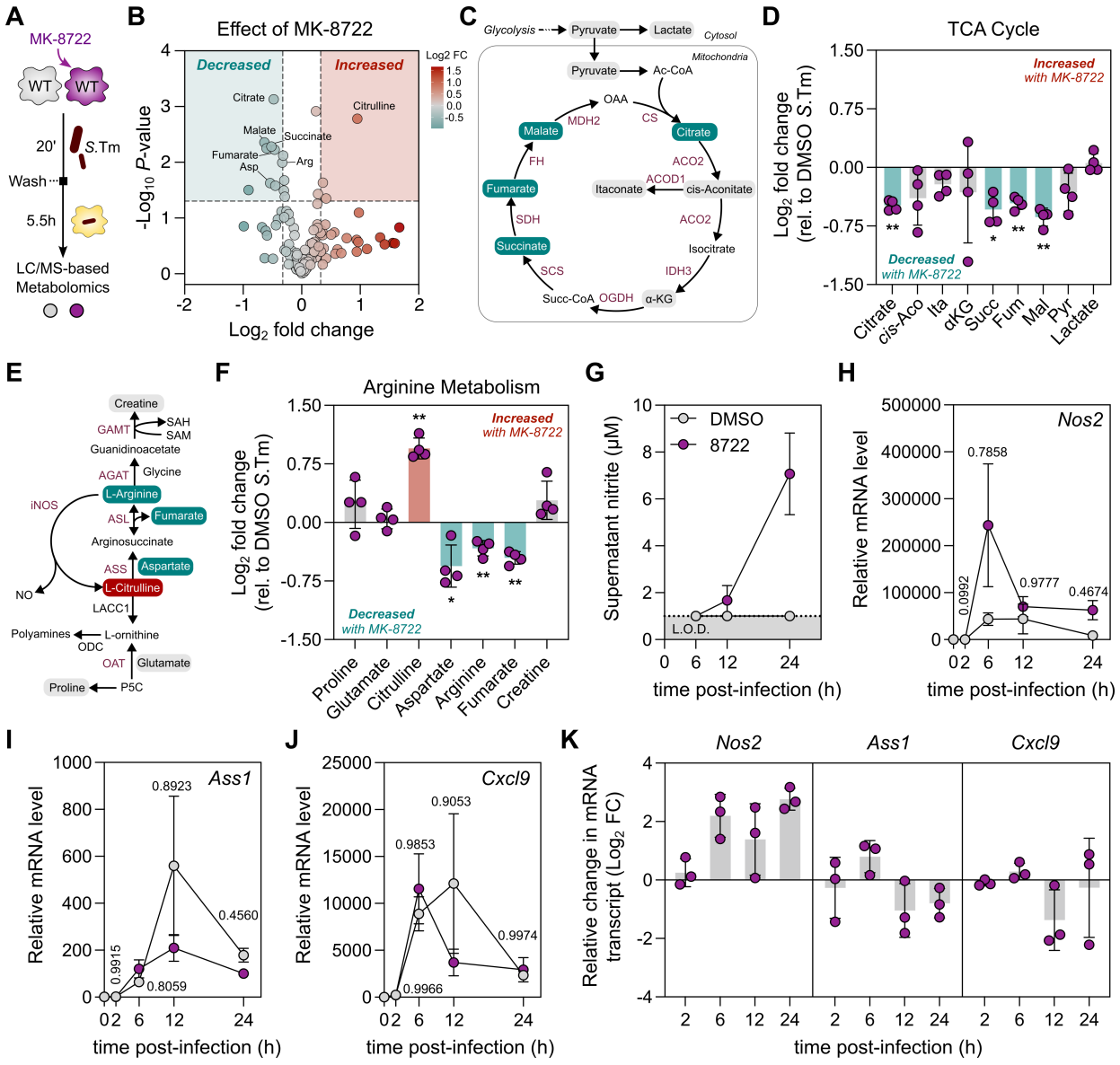

Figure 3.4: AMPK activation alters TCA cycle metabolites and arginine metabolism in infected macrophages. (A) Schematic of experiment: BMDM were activated with MK-8722 (2 μM) or equivalent DMSO (0.05%) for 30 min prior to spiking in *S*.Tm-GFP (MOI 10) for 20 min. Cells were washed three times with gentamicin-PBS (50 μg/ml) and media containing MK-8722 or DMSO supplemented with high gentamicin (50 μg/ml) was added until 6h post infection. **(B)** Volcano plot depicting most altered metabolites between vehicle and MK-8722-treated infected cells. **(C)** Schematic of the TCA cycle and detected metabolites, with green signifying significantly lower levels in MK-8722-activated conditions. **(D)** Log_2 fold change in TCA cycle metabolites relative to vehicle infected conditions. **(E)** Schematic of the arginine metabolism pathway, with green and red signifying significantly lower and higher levels in MK-8722 activated conditions, respectively. **(F)** Log_2 fold change in arginine-related metabolites relative to vehicle-treated infected conditions. **(G)** Supernatant nitrite levels determined by Griess assay from BMDM infected with *S*.Tm (MOI 10) as described above. **(H-J)** Relative mRNA levels of **(H)** *Nos2*, **(I)** *Ass1*, and **(J)** Cxcl9 at 2, 6, 12, and 24h post-infection. **(K)** Relative Log_2 fold change in mRNA levels between MK-8722 and vehicle-treated conditions. Data represented as mean ± SD in (D,F-K), or a volcano plot (B). Volcano plot raw *P*-value threshold was set to 0.05 and absolute fold change to 1.25. *P* values calculated using a paired, two-tailed Welch's t-test (B,D,F), where $P<0.05$ = *, $P<0.01$ = **, or a repeated measures two-way ANOVA with Sidak's post hoc test (H-J). Data are representative of one independent experiment (n=3-4 per group).

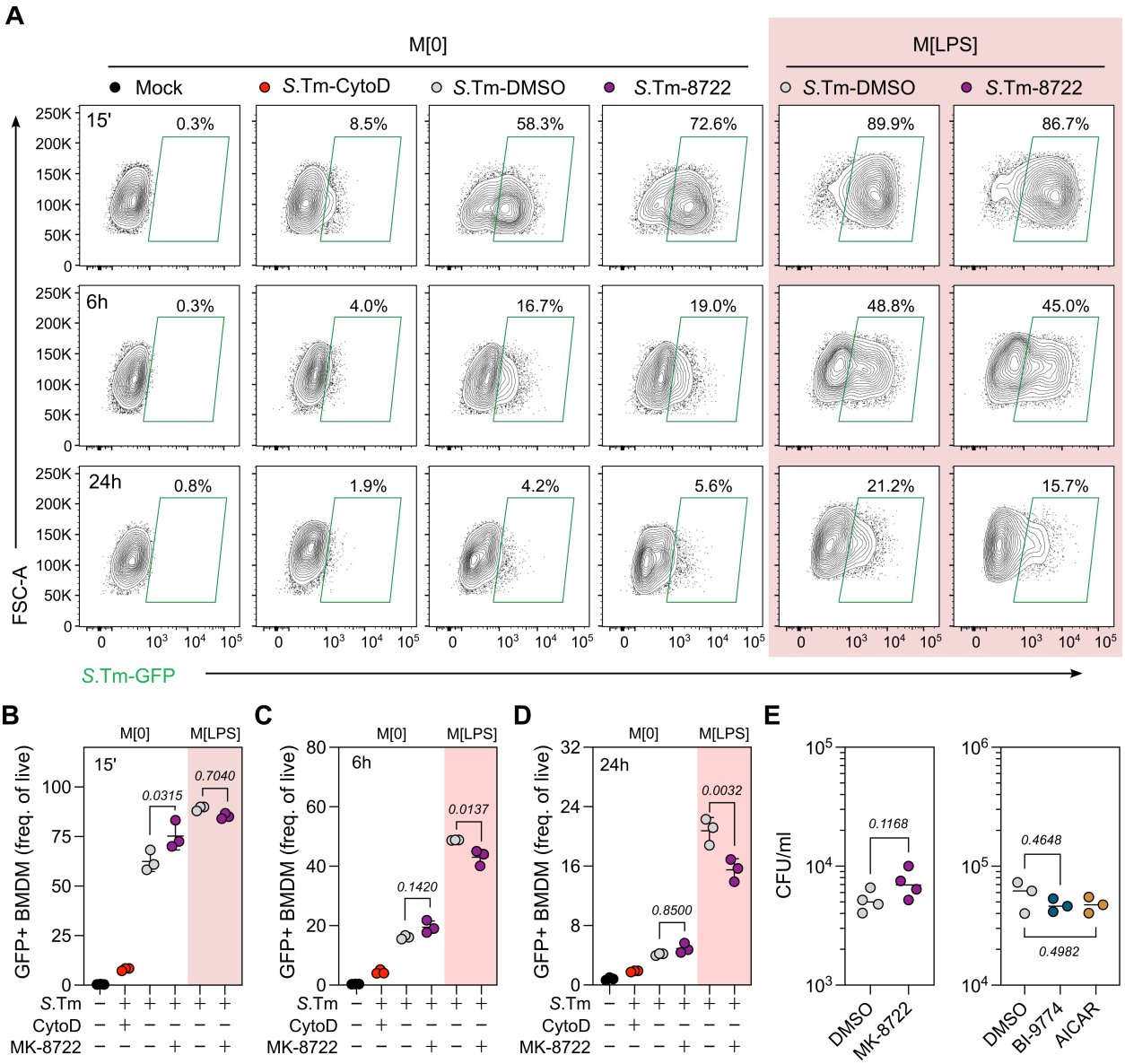

Figure 3.5: AMPK activation mildly affects *S*.Tm burden in macrophages. (A) Representative flow cytometry plots of live, singlet GFP+ BMDM. Naïve (M[0]) or LPS-polarized (M[LPS]; 100 ng/ml for 18h) BMDM were pretreated with MK-8722 (2 μM), cytochalasin D (10 μM; CytoD), or equivalent DMSO (0.05%) for 15 min prior to spiking in *S*.Tm-GFP (MOI 10), centrifuging the plate, then incubating for 15 min. Cells were washed three times with gentamicin-PBS (50 μg/ml) and media containing MK-8722, CytoD, or DMSO was supplemented with high gentamicin (50 μg/ml) and added for 1.5h. After a final wash, media was replaced with low gentamicin media (10 μg/ml) with MK-8722 or DMSO for the indicated times. Quantification of GFP+ BMDM cells at **(B)** 15 min, **(C)** 6h, and **(D)** 24h post-infection. Bacterial burden from naïve BMDM treated as above for 6h, but with additional BI-9774 (10 μM) or AICAR (200 μM) conditions. Data represented as individual points with mean ± SD in (B-D) and median (E). *P* values calculated using a one-way ANOVA followed by Tukey's post hoc test (B-D; E (right)), and a paired, two-tailed Student's t-test. Data representative of two independent experiments (B-D) or one independent experiment (E).

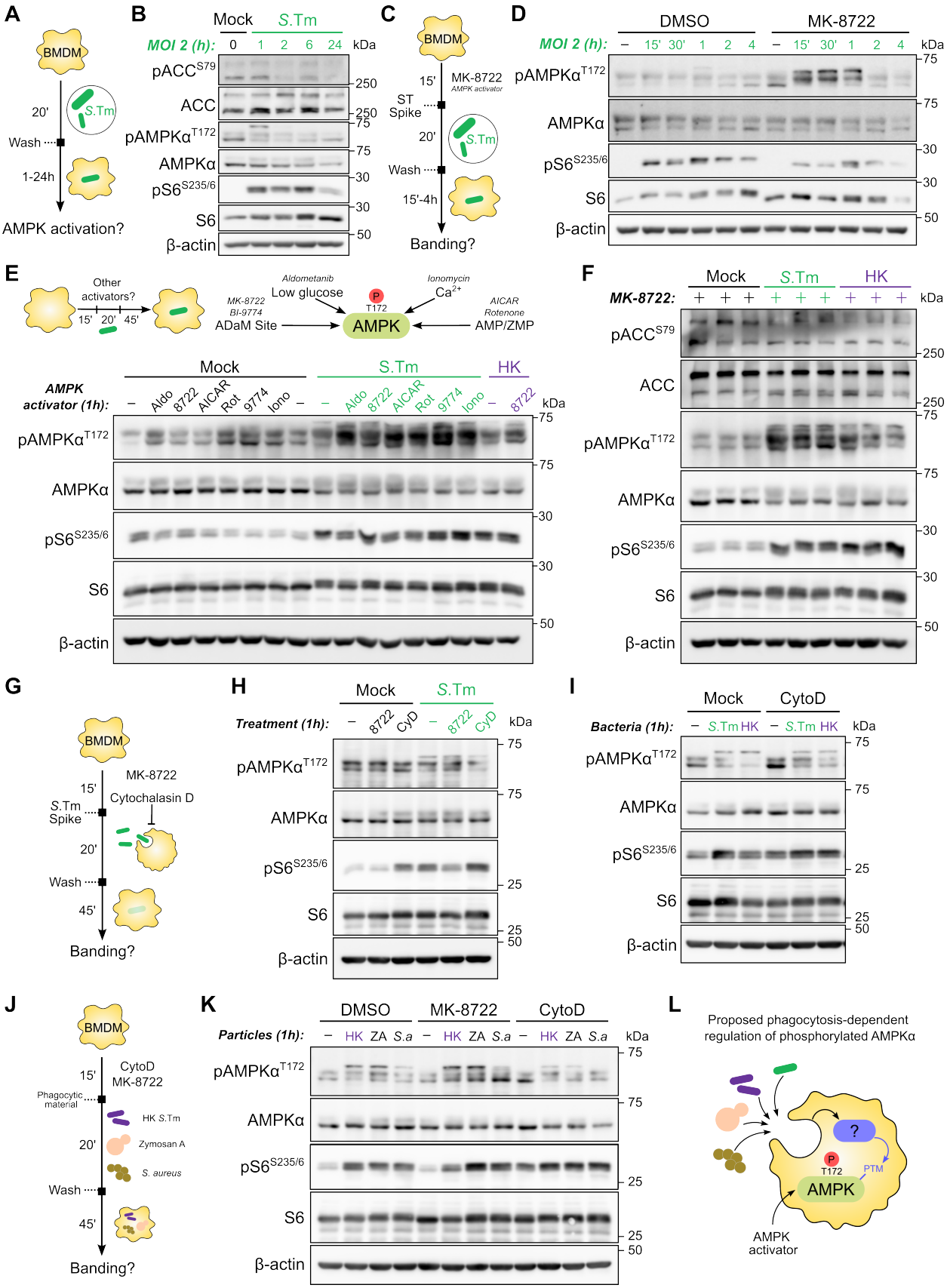
A
BMDM
20'
S.Tm
Wash
1-24h
AMPK activation?
B
Mock
S.Tm
MOI 2 (h):
0 1 2 6 24
kDa
pACC^{S79}
ACC
pAMPKα^{T172}
AMPKα
pS6$^{S235/6}$
S6
β-actin
C
BMDM
15'
MK-8722
AMPK activator
ST Spike
20'
S.Tm
Wash
15'-4h
Banding?
D
DMSO
MK-8722
MOI 2 (h):
– 15' 30' 1 2 4 – 15' 30' 1 2 4
kDa
pAMPKα^{T172}
AMPKα
pS6$^{S235/6}$
S6
β-actin
E
Other activators?
15' 20' 45'
Aldometanib
Low glucose
MK-8772
BI-9774
ADaM Site
P
T172
AMPK
Ionomycin
Ca^{2+}
AICAR
Rotenone
AMP/ZMP
Mock
S.Tm
HK
AMPK activator (1h):
– Aldo 8722 AICAR Rot 9774 Iono – – Aldo 8722 AICAR Rot 9774 Iono – 8722
kDa
pAMPKα^{T172}
AMPKα
pS6$^{S235/6}$
S6
β-actin
F
Mock
S.Tm
HK
MK-8722:
kDa
pACC^{S79}
ACC
pAMPKα^{T172}
AMPKα
pS6$^{S235/6}$
S6
β-actin
G
BMDM
15'
MK-8722
S.Tm Spike
Cytochalasin D
20'
Wash
45'
Banding?
H
Mock
S.Tm
Treatment (1h):
– 8722 CyD – 8722 CyD
kDa
pAMPKα^{T172}
AMPKα
pS6$^{S235/6}$
S6
β-actin
I
Mock
CytoD
Bacteria (1h):
– S.Tm HK – S.Tm HK
kDa
pAMPKα^{T172}
AMPKα
pS6$^{S235/6}$
S6
β-actin
J
BMDM
15'
CytoD
MK-8722
Phagocytic material
HK S.Tm
20'
Zymosan A
S. aureus
Wash
45'
Banding?
K
DMSO
MK-8722
CytoD
Particles (1h):
– HK ZA S.a – HK ZA S.a – HK ZA S.a
kDa
pAMPKα^{T172}
AMPKα
pS6$^{S235/6}$
S6
β-actin
L
Proposed phagocytosis-dependent regulation of phosphorylated AMPKα
?
P
T172
PTM
AMPK
AMPK activator

Figure 3.6: *S*.Tm infection does not acutely increase AMPK activity, but does produce a high molecular weight banding pattern partially dependent on phagocytosis. (A) Schematic of experiment: *S*.Tm was spiked in (MOI 2) to BMDM cultured in RPMI. After 20 min, extracellular bacterial were washed out three times with gentamicin-PBS (50 µg/ml) and media was replaced with RPMI with high gentamicin (50 µg/ml). For timepoints beyond 2h, cells were washed a second time and media replaced with RPMI and low gentamicin (10 µg/ml). **(B)** Immunoblots of AMPK and mTORC1 signaling targets. **(C)** Schematic of experiment: same as in (A), but MK-8722 (2 µM) was added 15 min before spiking in *S*.Tm (MOI 2). **(D)** Immunoblots of AMPK and mTORC1 signaling over short time periods post infection. **(E)** Schematic of experiment: same as in (A), except BMDM were pretreated for 15 min prior to infection with *S*.Tm (MOI 2) or exposure to heat-killed *S*.Tm (MOI 2) with AMPK activators including aldometanib (5 µM; Aldo), MK-8722 (2 µM; 8722), AICAR (200 µM), rotenone (5 µM; Rot), BI-9774 (10 µM; 9774), and ionomycin (10 µM; Iono). Immunoblots of AMPK and mTORC1 signaling targets 1h post infection. **(F)** Immunoblots of AMPK and mTORC1 signaling following a 15 min pretreatment with MK-8722 (2 µM) followed by 1h *S*.Tm infection or exposure to heat killed *S*.Tm at MOI 2. **(G)** Schematic of experiment: same as in (A), except MK-8722 (2 µM) or cytochalasin D (10 µM; CyD) were added to cells before addition of live or heat killed *S*.Tm at an MOI of 4 for 20 min before washing away extracellular bacteria. **(H,I)** Immunoblots of AMPK and mTORC1 signaling targets. **(J)** Schematic of experiment: same as in (A), except BMDM were treated with MK-8722 (2 µM) or cytochalasin D (10 µM) for 15 min before spiking in heat killed *S*.Tm (MOI 4), zymosan A bioparticles (MOI 4), or *Staphylococcus aureus* bioparticles (MOI 4) for 20 min followed by washing away particles and replacing with RPMI for a further 45 min. **(K)** Immunoblots of AMPK and mTORC1 signaling targets. **(L)** Proposed model: phagocytosis of a broad range of cargo generates a signaling response leading to a transient modification of AMPKα that is only detectable around 1h post initial uptake. This modification affects phosphorylated AMPKα, which can be augmented by preactivation of AMPK either using an allosteric activator, or under nutrient conditions that activate AMPK (low glucose, high AMP levels, etc). Immunoblots are representative of three biological replicates (B,E,H,I,K), or contain three biological replicates on the same blot (F).

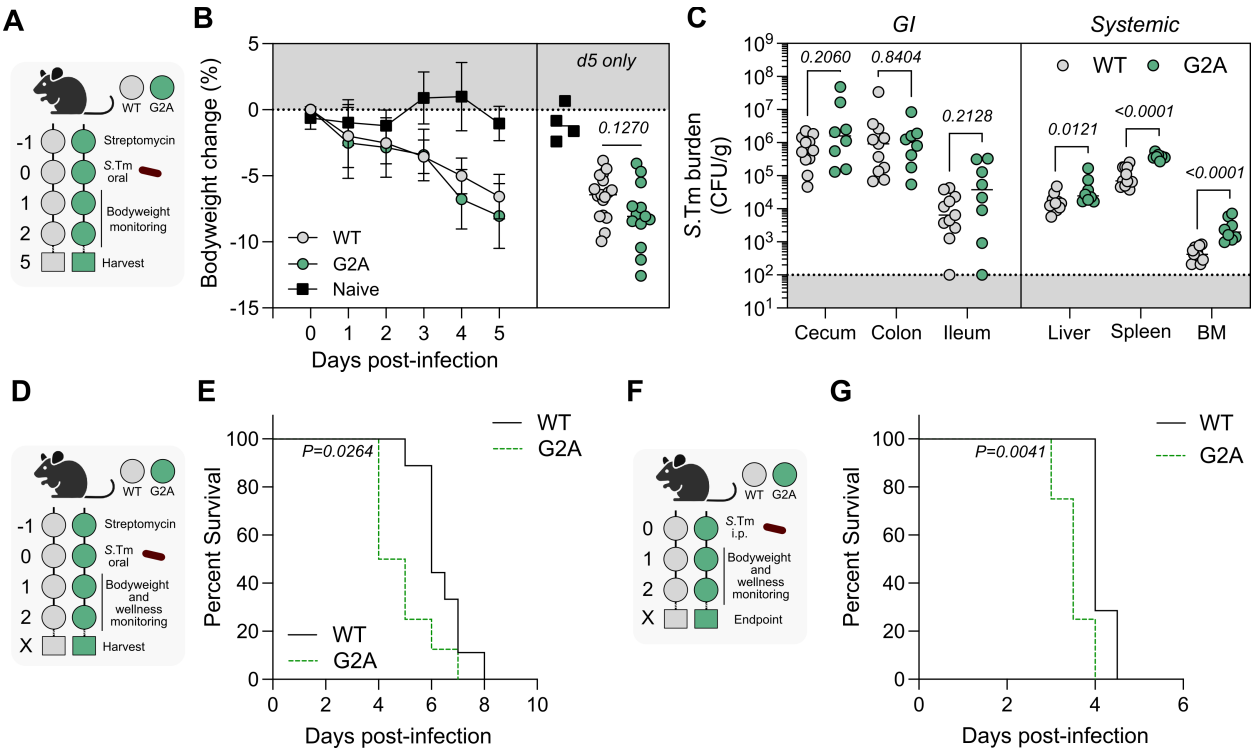

Figure 3.7: Mice lacking AMPK myristoylation have increased *S*.Tm burden in systemic tissues and succumb to infection more rapidly. (A) Schematic of experiment: 6-10 week old WT (n=17 in (B) and n=11 in (C)) or G2A knock-in (n=13 in (B) and n=8 in (C)) mice were gavaged with streptomycin (20 mg) 24h before oral inoculation with *S*.Tm-GFP ($5x10^7$ CFU) or PBS and harvested at day 5. **(B)** Percent change in bodyweight and at harvest on day 5. **(C)** *S*.Tm bacterial burden (CFU/g) in gastrointestinal (cecum, colon, ileum) or systemic (liver, spleen, bone marrow (CFU/leg)) tissues. **(D)** Schematic of experiment: 6-10 week old WT (n=9) or G2A knock-in (n=8) mice were infected as in (A) except that WT *S*.Tm was used instead of *S*.Tm-GFP. Mice were considered at endpoint when reaching either 20% bodyweight loss or a predetermined symptom cutoff. **(E)** Survival curve. **(F)** Schematic of experiment: 6-10 week old WT (n=7) or G2A knock-in (n=8) mice were inoculated intraperitoneally with *S*.Tm ($1x10^4$ CFU). **(G)** Survival curve. Data represented as mean ± SD in (B), individual values with a solid line at the median (B,C), or Kaplan-Meier curves (E,G). *P* values calculated using a one-way ANOVA with Tukey's post-hoc test for (B), an unpaired, two-tailed Mann-Whitney U test for (C), and a two-sided log-rank (Mantel-Cox) test for (E,G). Data are representative of three (B) or two (C,E,G) pooled independent experiments with at least an n=3 per group.

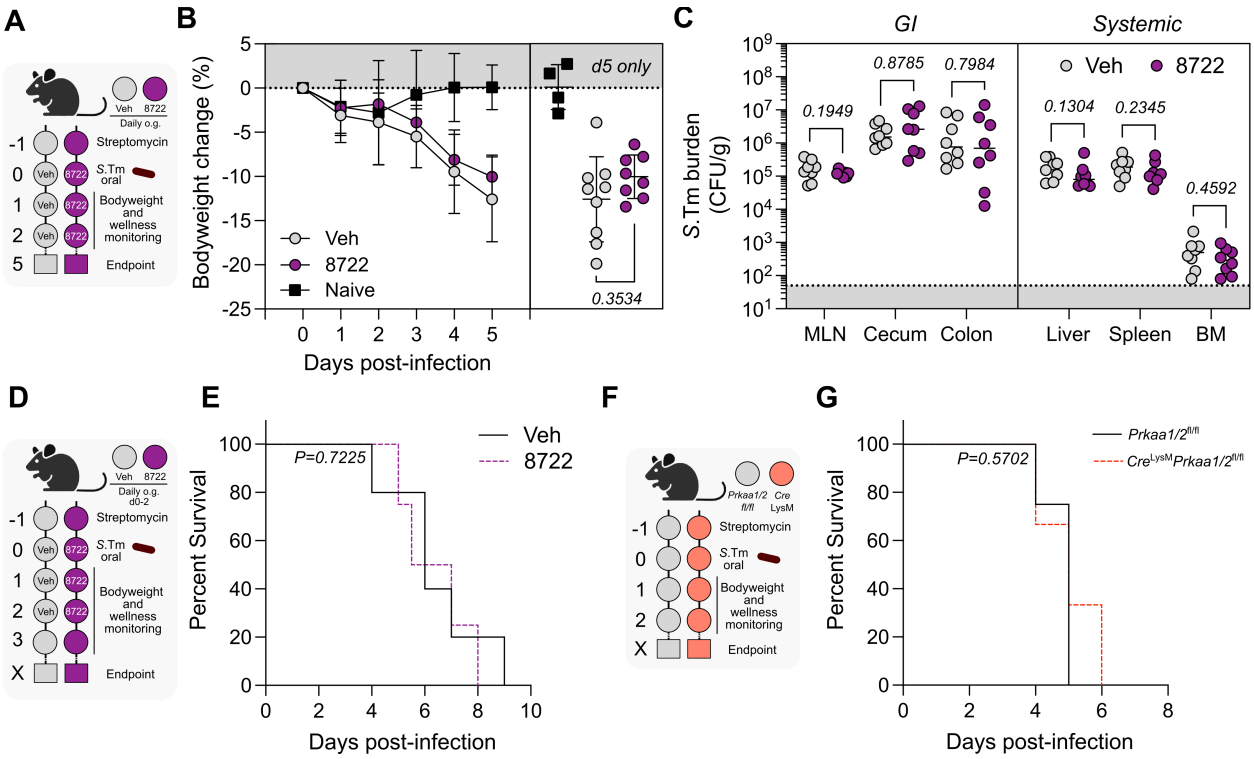

Figure 3.8: Acute pharmacological AMPK activation does not affect S.Tm infection. (A) Schematic of experiment: 6-10 week old WT C57BL/6J mice were gavaged with streptomycin (20 mg) 24h before gavage with MK-8722 (10 mg/kg; n=8) or vehicle (n=9). Three hours later, mice were inoculated with *S*.Tm-GFP ($5x10^7$ CFU) or PBS. MK-8722 treatments were repeated on day 1, 2, and 3 and mice were euthanized on day 5 post-infection. **(B)** Percent change in bodyweight and at harvest on day 5. **(C)** *S*.Tm bacterial burden (CFU/g) in gastrointestinal (mesenteric lymph nodes, cecum, colon) or systemic (liver, spleen, bone marrow (CFU/leg)) tissues. **(D)** Schematic of experiment: 6-10 week old mice were infected as described in (A) with either vehicle (n=5) or MK-8722 (n=4), but with wild-type *S*.Tm and MK-8722 treatments on day 0, 1, and 2. Mice were euthanized when reaching either 20% bodyweight loss or a predetermined symptom cutoff. **(E)** Survival curve. **(F)** Schematic of experiment: 12 week old *Cre*^{LysM}*Prkaa1/2*$^{fl/fl}$ (n=4) or *Prkaa1/2*$^{fl/fl}$ (n=3) were gavaged with streptomycin (20 mg) 24h before oral inoculation with wild-type *S*.Tm ($5x10^7$ CFU). **(G)** Survival curve. Data represented as mean ± SD in (B), individual values with a solid line at the median (B,C), or Kaplan-Meier curves (E,G). *P* values calculated using a one-way ANOVA with Tukey's post-hoc test for (B), an unpaired, two-tailed Mann-Whitney U test for (C), and a two-sided log-rank (Mantel-Cox) test for (E,G). Data are representative of two (B,C) or one (E,G) independent experiment with at least an n=3 per group.

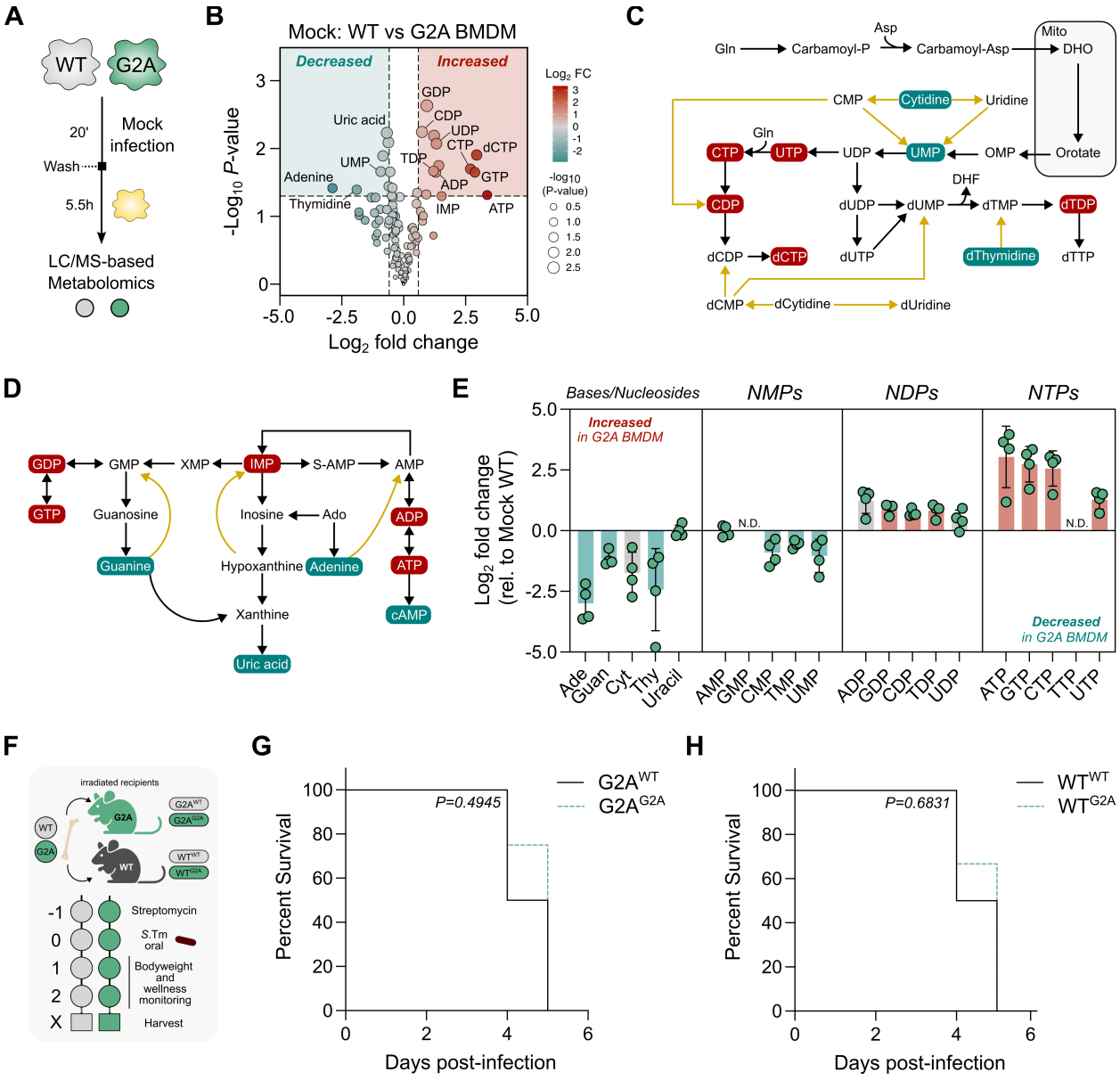

Figure 3.9: The immune compartment does not contribute to G2A infection, despite significant alterations in basal macrophage nucleotide metabolism. (A) Schematic of experiment: WT and G2A BMDM were mock infected for 20 min before washing cells three times with gentamicin-PBS (50 μg/ml) and adding media supplemented with high gentamicin (50 μg/ml) until 6h post infection. **(B)** Volcano plot depicting most altered metabolites between uninfected WT and G2A BMDM. **(C,D)** Schematic of **(C)** pyrimidine and **(D)** purine metabolic pathways, with green and red metabolites signifying significantly lower or higher levels in G2A cells, respectively. Yellow arrows indicate steps involved in nucleotide salvage. **(E)** Log_2 fold change in nucleotide-related metabolites relative to WT cells. **(F)** Schematic of experiment: 7 week old WT (n=7) and G2A (n=8) mice were lethally irradiated with two doses of 4.5 Gy of X-ray radiation before transferring $5x10^6$ whole bone marrow cells from either WT or G2A donors via tail vein injection. Following 8 weeks of recovery, mice were gavaged with streptomycin (20 mg) 24h before oral inoculation with wild-type *S*.Tm ($5x10^7$ CFU). **(G,H)** Survival curves. Data represented as mean ± SD in (E), volcano plot in (B), or Kaplan-Meier curves (G,H). Volcano plot raw *P*-value threshold was set to 0.05 and absolute fold change to 1.25. *P* values calculated using an unpaired, two-tailed Welch's t-test (B,E), or a two-sided log-rank (Mantel-Cox) test for (G,H). Bars highlighted in green or red if $P<0.05$ in (E). Data are representative of one independent experiment with n=3-4 per group.

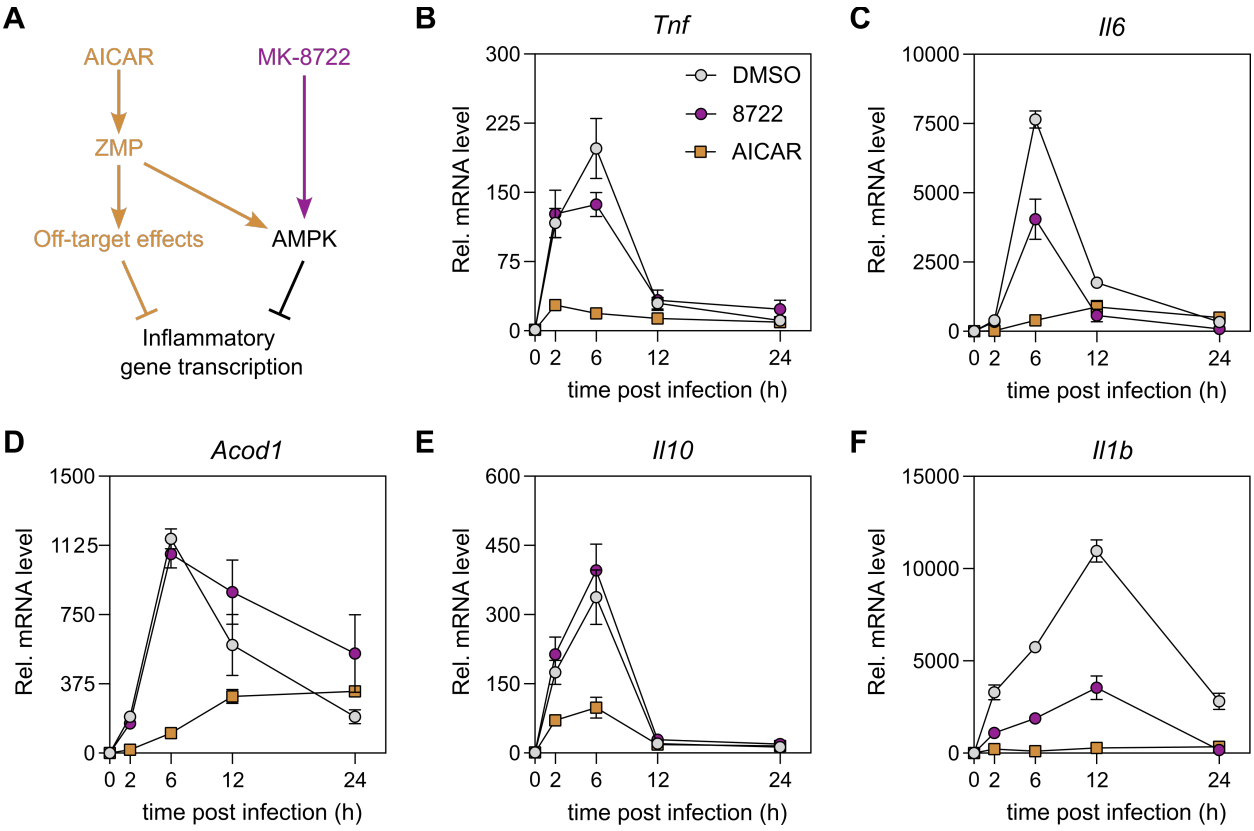

Supplemental Figure 3.1: AMPK activation with AICAR broadly suppresses proinflammatory cytokines at early and late stages of infection. (A) Schematic of AICAR versus MK-8722 mode of activation. **(B-F)** BMDM were activated with MK-8722 (2 μM), AICAR (200 μM), or equivalent DMSO (0.05%) for 15 min prior to spiking in *S*.Tm-GFP (MOI 10), centrifuging the plate, then incubating for 15 min. Cells were washed three times with gentamicin-PBS (50 μg/ml) and media containing MK-8722 or DMSO supplemented with high gentamicin (50 μg/ml) was added for 1.5h before washing the cells again and replacing with low gentamicin media (10 μg/ml) for the indicated times. Relative mRNA expression of **(B)** *Tnf*, **(C)** *Il6*, **(D)** *Acod1*, **(E)** *Il10*, and **(F)** *Il1b* at 2, 6, 12, and 24h post infection. Data represented as mean ± SD. Data are representative of two (DMSO and MK-8722) or one (AICAR) independent experiments. Note: DMSO and MK-8722 conditions are the same as in Figure 3.3.

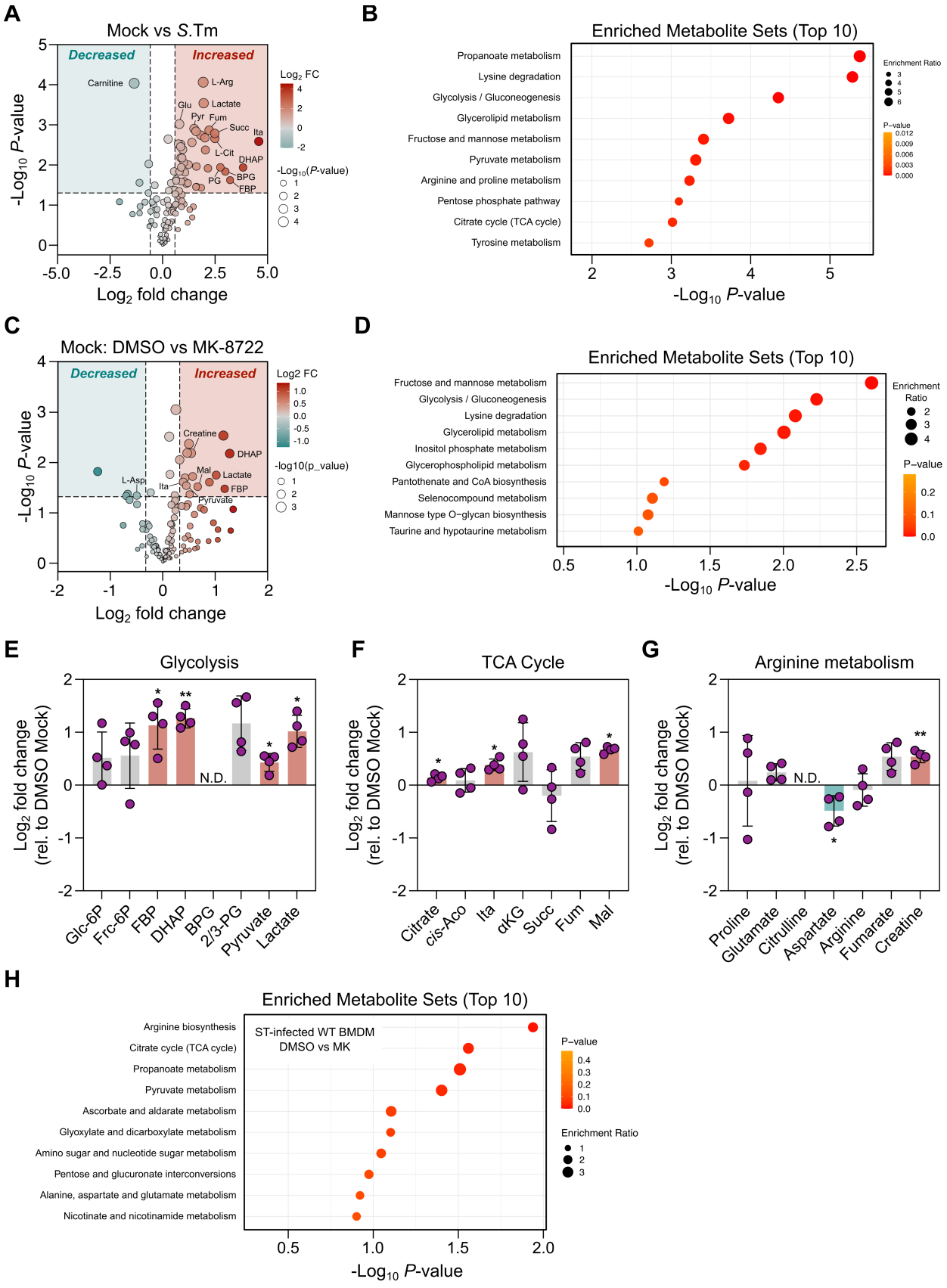
A
Mock vs S.Tm
Decreased
Increased
Carnitine
L-Arg
Glu
Lactate
Pyr
Fum
Succ
Ita
L-Cit
DHAP
PG
BPG
FBP
Log2 FC
-Log10(P-value)
-Log10 P-value
Log2 fold change
B
Enriched Metabolite Sets (Top 10)
Propanoate metabolism
Lysine degradation
Glycolysis / Gluconeogenesis
Glycerolipid metabolism
Fructose and mannose metabolism
Pyruvate metabolism
Arginine and proline metabolism
Pentose phosphate pathway
Citrate cycle (TCA cycle)
Tyrosine metabolism
Enrichment Ratio
P-value
-Log10 P-value
C
Mock: DMSO vs MK-8722
Decreased
Increased
Creatine
DHAP
L-Asp
Ita
Mal
Lactate
FBP
Pyruvate
Log2 FC
-log10(p_value)
-Log10 P-value
Log2 fold change
D
Enriched Metabolite Sets (Top 10)
Fructose and mannose metabolism
Glycolysis / Gluconeogenesis
Lysine degradation
Glycerolipid metabolism
Inositol phosphate metabolism
Glycerophospholipid metabolism
Pantothenate and CoA biosynthesis
Selenocompound metabolism
Mannose type O-glycan biosynthesis
Taurine and hypotaurine metabolism
Enrichment Ratio
P-value
-Log10 P-value
E
Glycolysis
Log2 fold change (rel. to DMSO Mock)
N.D.
Glc-6P
Frc-6P
FBP
DHAP
BPG
2/3-PG
Pyruvate
Lactate
F
TCA Cycle
Log2 fold change (rel. to DMSO Mock)
Citrate
cis-Aco
Ita
αKG
Succ
Fum
Mal
G
Arginine metabolism
Log2 fold change (rel. to DMSO Mock)
N.D.
Proline
Glutamate
Citrulline
Aspartate
Arginine
Fumarate
Creatine
H
Enriched Metabolite Sets (Top 10)
ST-infected WT BMDM
DMSO vs MK
Arginine biosynthesis
Citrate cycle (TCA cycle)
Propanoate metabolism
Pyruvate metabolism
Ascorbate and aldarate metabolism
Glyoxylate and dicarboxylate metabolism
Amino sugar and nucleotide sugar metabolism
Pentose and glucuronate interconversions
Alanine, aspartate and glutamate metabolism
Nicotinate and nicotinamide metabolism
P-value
Enrichment Ratio
-Log10 P-value

Supplemental Figure 3.2: Metabolic effects of *S*.Tm infection and AMPK activation. (A,B) BMDM were infected with *S*.Tm for 20 min before washing cells three times with gentamicin-PBS (50 µg/ml) and replacing with high gentamicin RPMI (50 µg/ml) was added until 6h post infection. **(A)** Volcano plot depicting most altered metabolites between uninfected and infected BMDM. **(B)** KEGG pathway enrichment analysis of most altered metabolite sets for (A). **(C-G)** BMDM were activated with MK-8722 (2 µM) or equivalent DMSO (0.05%) for 30 min prior to repeating conditions as in (A) in the absence of bacteria. **(C)** Volcano plot depicting most altered metabolites between DMSO and MK-8722-treated in uninfected BMDM. **(D)** KEGG pathway enrichment analysis of most altered metabolite sets for (C). Log_2 fold change in **(E)** Glycolytic, **(F)** TCA cycle and **(G)** arginine metabolism metabolites relative to vehicle conditions. **(H)** KEGG pathway enrichment analysis for samples pretreated with either MK-8722 or DMSO and then infected with *S*.Tm for 6h (related to Figure 3.4). Data represented as mean ± SD in (E-G), volcano plot (A,C), or enrichment plot (B,D,H). Volcano plot raw *P*-value threshold was set to 0.05 and absolute fold change to 1.25. *P* values calculated using a paired, two tailed Student's t-test (E-G), where $P<0.05$ = *, $P<0.01$ = **. Data are representative of one independent experiment (n=4 per group).

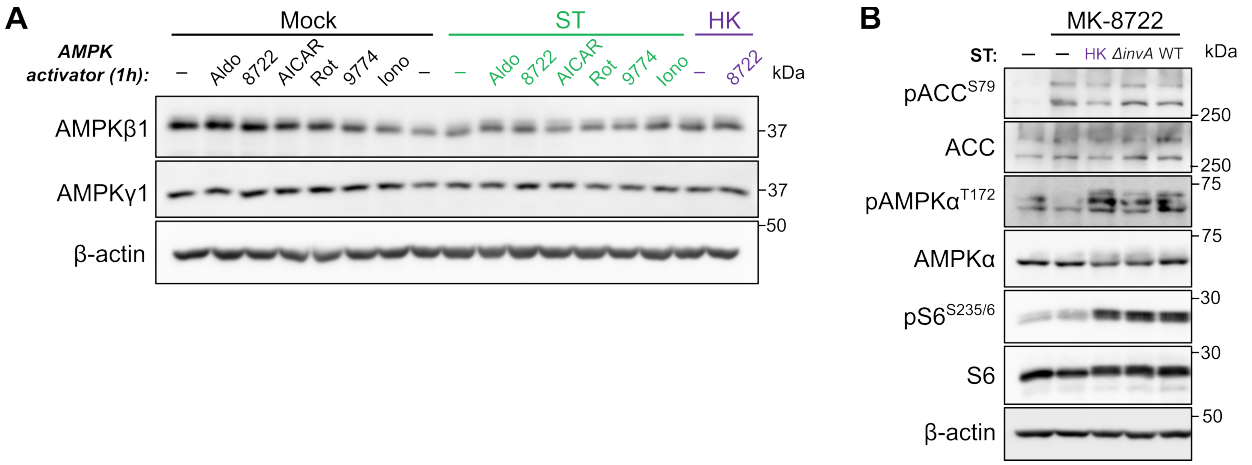

Supplemental Figure 3.3: AMPK modification is specific to the α subunit and does not depend on live virulence mechanisms of *S*.Tm. (A) BMDM were pretreated for 15 min with AMPK activators including aldometanib (5 μM; Aldo), MK-8722 (2 μM; 8722), AICAR (200 μM), rotenone (5 μM; Rot), BI-9774 (10 μM; 9774), and ionomycin (10 μM; Iono). *S*.Tm (MOI 2) or heat-killed *S*.Tm (MOI 2), was spiked in for 20 min, then extracellular bacterial were washed out three times with gentamicin-PBS (50 μg/ml) and media was replaced with RPMI with high gentamicin (50 μg/ml) for a further 45 min. **(B)** Same as in (A), except BMDM were only pretreated with MK-8722 (2 μM), and heat killed *S*.Tm, *ΔinvA S*.Tm, and WT *S*.Tm (all MOI 2) were spiked in for 20 min. Immunoblots are representative of three biological replicates.

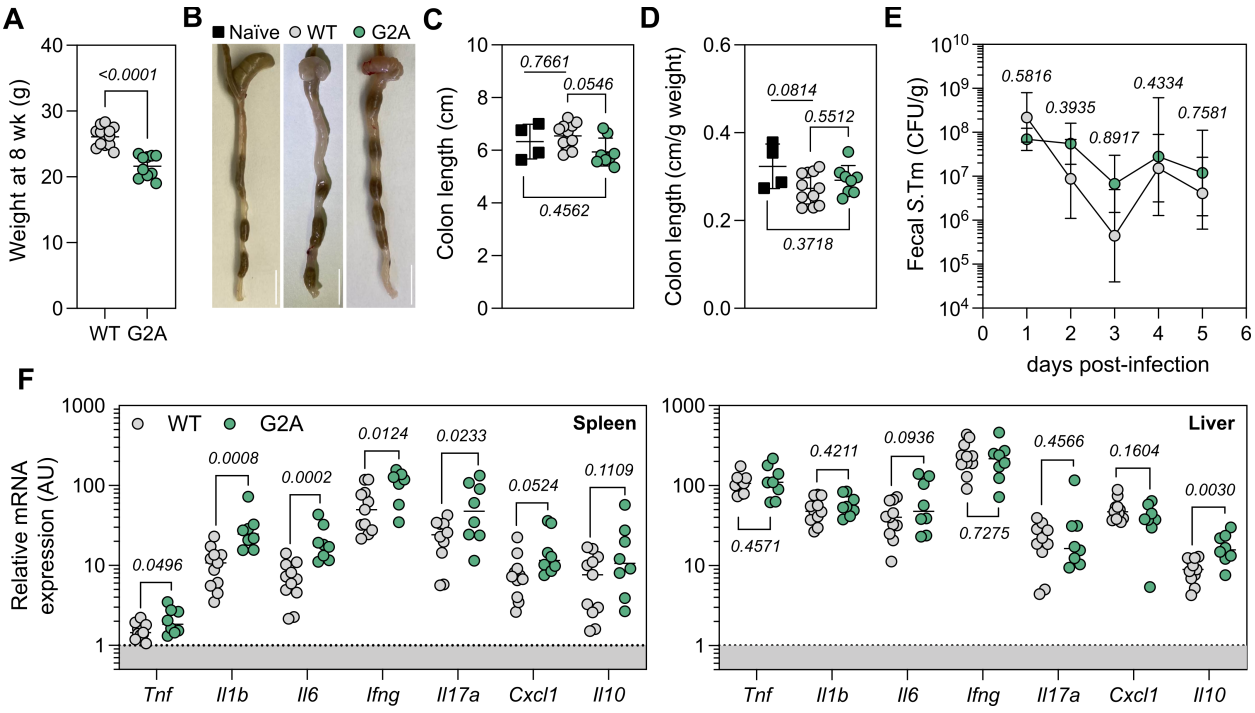

Supplemental Figure 3.4: G2A mice display greater systemic inflammatory indicators. (A) Bodyweights of male G2A mice at 8 weeks of age (n=13 WT and n=10 G2A). **(B-F)** 6-10 week old WT or G2A knock-in mice were gavaged with streptomycin (20 mg) 24h before oral inoculation with *S*.Tm-GFP ($5x10^7$ CFU) or PBS and harvested at day 5. **(B)** Representative images of colon and cecum in naïve and infected mice (scale bar = 1 cm). Colon length in cm **(C)** and normalized to bodyweight **(D)**. **(E)** Fecal *S*.Tm burden by day. **(F)** Relative mRNA levels of inflammatory genes in the spleen (left) and liver (right). Data represented as individual values with mean ± SD in (A,C,D), geometric mean ± geometric SD (E), or individual values with median (F). *P* values calculated using a one-way ANOVA with Tukey's post hoc test (C,D), a mixed-effects model with Sidak's post hoc test (E), an unpaired, two-tailed Mann-Whitney U test (F – spleen: *Il1b*, *Il6*, *Cxcl1*, *Il10*; liver: *Cxcl1*, *Il17a*), and an unpaired, two-tailed Student's t-test (A,F – all other genes). Data are representative of three (A) or two (C-F) pooled independent experiments with at least an n=3 per group.

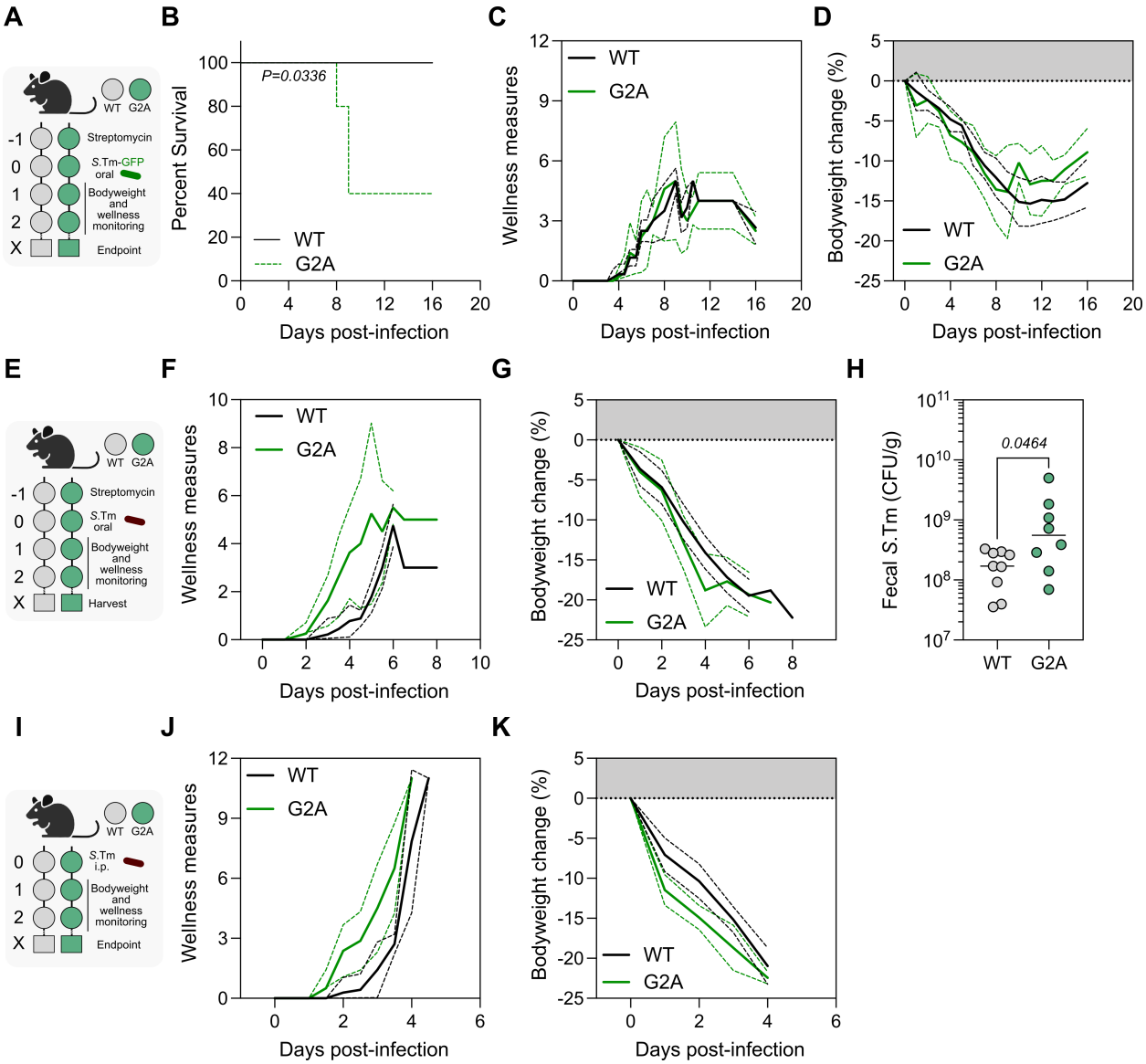

Supplemental Figure 3.5: *S*.Tm induces mortality more rapidly in G2A mice. (A) Schematic of experiment: 6-10 week old WT (n=6) and G2A knock-in (n=5) mice were gavaged with streptomycin (20 mg) 24h before gavage with *S*.Tm-GFP ($5x10^7$ CFU) or PBS. Bodyweights and wellness measures were recorded daily until reaching either 20% bodyweight loss or a predetermined wellness cutoff. **(B)** Survival curve, **(C)** wellness measures, and **(D)** percent change in bodyweight. **(E)** Schematic of experiment: same as in (A), WT (n=9) and G2A (n=8) mice were inoculated with wild-type *S*.Tm ($5x10^7$ CFU). **(F)** Wellness measures, **(G)** percent change in bodyweight, and **(H)** fecal *S*.Tm 24h after inoculation. **(I)** Schematic of experiment: WT (n=7) or G2A (n=8) mice were inoculated intraperitoneally with *S*.Tm ($1x10^4$ CFU). **(J)** Wellness measures, or **(K)** percent change in bodyweight. Data represented as Kaplan-Meier curves (B), curves representing mean (thick lines) ± SD (dotted lines) (C,D,F,G,J,K), or individual values with median (H). *P* values calculated using a two-sided log-rank (Mantel-Cox) test for (B), or an unpaired, two-tailed Mann-Whitney U test (H). Data are representative of one (A-D) or two (E-K) independent experiments.

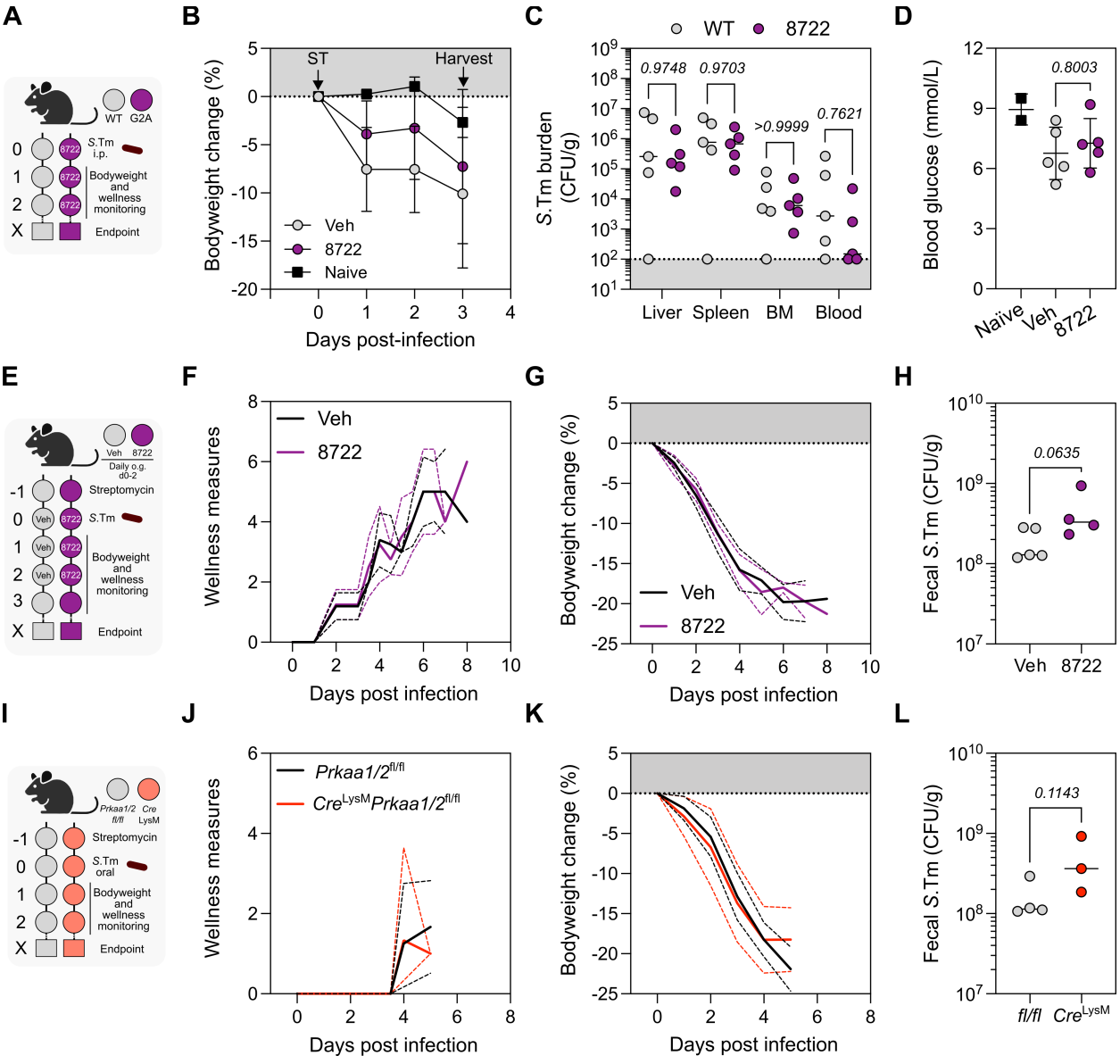

Supplemental Figure 3.6: Systemic MK-8722 administration or myeloid AMPK signaling has minimal effect on survival. (A) Schematic of experiment: 10-12 week old WT mice were administered intraperitoneally MK-8722 (10 mg/kg; n=5)) or vehicle (n=5) 3h before inoculation with *S*.Tm-GFP ($1x10^4$ CFU). **(B)** Percent change in bodyweight. **(C)** *S*.Tm burden by tissue, where BM is in CFU/hind limb and blood is in CFU/ml. **(D)** Blood glucose at endpoint. **(E)** Schematic of experiment: 9-12 week old WT mice were gavaged with streptomycin (20 mg) 24h before gavage with MK-8722 (10 mg/kg; n=5) or vehicle (n=4). Three hours later, mice were inoculated with *S*.Tm ($5x10^7$ CFU) or PBS. MK-8722 treatments were repeated on day 1 and 2, and mice were euthanized at humane endpoint. Bodyweights and wellness measures were recorded daily until reaching either 20% bodyweight loss or a predetermined wellness cutoff. **(F)** Wellness measures, **(G)** percent change in bodyweight, and **(H)** *S*.Tm burden in feces 24h after infection. **(I)** Schematic of experiment: *Prkaa1/2*$^{fl/fl}$ (n=4) or *Cre*^{LysM}*Prkaa1*$^{fl/fl}$ mice (n=3) were infected as in (A). **(J)** Wellness measures, **(K)** percent change in bodyweight, and **(L)** *S*.Tm burden in feces 24h after infection. Data represented as mean ± SD (B), individual values and mean ± SD (D), individual values and median (C,H,L), or curves representing mean (thick lines) ± SD (dotted lines) (F,G,J,K). *P* values calculated using an unpaired, two-tailed Mann-Whitney U test (C,H,L) or a one-way ANOVA with Tukey's post hoc test (D). Data are representative of one independent experiment.

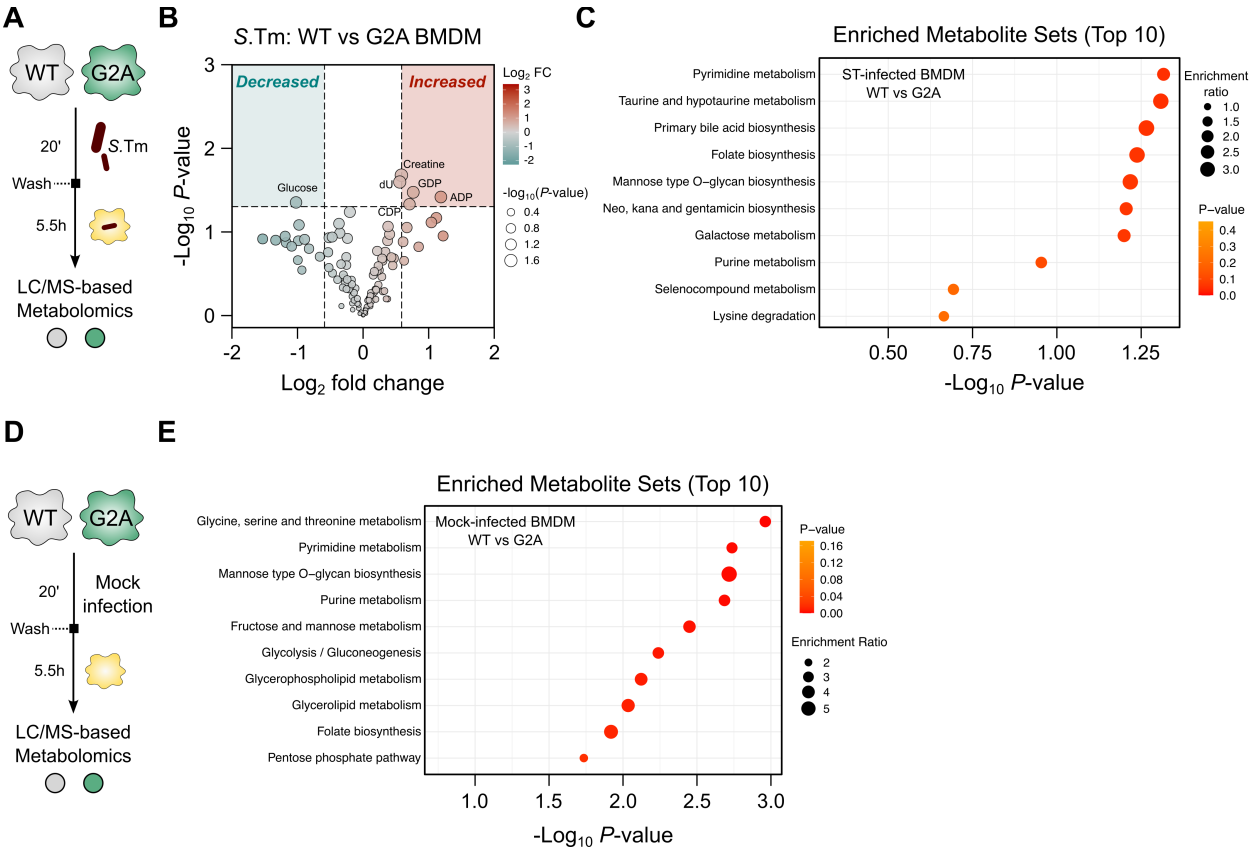

Supplemental Figure 3.7: Additional infection severity measures for AMPK activity-modulating cohorts. (A) Schematic of experiment: WT and G2A BMDM were infected with S.Tm for 20 min before washing cells three times with gentamicin-PBS (50 µg/ml) and adding media supplemented with high gentamicin (50 µg/ml) until 6h post infection. **(B)** Volcano plot depicting most altered metabolites between infected WT and G2A BMDM. **(D)** KEGG pathway enrichment analysis of most altered metabolite sets for (B). **(D)** Schematic of experiment: same as in (A), but in the absence of *S*.Tm. **(E)** KEGG pathway enrichment analysis of most altered metabolite sets between uninfected WT and G2A BMDM. Data represented as a volcano plot (B), or enrichment plot (C,E). Volcano plot raw *P*-value threshold was set to 0.05 and absolute fold change to 1.25. *P* values calculated using an unpaired, two-tailed Welch's t-test (B). Data are representative of one independent experiment (n=4).

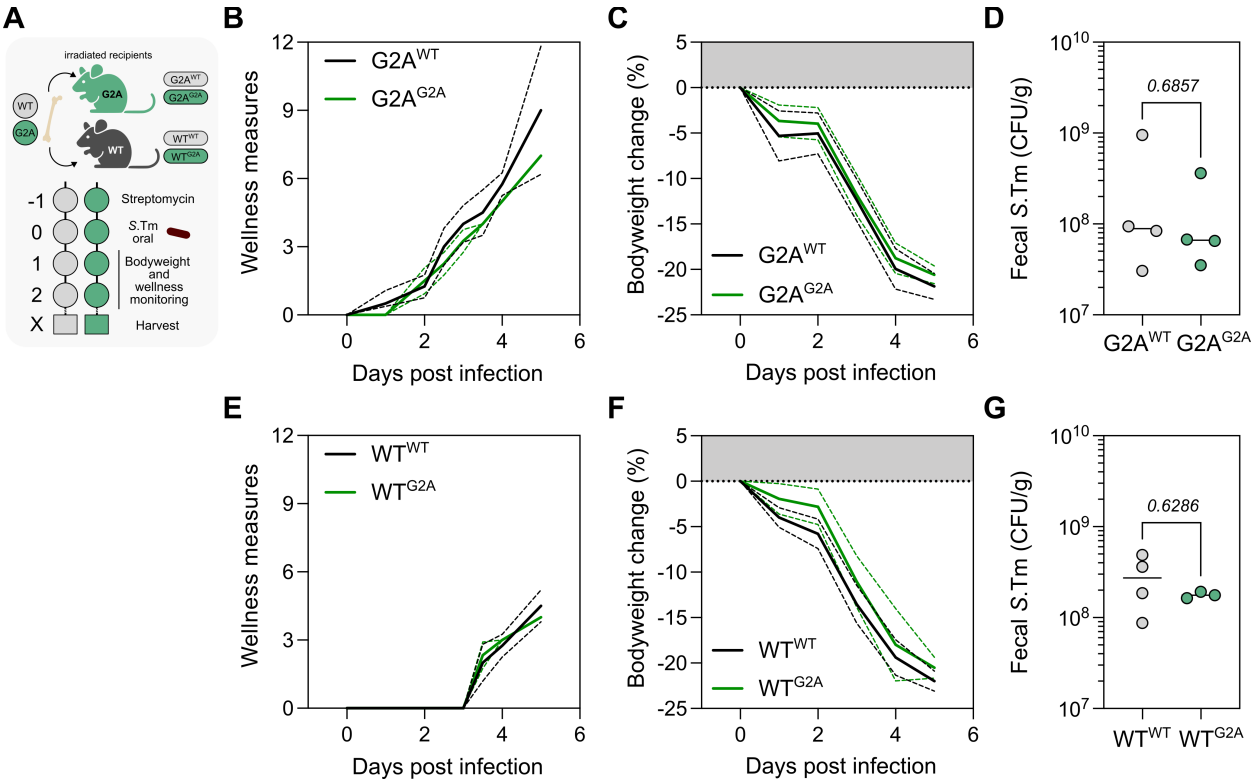

Supplemental Figure 3.8: Circulating immune cells do not significantly contribute to the response to *S*.Tm. (A) Schematic of experiment: 7 week old WT (n=7) and G2A (n=8) mice were lethally irradiated with two doses of 4.5 Gy of X-ray radiation before transferring $5x10^6$ whole bone marrow cells from either WT or G2A donors via tail vein injection. Following 8 weeks of recovery, mice were gavaged with streptomycin (20 mg) 24h before oral inoculation with wild-type *S*.Tm ($5x10^7$ CFU). **(B,E)** Wellness measures, **(C,F)** percent change in bodyweight, **(D,G)** *S*.Tm burden in feces 24h after infection. Data represented as individual values and median (D,G), or curves representing mean (thick lines) ± SD (dotted lines) (B,C,E,F). *P* values calculated using an unpaired, two-tailed Mann-Whitney U test (D,G). Data are representative of one independent experiment.

Table 3.1: Metabolite changes in uninfected versus infected cells.

Increased Metabolites	P value[a]	Fold Change	log_2FC
L-Arginine	8.86E-05	3.7915	1.9228
Lactic acid	0.0003	3.8494	1.9446
Glutamic acid	0.0010	1.7380	0.7974
Pyruvic acid	0.0013	2.8139	1.4925
Fumaric acid	0.0014	4.6126	2.2056
Uracil	0.0015	2.9959	1.5830
Succinic acid	0.0017	5.5417	2.4703
Malic acid	0.0018	3.5069	1.8102
4-Hydroxyproline	0.0021	4.0126	2.0045
Citrulline	0.0022	5.5632	2.4759
Creatine	0.0023	1.2004	0.2635
Itaconic acid	0.0026	23.5301	4.5564
Homocitric acid	0.0028	2.6214	1.3904
Pantothenic acid	0.0030	1.6809	0.7492
Isoleucine	0.0031	1.8177	0.8621
UDP-glucuronic acid	0.0036	1.8107	0.8565
Oxoglutaric acid	0.0042	1.9383	0.9548
Aminoadipic acid	0.0043	4.0787	2.0281
Pyroglutamic acid	0.0067	1.8147	0.8597
D-Ribose 5-phosphate	0.0068	1.8939	0.9213
2-Hydroxyglutarate	0.0089	2.0033	1.0024
Erythronic acid	0.0099	2.3411	1.2272
Glyceric acid	0.0110	3.0310	1.5998
L-Valine	0.0115	1.8459	0.8843
Phosphoglyceric acid	0.0116	6.6631	2.7362
Dihydroxyacetone phosphate	0.0116	14.0634	3.8139
2-deoxy-D-ribose	0.0122	4.4290	2.1470
Methionine	0.0145	1.4521	0.5382
Bisphosphoglyceric acid	0.0147	7.8499	2.9727
Serine	0.0147	1.7447	0.8030
D-Ribulose 5-phosphate	0.0154	2.0896	1.0633
Glutathione	0.0231	1.5615	0.6430
Fructose-1,6-bisphosphate	0.0240	9.1758	3.1978
UDP-glucose	0.0248	1.5612	0.6426
L-Dihydroorotic acid	0.0254	2.0525	1.0373
Nicotinamide riboside	0.0261	1.8511	0.8884
S-Adenosylhomocysteine	0.0284	1.3117	0.3914
Oxidized glutathione	0.0284	2.2966	1.1995
Fructose-6-phosphate	0.0300	2.1847	1.1274
Orotic acid	0.0348	3.0333	1.6009
Xylulose 5-phosphate	0.0353	2.9974	1.5837

Proline	0.0371	3.5477	1.8269
L-Alanine	0.0412	1.4901	0.5754
Leucine	0.0435	1.2235	0.2910
Glucose	0.0441	1.7275	0.7887
Decreased Metabolites	P value[a]	Fold Change	log_2FC
L-Carnitine	9.41E-05	0.3933	-1.3463
Uric acid	0.0095	0.6351	-0.6550
TMP	0.0279	0.4681	-1.0952
Alanylglutamine	0.0322	0.7727	-0.3720

[a]*P* values calculated using a paired, two-tailed Welch's t-test.

Table 3.2: Metabolite changes in uninfected BMDM treated with MK-8722.

Increased Metabolites	P value[a]	Fold Change	log_2FC
UDP	0.0009	1.1883	0.2489
Erythronic acid	0.0030	2.2204	1.1508
Hypotaurine	0.0032	1.0890	0.1230
L-Alanine	0.0044	1.4116	0.4973
4-Hydroxyproline	0.0068	1.3796	0.4643
Creatine	0.0068	1.4541	0.5402
Dihydroxyacetone phosphate	0.0069	2.4123	1.2704
L-Carnitine	0.0092	1.2492	0.3210
Citric acid	0.0180	1.0992	0.1364
Lactic acid	0.0186	2.0204	1.0146
2-Hydroxyglutarate	0.0198	1.4819	0.5674
Aminoadipic acid	0.0211	1.3409	0.4233
Itaconic acid	0.0255	1.3081	0.3874
Glyceric acid	0.0257	1.8473	0.8855
Pyruvic acid	0.0301	1.3629	0.4467
Malic acid	0.0316	1.5832	0.6628
Fructose-1,6-bisphosphate	0.0348	2.2578	1.1749
Pantothenic acid	0.0450	1.4249	0.5108
Glutamic acid	0.0468	1.1711	0.2279
Decreased Metabolites	P value[a]	Fold Change	log_2FC
Hypoxanthine	0.0158	0.4252	-1.2339
Glutathione	0.0413	0.8531	-0.2292
Deoxyribose 5-phosphate	0.0438	0.6305	-0.6654
L-Aspartic acid	0.0478	0.7110	-0.4921
Guanine	0.0485	0.6184	-0.6934

[a]*P* values calculated using a paired, two-tailed Welch's t-test.

Table 3.3: Metabolite changes in infected BMDM with MK-8722 treatment.

Increased Metabolites	P value[a]	Fold Change	log_2FC
Citrulline	0.0017	1.9254	0.9451
D-Ribose 5-phosphate	0.0449	1.3322	0.4138
Fructose-6-phosphate	0.0234	1.2824	0.3588
N-Acetylserine	0.0373	1.2113	0.2766
4-Hydroxyproline	0.0012	1.1824	0.2417
Decreased Metabolites	P value[a]	Fold Change	log_2FC
Citric acid	0.0008	0.7184	-0.4772
Malic acid	0.0045	0.6438	-0.6353
Succinic acid	0.0053	0.6993	-0.5161
Orotic acid	0.0057	0.6602	-0.5990
Fumaric acid	0.0060	0.7267	-0.4606
Deoxyribose 5-phosphate	0.0077	0.8039	-0.3150
L Arginine	0.0103	0.7948	-0.3313
UDP-glucose	0.0213	0.8141	-0.2967
L-Aspartic acid	0.0238	0.6889	-0.5376
UDP-glucuronic acid	0.0266	0.7322	-0.4496
Xanthine	0.0317	0.5342	-0.9046
Homocitric acid	0.0324	0.8107	-0.3028
NAD	0.0419	0.8190	-0.2881

[a]*P* values calculated using a paired, two-tailed Welch's t-test.

Table 3.4: Metabolite changes in uninfected WT versus G2A BMDM.

Increased Metabolites	P value[a]	Fold Change	log_2FC
GDP	0.0023	1.9047	0.9295
CDP	0.0057	1.6566	0.7283
Carnosine	0.0064	2.3230	1.2160
UTP	0.0084	2.4879	1.3149
dCTP	0.0124	7.6227	2.9303
Dihydroxyacetone phosphate	0.0177	2.6569	1.4097
CTP	0.0199	6.3963	2.6772
TDP	0.0214	2.2905	1.1956
GTP	0.0223	7.2524	2.8585
ADP	0.0224	2.4421	1.2881
Creatine	0.0448	1.4534	0.5394
IMP	0.0473	1.8692	0.9024
ATP	0.0483	10.1987	3.3503
Decreased Metabolites	P value[a]	Fold Change	log_2FC
Uric acid	0.0058	0.6256	-0.6768
L-Threonine	0.0081	0.6526	-0.6157
CMP	0.0128	0.5599	-0.8366
UMP	0.0218	0.5273	-0.9233
TMP	0.0219	0.6823	-0.5515
Acetylglycine	0.0359	0.6574	-0.6051
Xanthosine	0.0378	0.7286	-0.4567
Adenine	0.0382	0.1373	-2.8650
Thymidine	0.0403	0.2694	-1.8922
Serine	0.0493	0.7145	-0.4849

[a]*P* values calculated using an unpaired, two-tailed Welch's t-test.

Table 3.5: Metabolite changes in infected WT versus G2A BMDM.

Increased Metabolites	P value[a]	Fold Change	log_2FC
ADP	0.0384	2.2661	1.1802
GDP	0.0338	1.6942	0.7606
CDP	0.0468	1.6290	0.7040
Creatine	0.0211	1.4957	0.5808
Deoxyuridine	0.0254	1.4701	0.5560
Decreased Metabolites	**P value[a]**	**Fold Change**	**log_2FC**
Glucose	0.0446	0.4940	-1.0173

[a]*P* values calculated using an unpaired, two-tailed Welch's t-test.

Supplemental Table 3.1: Antibodies and dyes.

Antibody	Source	Company	CAT
ACC	Rabbit	Cell Signaling Technology	3662
pACC-S79	Rabbit	Cell Signaling Technology	3661
AMPKα	Rabbit	Cell Signaling Technology	2532
pAMPKα-T172	Rabbit	Cell Signaling Technology	2535
S6	Rabbit	Cell Signaling Technology	2217
pS6-S235/236	Rabbit	Cell Signaling Technology	2211
β-actin	Rabbit	Cell Signaling Technology	5125
AMPK β1/2	Rabbit	Cell Signaling Technology	4150
AMPK γ1	Rabbit	Abcam	ab32508
Zombie aqua	N/A	BioLegend	423101

Supplemental Table 3.2: Primers used in RT-qPCR.

Target (mouse)	Forward (5'-3')	Reverse (5'-3')
Tnf	CCCTCACACTCAGATCATCTTCT	GCTACGACGTGGGCTACAG
Il1b	GCAACTGTTCCTGAACTCAACT	ATCTTTTGGGGTCGGTCAACT
Il6	TAGTCCTTCCTACCCCAATTTCC	TTGGTCCTTAGCCACTCCTTC
Il12b	AGCACTAGTTTCAACACCAAGAAA	CCCAGCCTTTCAAAATTCTTT
Edn1	TCCTTGATGGACAAGGAGTGT	CCCAGTCCATACGGTACGA
Nfkbiz	TATCGGGTGACACAGTTGGA	TGAATGGACTTCCCCTTCAG
Il10	GCTCTTACTGACTGGCATGAG	CGCAGCTCTAGGAGCATGTG
Acod1	GCAACATGATGCTCAAGTCTG	TGCTCCTCCGAATGATACCA
Nos2	TACTGAGACAGGGAAGTCTGAA	AGTAGTTGCTCCTCTTCCAAGGT
Ass1	ACACCTCCTGCATCCTCGT	GCTCACATCCTCAATGAACACCT
Cxcl9	TGAAATCATTGCTACACTGAAG	TTTGGCTGATCTTCTTTTCCCA
Ifng	ATGAACGCTACACACTGCATC	CCATCCTTTTGCCAGTTCCTC
Il17a	TTTAACTCCCTTGGCGCAAAA	CTTTCCCTCCGCATTGACAC
Cxcl1	ATGGCTGGGATTCACCTCAAG	ACTTGGGGACACCTTTTAGCA
Hprt1	TCAGTCAACGGGGGACATAAA	GGGGCTGTACTGCTTAACCAG

3.8 Acknowledgments

We gratefully acknowledge the support and services provided by the University of Ottawa Flow Cytometry and Virometry Core (RRID:SCR_023306), the Louise Pelletier Histology Core, Animal Care and Veterinary Services, and the University of Ottawa Metabolomics Core Facility, which is supported by the Terry Fox Foundation and the University of Ottawa. Figures were created in part using BioRender.com. The authors would like to apologize to colleagues whose significant work could not be included due to length, citation limitations, or author oversight.

Conflicts of Interest: The authors declare no competing interests.

Chapter 4: AMPK myristoylation affects its protein stability

4.1 Preface

This chapter includes unpublished work that will be combined with data contained in Chapter 3 for publication.

Tyler K.T. Smith[1,2,4], Lara Abou-Chakra[1,2], Sandra Galic[5,6,7], Bruce E. Kemp[5,6,7], Morgan D. Fullerton[1,2,3,4]

Affiliations

[1]Department of Biochemistry, Microbiology and Immunology, Faculty of Medicine, University of Ottawa, Ottawa, ON, Canada

[2]Centre for Infection, Immunity and Inflammation, Ottawa ON, Canada

[3]Centre for Catalysis Research and Innovation, Ottawa ON, Canada

[4]Ottawa Institute of Systems Biology, Ottawa, ON, Canada

[5]Protein Chemistry and Metabolism, St. Vincent's Institute of Medical Research; Fitzroy, Australia

[6]Mary MacKillop Institute for Health Research, Australian Catholic University; Melbourne, Australia

[7]Department of Medicine, University of Melbourne; Melbourne, Australia.

CEediT Authorship Statement

Tyler K.T. Smith: Conceptualization, Methodology, Validation, Formal analysis, Investigation, Visualization. **Lara Abou-Chakra:** Investigation. **Sandra Galic:** Methodology, Resources.

Bruce E. Kemp: Methodology, Resources. **Morgan D. Fullerton:** Conceptualization, Resources, Supervision, Funding acquisition.

4.2 Abstract

Background and Aims

AMPK is a multifaceted regulator of metabolism that requires time and localization-dependent signaling to transmit nutrient cues. Myristoylation describes the attachment of a 14-carbon fatty acid chain to glycine residues of target proteins and can affect subcellular localization and function. The β subunits are myristoylated at the N-terminal glycine residues (G2) by the enzyme NMT1. Myristoylation has been shown to affect AMPK subcellular localization and activity, as well as its protein stability, though the latter effect remains understudied. We interrogated the impact of known protein stability regulators using pharmacological and genetic models reducing endogenous AMPK myristoylation.

Methods

WT and AMPK β1/β2 G2A knock-in mouse embryonic fibroblasts (MEFs) and mice, which lack the AMPK myristoylation site, were used to investigate protein stability parameters of AMPK.

Results

Cells either expressing a non-myristoylatable version of AMPK β or treated with the myristoyltransferase inhibitor IMP-1088 had reduced protein levels of AMPK subunits, particularly the γ subunit without affecting mRNA levels. Subsequent treatment with the proteasome inhibitor MG132 or translation inhibitor cycloheximide failed to consistently alter AMPK protein levels. siRNA-mediated knockdown of proposed myristoylation-dependent E3

ubiquitin ligases ZYG11B and ZER1 had no effect on AMPK protein subunit level. In G2A mice, protein levels were significantly lower and differed depending on tissue type.

Conclusions

It remains unclear which mechanism generates faster turnover of AMPK protein levels when non-myristoylated. However, our results suggest that previously suspected ubiquitin proteasome regulators are not key players in myristoylation-dependent AMPK protein stability.

4.3 Introduction

AMPK signaling is dependent on time, space, and protein abundance. Myristoylation is a co- or post-translational modification in which a 14-carbon fatty acid chain is attached to N-terminal glycine residues[87]. The AMPK β subunits are myristoylated by the enzyme N-myristoyltransferase 1 (NMT1) in a co-translational manner[43,88], and affects AMPK responsiveness to low glucose levels[103] and ADP[54], as well as its physical localization to the lysosome[103] and mitochondria[91], though not the Golgi[537]. However, multiple groups have observed AMPK subunit levels being lower in cells and mice lacking AMPK myristoylation[43,91,92], the mechanism of which remains unknown.

Proteostasis describes the combined mechanisms leading to a protein level at a given time in a cell. Certain processes such as transcription and translation contribute to protein addition, while degradative processes such as the UPS and autophagy contribute to reduced protein levels. The UPS depends on ubiquitination as a post-translational modification for covalent attachment to lysine residues[557]. This is facilitated by a series of three enzyme classes that catalyze ubiquitin activation (E1), transfer (E2), and ligation (E3). Various branches of ubiquitin chains can dictate the fate of the ubiquitinated protein, where K48-linked chains typically result in degradation in the 26S proteasome[558].

Within the UPS, several substrate receptors for the cullin 2-RING E3 ubiquitin ligase (CRL2) including zyg-11 family member B (ZYG11B) and zyg-11 homolog B-like protein (ZER1) recognize and target non-myristoylated proteins for degradation as a result of exposed N-terminal glycine residues[559]. Additionally, numerous E3[171,174–182] ubiquitin ligases and E2[172] enzymes have been shown to ubiquitinate AMPK and target various subunits for degradation. However, their relevance in the context of regulating non-myristoylated AMPK protein levels is unknown.

Using mice and MEFs harbouring a glycine-to-alanine point mutation at the myristoylation site (G2A) on AMPK β1 and β2 subunits, we have interrogated how myristoylation influences AMPK subunit protein stability. We report that G2A MEFs and various tissues exhibit a 50% reduction in steady state protein levels of the AMPK subunits, though the $\gamma 1$ subunit appears to be the most sensitive. These changes are likely not due to changes in heterotrimer assembly or transcription and may be ubiquitin-dependent. We do not report convincing evidence for ZYG11B and ZER1 being regulators of non-myristoylated AMPK. This work highlights the importance of AMPK myristoylation beyond its regulation of activity and subcellular localization.

4.4 Materials and Methods

Mouse embryonic fibroblast generation and culture

MEFs from WT and G2A mice were generated as previously described[92]. Briefly, MEFs were isolated from homozygous WT, β1-G2A KI, β2-G2A KI or β1/β2-G2A DKI embryos. The head and internal organs were removed, and the remaining embryo body minced and trypsinized. Cells were centrifuged in 10% FBS/DMEM (500 g, 5 min, 4°C) and medium replaced and the cell suspension was passed through a 40-µm cell strainer and plated in 10-cm dishes. Cells were cultured in DMEM supplemented with 10% FBS and 1% penicillin-streptomycin and passaged at 1:2 or 1:4 when confluent. MEFs were immortalized by transfection with an SV40 large T-antigen expression construct using Fugene HD transfection reagent (Promega).

SDS-PAGE and western blotting

Total cellular lysates were collected by adding 8.33 µl/cm^2 western lysis buffer (0.5% Triton X-100; 0.5% NP-40; 50 mM Tris-HCl, pH 7.5; 150 mM NaCl; 1 mM EDTA; protease inhibitor cocktail, EDTA-free (Roche #11697498001)) and transferring lysate to pre-chilled 1.5 ml tubes. Lysates were then clarified at 14,000 *x g* for 20 minutes at 4°C. After transferring supernatants to new tubes, lysate protein concentrations were determined by bicinchoninic acid (BCA) assay (Thermo Fisher #23225) according to the manufacturer's protocol. Lysate protein concentration was then equalized using western lysis buffer before adding 6X SDS loading buffer (300 mM Tris-HCl, pH 6.8; 600 mM DTT; 12% SDS; 0.6% bromophenol blue; 60% glycerol). The samples were then boiled at 95 ºC for 5 minutes and stored at -20 ºC. For SDS-PAGE, 8 – 15% polyacrylamide resolving (375 mM Tris-HCl, pH 8.8; 0.1% SDS; 0.05% TCE) and 5% stacking (130 mM Tris-HCl, pH 6.8; 0.1% SDS) gels were made in-house the day before sample running. Samples in 1X SDS loading buffer or Protein Ladder (Bio-Rad #1610374) were loaded into 10-

or 15-well gels and run at 110V. The proteins were transferred to methanol-activated PVDF (Bio-Rad #1620177) using the TransBlot system (BioRad) in Turbo Buffer (48 mM Tris; 39 mM glycine; 20% methanol) for 20 minutes at 25V. Membranes were then blocked in 5% BSA (BioShop #ALB001) in TBS-T (20 mM Tris; 150 mM NaCl; 0.1% volume fraction Tween-20) for 1 hour, before distributing membranes into appropriate primary antibody dishes for overnight incubation at 4 ºC with gentle rocking (all antibodies diluted 1:1000 in 5% BSA in TBS-T; listed in Supplemental Table 4.1). The next day, membranes were washed 4X with TBS-T and then incubated with HRP-conjugated rabbit IgG secondary antibody (Cell Signaling Technology #7074S; 1:10000 in 5% BSA in TBS-T) for 1 hour at RT. The membranes were again washed 4X with TBS-T and then blots were activated with Clarity Western ECL substrate (Bio-Rad #1705061) before being imaged on the LAS ImageQuant 4000.

RNA isolation, cDNA synthesis, and RT-qPCR.

Cells were treated as described and washed once with PBS before adding 115 µl/cm^2 TriPure RNA isolation reagent (Roche #11667165001). RNA isolation was carried out according to the manufacturer's instructions with all centrifugation steps at 4°C. RNA concentration and quality (A260/280) was measured using the Take3 Plate (Agilent #TAKE3-SN) on the Synergy H1 Plate Reader (BioTek). RNA concentration was equalized using DNase/RNase free H_2O, after which 300-400 ng of RNA was transferred to 8-strip PCR tubes (Diamed #DIATEC420-1378) and reverse transcribed into cDNA using the All-in-One 5X RT Master Mix (Applied Biological Materials #G592) in a T100 thermal cycler (Bio-Rad). Synthesized cDNA was diluted to a final concentration of ~2.5 ng/µl in DNase/RNase free H_2O such that each qPCR reaction contained ~10 ng of cDNA. qPCR was performed using the BlasTaq 2X qPCR MasterMix (Applied Biological Materials #G891) according to manufacturers instructions. Relative expression was

calculated with the $^{\Delta\Delta}$Ct method using *Hprt1* as a housekeeping gene. Primer sequences are listed in Supplemental Table 4.2.

siRNA knockdown

Silencer Select siRNA stocks (Thermo Fisher #4390771) for respective targets were diluted to 20X in Opti-MEM (Thermo Fisher #31985062) then mixed 1:1 with 20X Lipofectamine RNAiMAX (Thermo Fisher #13778075) and incubated at room temperature for 5 min. For 6 well plates, 200 µl of 10X siRNA-liposome mix was added per well and incubated for 24h at 37°C.

Immunoprecipitation

Protein A Dynabeads (Thermo Fisher #10001D) were prewashed three times using cold western lysis buffer. The beads were then distributed to tubes, where 3 µl of mouse anti-AMPKβ1 (Signalway #27201) or isotype control IgG2a were added. After 5 min at RT, 200 µg of lysate was added to the bead slurry and brought to a final volume of 500 µl. The mixture was then incubated overnight rotating at 4°C and 15 RPM. The next day, the beads were pelleted and the supernatant fraction was collected before washing the beads three times with lysis buffer. To the pellet, 40 µl of 1X SDS loading buffer was added before boiling samples at 95°C for 8 min. The beads were pelleted a final time, and the resulting elution collected and loaded onto an SDS-polyacrylamide gel.

TUBE pulldown

MEFs in 15 cm dishes were treated as described, then washed once with cold 1X PBS before adding deubiquitinase inhibitor (DUBi) lysis buffer (1% Triton X-100, 10% glycerol, 2 mM O-Phenanthroline (MedChemExpress #HY-W004544), 50 µM PR-619 (MedChemExpress #HY-13814), 10 µM Spautin-1 (MedChemExpress #HY-12990), 10 µM MG132 (MedChemExpress #HY-13259), 2 mM EDTA, 130 mM NaCl, 20 mM Tris-HCl pH 7.4) and scraping to collect lysate. Lysates were rocked on ice for 15 min

then clarified by centrifugation at 14,000 *x g* for 10 min at 4°C. The supernatant was transferred to new tubes, and an aliquot reserved for BCA-based protein quantification. Following quantification, 0.5 mg of protein lysate was transferred to new tubes and diluted 1:4 in DUBi to reduce Triton X-100 concentration to 0.2%. 20 µl of tandem ubiquitin binding entities (TUBE) 1 (LifeSensors #UM401M) or control magnetic bead slurries (LifeSensors #UM400M) were added to each tube and incubated, rotating overnight at 4°C and 15 RPM. The next day, the beads were pelleted and the supernatant fraction was collected. The beads were then resuspended in 400 µl of DUBi wash buffer (DUBi lysis buffer without Triton X-100) before pelleting and discarding the supernatant. A total of three washes were performed before resuspending the beads in 40 µl of 1X SDS loading buffer. Samples were then boiled at 95°C for 8 min, then run via SDS-PAGE.

Mouse models

C57BL/6J mice were purchased from The Jackson Laboratory and bred in house. AMPK β1/β2 G2A mice were generated as previously described[92]. All mice were housed in ventilated cages at ~23 °C and maintained on a 12/12 h light-dark cycle with *ad libitum* access to a standard rodent chow (58% kcal from carbohydrates, 18% kcal from fat, and 24% kcal from crude protein; Harlan Teklad #2018) and water. All experiments conducted were in accordance with the Canadian Council of Animal Care and approved by the Animal Care Committee at the University of Ottawa (BMIe-3644).

4.5 Results

Non-myristoylated AMPK has higher activity despite lower protein levels

AMPK myristoylation depends on N-terminal glycine recognition by NMT1 during β subunit translation, regulating AMPK activity and subcellular localization following heterotrimer formation (Figure 4.1A). To selectively disrupt NMT1 recognition of the β subunit N-terminus, we generated knock-in mice using CRISPR-Cas9 to replace the N-terminal glycine with an alanine residue (G2A). To assess how AMPK protein levels vary between myristoylated and non-myristoylated forms, we measured basal protein expression in immortalized MEFs that endogenously express the G2A mutation on β1 (β1-G2A), β2 (β2-G2A), or both β1 and β2 (β1/2-G2A) isoforms. In MEFs, the predominantly expressed isoforms are α1, β1 and γ1, though there is some expression of β2 and γ2 as well[560]. In line with this, we observed the largest increase in AMPK activity in β1/2-G2A MEFs, wherein all AMPK heterotrimers would be non-myristoylated, as measured by increased pACC-S79 and pAMPKα-T172 signal (Figure 4.1B). This was followed closely by β1-G2A MEFs, whereas β2-G2A cells exhibited activity more similar activity to WT cells, aligning with their expected β subunit stoichiometries (Figure 4.1B). Surprisingly, the inverse was true for protein levels. Compared to WT MEFs, β1/2-G2A and β1-G2A cells had lower steady state protein levels of AMPK α1, β1, and γ1 subunits, though the decline in γ1 subunit levels were the most prominent (Figure 4.1B).

To compare how myristoylation-dependent AMPK activity changes in response to different activators, we treated WT and β1/2-G2A MEFs (all experiments hereafter use the β1/β2 double knock-in; referred to simply as G2A) with either MK-8722 as an allosteric activator that binds to the ADaM site, or a high dose of metformin, which primarily activates AMPK via increasing AMP levels[105]. We observed that both MK-8722 and metformin increased pAMPKα-

T172 levels in WT MEFs, although metformin this did not increase ACC phosphorylation at 2 hours (Figure 4.1C). In contrast, at baseline G2A cells had elevated pACC-S79 signal that was equivalent to allosterically activated WT MEFs. Interestingly, allosteric activation and metformin treatment had a minimal effect on ACC phosphorylation in G2A MEFs, while pAMPK-T172 was strongly induced (Figure 4.1C). This suggests that while the basal increase in non-myristoylated AMPK activity is sufficient to saturate some downstream target phosphosites, not all AMPK complexes are active. In line with other data, we again observed clear decreases in the steady state levels of AMPK subunits (Figure 4.1C). Altogether, non-myristoylated AMPK exhibits higher basal activity that varies by the stoichiometric amount of the β1 or β2 subunit and is still responsive to allosteric activation, particularly at the ADaM site.

While increased non-myristoylated AMPK activity has been ascribed to conformational changes that invite phosphorylation by upstream kinases[43,54,92], there remains no explanation for why AMPK subunit levels are decreased. To test whether this decrease in protein levels was due to transcriptional feedback, we measured mRNA levels in WT and G2A cells. Across all detectable subunits, we did not measure any genotypic changes in mRNA, arguing against a transcription-dependent reduction in non-myristoylated AMPK subunit levels (Figure 4.1D). Individual AMPK subunits are more susceptible to degradation than when part of the heterotrimer[561]. Therefore, we next investigated whether myristoylation affects heterotrimer formation. We postulated that if the lack of β subunit myristoylation negatively impacted heterotrimer assembly, we would recover the subunits in a non-stoichiometric manner following immunoprecipitation in G2A cells. Following immunoprecipitation of the β1 subunit, both AMPK α and β subunits were detected in equal amounts between WT and G2A cells, though AMPK γ1 may have been slightly lower (Figure 4.1E,F). However, since we also observe lower

protein levels in the α subunit, it is unlikely that heterotrimer formation is affecting our overall phenotype. Therefore, the decrease in non-myristoylated AMPK protein levels is not reliant on transcription and is minimally affected by heterotrimer association.

Pharmacological inhibition of N-myristoyltransferase recapitulates the G2A phenotype

Given that co-translational myristoylation is catalyzed by the enzyme N-myristoyltransferase (NMT)[562], we wondered if inhibition of NMT could recapitulate our observations in G2A MEFs. These two models of non-myristoylated AMPK β, NMTi-induced and G2A-related, would allow us to compare the relevance of the N-terminal amino acid residue, especially since alanine residues at N-termini can also trigger degradative processes[563] (Figure 4.2A). Therefore, we treated WT and G2A cells with the pharmacological NMT inhibitor IMP-1088 (NMTi) for 16 hours (Figure 4.2B). We observed an increase in AMPK activity in WT cells treated with NMTi, though this remained lower than in untreated G2A MEFs (Figure 4.2C). Protein levels of each of the AMPK subunits also decreased following NMTi treatment, aligning with the G2A phenotype (Figure 4.2C). With both transcription and heterotrimer assembly seeming improbable contributors to non-myristoylated AMPK protein levels, we hypothesized that proteostatic control mechanisms such as the UPS played a role in our observed decrease, potentially through elevated ubiquitination and degradation in the 26S proteasome (Figure 4.2A). To test whether there was any involvement of the UPS, we treated WT and G2A MEFs overnight with NMTi before adding the proteasome inhibitor MG132 to cause an accumulation of ubiquitinated proteins that would have otherwise been destined for proteasomal degradation (Figure 4.2D,E). In WT cells, we did not detect any effect of MG132 on AMPK subunit levels in vehicle or NMTi-treated conditions over the course of 8 hours (Figure 4.2D). However, the

NMTi-induced decrease in subunit protein levels was evident, particularly for the $\gamma 1$ subunit (Figure 4.2E). While G2A MEFs similarly displayed no response to MG132, NMTi did not cause a further reduction in AMPK protein levels, supporting that NMTi affects AMPK subunit levels in a myristoylation-dependent manner (Figure 4.2C). While MG132 treatment is designed to cause an accumulation of ubiquitinated AMPK subunits, the translation inhibitor, cycloheximide (CHX) would cause a depletion in subunits due to reduced replenishment of protein stores (Figure 4.2A). We treated cells similarly with CHX and observed no CHX-dependent changes, though the effects of NMTi were again evident (Figure 4.2D,E). Collectively, these data suggest that while NMTi can replicate the G2A phenotype in WT cells, there is no overt accumulation or decrease in protein levels following inhibition of proteostasis regulators.

AMPK α and γ subunits are ubiquitinated to the same extent in G2A MEFs.

Measurement of steady state protein levels following proteasomal inhibition is challenging due to the rapid nature of ubiquitination and may not yield changes in the nascent protein banding pattern. Since each ubiquitin residue is ~9kDa[564], an accumulation of ubiquitinated AMPK would result in higher molecular weight complexes detectable as a smear by western blot. To more comprehensively probe the rapidly changing ubiquitin landscape, we used tandem ubiquitin binding elements (TUBEs) in combination with a 2 hours MG132 treatment to enrich for ubiquitinated proteins (Figure 4.3A). Our TUBE pulldown enrichment was near complete, as there was little residual ubiquitin detected in the supernatant fraction, and none detected when using control magnetic beads (Figure 4.3A). We then repeated this experiment, this time also treating G2A MEFs with MG132 (Figure 4.3C). We observed an

equivalent increase in ubiquitin signal in both WT and G2A MEFs treated with MG132, indicative of polyubiquitinated protein accumulation and a successful enrichment (Figure 4.3B). For the AMPKα subunit, we observed high molecular weight smears in MG132-treated samples, suggesting these were polyubiquitinated AMPK α species. Interestingly, we did not detect any high molecular weight species for AMPKβ1 (Figure 4.3C), while AMPKγ1 produced smears similar to AMPKα. Across all the subunits, the high molecular weight intensity was comparable between WT and G2A MEFs. However, considering there was much less input γ1 in the G2A samples, there may have been a higher proportion of high molecular weight γ1. While this could suggest that AMPK γ1 is ubiquitinated at a higher rate when part of the non-myristoylated heterotrimer, more experiments would be required to definitively test this.

Knockdown of candidate myristoylation-dependent E3 ubiquitin ligases has no effect on G2A subunit levels.

There are more than 600 E3 ubiquitin ligases encoded in the genome. The majority belong to the Cullin-RING E3 ligase family (CRL), which rely on Cullin scaffolds to form multisubunit complexes[565]. The specificity of ubiquitination is conferred by substrate receptors that directly bind to select targets so that the CRL complex can load ubiquitin units onto the target residues. N-terminally exposed glycine residues represent an N-degron motif that is targeted by a pair of widely expressed CRL2 substrate receptors in ZER1 and ZYG11B[559]. Given that these are the only known myristoylation-dependent regulators to date, we wondered if these proteins played any role in regulating non-myristoylated AMPK protein levels. To answer this, we performed siRNA knockdown experiments in both WT and G2A MEFs. Using *Gapdh* as a positive control, we achieved 80-90% knockdown at the mRNA level for both *Zer1* and *Zyg11b*

(Figure 4.4B). Due to the lack of commercially available antibodies for ZYG11B, we could only validate the knockdown of ZER1 at the protein level, where we observed efficient reduction of ZER1 within 24 hours (Figure 4.4C). Despite this, there were no apparent increases, and perhaps even a decrease, in AMPKα and γ1 (Figure 4.4D), though in the absence of any myristoylation or proteasomal degradation inhibitors. We then proceeded to knock down *Zer1* in both WT and G2A MEFs while inhibiting proteasomal degradation via MG132 (Figure 4.4E). Again, we did not observe an overt effect when using MG132, and there were no differences in any of the AMPK subunit levels following *Zer1* knockdown (Figure 4.4E). In a similar experiment, we treated MEFs with MG132 or CHX for 4h, this time including *Zyg11b* siRNA conditions, where we again observed no effect of the E3 ubiquitin ligases on AMPK subunit levels (Figure 4.4F). Together, these data suggest that ZER1 and ZYG11B are not key drivers of the reduced non-myristoylated AMPK subunit levels.

Autophagic degradation mechanisms do not target non-myristoylated AMPK.

Beyond the UPS, bulk and selective forms of autophagy can contribute to protein turnover. To address whether autophagic degradation regulates non-myristoylated AMPK turnover, we inhibited late phase autophagy using the vacuolar H^+-ATPase inhibitor, bafilomycin A1 (Baf A1), in WT and G2A MEFs for 4, 8, and 12 hours. While there may have been a trending time-dependent increase in AMPKα due to Baf A1 treatment in WT cells, there was no effect on the β or γ subunits in WT or G2A MEFs (Figure 4.5A). With no changes in the non-myristoylated condition, it appears that macropautophagy is not a major contributing factor to non-myristoylated AMPK subunit levels. Beyond bulk autophagy, selective autophagy can regulate protein turnover as well. Chaperone-mediated autophagy, which relies on recognition of

a KFERQ motif in target proteins, binds to the cytosolic chaperone HSC70 and brings the target protein to the lysosome for degradation[566,567]. AMPKα1 exhibits a canonical KFERQ-like motif (RREIQ), leaving open the possibility that non-myristoylated AMPK leads to greater exposure of this peptide sequence. To test this, we treated WT and G2A MEFs with a chemical inducer of chaperone mediated autophagy in AR7[568]. However, across all subunits, there was no effect in AR7 in G2A or WT cells (Figure 4.5B). These data make it unlikely that non-myristoylated AMPK is being regulated by autophagic forms of degradation.

Non-myristoylated AMPK subunit levels display similar decreases across diverse tissues.

Given that we were unable to identify candidate E3 ubiquitin ligases from our targeted knockdown of ZER1 and ZYG11B, we turned to G2A mice to ask whether tissue-specific differences in non-myristoylated AMPK protein could direct us to potential tissue-restricted degradative mechanisms. This also allows for expansion beyond the predominant α1β1γ1 heterotrimer in MEFs to the heterotrimeric diversity across tissues. From WT and β1/β2-G2A knock-in mice, we isolated tissue from the brain, liver, and heart, which express different combinations of α, β, and γ subunits. The brain expresses predominantly α1/2 and γ1/2 subunits, as well as solely β2. We observed greater than a 50% decrease in both α1 and α2 subunit levels and a similar decrease in β2, though this was more variable. The γ1 subunit was virtually undetectable G2A brain samples. The liver also expresses α1/2 and γ1/2, though differs from the brain in that it favours β1 expression over β2. We observed similar trends for the α and γ1 subunits when compared to the brain, though the β1 subunit was decreased less in G2A samples. In the heart, which expresses a combination of the β subunits, again demonstrated a strong reduction in γ1 subunit levels. However, while α1 was clearly decreased in G2A mice, the α2 subunit was largely unchanged. Furthermore, though the expression was somewhat variable,

there was a stronger reduction in β2 subunits compared to β1. Collectively, these data point to the potential for tissue-specific regulation of certain subunits, though $\gamma 1$ protein levels are universally lower in all tissues assessed.

4.6 Discussion

In this work, we have examined how AMPK myristoylation regulates its protein stability. In cells selectively lacking AMPK myristoylation (G2A), we observed reduced steady state protein levels of AMPK subunits in MEFs, though the most striking decrease was consistently in the $\gamma 1$ subunit (Figure 1). We established that these myristoylation-dependent changes are unlikely to result from decreased transcription, or from defects in heterotrimer assembly. Through targeted siRNA knockdown experiments, as well as polyubiquitinated protein enrichment strategies, we were unable to detect obvious changes in ubiquitin-dependent non-myristoylated protein subunit levels. However, the decrease in steady state protein levels was conserved across several tissues *in vivo*, suggesting that this is universal regulatory node for AMPK proteostasis.

When selecting candidate E3 ubiquitin ligases for our knockdown experiments, we decided to focus on ZER1 and ZYG11B due to their established role in sensing myristoylation-specific N-degron motifs[559]. While our knockdown experiments preliminarily suggest that it is unlikely ZER1 or ZYG11B play significant roles in regulating non-myristoylated AMPK protein levels, a caveat with our approach is that G2A cells do not express the N-terminal glycine residue. However, structural analysis of ZER1 binding efficiency has revealed that it exhibits a high preference for N-terminal alanine residues, while ZYG11B also recognizes alanine, though to a lesser extent than glycine residues[569]. An additional structural study suggests that the AMPK

β1 and β2 N-termini are favourable for both ZER1 and ZYG11B binding[570]. Regardless, further experiments including simultaneous knockdown of both ZER1 and ZYG11B, in addition to NMT inhibition to retain the N-terminal glycine residue, would be required to completely rule out a role for ZER1 and ZYG11B.

Non-myristoylated AMPK exhibited lower steady state subunit levels; however, that does not necessarily mean that the myristoylation site is the recognition site for potential upstream regulators. Indeed, it is thought that non-myristoylated AMPK adopts a more open conformation, allowing for easier access to T172 by upstream kinases[43,54]. Therefore, it is possible that any of the validated E3 ubiquitin ligases for AMPK, of which there are several for the α[171,174–177], β[179,180], and γ subunits[178], could have greater affinity for specific residues in the more open conformation of non-myristoylated AMPK. Intriguingly, there are also reported AMPKα-pT172-specific E3 ubiquitin ligases[181,182] that could be relevant given the G2A mutation results in chronic overactivity. Additional experiments using a kinase dead G2A mutant would be the most helpful in understanding this relationship.

When could this potential myristoylation-dependent regulation of AMPK be relevant in a physiological setting? NMT1 expression has been shown to be decreased in CD4 T cells during rheumatoid arthritis[97]. While this did not lead to reduced AMPK subunit levels, it did decrease AMPK activity, which opposes what we and others have observed when AMPK myristoylation is dysregulated[43,54,92]. However, to date this remains one of the few pathologies with reduced NMT1 expression. Beyond protein expression, little is known of the post-translational regulation of NMT1 except that Src family kinases can stimulate its activity[571]. However, numerous high throughput phosphoproteomics studies have identified uncharacterized phosphosites on NMT1[572] that could affect myristoylation rates under certain cellular conditions. Additionally, the physical

accessibility and intracellular concentration of myristoyl-CoA will also influence the overall rate of myristoylation. While NMT1 protein levels have typically been observed to increase in several disease states such as cancers or fatty liver disease, it remains and understudied enzyme, despite over 100 proteins relying on myristoylation for proper function[573].

Protein turnover is complex and is reliant on layers of transcriptional, post-transcriptional, translational, and post-translational regulation. While we had ruled out transcriptional changes and heterotrimer assembly as being contributors to non-myristoylated AMPK protein stability in line with prior literature[92], we did not explicitly investigate differences in translational rates between WT or G2A cells. Translation rates can be affected by ribosomal recognition of the first four ribonucleotides of an mRNA transcript[574]. However, our G2A mutation was induced at the +5 position, making it unlikely that it would appreciably affect β subunit translation. Another possibility is that the G2A substitution generated an alternative N-degron signal, as N-terminal alanines can be acetylated and subjected to degradation[575]. However, since we also observed a similar decrease when treating cells with a pharmacological inhibitor of NMT, thereby preserving the N-terminal glycine residue, it is unlikely, though still possible, that an acetylation-dependent mechanism could explain the decrease in AMPK subunit levels in G2A cells and mice. While the experiments contained within this chapter represent preliminary work, our data confirms observations from published literature and highlights that myristoylation plays an important role in regulating AMPK protein stability. However, given that non-myristoylated heterotrimers exhibit chronic overactivity, it is likely that if AMPK myristoylation is compromised *in vivo*, any resulting phenotype would be driven by this overactivity and not from a reduction in protein levels.

4.7 Figures

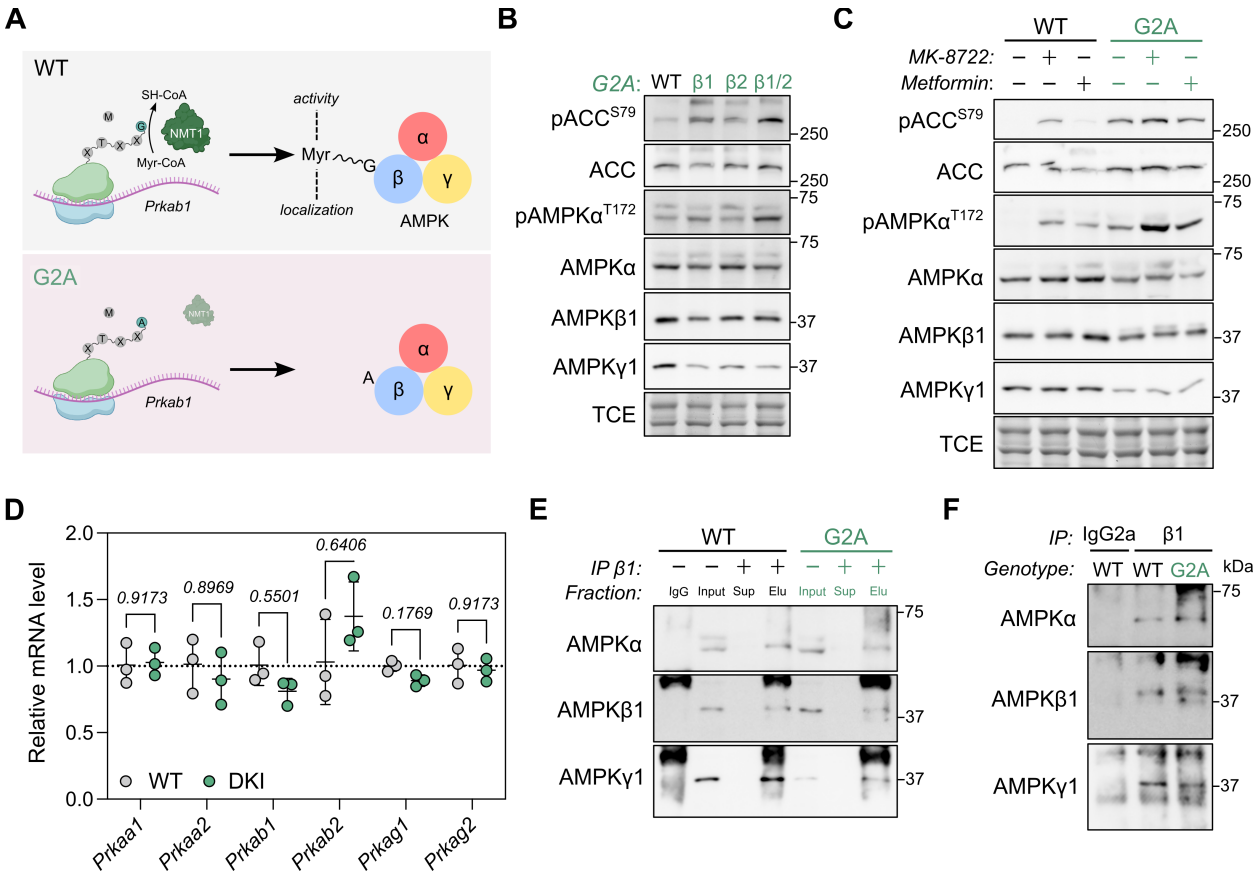

Figure 4.1: Non-myristoylated AMPK has lower steady state subunit levels independent of mRNA. **(A)** Schematic of model: NMT1 recognizes N-terminal glycine residues and myristoylates AMPK β, conferring activity and localization regulation. Mutation of the glycine residue to alanine selectively prevents myristoylation. **(B)** Immunoblots of AMPK subunit levels in WT and G2A MEFs. **(C)** WT and G2A MEFs were treated with MK-8722 (2 μM) or metformin (0.2 mM) for 2h. Immunoblots of AMPK targets and subunit levels. **(D)** Relative mRNA levels of AMPK subunits (n=3). **(E,F)** Immunoprecipitation of AMPK β1 followed by blotting of all fractions **(F)** or eluate only **(F)**. Data are represented as mean ± SD. Blots are representative of 3 (B) or 1 (D-F) independent experiment.

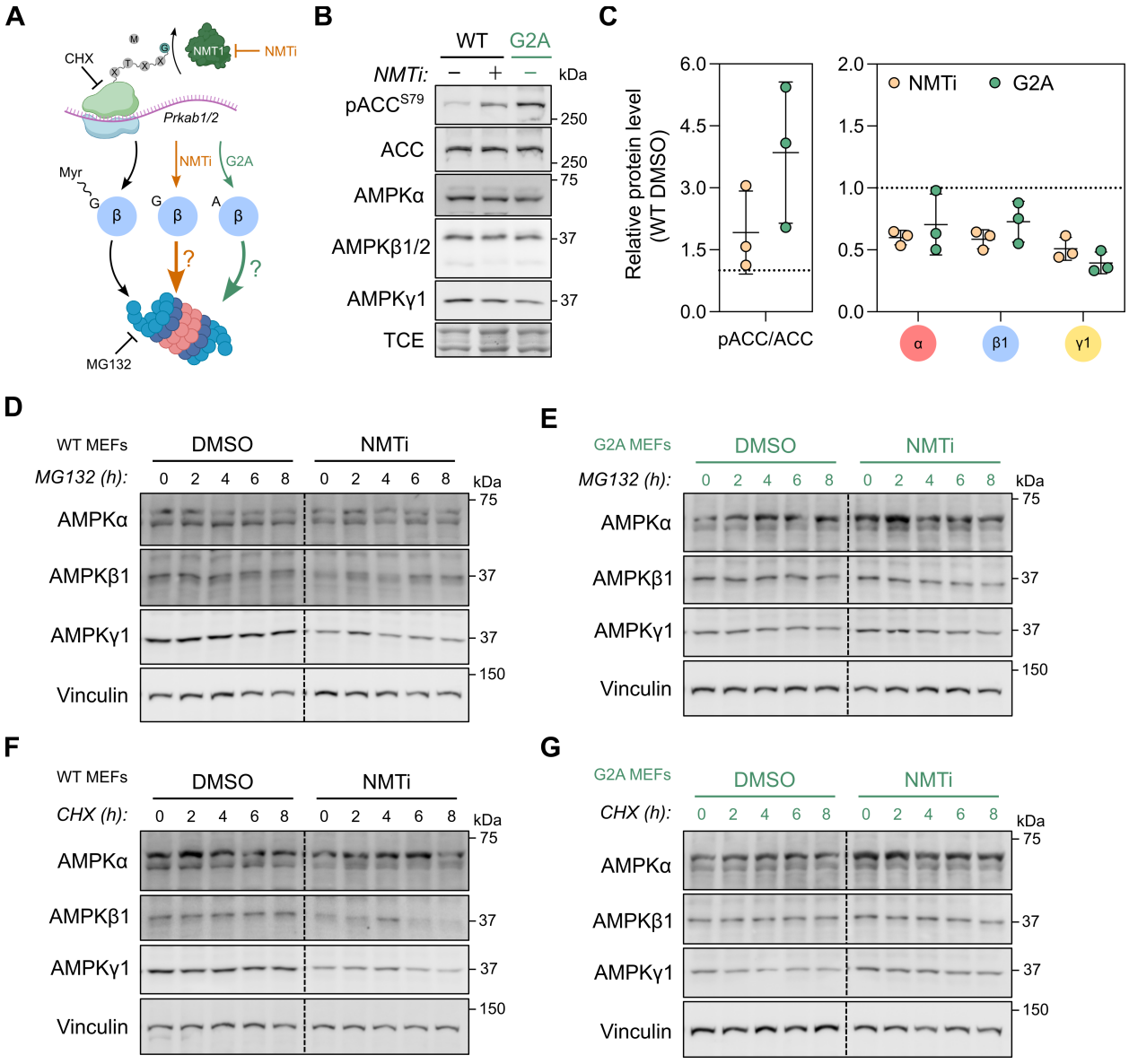

Figure 4.2: Pharmacological inhibition of N-myristoyltransferase recapitulates the G2A phenotype. **(A)** Schematic of model: three distinct pools of AMPK β can be generated depending on whether NMT1 is fully functional (myristoylated), inhibited (non-myristoylated with N-terminal glycine), or unable to recognize the N-terminus (non-myristoylated with N-terminal alanine). **(B)** WT or G2A MEFs were treated with DMSO or IMP-1088 (NMTi; 0.5 μM) for 16h. Immunoblots of AMPK subunit levels and activity. **(C)** Densitometry quantification of (B). **(D-E)** WT or G2A MEFs were treated with NMTi (0.5 μM) for 16h before spiking in MG132 (10 μM; **(B,C)**) or cycloheximide (CHX; 5 μM; **(D,E)**) for indicated times. Immunoblots of AMPK subunit levels. Blots are representative of three (B,C) or one (D-G) independent experiment.

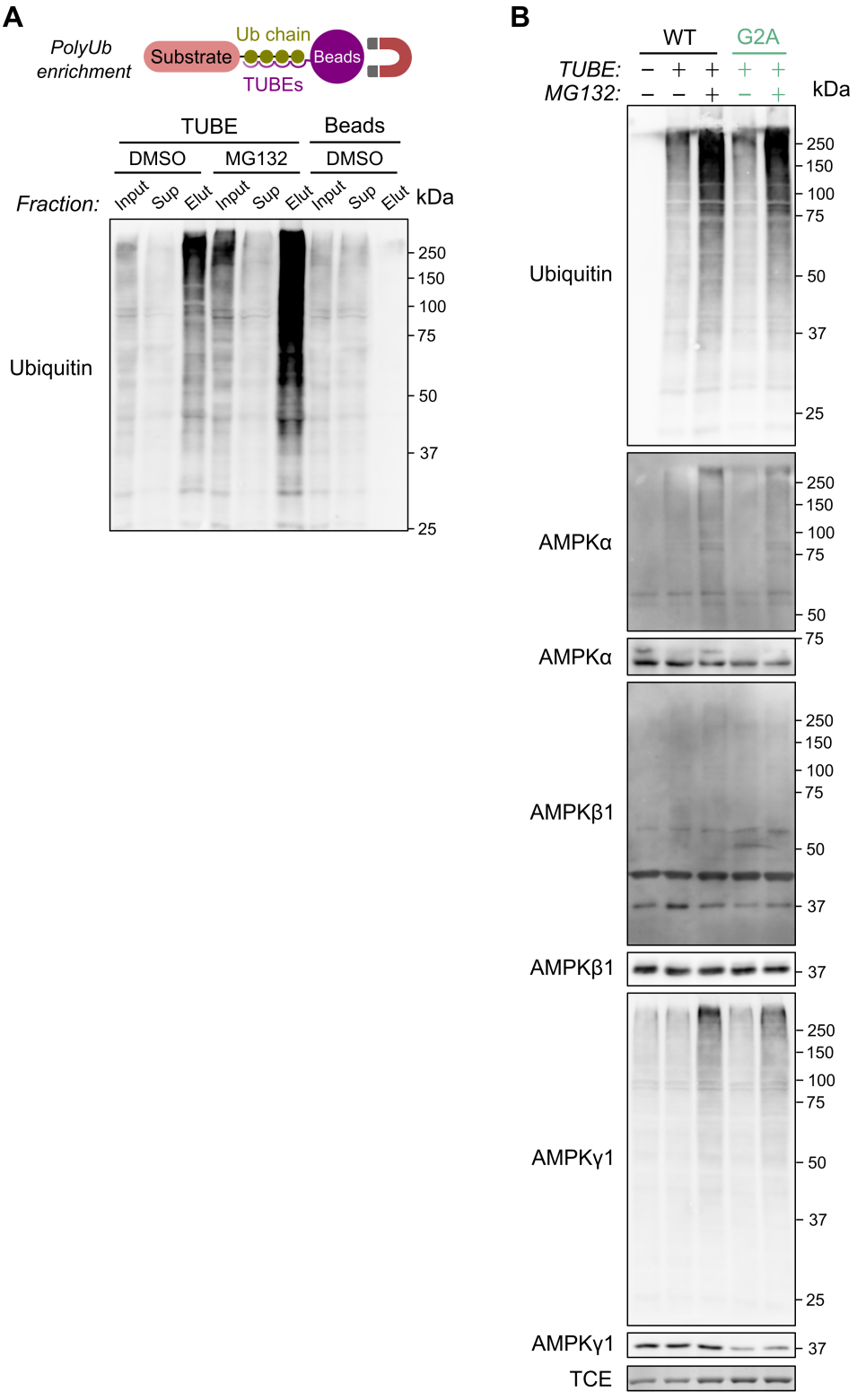

Figure 4.3: AMPK α and γ subunits are ubiquitinated to the same extent in G2A MEFs. (A) Tandem ubiquitin binding entity (TUBE) pulldown allows for enrichment of polyubiquitinated proteins. WT MEFs were treated with MG132 (10 μM) or DMSO for 2h. Enrichment of polyubiquitinated proteins was carried out by incubating with either TUBE-conjugated beads or control beads. Immunoblot of ubiquitin from all fractions. **(B)** WT and G2A MEFs were treated with MG132 (10 μM) for 2h and ubiquitinated proteins enriched as in (A). Immunoblots of AMPK subunits following TUBE enrichment. Blots are representative of one independent experiment.

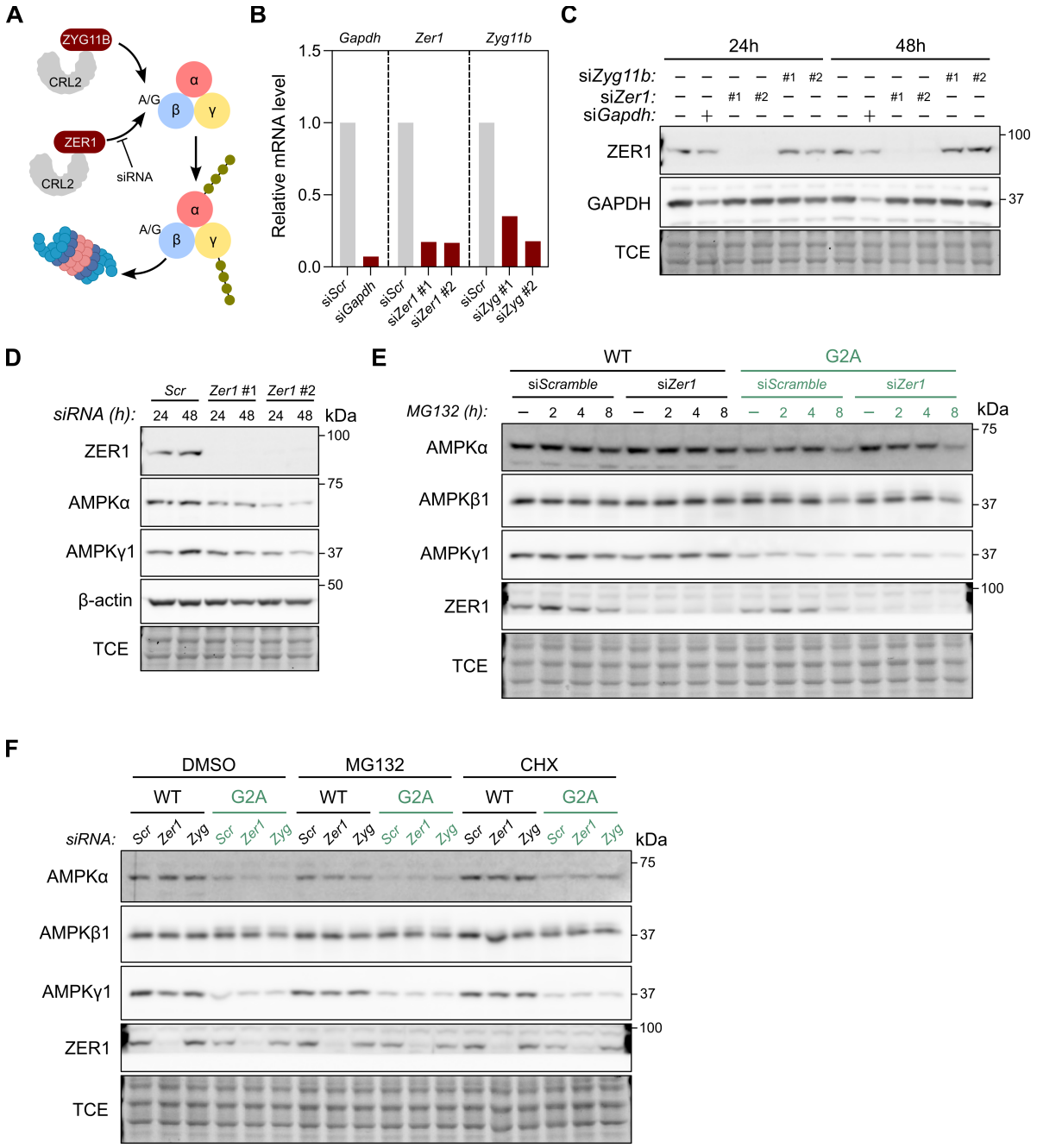

Figure 4.4: Knockdown of candidate myristoylation-dependent E3 ubiquitin ligases has no effect on G2A subunit levels. (A) Schematic of proposed model: ZER1 and ZYG11B recognize non-myristoylated AMPK, leading to its polyubiquitination and subsequent degradation in the 26S proteasome. **(B)** WT MEFs were treated with siRNA (10 nM) specific to *Gapdh* (positive control), *Zer1* or *Zyg11b* for 24h. Relative mRNA levels compared to scrambled siRNA. **(C)** Immunoblots of ZER1 and GAPDH following 24h and 48h of knockdown. **(D)** Immunoblots of ubiquitinated AMPK subunits α and γ and ZER1 after indicated knockdown durations. **(E)** siRNA knockdown of *Zer1* (10 nM) for 24h in WT or G2A MEFs was followed by incubation for MG132 (10 μM) for indicated times. Immunoblots of AMPK subunits and ZER1. **(F)** siRNA knockdown of *Zer1* or *Zyg11b* (10 nM) for 24h in WT or G2A MEFs was followed by incubation with either MG132 (10 μM) or CHX (5 μM) for 4h. Immunoblots of AMPK subunits and ZER1. All blots are representative of one independent experiment.

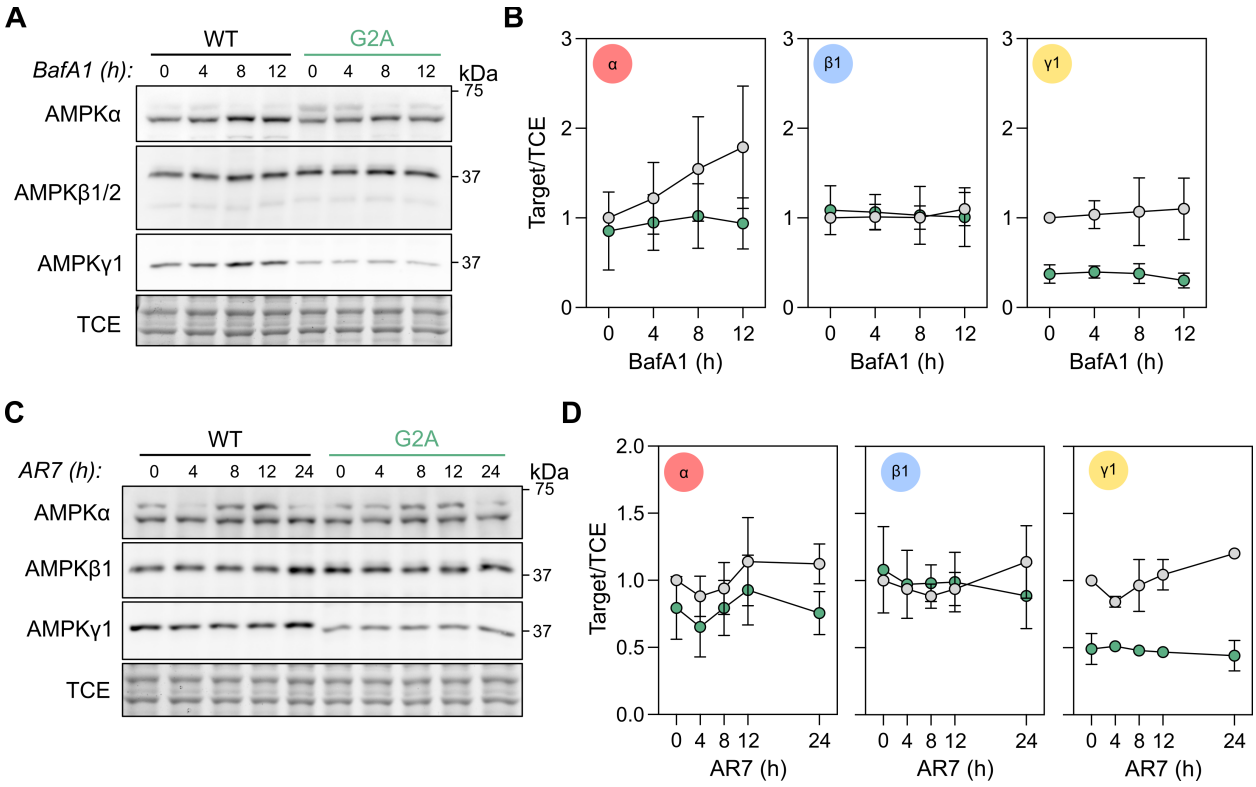

Figure 4.5: Autophagic degradative mechanisms do not target non-myristoylated AMPK. (A) WT or G2A MEFs were treated with bafilomycin A1 (25 nM) for indicated times. Immunoblots of AMPK subunit levels. **(B)** Densitometry for (A). **(C)** WT or G2A MEFs were treated with AR7 (10 μM) for indicated times. **(D)** Densitometry for (C). Blots are representative of three biological replicates from two independent experiments.

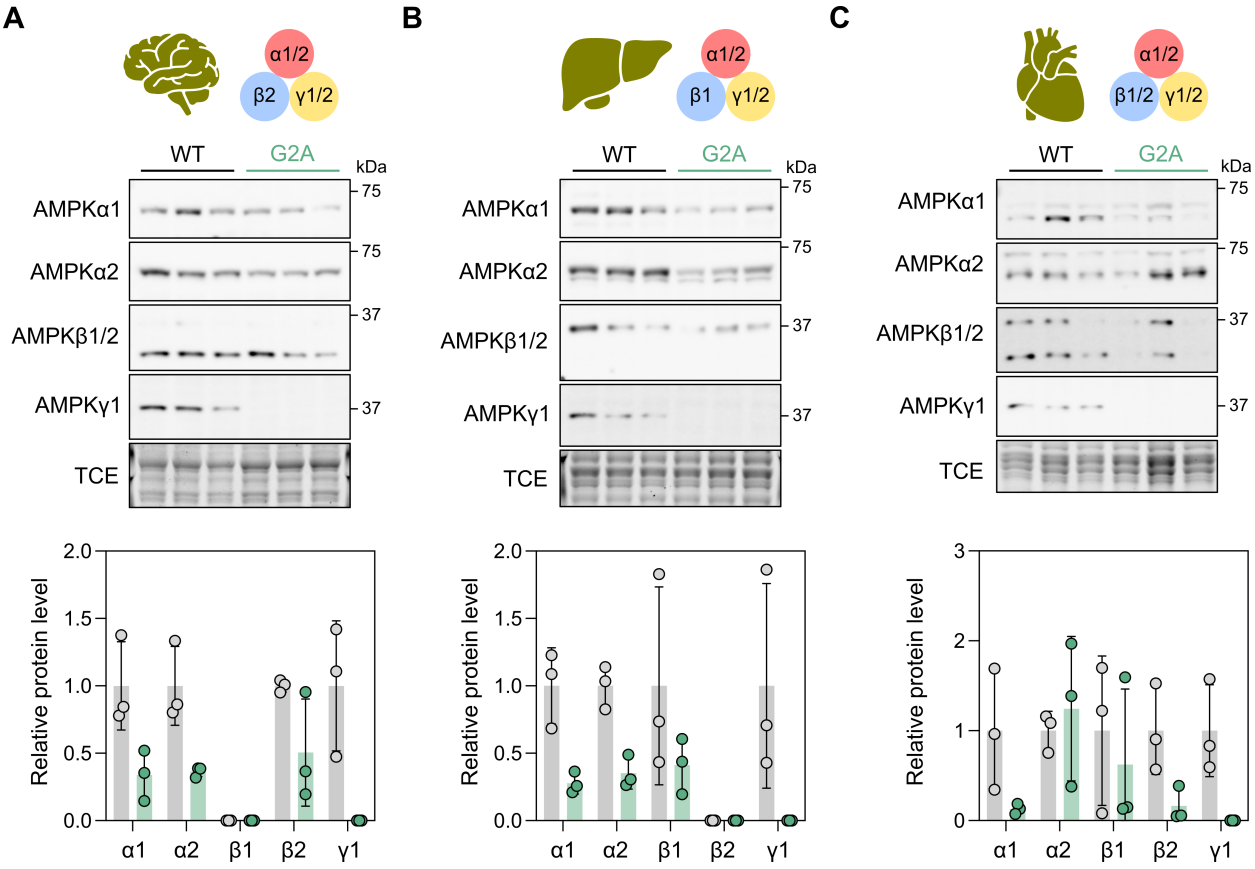

Figure 4.6: Non-myristoylated AMPK subunit levels display similar decreases across diverse tissues. Protein samples from indicated tissues from WT (n=3) and β1/β2 G2A (n=3) mice were run on SDS-PAGE. AMPK subunit protein levels in **(A)** brain, **(B)** liver, and **(C)** heart tissue with densitometric quantification below each panel. Data represented as mean ± SD (A-C, lower). Data are representative of one independent experiment.

Supplemental Table 4.1: Antibodies and stains.

Antibody	Source	Company	CAT
ACC	Rabbit	Cell Signaling Technology	3662
pACC-S79	Rabbit	Cell Signaling Technology	3661
AMPKα	Rabbit	Cell Signaling Technology	2532
pAMPKα-T172	Rabbit	Cell Signaling Technology	2535
AMPK β1/2	Rabbit	Cell Signaling Technology	4150
AMPKβ1	Mouse	Signalway	27201
AMPK γ1	Rabbit	Abcam	ab32508
Ubiquitin	Mouse	Novus Biologicals	NB300-130
β-actin	Rabbit	Cell Signaling Technology	5125
Vinculin	Rabbit	Cell Signaling Technology	4650
ZER1	Rabbit	Thermo Fisher	16647-1-AP
GAPDH	Rabbit	Cell Signaling Technology	8884
2,2,2-Trichloroethanol (TCE)	N/A	MilliporeSigma	T54801

Supplemental Table 4.2: Primers used in RT-qPCR.

TaqMan Probes	
Target (mouse)	Assay ID (Invitrogen)
Prkaa1	Mm01296700_m1
Prkaa2	Mm01264789_m1
Prkab1	Mm01201921_m1
Prkab2	Mm01257133_m1
Prkag1	Mm00450298_g1
Prkag2	Mm00513977_m1
Actb	Mm00607939_s1

Oligos for use with SYBR Green		
Target (mouse)	Forward (5'-3')	Reverse (5'-3')
Zer1	CACCTGACAACTGCGAGATGT	CCTAGCATGTTACGGTGTAGC
Zyg11b	TTCCGTGGACACTACGTTGAA	TGACTCAGTTGGGAAAGACTCT
Gapdh	AGGTCGGTGTGAACGGATTTG	TGTAGACCATGTAGTTGAGGTCA
Actb	GGCTGTATTCCCCTCCATGG	CCAGTTGGTAACAATGCCATGT
Hprt1	TCAGTCAACGGGGGACATAAA	GGGGCTGTACTGCTTAACCAG

4.8 Acknowledgments

We gratefully acknowledge the support and services provided by the University of Ottawa Animal Care and Veterinary Services, as well as important discussions with Dr. Kei Sakamoto during this project. The authors would like to apologize to colleagues whose significant work could not be included due to length, citation limitations, or author oversight.

Chapter 5: General conclusions and future perspectives

In my thesis, I have investigated how metabolic signaling in immune cells influences disease across acute and chronic inflammatory contexts. In my first chapter, I explored how AMPK regulates and is regulated by changes in metabolism and nutrient levels. In my work with HMGCR, I found that different atherosclerosis models can produce diverging immune cell phenotypes and argue that multiple hypercholesterolemia models should be used to validate immune cell-related findings. My work on *Salmonella enterica* in chapter 3 elucidated how AMPK signaling affects metabolism during the inflammatory response to gram-negative bacteria. Finally, we investigated how myristoylation affected AMPK protein stability. While we did not uncover a specific mechanism for this process, we did exclude several suggested regulatory processes, and surmise that there is some additional layer of regulation that influences non-myristoylated AMPK protein stability.

There remains a pressing need to develop anti-inflammatory therapeutics given the role inflammation plays in various diseases such as obesity and ACVD. However, this must be tempered with an understanding that inhibiting inflammation can have adverse outcomes on susceptibility to pathogens. Our results demonstrate that AMPK activation selectively inhibits inflammatory cytokine production without completely disrupting core inflammatory pathways. The use of neutralizing antibodies against targets such as IL-1β have shown clinical promise in reducing inflammation, though this comes with increased risk of infection[576]. Furthermore, acute administration of the AMPK activator MK-8722, which is known to improve metabolic disease outcomes and glucose homeostasis[199], had minimal effects on bacterial pathogenesis in our model of *S.*Tm infection. In this way, AMPK activators still hold promise for resolving some of the inflammatory phenotypes observed in metabolic disorders, without significantly impacting

immune cell function. While my thesis supports this view, more work will be required to understand how AMPK activators affect the response to diverse pathogens in preclinical models across longer timescales.

Where does the AMPK field go next? For one, AMPK targets are broadly expressed across diverse cell types and in different subcellular compartments. The forthcoming challenge now rests in linking the temporal and localization-specific signals to their respective tissue and disease states. I envision that optimizing real-time biosensors such as ExRai AMPKAR[81] for use in intravital imaging will be a key step in understanding AMPK signaling dynamics *in vivo*[577]. This will be important in the context of nuclear AMPK signaling since the long-term effects of AMPK activators will be driven in part by transcriptional rewiring, of which the exact mechanism requires clarification.

Other important steps moving forward should include consolidation and characterization. For one, there remain numerous posttranslational modifications on the AMPK heterotrimer itself that are uncharacterized. As a start, recent work from Jon Oakhill's group stoichiometrically measured the extent of mTORC1-driven phosphorylation on various combinations of the AMPK heterotrimer[578]. More studies such as this one, particularly in the context of well-characterized AMPK activation states such as glucose starvation[90], elevated intracellular calcium[59] and fatty acyl-CoAs[42], as well as oxidative stress[141], will help identify differential signals that lead to altered localization and activity. Too many phosphorylation, acetylation, and ubiquitination sites identified by high throughput studies remain uncharacterized[572]. And that says nothing of modifications that are less thoroughly explored such as itaconation[579] or other direct metabolite interactions. While these types of systematic interrogations require time, there is a need to unify the rapidly expanding inputs on AMPK activity.

Looking downstream, the number of AMPK targets now exceeds over 120 validated substrates. However, among this body of work, only eleven targets have been tested in mouse models with point mutations at the AMPK phosphosites[580]. Just as inducible and tissue-specific AMPK knockout models have been applied to numerous disease states, we have reached a point where more precise models are required to ascertain the physiological relevance of new and established targets. The generation of Ser-Ala point mutant mouse models, as well as the reciprocal Ser-Glu/Asp point mutants will be essential for confirming observations made *in vitro*. Considering AMPK target sites are typically identified near the conclusion of a study, it is often unfeasible to generate and thoroughly investigate a new mouse line. However, with the advancement of genome editing tools and the relative ease at which these mouse models can be produced[581], these barriers will hopefully be reduced. One particular area that could benefit from point mutant studies is in AMPK-mediated transcriptional regulation. With numerous transcription factors and epigenetic regulators under AMPK control[475], knockout models can cloud interpretations of changes in gene expression. Furthermore, to my knowledge, there are no examples of inducible, nor tissue-specific knock-in models for downstream AMPK targets. This has been applied in cancer fields[582], and could be of use when assessing causality due to AMPK signaling.

On a more personal note, while AMPK has been challenging to study at times due to the expansive and rich history of the AMPK field, as well as its intersection with so many integral pathways, I will forever be grateful for the opportunity to study such an adaptable kinase. I still have many unanswered questions: how is AMPK transported into the nucleus? How does AMPK translocate around the cell? Why does AMPK associate with membranes in the absence of activating stimuli? However, I have learned through my degree to expect the unexpected. Just in

the past two years, there have been studies linking AMPK activity to context-dependent *increases* in protein translation[101], as well as *inhibition* of autophagy initiation[417]. These ideas are far cries from the consensus on AMPK signaling a decade ago. I suspect that many surprises await us yet, and I eagerly look forward to their discovery.

References

1. Manning, G., Whyte, D. B., Martinez, R., Hunter, T. & Sudarsanam, S. The protein kinase complement of the human genome. *Science* **298**, 1912–1934 (2002).
2. Arter, C., Trask, L., Ward, S., Yeoh, S. & Bayliss, R. Structural features of the protein kinase domain and targeted binding by small-molecule inhibitors. *J Biol Chem* **298**, 102247 (2022).
3. Chen, C. *et al.* Identification of a Major Determinant for Serine-Threonine Kinase Phosphoacceptor Specificity. *Mol Cell* **53**, 140–147 (2014).
4. Fischer, E. H. Phosphorylase and the origin of reversible protein phosphorylation. *Biol Chem* **391**, 131–137 (2010).
5. Fischer, E. H. & Krebs, E. G. Conversion of phosphorylase b to phosphorylase a in muscle extracts. *J Biol Chem* **216**, 121–132 (1955).
6. Krebs, E. G. & Fischer, E. H. The phosphorylase b to a converting enzyme of rabbit skeletal muscle. *Biochim Biophys Acta* **20**, 150–157 (1956).
7. Walsh, D. A., Perkins, J. P. & Krebs, E. G. An adenosine 3',5'-monophosphate-dependant protein kinase from rabbit skeletal muscle. *J Biol Chem* **243**, 3763–3765 (1968).
8. Beg, Z. H., Allmann, D. W. & Gibson, D. M. Modulation of 3-hydroxy-3-methylglutaryl coenzyme A reductase activity with cAMP and wth protein fractions of rat liver cytosol. *Biochemical and biophysical research communications* **54**, 1362–9 (1973).
9. Carlson, C. A. & Kim, K.-H. Regulation of Hepatic Acetyl Coenzyme A Carboxylase by Phosphorylation and Dephosphorylation. *J. Biol. Chem.* **248**, 378–380 (1973).
10. Hardie, D. G. & Cohen, P. The regulation of fatty acid biosynthesis: simple procedure for the purification of acetyl CoA carboxylase from lactating rabbit mammary gland, and its phosphorylation by endogenous cyclic AMP-dependent and -independent protein kinase activities. *FEBS Lett* **91**, 1–7 (1978).
11. Munday, M. R. & Hardie, D. G. Isolation of three cyclic-AMP-independent acetyl-CoA carboxylase kinases from lactating rat mammary gland and characterization of their effects on enzyme activity. *Eur J Biochem* **141**, 617–627 (1984).
12. Hardie, D. G. & Guy, P. S. Reversible Phosphorylation and Inactivation of Acetyl-CoA Carboxylase from Lactating Rat Mammary Gland by Cyclic AMP-Dependent Protein Kinase. *European Journal of Biochemistry* **110**, 167–177 (1980).
13. Holland, R., Witters, L. A. & Hardie, D. G. Glucagon inhibits fatty acid synthesis in isolated hepatocytes via phosphorylation of acetyl-CoA carboxylase by cyclic-AMP-dependent protein kinase. *Eur J Biochem* **140**, 325–333 (1984).
14. Ingebritsen, T. S., Lee, H. S., Parker, R. A. & Gibson, D. M. Reversible modulation of the activities of both liver microsomal hydroxymethylglutaryl coenzyme A reductase and its inactivating enzyme. Evidence for regulation by phosphorylation-dephosphorylation. *Biochem Biophys Res Commun* **81**, 1268–1277 (1978).
15. Ferrer, A. & Hegardt, F. G. Phosphorylation of 3-hydroxy-3-methylglutaryl coenzyme A reductase by microsomal 3-hydroxy-3-methylglutaryl coenzyme A reductase kinase. *Archives of Biochemistry and Biophysics* **230**, 227–237 (1984).
16. Ferrer, A., Caelles, C., Massot, N. & Hegardt, F. G. Activation of rat liver cytosolic 3-hydroxy-3-methylglutaryl coenzyme A reductase kinase by adenosine 5'-monophosphate. *Biochem Biophys Res Commun* **132**, 497–504 (1985).
17. Carling, D. & Hardie, D. G. Isolation of a cyclic-AMP-independent protein kinase from rat liver and its effect on the enzymic activity of acetyl-CoA carboxylase. *Biochemical Society Transactions* **14**, 1076–1077 (1986).
18. Carling, D., Zammit, V. A. & Hardie, D. G. A common bicyclic protein kinase cascade inactivates the regulatory enzymes of fatty acid and cholesterol biosynthesis. *FEBS Letters* **223**, 217–222 (1987).

19. Sim, A. T. R. & Hardie, D. G. The low activity of acetyl-CoA car□ylase in basal and glucagon-stimulated hepatocytes is due to phosphorylation by the AMP-activated protein kinase and not cyclic AMP-dependent protein kinase. *FEBS Letters* **233**, 294–298 (1988).
20. Carling, D. & Hardie, D. G. The substrate and sequence specificity of the AMP-activated protein kinase. Phosphorylation of glycogen synthase and phosphorylase kinase. *Biochim. Biophys. Acta* **1012**, 81–86 (1989).
21. Davies, S. P., Carling, D. & Hardie, D. G. Tissue distribution of the AMP-activated protein kinase, and lack of activation by cyclic-AMP-dependent protein kinase, studied using a specific and sensitive peptide assay. *European Journal of Biochemistry* **186**, 123–128 (1989).
22. Carling, D., Clarke, P. R., Zammit, V. A. & Hardie, D. G. Purification and characterization of the AMP-activated protein kinase. Copurification of acetyl-CoA carboxylase kinase and 3-hydroxy-3-methylglutaryl-CoA reductase kinase activities. *Eur J Biochem* **186**, 129–136 (1989).
23. Moore, F., Weekes, J. & Hardie, D. G. Evidence that AMP triggers phosphorylation as well as direct allosteric activation of rat liver AMP-activated protein kinase. *European Journal of Biochemistry* **199**, 691–697 (1991).
24. Kemp, B. E., Graves, D. J., Benjamini, E. & Krebs, E. G. Role of multiple basic residues in determining the substrate specificity of cyclic AMP-dependent protein kinase. *J. Biol. Chem.* **252**, 4888–4894 (1977).
25. Kemp, B. E., Pearson, R. B., Guerriero, V., Bagchi, I. C. & Means, A. R. The calmodulin binding domain of chicken smooth muscle myosin light chain kinase contains a pseudosubstrate sequence. *J Biol Chem* **262**, 2542–2548 (1987).
26. House, C. & Kemp, B. E. Protein kinase C contains a pseudosubstrate prototope in its regulatory domain. *Science* **238**, 1726–1728 (1987).
27. Witters, L. A. & Kemp, B. E. Insulin activation of acetyl-CoA carboxylase accompanied by inhibition of the 5'-AMP-activated protein kinase. *J Biol Chem* **267**, 2864–2867 (1992).
28. Celenza, J. & Carlson, M. Cloning and Genetic-Mapping of Snf1, a Gene Required for Expression of Glucose-Repressible Genes in Saccharomyces-Cerevisiae. *Mol. Cell. Biol.* **4**, 49–53 (1984).
29. Carling, D. *et al.* Mammalian AMP-activated protein kinase is homologous to yeast and plant protein kinases involved in the regulation of carbon metabolism. *J. Biol. Chem.* **269**, 11442–11448 (1994).
30. Mitchelhill, K. I. *et al.* Mammalian AMP-activated protein kinase shares structural and functional homology with the catalytic domain of yeast Snf1 protein kinase. *J. Biol. Chem.* **269**, 2361–2364 (1994).
31. Woods, A. *et al.* Yeast SNF1 is functionally related to mammalian AMP-activated protein kinase and regulates acetyl-CoA carboxylase in vivo. *J Biol Chem* **269**, 19509–19515 (1994).
32. Davies, S. P. *et al.* Purification of the AMP-activated protein kinase on ATP-gamma-sepharose and analysis of its subunit structure. *Eur J Biochem* **223**, 351–357 (1994).
33. Stapleton, D. *et al.* Mammalian 5'-AMP-activated protein kinase non-catalytic subunits are homologs of proteins that interact with yeast Snf1 protein kinase. *J Biol Chem* **269**, 29343–29346 (1994).
34. Woods, A. *et al.* Characterization of AMP-activated protein kinase beta and gamma subunits. Assembly of the heterotrimeric complex in vitro. *J. Biol. Chem.* **271**, 10282–10290 (1996).
35. Stapleton, D. *et al.* Mammalian AMP-activated Protein Kinase Subfamily (∗). *Journal of Biological Chemistry* **271**, 611–614 (1996).
36. Dyck, J. R. *et al.* Regulation of 5'-AMP-activated protein kinase activity by the noncatalytic beta and gamma subunits. *J Biol Chem* **271**, 17798–17803 (1996).
37. Woods, A., Salt, I., Scott, J., Hardie, D. G. & Carling, D. The alpha1 and alpha2 isoforms of the AMP-activated protein kinase have similar activities in rat liver but exhibit differences in substrate specificity in vitro. *FEBS Lett.* **397**, 347–351 (1996).
38. Mitchelhill, K. I. *et al.* Posttranslational Modifications of the 5′-AMP-activated Protein Kinase β1 Subunit. *J. Biol. Chem.* **272**, 24475–24479 (1997).

39. Hawley, S. A. *et al.* Characterization of the AMP-activated protein kinase kinase from rat liver and identification of threonine 172 as the major site at which it phosphorylates AMP-activated protein kinase. *J Biol Chem* **271**, 27879–27887 (1996).
40. Smiles, W. J., Ovens, A. J., Oakhill, J. S. & Kofler, B. The metabolic sensor AMPK: Twelve enzymes in one. *Mol Metab* **90**, 102042 (2024).
41. Yan, Y. *et al.* Structure of an AMPK complex in an inactive, ATP-bound state. *Science* **373**, 413–419 (2021).
42. Pinkosky, S. L. *et al.* Long-chain fatty acyl-CoA esters regulate metabolism via allosteric control of AMPK β1 isoforms. *Nat Metab* **2**, 873–881 (2020).
43. Oakhill, J. S. *et al.* β-Subunit myristoylation is the gatekeeper for initiating metabolic stress sensing by AMP-activated protein kinase (AMPK). *Proc Natl Acad Sci U S A* **107**, 19237–19241 (2010).
44. Ignoul, S. & Eggermont, J. CBS domains: structure, function, and pathology in human proteins. *Am J Physiol Cell Physiol* **289**, C1369-1378 (2005).
45. Xiao, B. *et al.* Structural basis for AMP binding to mammalian AMP-activated protein kinase. *Nature* **449**, 496–500 (2007).
46. Wilson, W. A., Hawley, S. A. & Hardie, D. G. Glucose repression/derepression in budding yeast: SNF1 protein kinase is activated by phosphorylation under derepressing conditions, and this correlates with a high AMP:ATP ratio. *Curr Biol* **6**, 1426–1434 (1996).
47. Mayer, F. V. *et al.* ADP regulates SNF1, the Saccharomyces cerevisiae homolog of AMP-activated protein kinase. *Cell Metab* **14**, 707–714 (2011).
48. Roustan, V., Jain, A., Teige, M., Ebersberger, I. & Weckwerth, W. An evolutionary perspective of AMPK-TOR signaling in the three domains of life. *J Exp Bot* **67**, 3897–3907 (2016).
49. Wojtaszewski, J. F. P. *et al.* 5'AMP activated protein kinase expression in human skeletal muscle: effects of strength training and type 2 diabetes. *J Physiol* **564**, 563–573 (2005).
50. Kristensen, D. E. *et al.* Human muscle fibre type-specific regulation of AMPK and downstream targets by exercise. *J Physiol* **593**, 2053–2069 (2015).
51. Wu, J. *et al.* Chemoproteomic analysis of intertissue and interspecies isoform diversity of AMP-activated protein kinase (AMPK). *J Biol Chem* **288**, 35904–35912 (2013).
52. Heng, T. S. P., Painter, M. W., & Immunological Genome Project Consortium. The Immunological Genome Project: networks of gene expression in immune cells. *Nat Immunol* **9**, 1091–1094 (2008).
53. Hawley, S. A. *et al.* Calmodulin-dependent protein kinase kinase-beta is an alternative upstream kinase for AMP-activated protein kinase. *Cell Metab.* **2**, 9–19 (2005).
54. Oakhill, J. S. *et al.* AMPK is a direct adenylate charge-regulated protein kinase. *Science* **332**, 1433–1435 (2011).
55. Gowans, G. J., Hawley, S. A., Ross, F. A. & Hardie, D. G. AMP is a true physiological regulator of AMP-activated protein kinase by both allosteric activation and enhancing net phosphorylation. *Cell Metab* **18**, 556–566 (2013).
56. Atkinson, D. E. The energy charge of the adenylate pool as a regulatory parameter. Interaction with feedback modifiers. *Biochemistry* **7**, 4030–4034 (1968).
57. Hardie, D. G. & Hawley, S. A. AMP-activated protein kinase: the energy charge hypothesis revisited. *Bioessays* **23**, 1112–1119 (2001).
58. Rajamohan, F. *et al.* Probing the enzyme kinetics, allosteric modulation and activation of α1- and α2-subunit-containing AMP-activated protein kinase (AMPK) heterotrimeric complexes by pharmacological and physiological activators. *Biochem J* **473**, 581–592 (2016).
59. Woods, A. *et al.* Ca2+/calmodulin-dependent protein kinase kinase-β acts upstream of AMP-activated protein kinase in mammalian cells. *Cell Metabolism* **2**, 21–33 (2005).
60. Vara-Ciruelos, D. *et al.* Genotoxic Damage Activates the AMPK-α1 Isoform in the Nucleus via Ca2+/CaMKK2 Signaling to Enhance Tumor Cell Survival. *Molecular Cancer Research* **16**, 345–357 (2018).
61. Li, S. *et al.* Ca2+-Stimulated AMPK-Dependent Phosphorylation of Exo1 Protects Stressed Replication Forks from Aberrant Resection. *Molecular Cell* **74**, 1123-1137.e6 (2019).

62. Jiang, W. *et al.* A mitochondrial EglN1-AMPKα axis drives breast cancer progression by enhancing metabolic adaptation to hypoxic stress. *The EMBO Journal* **42**, e113743 (2023).
63. Anderson, K. A. *et al.* Hypothalamic CaMKK2 contributes to the regulation of energy balance. *Cell Metab* **7**, 377–388 (2008).
64. Yang, Y., Atasoy, D., Su, H. H. & Sternson, S. M. Hunger states switch a flip-flop memory circuit via a synaptic AMPK-dependent positive feedback loop. *Cell* **146**, 992–1003 (2011).
65. Hedman, A. C. *et al.* IQGAP1 binds AMPK and is required for maximum AMPK activation. *J Biol Chem* **296**, 100075 (2021).
66. Momcilovic, M., Hong, S.-P. & Carlson, M. Mammalian TAK1 activates Snf1 protein kinase in yeast and phosphorylates AMP-activated protein kinase in vitro. *J Biol Chem* **281**, 25336–25343 (2006).
67. Neumann, D. Is TAK1 a Direct Upstream Kinase of AMPK? *Int J Mol Sci* **19**, 2412 (2018).
68. Jia, J. *et al.* AMPK, a Regulator of Metabolism and Autophagy, Is Activated by Lysosomal Damage via a Novel Galectin-Directed Ubiquitin Signal Transduction System. *Molecular Cell* **77**, 951-969.e9 (2020).
69. Galic, S. *et al.* Hematopoietic AMPK beta 1 reduces mouse adipose tissue macrophage inflammation and insulin resistance in obesity. *Journal of Clinical Investigation* **121**, 4903–4915 (2011).
70. Gong, H. *et al.* Nrf2-SHP Cascade-Mediated STAT3 Inactivation Contributes to AMPK-Driven Protection Against Endotoxic Inflammation. *Front Immunol* **11**, 414 (2020).
71. Liu, Y., Wang, T. V., Cui, Y., Gao, S. & Rao, Y. Biochemical purification uncovers mammalian sterile 3 (MST3) as a new protein kinase for multifunctional protein kinases AMPK and SIK3. *J Biol Chem* **298**, 101929 (2022).
72. Liu, Y. *et al.* STE20 phosphorylation of AMPK-related kinases revealed by biochemical purifications combined with genetics. *J Biol Chem* **298**, 101928 (2022).
73. Zhou, X., Mehta, S. & Zhang, J. Genetically Encodable Fluorescent and Bioluminescent Biosensors Light Up Signaling Networks. *Trends Biochem.Sci.* **45**, 889–905 (2020).
74. Tsou, L., Zheng, B., Hsu, C.-H., Sasaki, A. T. & Cantley, L. C. A Fluorescent Reporter of AMPK Activity and Cellular Energy Stress. *Cell Metab.* **13**, 476–486 (2011).
75. Konagaya, Y. *et al.* A Highly Sensitive FRET Biosensor for AMPK Exhibits Heterogeneous AMPK Responses among Cells and Organs. *Cell Reports* **21**, 2628–2638 (2017).
76. Hung, Y. P. *et al.* Akt regulation of glycolysis mediates bioenergetic stability in epithelial cells. *eLife* **6**, e27293 (2017).
77. Kosaisawe, N., Sparta, B., Pargett, M., Teragawa, C. K. & Albeck, J. G. Transient phases of OXPHOS inhibitor resistance reveal underlying metabolic heterogeneity in single cells. *Cell Metab* **33**, 649-665.e8 (2021).
78. Sample, V., Ramamurthy, S., Gorshkov, K., Ronnett, G. V. & Zhang, J. Polarized activities of AMPK and BRSK in primary hippocampal neurons. *Mol Biol Cell* **26**, 1935–1946 (2015).
79. Miyamoto, T. *et al.* Compartmentalized AMPK Signaling Illuminated by Genetically Encoded Molecular Sensors and Actuators. *Cell Reports* **11**, 657–670 (2015).
80. Pelosse, M. *et al.* Synthetic energy sensor AMPfret deciphers adenylate-dependent AMPK activation mechanism. *Nat Commun* **10**, 1038 (2019).
81. Schmitt, D. L. *et al.* Spatial regulation of AMPK signaling revealed by a sensitive kinase activity reporter. *Nat Commun* **13**, 3856 (2022).
82. Zhang, Q. *et al.* AMPK directly phosphorylates TBK1 to integrate glucose sensing into innate immunity. *Molecular Cell* (2022) doi:10.1016/j.molcel.2022.10.026.
83. He, J. *et al.* Two-photon AMPK and ATP imaging reveals the bias between rods and cones in glycolysis utility. *Faseb J.* **35**, e21880 (2021).
84. Guo, Y., Steele, H. E., Li, B.-Y. & Na, S. Fluid flow-induced activation of subcellular AMPK and its interaction with FAK and Src. *Arch. Biochem. Biophys.* **679**, 108208 (2020).

85. Hatsuda, A. *et al.* Calcium signals tune AMPK activity and mitochondrial homeostasis in dendrites of developing neurons. *Development* **150**, dev201930 (2023).
86. Yang, J.-M. *et al.* Deciphering cell signaling networks with massively multiplexed biosensor barcoding. *Cell* **184**, 6193-6206.e14 (2021).
87. Resh, M. D. Fatty acylation of proteins: The long and the short of it. *Progress in Lipid Research* **63**, 120–131 (2016).
88. Warden, S. M. *et al.* Post-translational modifications of the beta-1 subunit of AMP-activated protein kinase affect enzyme activity and cellular localization. *Biochem J* **354**, 275–283 (2001).
89. Zhang, C.-S. *et al.* The lysosomal v-ATPase-Ragulator complex is a common activator for AMPK and mTORC1, acting as a switch between catabolism and anabolism. *Cell Metab.* **20**, 526–540 (2014).
90. Zhang, C.-S. *et al.* Fructose-1,6-bisphosphate and aldolase mediate glucose sensing by AMPK. *Nature* **548**, 112–116 (2017).
91. Liang, J. Y. *et al.* Myristoylation confers noncanonical AMPK functions in autophagy selectivity and mitochondrial surveillance. *Nature Communications* **6**, (2015).
92. Neopane, K. *et al.* Blocking AMPK β1 myristoylation enhances AMPK activity and protects mice from high-fat diet-induced obesity and hepatic steatosis. *Cell Reports* **41**, 111862 (2022).
93. de Buhr, S. & Gräter, F. Myristoyl's dual role in allosterically regulating and localizing Abl kinase. *Elife* **12**, e85216 (2023).
94. Yang, C. *et al.* De novo pyrimidine biosynthetic complexes support cancer cell proliferation and ferroptosis defence. *Nat Cell Biol* **25**, 836–847 (2023).
95. Alberti, S., Gladfelter, A. & Mittag, T. Considerations and Challenges in Studying Liquid-Liquid Phase Separation and Biomolecular Condensates. *Cell* **176**, 419–434 (2019).
96. Li, Q. *et al.* CircACC1 Regulates Assembly and Activation of AMPK Complex under Metabolic Stress. *Cell Metab* **30**, 157-173.e7 (2019).
97. Wen, Z. *et al.* N-myristoyltransferase deficiency impairs activation of kinase AMPK and promotes synovial tissue inflammation. *Nature Immunology* **20**, 313 (2019).
98. Sun, Y. & Du, K. DHHC17 Is a New Regulator of AMPK Signaling. *Molecular and Cellular Biology* **42**, e00131-22 (2022).
99. Göransson, O. *et al.* Mechanism of Action of A-769662, a Valuable Tool for Activation of AMP-activated Protein Kinase*. *Journal of Biological Chemistry* **282**, 32549–32560 (2007).
100. Hawley, S. A. *et al.* The Ancient Drug Salicylate Directly Activates AMP-Activated Protein Kinase. *Science* **336**, 918–922 (2012).
101. Yang, H. *et al.* Remodelling of the translatome controls diet and its impact on tumorigenesis. *Nature* **633**, 189–197 (2024).
102. Li, M. *et al.* Transient Receptor Potential V Channels Are Essential for Glucose Sensing by Aldolase and AMPK. *Cell Metabolism* **30**, 508-524.e12 (2019).
103. Zhang, Y.-L. *et al.* AMP as a low-energy charge signal autonomously initiates assembly of AXIN-AMPK-LKB1 complex for AMPK activation. *Cell Metab.* **18**, 546–555 (2013).
104. Orozco, J. M. *et al.* Dihydroxyacetone phosphate signals glucose availability to mTORC1. *Nat Metab* **2**, 893–901 (2020).
105. Ma, T. *et al.* Low-dose metformin targets the lysosomal AMPK pathway through PEN2. *Nature* **603**, 159–165 (2022).
106. Zhang, C.-S. *et al.* The aldolase inhibitor aldometanib mimics glucose starvation to activate lysosomal AMPK. *Nat Metab* **4**, 1369–1401 (2022).
107. Zong, Y. *et al.* Hierarchical activation of compartmentalized pools of AMPK depends on severity of nutrient or energy stress. *Cell Res* **29**, 460–473 (2019).
108. Hsu, C.-C. *et al.* Inositol serves as a natural inhibitor of mitochondrial fission by directly targeting AMPK. *Molecular Cell* **81**, 3803-3819.e7 (2021).
109. Lin, R. *et al.* 6-Phosphogluconate dehydrogenase links oxidative PPP, lipogenesis and tumour growth by inhibiting LKB1-AMPK signalling. *Nat. Cell Biol.* **17**, 1484–1496 (2015).

110. Gao, X. *et al.* γ-6-Phosphogluconolactone, a Byproduct of the Oxidative Pentose Phosphate Pathway, Contributes to AMPK Activation through Inhibition of PP2A. *Mol Cell* **76**, 857-871.e9 (2019).
111. Hoffman, N. J. *et al.* Genetic loss of AMPK-glycogen binding destabilizes AMPK and disrupts metabolism. *Molecular Metabolism* 101048 (2020) doi:10.1016/j.molmet.2020.101048.
112. Jin, X. *et al.* Glucose-6-phosphate dehydrogenase exerts antistress effects independently of its enzymatic activity. *J Biol Chem* **298**, 102587 (2022).
113. Horman, S. *et al.* Insulin antagonizes ischemia-induced Thr172 phosphorylation of AMP-activated protein kinase alpha-subunits in heart via hierarchical phosphorylation of Ser485/491. *J Biol Chem* **281**, 5335–5340 (2006).
114. Berggreen, C., Gormand, A., Omar, B., Degerman, E. & Göransson, O. Protein kinase B activity is required for the effects of insulin on lipid metabolism in adipocytes. *Am J Physiol Endocrinol Metab* **296**, E635-646 (2009).
115. Hawley, S. A. *et al.* Phosphorylation by Akt within the ST loop of AMPK-α1 down-regulates its activation in tumour cells. *Biochem J* **459**, 275–287 (2014).
116. Valentine, R. J., Coughlan, K. A., Ruderman, N. B. & Saha, A. K. Insulin inhibits AMPK activity and phosphorylates AMPK $Ser^{485/491}$ through Akt in hepatocytes, myotubes and incubated rat skeletal muscle. *Arch Biochem Biophys* **562**, 62–69 (2014).
117. Kopietz, F. *et al.* Inhibition of AMPK activity in response to insulin in adipocytes: involvement of AMPK pS485, PDEs, and cellular energy levels. *Am J Physiol Endocrinol Metab* **319**, E459–E471 (2020).
118. Koh, A. *et al.* Microbial Imidazole Propionate Affects Responses to Metformin through p38γ-Dependent Inhibitory AMPK Phosphorylation. *Cell Metab* **32**, 643-653.e4 (2020).
119. Dagon, Y. *et al.* p70S6 kinase phosphorylates AMPK on serine 491 to mediate leptin's effect on food intake. *Cell Metab* **16**, 104–112 (2012).
120. Zhou, B. *et al.* Serum- and glucocorticoid-induced kinase drives hepatic insulin resistance by directly inhibiting AMP-activated protein kinase. *Cell Reports* **37**, 109785 (2021).
121. Heathcote, H. R. *et al.* Protein kinase C phosphorylates AMP-activated protein kinase α1 Ser487. *Biochem J* **473**, 4681–4697 (2016).
122. Djouder, N. *et al.* PKA phosphorylates and inactivates AMPKalpha to promote efficient lipolysis. *EMBO J* **29**, 469–481 (2010).
123. Hurley, R. L. *et al.* Regulation of AMP-activated protein kinase by multisite phosphorylation in response to agents that elevate cellular cAMP. *J Biol Chem* **281**, 36662–36672 (2006).
124. Coughlan, K. A. *et al.* PKD1 Inhibits AMPKα2 through Phosphorylation of Serine 491 and Impairs Insulin Signaling in Skeletal Muscle Cells. *J Biol Chem* **291**, 5664–5675 (2016).
125. Löffler, M. C. *et al.* Protein kinase D1 deletion in adipocytes enhances energy dissipation and protects against adiposity. *EMBO J* **37**, e99182 (2018).
126. Ling, N. X. Y. *et al.* mTORC1 directly inhibits AMPK to promote cell proliferation under nutrient stress. *Nat Metab* **2**, 41–49 (2020).
127. Morrison, K. R. *et al.* An AMPKa2-specific phospho-switch controls lysosomal targeting for activation. *Cell Reports* **38**, 110365 (2022).
128. Puustinen, P. *et al.* DNA-dependent protein kinase regulates lysosomal AMP-dependent protein kinase activation and autophagy. *Autophagy* **16**, 1871–1888 (2020).
129. Pearah, A. *et al.* Blocking AMPKαS496 phosphorylation improves mitochondrial dynamics and hyperglycemia in aging and obesity. *Cell Chem Biol* **30**, 1585-1600.e6 (2023).
130. Suzuki, T. *et al.* Inhibition of AMPK Catabolic Action by GSK3. *Molecular Cell* **50**, 407–419 (2013).
131. Han, X. *et al.* Negative regulation of AMPKα1 by PIM2 promotes aerobic glycolysis and tumorigenesis in endometrial cancer. *Oncogene* **38**, 6537–6549 (2019).

132. Woods, A. *et al.* Identification of phosphorylation sites in AMP-activated protein kinase (AMPK) for upstream AMPK kinases and study of their roles by site-directed mutagenesis. *J. Biol. Chem.* **278**, 28434–28442 (2003).
133. Chen, Y.-L. *et al.* Protein phosphatase 5 promotes hepatocarcinogenesis through interaction with AMP-activated protein kinase. *Biochem Pharmacol* **138**, 49–60 (2017).
134. Behera, S. *et al.* ERK1/2 activated PHLPP1 induces skeletal muscle ER stress through the inhibition of a novel substrate AMPK. *Biochim Biophys Acta Mol Basis Dis* **1864**, 1702–1716 (2018).
135. Xu, X. *et al.* Nuclear UHRF1 is a gate-keeper of cellular AMPK activity and function. *Cell Res* **32**, 54–71 (2022).
136. Yan, Y. *et al.* Phosphatase PHLPP2 regulates the cellular response to metabolic stress through AMPK. *Cell Death Dis* **12**, 1–10 (2021).
137. Deng, L., Lee, M. E., Schutt, K. L. & Moseley, J. B. Phosphatases Generate Signal Specificity Downstream of Ssp1 Kinase in Fission Yeast. *Mol Cell Biol* **37**, e00494-16 (2017).
138. Yang, Y. *et al.* SAPS3 subunit of protein phosphatase 6 is an AMPK inhibitor and controls metabolic homeostasis upon dietary challenge in male mice. *Nat Commun* **14**, 1368 (2023).
139. Ren, Y. & Shen, H.-M. Critical role of AMPK in redox regulation under glucose starvation. *Redox Biol* **25**, 101154 (2019).
140. Zmijewski, J. W. *et al.* Exposure to hydrogen peroxide induces oxidation and activation of AMP-activated protein kinase. *J Biol Chem* **285**, 33154–33164 (2010).
141. Emerling, B. M. *et al.* Hypoxic activation of AMPK is dependent on mitochondrial ROS but independent of an increase in AMP/ATP ratio. *Free Radical Biology and Medicine* **46**, 1386–1391 (2009).
142. Choi, S. L. *et al.* The regulation of AMP-activated protein kinase by H2O2. *Biochem. Biophys. Res. Commun.* **287**, 92–97 (2001).
143. Hawley, S. A. *et al.* Use of cells expressing gamma subunit variants to identify diverse mechanisms of AMPK activation. *Cell Metab.* **11**, 554–565 (2010).
144. Auciello, F. R., Ross, F. A., Ikematsu, N. & Hardie, D. G. Oxidative stress activates AMPK in cultured cells primarily by increasing cellular AMP and/or ADP. *FEBS Lett.* **588**, 3361–3366 (2014).
145. Hinchy, E. C. *et al.* Mitochondria-derived ROS activate AMP-activated protein kinase (AMPK) indirectly. *J Biol Chem* **293**, 17208–17217 (2018).
146. Shao, D. *et al.* A redox-dependent mechanism for regulation of AMPK activation by Thioredoxin1 during energy starvation. *Cell Metab.* **19**, 232–245 (2014).
147. Xiao, H. *et al.* A Quantitative Tissue-Specific Landscape of Protein Redox Regulation during Aging. *Cell* **180**, 968-983.e24 (2020).
148. Shen, K. *et al.* Mitochondria as Cellular and Organismal Signaling Hubs. *Annual Review of Cell and Developmental Biology* **38**, 179–218 (2022).
149. Dite, T. A. *et al.* The autophagy initiator ULK1 sensitizes AMPK to allosteric drugs. *Nat Commun* **8**, 571 (2017).
150. Byrne, D. P. *et al.* Aurora A regulation by reversible cysteine oxidation reveals evolutionarily conserved redox control of Ser/Thr protein kinase activity. *Sci Signal* **13**, eaax2713 (2020).
151. Bendzunas, G. N. *et al.* Redox Regulation of Brain Selective Kinases BRSK1/2: Implications for Dynamic Control of the Eukaryotic AMPK family through Cys-based mechanisms. *bioRxiv* 2023.10.05.561145 (2024) doi:10.1101/2023.10.05.561145.
152. Drake, J. C. *et al.* Mitochondria-localized AMPK responds to local energetics and contributes to exercise and energetic stress-induced mitophagy. *Proc. Natl. Acad. Sci. U. S. A.* **118**, e2025932118 (2021).
153. Tilokani, L. *et al.* AMPK-dependent phosphorylation of MTFR1L regulates mitochondrial morphology. *Science Advances* **8**, eabo7956 (2022).
154. Abu-Elheiga, L. *et al.* The subcellular localization of acetyl-CoA carboxylase 2. *Proceedings of the National Academy of Sciences* **97**, 1444–1449 (2000).

155. Fullerton, M. D. *et al.* Single phosphorylation sites in Acc1 and Acc2 regulate lipid homeostasis and the insulin-sensitizing effects of metformin. *Nature medicine* **19**, 1649–54 (2013).
156. Toyama, E. Q. *et al.* AMP-activated protein kinase mediates mitochondrial fission in response to energy stress. *Science* **351**, 275–281 (2016).
157. Chen, Z. *et al.* Global phosphoproteomic analysis reveals ARMC10 as an AMPK substrate that regulates mitochondrial dynamics. *Nat Commun* **10**, 104 (2019).
158. Hoffman, N. J. *et al.* Global Phosphoproteomic Analysis of Human Skeletal Muscle Reveals a Network of Exercise-Regulated Kinases and AMPK Substrates. *Cell Metab* **22**, 922–935 (2015).
159. Zhao, H. *et al.* AMPK-mediated activation of MCU stimulates mitochondrial Ca2+ entry to promote mitotic progression. *Nat Cell Biol* **21**, 476–486 (2019).
160. Cai, Z. *et al.* Phosphorylation of PDHA by AMPK Drives TCA Cycle to Promote Cancer Metastasis. *Mol Cell* **80**, 263-278.e7 (2020).
161. Hung, C.-M. *et al.* AMPK/ULK1-mediated phosphorylation of Parkin ACT domain mediates an early step in mitophagy. *Sci. Adv.* **7**, eabg4544 (2021).
162. Kleele, T. *et al.* Distinct fission signatures predict mitochondrial degradation or biogenesis. *Nature* **593**, 435–439 (2021).
163. Friedman, J. R. *et al.* ER tubules mark sites of mitochondrial division. *Science* **334**, 358–362 (2011).
164. Ngo, J. *et al.* Mitochondrial morphology controls fatty acid utilization by changing CPT1 sensitivity to malonyl-CoA. *EMBO J* **42**, e111901 (2023).
165. Lu, J. *et al.* Types of nuclear localization signals and mechanisms of protein import into the nucleus. *Cell Communication and Signaling* **19**, 60 (2021).
166. Kazgan, N., Williams, T., Forsberg, L. J. & Brenman, J. E. Identification of a Nuclear Export Signal in the Catalytic Subunit of AMP-activated Protein Kinase. *Mol Biol Cell* **21**, 3433–3442 (2010).
167. Salt, I. *et al.* AMP-activated protein kinase: greater AMP dependence, and preferential nuclear localization, of complexes containing the alpha2 isoform. *Biochem. J.* **334 (Pt 1)**, 177–187 (1998).
168. Suzuki, A. *et al.* Leptin Stimulates Fatty Acid Oxidation and Peroxisome Proliferator-Activated Receptor α Gene Expression in Mouse C2C12 Myoblasts by Changing the Subcellular Localization of the α2 Form of AMP-Activated Protein Kinase. *Molecular and Cellular Biology* **27**, 4317–4327 (2007).
169. Karacosta, L. G., Foster, B. A., Azabdaftari, G., Feliciano, D. M. & Edelman, A. M. A Regulatory Feedback Loop Between Ca2+/Calmodulin-dependent Protein Kinase Kinase 2 (CaMKK2) and the Androgen Receptor in Prostate Cancer Progression*. *Journal of Biological Chemistry* **287**, 24832–24843 (2012).
170. Cheratta, A. R. *et al.* Caspase cleavage and nuclear retention of the energy sensor AMPK-a1 during apoptosis. *Cell Reports* **39**, 110761 (2022).
171. Pineda, C. T. *et al.* Degradation of AMPK by a Cancer-Specific Ubiquitin Ligase. *Cell* **160**, 715–728 (2015).
172. Vila, I. K. *et al.* A UBE2O-AMPKα2 Axis that Promotes Tumor Initiation and Progression Offers Opportunities for Therapy. *Cancer Cell* **31**, 208–224 (2017).
173. Vila, I. K. *et al.* A muscle-specific UBE2O/AMPKα2 axis promotes insulin resistance and metabolic syndrome in obesity. *JCI Insight* **4**, e128269, 128269 (2019).
174. Lee, J. O. *et al.* E3 ubiquitin ligase, WWP1, interacts with AMPKα2 and down-regulates its expression in skeletal muscle C2C12 cells. *J Biol Chem* **288**, 4673–4680 (2013).
175. Jiang, P. *et al.* Negative regulation of AMPK signaling by high glucose via E3 ubiquitin ligase MG53. *Mol. Cell* **81**, (2021).
176. Lee, M.-S. *et al.* Loss of the E3 ubiquitin ligase MKRN1 represses diet-induced metabolic syndrome through AMPK activation. *Nat Commun* **9**, 1–14 (2018).
177. Kwon, E., Li, X., Deng, Y., Chang, H. W. & Kim, D. Y. AMPK is down-regulated by the CRL4A-CRBN axis through the polyubiquitination of AMPKα isoforms. *The FASEB Journal* **33**, 6539–6550 (2019).

178. Yang, S.-J. *et al.* Ubiquitin-dependent proteasomal degradation of AMPK gamma subunit by Cereblon inhibits AMPK activity. *Biochim Biophys Acta Mol Cell Res* **1867**, 118729 (2020).
179. Qi, J. *et al.* Downregulation of AMP-activated protein kinase by Cidea-mediated ubiquitination and degradation in brown adipose tissue. *The EMBO Journal* **27**, 1537–1548 (2008).
180. Moreno, D., Towler, M. C., Hardie, D. G., Knecht, E. & Sanz, P. The laforin-malin complex, involved in Lafora disease, promotes the incorporation of K63-linked ubiquitin chains into AMP-activated protein kinase beta subunits. *Mol Biol Cell* **21**, 2578–2588 (2010).
181. Liu, H. *et al.* The GID ubiquitin ligase complex is a regulator of AMPK activity and organismal lifespan. *Autophagy* **0**, 1–17 (2019).
182. Liu, Y. *et al.* A Fbxo48 inhibitor prevents pAMPKα degradation and ameliorates insulin resistance. *Nature Chemical Biology* **17**, 298–306 (2021).
183. Elbæk, C. R. *et al.* M1-linked Ubiquitination by LUBAC Regulates AMPK Activity and the Response to Energetic Stress. 2024.11.08.622598 Preprint at https://doi.org/10.1101/2024.11.08.622598 (2024).
184. Zhang, F.-K. *et al.* Targeting USP9X–AMPK Axis in ARID1A-Deficient Hepatocellular Carcinoma. *Cellular and Molecular Gastroenterology and Hepatology* **14**, 101–127 (2022).
185. Al-Hakim, A. K. *et al.* Control of AMPK-related kinases by USP9X and atypical Lys(29)/Lys(33)-linked polyubiquitin chains. *Biochem. J.* **411**, 249–260 (2008).
186. Deng, M. *et al.* Deubiquitination and Activation of AMPK by USP10. *Mol. Cell* **61**, 614–624 (2016).
187. Henning, N. J. *et al.* Deubiquitinase-targeting chimeras for targeted protein stabilization. *Nat Chem Biol* **18**, 412–421 (2022).
188. Liu, J. *et al.* USP7-Based Deubiquitinase-Targeting Chimeras Stabilize AMPK. *J Am Chem Soc* (2024) doi:10.1021/jacs.4c02373.
189. Rubio, T., Vernia, S. & Sanz, P. Sumoylation of AMPKβ2 subunit enhances AMP-activated protein kinase activity. *Mol Biol Cell* **24**, 1801–1811, S1-4 (2013).
190. Yan, Y. *et al.* SUMOylation of AMPKα1 by PIAS4 specifically regulates mTORC1 signalling. *Nat Commun* **6**, 8979 (2015).
191. Dou, X. *et al.* The protease SENP2 controls hepatic gluconeogenesis by regulating the SUMOylation of the fuel sensor AMPKα. *J Biol Chem* **298**, 101544 (2022).
192. Sullivan, J. E. *et al.* Inhibition of lipolysis and lipogenesis in isolated rat adipocytes with AICAR, a cell-permeable activator of AMP-activated protein kinase. *FEBS Lett.* **353**, 33–36 (1994).
193. Višnjić, D., Lalić, H., Dembitz, V., Tomić, B. & Smoljo, T. AICAr, a Widely Used AMPK Activator with Important AMPK-Independent Effects: A Systematic Review. *Cells* **10**, 1095 (2021).
194. Foretz, M., Guigas, B. & Viollet, B. Metformin: update on mechanisms of action and repurposing potential. *Nat Rev Endocrinol* **19**, 460–476 (2023).
195. Malik, N. *et al.* Induction of lysosomal and mitochondrial biogenesis by AMPK phosphorylation of FNIP1. *Science* **380**, eabj5559 (2023).
196. Cool, B. *et al.* Identification and characterization of a small molecule AMPK activator that treats key components of type 2 diabetes and the metabolic syndrome. *Cell Metabolism* **3**, 403–416 (2006).
197. Sanders, M. J. *et al.* Defining the mechanism of activation of AMP-activated protein kinase by the small molecule A-769662, a member of the thienopyridone family. *J Biol Chem* **282**, 32539–32548 (2007).
198. Xiao, B. *et al.* Structural basis of AMPK regulation by small molecule activators. *Nat Commun* **4**, 3017 (2013).
199. Myers, R. W. *et al.* Systemic pan-AMPK activator MK-8722 improves glucose homeostasis but induces cardiac hypertrophy. *Science* **357**, 507–511 (2017).
200. Cokorinos, E. C. *et al.* Activation of Skeletal Muscle AMPK Promotes Glucose Disposal and Glucose Lowering in Non-human Primates and Mice. *Cell Metab* **25**, 1147-1159.e10 (2017).

201. Rawlins, J., Bhan, A. & Sharma, S. Left ventricular hypertrophy in athletes. *Eur J Echocardiogr* **10**, 350–356 (2009).
202. Ngoei, K. R. W. *et al.* Structural Determinants for Small-Molecule Activation of Skeletal Muscle AMPK α2β2γ1 by the Glucose Importagog SC4. *Cell Chemical Biology* **25**, 728-737.e9 (2018).
203. Vara-Ciruelos, D., Russell, F. M. & Hardie, D. G. The strange case of AMPK and cancer: Dr Jekyll or Mr Hyde? †. *Open Biol* **9**, 190099 (2019).
204. Zhou, G. *et al.* Role of AMP-activated protein kinase in mechanism of metformin action. *J Clin Invest* **108**, 1167–1174 (2001).
205. Yu, P. B. *et al.* Dorsomorphin inhibits BMP signals required for embryogenesis and iron metabolism. *Nat Chem Biol* **4**, 33–41 (2008).
206. Vogt, J., Traynor, R. & Sapkota, G. P. The specificities of small molecule inhibitors of the TGFß and BMP pathways. *Cell Signal* **23**, 1831–1842 (2011).
207. Dite, T. A. *et al.* AMP-activated protein kinase selectively inhibited by the type II inhibitor SBI-0206965. *J Biol Chem* **293**, 8874–8885 (2018).
208. Egan, D. F. *et al.* Small Molecule Inhibition of the Autophagy Kinase ULK1 and Identification of ULK1 Substrates. *Mol Cell* **59**, 285–297 (2015).
209. Hawley, S. A., Russell, F. M., Ross, F. A. & Hardie, D. G. BAY-3827 and SBI-0206965: Potent AMPK Inhibitors That Paradoxically Increase Thr172 Phosphorylation. *Int J Mol Sci* **25**, 453 (2023).
210. Roth, G. A. *et al.* Global Burden of Cardiovascular Diseases and Risk Factors, 1990-2019: Update From the GBD 2019 Study. *J Am Coll Cardiol* **76**, 2982–3021 (2020).
211. Anitschkow, N. Arteriosclerosis: A Survey of the Problem. *Journal of the American Medical Association* **101**, 1023 (1933).
212. Gofman, J. W., Lindgren, F. T. & Elliott, H. Ultracentrifugal studies of lipoproteins of human serum. *J Biol Chem* **179**, 973–979 (1949).
213. Goldstein, J. L. & Brown, M. S. Familial hypercholesterolemia: identification of a defect in the regulation of 3-hydroxy-3-methylglutaryl coenzyme A reductase activity associated with overproduction of cholesterol. *Proc Natl Acad Sci U S A* **70**, 2804–2808 (1973).
214. Ross, R. Atherosclerosis--an inflammatory disease. *N Engl J Med* **340**, 115–126 (1999).
215. Minelli, S., Minelli, P. & Montinari, M. R. Reflections on Atherosclerosis: Lesson from the Past and Future Research Directions. *J Multidiscip Healthc* **13**, 621–633 (2020).
216. Berndsen, Z. T. & Cassidy, C. K. The structure of apolipoprotein B100 from human low-density lipoprotein. *Nature* **638**, 836–843 (2025).
217. Skålén, K. *et al.* Subendothelial retention of atherogenic lipoproteins in early atherosclerosis. *Nature* **417**, 750–754 (2002).
218. Steinbrecher, U. P., Parthasarathy, S., Leake, D. S., Witztum, J. L. & Steinberg, D. Modification of low density lipoprotein by endothelial cells involves lipid peroxidation and degradation of low density lipoprotein phospholipids. *Proc Natl Acad Sci U S A* **81**, 3883–3887 (1984).
219. Watson, A. D. *et al.* Structural identification by mass spectrometry of oxidized phospholipids in minimally oxidized low density lipoprotein that induce monocyte/endothelial interactions and evidence for their presence in vivo. *J Biol Chem* **272**, 13597–13607 (1997).
220. Boring, L., Gosling, J., Cleary, M. & Charo, I. F. Decreased lesion formation in CCR2−/− mice reveals a role for chemokines in the initiation of atherosclerosis. *Nature* **394**, 894–897 (1998).
221. Combadière, C. *et al.* Combined inhibition of CCL2, CX3CR1, and CCR5 abrogates Ly6C(hi) and Ly6C(lo) monocytosis and almost abolishes atherosclerosis in hypercholesterolemic mice. *Circulation* **117**, 1649–1657 (2008).
222. Soehnlein, O. *et al.* Distinct functions of chemokine receptor axes in the atherogenic mobilization and recruitment of classical monocytes. *EMBO Mol Med* **5**, 471–481 (2013).
223. Lim, H. Y. *et al.* Hyaluronan Receptor LYVE-1-Expressing Macrophages Maintain Arterial Tone through Hyaluronan-Mediated Regulation of Smooth Muscle Cell Collagen. *Immunity* **49**, 326-341.e7 (2018).

224. Williams, J. W. *et al.* Limited proliferation capacity of aortic intima resident macrophages requires monocyte recruitment for atherosclerotic plaque progression. *Nat Immunol* **21**, 1194–1204 (2020).
225. Ensan, S. *et al.* Self-renewing resident arterial macrophages arise from embryonic CX3CR1(+) precursors and circulating monocytes immediately after birth. *Nat Immunol* **17**, 159–168 (2016).
226. Robbins, C. S. *et al.* Local proliferation dominates lesional macrophage accumulation in atherosclerosis. *Nat Med* **19**, 1166–1172 (2013).
227. Duewell, P. *et al.* NLRP3 inflammasomes are required for atherogenesis and activated by cholesterol crystals. *Nature* **464**, 1357–1361 (2010).
228. Sheedy, F. J. *et al.* CD36 coordinates NLRP3 inflammasome activation by facilitating intracellular nucleation of soluble ligands into particulate ligands in sterile inflammation. *Nat Immunol* **14**, 812–820 (2013).
229. Westerterp, M. *et al.* Cholesterol Efflux Pathways Suppress Inflammasome Activation, NETosis, and Atherogenesis. *Circulation* **138**, 898–912 (2018).
230. Castellano, B. M. *et al.* Lysosomal cholesterol activates mTORC1 via an SLC38A9-Niemann-Pick C1 signaling complex. *Science* **355**, 1306–1311 (2017).
231. Zhang, X. *et al.* High-protein diets increase cardiovascular risk by activating macrophage mTOR to suppress mitophagy. *Nat Metab* **2**, 110–125 (2020).
232. Zhang, X. *et al.* Identification of a leucine-mediated threshold effect governing macrophage mTOR signalling and cardiovascular risk. *Nat Metab* **6**, 359–377 (2024).
233. Karunakaran, D. *et al.* RIPK1 Expression Associates With Inflammation in Early Atherosclerosis in Humans and Can Be Therapeutically Silenced to Reduce NF-κB Activation and Atherogenesis in Mice. *Circulation* **143**, 163–177 (2021).
234. Allahverdian, S., Chehroudi, A. C., McManus, B. M., Abraham, T. & Francis, G. A. Contribution of intimal smooth muscle cells to cholesterol accumulation and macrophage-like cells in human atherosclerosis. *Circulation* **129**, 1551–1559 (2014).
235. Vengrenyuk, Y. *et al.* Cholesterol loading reprograms the microRNA-143/145-myocardin axis to convert aortic smooth muscle cells to a dysfunctional macrophage-like phenotype. *Arterioscler Thromb Vasc Biol* **35**, 535–546 (2015).
236. Wang, Y. *et al.* Smooth Muscle Cells Contribute the Majority of Foam Cells in ApoE (Apolipoprotein E)-Deficient Mouse Atherosclerosis. *Arterioscler Thromb Vasc Biol* **39**, 876–887 (2019).
237. Kim, K. *et al.* Transcriptome Analysis Reveals Nonfoamy Rather Than Foamy Plaque Macrophages Are Proinflammatory in Atherosclerotic Murine Models. *Circulation Research* **123**, 1127–1142 (2018).
238. De Meyer, G. R. Y., Zurek, M., Puylaert, P. & Martinet, W. Programmed death of macrophages in atherosclerosis: mechanisms and therapeutic targets. *Nat Rev Cardiol* **21**, 312–325 (2024).
239. Adkar, S. S. & Leeper, N. J. Efferocytosis in atherosclerosis. *Nat Rev Cardiol* **21**, 762–779 (2024).
240. Banerjee, C. & Chimowitz, M. I. Stroke Caused by Atherosclerosis of the Major Intracranial Arteries. *Circ Res* **120**, 502–513 (2017).
241. Swirski, F. K. *et al.* Ly-6Chi monocytes dominate hypercholesterolemia-associated monocytosis and give rise to macrophages in atheromata. *J Clin Invest* **117**, 195–205 (2007).
242. Yvan-Charvet, L. *et al.* ATP-binding cassette transporters and HDL suppress hematopoietic stem cell proliferation. *Science* **328**, 1689–1693 (2010).
243. Westerterp, M. *et al.* Regulation of hematopoietic stem and progenitor cell mobilization by cholesterol efflux pathways. *Cell Stem Cell* **11**, 195–206 (2012).
244. Rohde, D. *et al.* Bone marrow endothelial dysfunction promotes myeloid cell expansion in cardiovascular disease. *Nat Cardiovasc Res* **1**, 28–44 (2022).
245. Swirski, F. K. *et al.* Identification of Splenic Reservoir Monocytes and Their Deployment to Inflammatory Sites. *Science* **325**, 612–616 (2009).
246. Robbins, C. S. *et al.* Extramedullary Hematopoiesis Generates Ly-6C(high) Monocytes That Infiltrate Atherosclerotic Lesions. *Circulation* **125**, 364-U415 (2012).

247. Inra, C. N. *et al.* A perisinusoidal niche for extramedullary haematopoiesis in the spleen. *Nature* **527**, 466–471 (2015).
248. Divangahi, M. *et al.* Trained immunity, tolerance, priming and differentiation: distinct immunological processes. *Nat Immunol* **22**, 2–6 (2021).
249. Christ, A. *et al.* Western Diet Triggers NLRP3-Dependent Innate Immune Reprogramming. *Cell* **172**, 162-175.e14 (2018).
250. Bekkering, S. *et al.* Oxidized low-density lipoprotein induces long-term proinflammatory cytokine production and foam cell formation via epigenetic reprogramming of monocytes. *Arterioscler. Thromb. Vasc. Biol.* **34**, 1731–1738 (2014).
251. Edgar, L. *et al.* Hyperglycemia Induces Trained Immunity in Macrophages and Their Precursors and Promotes Atherosclerosis. *Circulation* **144**, 961–982 (2021).
252. Wakana, N. *et al.* Maternal high-fat diet exaggerates atherosclerosis in adult offspring by augmenting periaortic adipose tissue-specific proinflammatory response. *Arterioscler Thromb Vasc Biol* **35**, 558–569 (2015).
253. Li, K. *et al.* Maternal high-fat diet exacerbates atherosclerosis development in offspring through epigenetic memory. *Nat Cardiovasc Res* (2025) doi:10.1038/s44161-025-00622-4.
254. Jaiswal, S. *et al.* Clonal Hematopoiesis and Risk of Atherosclerotic Cardiovascular Disease. *N Engl J Med* **377**, 111–121 (2017).
255. Díez-Díez, M. *et al.* Unidirectional association of clonal hematopoiesis with atherosclerosis development. *Nat Med* **30**, 2857–2866 (2024).
256. Heyde, A. *et al.* Increased stem cell proliferation in atherosclerosis accelerates clonal hematopoiesis. *Cell* **184**, 1348-1361.e22 (2021).
257. Zekavat, S. M. *et al.* TP53-mediated clonal hematopoiesis confers increased risk for incident atherosclerotic disease. *Nat Cardiovasc Res* **2**, 144–158 (2023).
258. Yanagisawa, R. *et al.* The Impacts of Cholesterol, Oxysterols, and Cholesterol Lowering Dietary Compounds on the Immune System. *Int J Mol Sci* **23**, 12236 (2022).
259. Brown, M. S. & Goldstein, J. L. Receptor-mediated control of cholesterol metabolism. *Science* **191**, 150–154 (1976).
260. Brown, M. S., Goldstein, J. L., Krieger, M., Ho, Y. K. & Anderson, R. G. Reversible accumulation of cholesteryl esters in macrophages incubated with acetylated lipoproteins. *J Cell Biol* **82**, 597–613 (1979).
261. Moore, K. J. & Freeman, M. W. Scavenger receptors in atherosclerosis: beyond lipid uptake. *Arterioscler Thromb Vasc Biol* **26**, 1702–1711 (2006).
262. Lagace, T. A. *et al.* Secreted PCSK9 decreases the number of LDL receptors in hepatocytes and in livers of parabiotic mice. *J Clin Invest* **116**, 2995–3005 (2006).
263. Kwon, H. J., Lagace, T. A., McNutt, M. C., Horton, J. D. & Deisenhofer, J. Molecular basis for LDL receptor recognition by PCSK9. *Proc Natl Acad Sci U S A* **105**, 1820–1825 (2008).
264. Brown, M. S., Dana, S. E. & Goldstein, J. L. Receptor-dependent hydrolysis of cholesteryl esters contained in plasma low density lipoprotein. *Proc Natl Acad Sci U S A* **72**, 2925–2929 (1975).
265. Sleat, D. E. *et al.* Genetic evidence for nonredundant functional cooperativity between NPC1 and NPC2 in lipid transport. *Proc Natl Acad Sci U S A* **101**, 5886–5891 (2004).
266. Meiner, V. L. *et al.* Disruption of the acyl-CoA:cholesterol acyltransferase gene in mice: evidence suggesting multiple cholesterol esterification enzymes in mammals. *Proc Natl Acad Sci U S A* **93**, 14041–14046 (1996).
267. Dumesnil, C. *et al.* Cholesterol esters form supercooled lipid droplets whose nucleation is facilitated by triacylglycerols. *Nat Commun* **14**, 915 (2023).
268. Singh, R. *et al.* Autophagy regulates lipid metabolism. *Nature* **458**, 1131–1135 (2009).
269. Schott, M. B. *et al.* Lipid droplet size directs lipolysis and lipophagy catabolism in hepatocytes. *J Cell Biol* **218**, 3320–3335 (2019).
270. Wang, M. & Casey, P. J. Protein prenylation: unique fats make their mark on biology. *Nat Rev Mol Cell Biol* **17**, 110–122 (2016).

271. Endo, A., Kuroda, M. & Tsujita, Y. ML-236A, ML-236B, and ML-236C, new inhibitors of cholesterogenesis produced by Penicillium citrinium. *J Antibiot (Tokyo)* **29**, 1346–1348 (1976).
272. Collins, R. *et al.* Interpretation of the evidence for the efficacy and safety of statin therapy. *Lancet* **388**, 2532–2561 (2016).
273. Reynolds, G. A. *et al.* HMG CoA reductase: a negatively regulated gene with unusual promoter and 5' untranslated regions. *Cell* **38**, 275–285 (1984).
274. Goldstein, J. L. & Brown, M. S. REGULATION OF THE MEVALONATE PATHWAY. *Nature* **343**, 425–430 (1990).
275. Sever, N. *et al.* Insig-dependent ubiquitination and degradation of mammalian 3-hydroxy-3-methylglutaryl-CoA reductase stimulated by sterols and geranylgeraniol. *Journal of Biological Chemistry* **278**, 52479–52490 (2003).
276. Song, B.-L., Sever, N. & DeBose-Boyd, R. A. Gp78, a membrane-anchored ubiquitin ligase, associates with Insig-1 and couples sterol-regulated ubiquitination to degradation of HMG CoA reductase. *Mol Cell* **19**, 829–840 (2005).
277. Jo, Y., Lee, P. C. W., Sguigna, P. V. & DeBose-Boyd, R. A. Sterol-induced degradation of HMG CoA reductase depends on interplay of two Insigs and two ubiquitin ligases, gp78 and Trc8. *Proc Natl Acad Sci U S A* **108**, 20503–20508 (2011).
278. Menzies, S. A. *et al.* The sterol-responsive RNF145 E3 ubiquitin ligase mediates the degradation of HMG-CoA reductase together with gp78 and Hrd1. *Elife* **7**, e40009 (2018).
279. Sakai, J. *et al.* Sterol-regulated release of SREBP-2 from cell membranes requires two sequential cleavages, one within a transmembrane segment. *Cell* **85**, 1037–1046 (1996).
280. Radhakrishnan, A., Goldstein, J. L., McDonald, J. G. & Brown, M. S. Switch-like control of SREBP-2 transport triggered by small changes in ER cholesterol: a delicate balance. *Cell Metab* **8**, 512–521 (2008).
281. Yang, T. *et al.* Crucial step in cholesterol homeostasis: Sterols promote binding of SCAP to INSIG-1, a membrane protein that facilitates retention of SREBPs in ER. *Cell* **110**, 489–500 (2002).
282. Sakai, J. *et al.* Molecular identification of the sterol-regulated luminal protease that cleaves SREBPs and controls lipid composition of animal cells. *Mol Cell* **2**, 505–514 (1998).
283. Hua, X. *et al.* SREBP-2, a second basic-helix-loop-helix-leucine zipper protein that stimulates transcription by binding to a sterol regulatory element. *Proc Natl Acad Sci U S A* **90**, 11603–11607 (1993).
284. Kamisuki, S. *et al.* A small molecule that blocks fat synthesis by inhibiting the activation of SREBP. *Chem Biol* **16**, 882–892 (2009).
285. Wang, X. *et al.* Macrophage ABCA1 and ABCG1, but not SR-BI, promote macrophage reverse cholesterol transport in vivo. *J Clin Invest* **117**, 2216–2224 (2007).
286. Lehmann, J. M. *et al.* Activation of the nuclear receptor LXR by oxysterols defines a new hormone response pathway. *J Biol Chem* **272**, 3137–3140 (1997).
287. Venkateswaran, A. *et al.* Control of cellular cholesterol efflux by the nuclear oxysterol receptor LXRα. *Proceedings of the National Academy of Sciences* **97**, 12097–12102 (2000).
288. Venkateswaran, A. *et al.* Human white/murine ABC8 mRNA levels are highly induced in lipid-loaded macrophages. A transcriptional role for specific oxysterols. *J Biol Chem* **275**, 14700–14707 (2000).
289. Ouimet, M., Barrett, T. J. & Fisher, E. A. HDL and Reverse Cholesterol Transport. *Circ Res* **124**, 1505–1518 (2019).
290. Zhong, S. *et al.* Acetaldehyde dehydrogenase 2 interactions with LDLR and AMPK regulate foam cell formation. *J. Clin. Invest.* **129**, 252–267 (2019).
291. Ahmadian, M. *et al.* Desnutrin/ATGL Is Regulated by AMPK and Is Required for a Brown Adipose Phenotype. *Cell Metabolism* **13**, 739–748 (2011).
292. Kaushik, S. & Cuervo, A. M. AMPK-dependent phosphorylation of lipid droplet protein PLIN2 triggers its degradation by CMA. *Autophagy* **12**, 432–438 (2016).

293. Zhu, J. *et al.* Phosphorylation of PLIN3 by AMPK promotes dispersion of lipid droplets during starvation. *Protein & Cell* **10**, 382–387 (2019).
294. Liu, R. *et al.* Choline kinase alpha 2 acts as a protein kinase to promote lipolysis of lipid droplets. *Mol Cell* **81**, 2722-2735.e9 (2021).
295. Herms, A. *et al.* AMPK activation promotes lipid droplet dispersion on detyrosinated microtubules to increase mitochondrial fatty acid oxidation. *Nat Commun* **6**, 7176 (2015).
296. Pu, M. *et al.* ORP8 acts as a lipophagy receptor to mediate lipid droplet turnover. *Protein Cell* **14**, 653–667 (2023).
297. Sato, R., Goldstein, J. L. & Brown, M. S. Replacement of serine-871 of hamster 3-hydroxy-3-methylglutaryl-CoA reductase prevents phosphorylation by AMP-activated kinase and blocks inhibition of sterol synthesis induced by ATP depletion. *Proc Natl Acad Sci U S A* **90**, 9261–9265 (1993).
298. Han, Y. *et al.* Post-translational regulation of lipogenesis via AMPK-dependent phosphorylation of insulin-induced gene. *Nat Commun* **10**, 623 (2019).
299. Li, Y. *et al.* AMPK phosphorylates and inhibits SREBP activity to attenuate hepatic steatosis and atherosclerosis in diet-induced insulin-resistant mice. *Cell Metab.* **13**, 376–388 (2011).
300. Fullerton, M. D. *et al.* Salicylate improves macrophage cholesterol homeostasis via activation of Ampk. *J. Lipid Res.* **56**, 1025–1033 (2015).
301. Wang, J.-Q. *et al.* Inhibition of ASGR1 decreases lipid levels by promoting cholesterol excretion. *Nature* **608**, 413–420 (2022).
302. Li, D. *et al.* Adenosine Monophosphate-activated Protein Kinase Induces Cholesterol Efflux from Macrophage-derived Foam Cells and Alleviates Atherosclerosis in Apolipoprotein E-deficient Mice. *J. Biol. Chem.* **285**, 33499–33509 (2010).
303. Paigen, B., Morrow, A., Brandon, C., Mitchell, D. & Holmes, P. Variation in susceptibility to atherosclerosis among inbred strains of mice. *Atherosclerosis* **57**, 65–73 (1985).
304. Zhao, Y. *et al.* Small rodent models of atherosclerosis. *Biomed Pharmacother* **129**, 110426 (2020).
305. Greeve, J., Altkemper, I., Dieterich, J. H., Greten, H. & Windler, E. Apolipoprotein B mRNA editing in 12 different mammalian species: hepatic expression is reflected in low concentrations of apoB-containing plasma lipoproteins. *J Lipid Res* **34**, 1367–1383 (1993).
306. Brown, M. L. *et al.* Molecular basis of lipid transfer protein deficiency in a family with increased high-density lipoproteins. *Nature* **342**, 448–451 (1989).
307. Zhang, S. H., Reddick, R. L., Piedrahita, J. A. & Maeda, N. Spontaneous hypercholesterolemia and arterial lesions in mice lacking apolipoprotein E. *Science* **258**, 468–471 (1992).
308. Plump, A. S. *et al.* Severe hypercholesterolemia and atherosclerosis in apolipoprotein E-deficient mice created by homologous recombination in ES cells. *Cell* **71**, 343–353 (1992).
309. Ishibashi, S. *et al.* Hypercholesterolemia in low density lipoprotein receptor knockout mice and its reversal by adenovirus-mediated gene delivery. *J Clin Invest* **92**, 883–893 (1993).
310. Tani, M. *et al.* The influence of apoE-deficiency and LDL-receptor-deficiency on the HDL subpopulation profile in mice and in humans. *Atherosclerosis* **233**, 39–44 (2014).
311. Murphy, A. J. *et al.* ApoE regulates hematopoietic stem cell proliferation, monocytosis, and monocyte accumulation in atherosclerotic lesions in mice. *J Clin Invest* **121**, 4138–4149 (2011).
312. Linton, M. F., Atkinson, J. B. & Fazio, S. Prevention of Atherosclerosis in Apolipoprotein E-Deficient Mice by Bone Marrow Transplantation. *Science* **267**, 1034–1037 (1995).
313. Abifadel, M. *et al.* Mutations in PCSK9 cause autosomal dominant hypercholesterolemia. *Nat Genet* **34**, 154–156 (2003).
314. Maxwell, K. N. & Breslow, J. L. Adenoviral-mediated expression of Pcsk9 in mice results in a low-density lipoprotein receptor knockout phenotype. *Proc Natl Acad Sci U S A* **101**, 7100–7105 (2004).
315. Bjørklund, M. M. *et al.* Induction of Atherosclerosis in Mice and Hamsters Without Germline Genetic Engineering. *Circulation Research* **114**, 1684–1689 (2014).
316. Marfella, R. *et al.* Evidence of an anti-inflammatory effect of PCSK9 inhibitors within the human atherosclerotic plaque. *Atherosclerosis* **378**, 117180 (2023).

317. Gomes, D. *et al.* Comparison between genetic and pharmaceutical disruption of Ldlr expression for the development of atherosclerosis. *J Lipid Res* **63**, 100174 (2022).
318. Jarrett, K. E. *et al.* Somatic Editing of Ldlr With Adeno-Associated Viral-CRISPR Is an Efficient Tool for Atherosclerosis Research. *Arteriosclerosis, Thrombosis, and Vascular Biology* **38**, 1997–2006 (2018).
319. von Scheidt, M. *et al.* Applications and Limitations of Mouse Models for Understanding Human Atherosclerosis. *Cell Metab* **25**, 248–261 (2017).
320. Wang, J., Ma, A., Zhao, M. & Zhu, H. AMPK activation reduces the number of atheromata macrophages in ApoE deficient mice. *Atherosclerosis* **258**, 97–107 (2017).
321. Day, E. A. *et al.* Salsalate reduces atherosclerosis through AMPK beta 1 in mice. *Mol. Metab.* **53**, 101321 (2021).
322. Ma, A., Wang, J., Yang, L., An, Y. & Zhu, H. AMPK activation enhances the anti-atherogenic effects of high density lipoproteins in apoE−/− mice. *J Lipid Res* **58**, 1536–1547 (2017).
323. Day, E. A. *et al.* Macrophage AMPK β1 activation by PF-06409577 reduces the inflammatory response, cholesterol synthesis, and atherosclerosis in mice. *iScience* **26**, 108269 (2023).
324. Cao, Q. *et al.* Myeloid Deletion of α1AMPK Exacerbates Atherosclerosis in LDL Receptor Knockout (LDLRKO) Mice. *Diabetes* **65**, 1565–1576 (2016).
325. Sag, D., Carling, D., Stout, R. D. & Suttles, J. Adenosine 5'-monophosphate-activated protein kinase promotes macrophage polarization to an anti-inflammatory functional phenotype. *J. Immunol.* **181**, 8633–8641 (2008).
326. Zhang, M. *et al.* AMP-activated protein kinase alpha 1 promotes atherogenesis by increasing monocyte-to-macrophage differentiation. *J. Biol. Chem.* **292**, 7888–7903 (2017).
327. Yang, Q. *et al.* Prkaa1 Metabolically Regulates Monocyte/Macrophage Recruitment and Viability in Diet-Induced Murine Metabolic Disorders. *Front Cell Dev Biol* **8**, 611354 (2020).
328. Fisslthaler, B. *et al.* Myeloid-Specific Deletion of the AMPKα2 Subunit Alters Monocyte Protein Expression and Atherogenesis. *International Journal of Molecular Sciences* **20**, 3005 (2019).
329. LeBlond, N. D. *et al.* Myeloid deletion and therapeutic activation of AMPK do not alter atherosclerosis in male or female mice. *J Lipid Res* **61**, 1697–1706 (2020).
330. Yang, Q. *et al.* PRKAA1/AMPKα1-driven glycolysis in endothelial cells exposed to disturbed flow protects against atherosclerosis. *Nat Commun* **9**, 4667 (2018).
331. Ding, Y. *et al.* AMP-Activated Protein Kinase Alpha 2 Deletion Induces VSMC Phenotypic Switching and Reduces Features of Atherosclerotic Plaque Stability. *Circ.Res.* **119**, 718–730 (2016).
332. Dong, Y. *et al.* Reduction of AMP-Activated Protein Kinase alpha 2 Increases Endoplasmic Reticulum Stress and Atherosclerosis In Vivo. *Circulation* **121**, 792–803 (2010).
333. Ouimet, M. *et al.* MicroRNA-33–dependent regulation of macrophage metabolism directs immune cell polarization in atherosclerosis. *J Clin Invest* **125**, 4334–4348 (2015).
334. Brenner, F. W., Villar, R. G., Angulo, F. J., Tauxe, R. & Swaminathan, B. Salmonella Nomenclature. *J Clin Microbiol* **38**, 2465–2467 (2000).
335. Issenhuth-Jeanjean, S. *et al.* Supplement 2008-2010 (no. 48) to the White-Kauffmann-Le Minor scheme. *Res Microbiol* **165**, 526–530 (2014).
336. Thomas, M. & Murray, R. Estimating the burden of food-borne illness in Canada. *Can Commun Dis Rep* **40**, 299–302 (2014).
337. Spragge, F. *et al.* Microbiome diversity protects against pathogens by nutrient blocking. *Science* **382**, eadj3502 (2023).
338. Barthel, M. *et al.* Pretreatment of mice with streptomycin provides a Salmonella enterica serovar Typhimurium colitis model that allows analysis of both pathogen and host. *Infect Immun* **71**, 2839–2858 (2003).
339. Meizlish, M. L., Franklin, R. A., Zhou, X. & Medzhitov, R. Tissue Homeostasis and Inflammation. *Annu Rev Immunol* **39**, 557–581 (2021).

340. Jones, B. D., Ghori, N. & Falkow, S. Salmonella typhimurium initiates murine infection by penetrating and destroying the specialized epithelial M cells of the Peyer's patches. *J Exp Med* **180**, 15–23 (1994).
341. Tahoun, A. *et al.* Salmonella transforms follicle-associated epithelial cells into M cells to promote intestinal invasion. *Cell Host Microbe* **12**, 645–656 (2012).
342. Hapfelmeier, S. *et al.* The Salmonella Pathogenicity Island (SPI)-2 and SPI-1 Type III Secretion Systems Allow Salmonella Serovar typhimurium to Trigger Colitis via MyD88-Dependent and MyD88-Independent Mechanisms1. *The Journal of Immunology* **174**, 1675–1685 (2005).
343. Winter, S. E. *et al.* Gut inflammation provides a respiratory electron acceptor for Salmonella. *Nature* **467**, 426–429 (2010).
344. Stecher, B. *et al.* Motility allows S. Typhimurium to benefit from the mucosal defence. *Cellular Microbiology* **10**, 1166–1180 (2008).
345. Rivera-Chávez, F. *et al.* Salmonella uses energy taxis to benefit from intestinal inflammation. *PLoS Pathog* **9**, e1003267 (2013).
346. Rivera-Chávez, F. *et al.* Energy Taxis toward Host-Derived Nitrate Supports a Salmonella Pathogenicity Island 1-Independent Mechanism of Invasion. *mBio* **7**, e00960-16 (2016).
347. Nguyen, B. D. *et al.* Import of Aspartate and Malate by DcuABC Drives H2/Fumarate Respiration to Promote Initial Salmonella Gut-Lumen Colonization in Mice. *Cell Host Microbe* **27**, 922-936.e6 (2020).
348. Yoo, W. *et al.* Salmonella Typhimurium expansion in the inflamed murine gut is dependent on aspartate derived from ROS-mediated microbiota lysis. *Cell Host Microbe* S1931-3128(24)00142–2 (2024) doi:10.1016/j.chom.2024.05.001.
349. Flo, T. H. *et al.* Lipocalin 2 mediates an innate immune response to bacterial infection by sequestrating iron. *Nature* **432**, 917–921 (2004).
350. Raffatellu, M. *et al.* Lipocalin-2 resistance confers an advantage to Salmonella enterica serotype Typhimurium for growth and survival in the inflamed intestine. *Cell Host Microbe* **5**, 476–486 (2009).
351. Sun, Y. H. *et al.* Surface Glycans Regulate Salmonella Infection-Dependent Directional Switch in Macrophage Galvanotaxis Independent of NanH. *Infection and Immunity* **90**, e00516-21 (2022).
352. Sun, Y. *et al.* Gut epithelial electrical cues drive differential localization of enterobacteria. *Nat Microbiol* 1–13 (2024) doi:10.1038/s41564-024-01778-8.
353. Monack, D. M., Bouley, D. M. & Falkow, S. Salmonella typhimurium persists within macrophages in the mesenteric lymph nodes of chronically infected Nramp1+/+ mice and can be reactivated by IFNgamma neutralization. *J Exp Med* **199**, 231–241 (2004).
354. Kurtz, J. R. *et al.* Salmonella Persistence and Host Immunity Are Dictated by the Anatomical Microenvironment. *Infect Immun* **88**, e00026-20 (2020).
355. Gal-Mor, O. Persistent Infection and Long-Term Carriage of Typhoidal and Nontyphoidal Salmonellae. *Clin Microbiol Rev* **32**, e00088-18 (2019).
356. Orecchioni, M., Ghosheh, Y., Pramod, A. B. & Ley, K. Macrophage Polarization: Different Gene Signatures in M1(LPS+) vs. Classically and M2(LPS-) vs. Alternatively Activated Macrophages. *Front Immunol* **10**, 1084 (2019).
357. Suchanek, O. *et al.* Tissue-resident B cells orchestrate macrophage polarisation and function. *Nat Commun* **14**, 7081 (2023).
358. Goldberg, M. F. *et al.* Salmonella Persist in Activated Macrophages in T Cell-Sparse Granulomas but Are Contained by Surrounding CXCR3 Ligand-Positioned Th1 Cells. *Immunity* **49**, 1090-1102.e7 (2018).
359. Pham, T. H. M. *et al.* Salmonella-Driven Polarization of Granuloma Macrophages Antagonizes TNF-Mediated Pathogen Restriction during Persistent Infection. *Cell Host & Microbe* **27**, 54-67.e5 (2020).
360. Leiba, J. *et al.* Dynamics of macrophage polarization support Salmonella persistence in a whole living organism. *Elife* **13**, e89828 (2024).

361. Stapels, D. A. C. *et al.* Salmonella persisters undermine host immune defenses during antibiotic treatment. *Science* **362**, 1156–1160 (2018).
362. Vidal, S. *et al.* The Ity/Lsh/Bcg locus: natural resistance to infection with intracellular parasites is abrogated by disruption of the Nramp1 gene. *J Exp Med* **182**, 655–666 (1995).
363. Gruenheid, S., Pinner, E., Desjardins, M. & Gros, P. Natural resistance to infection with intracellular pathogens: the Nramp1 protein is recruited to the membrane of the phagosome. *J Exp Med* **185**, 717–730 (1997).
364. Govoni, G. *et al.* The Bcg/Ity/Lsh locus: genetic transfer of resistance to infections in C57BL/6J mice transgenic for the Nramp1 Gly169 allele. *Infect Immun* **64**, 2923–2929 (1996).
365. Fields, P. I., Swanson, R. V., Haidaris, C. G. & Heffron, F. Mutants of Salmonella typhimurium that cannot survive within the macrophage are avirulent. *Proc Natl Acad Sci U S A* **83**, 5189–5193 (1986).
366. Feuillet, V. *et al.* Involvement of Toll-like receptor 5 in the recognition of flagellated bacteria. *Proc Natl Acad Sci U S A* **103**, 12487–12492 (2006).
367. Zhan, R., Han, Q., Zhang, C., Tian, Z. & Zhang, J. Toll-Like receptor 2 (TLR2) and TLR9 play opposing roles in host innate immunity against Salmonella enterica serovar Typhimurium infection. *Infect Immun* **83**, 1641–1649 (2015).
368. Arpaia, N. *et al.* TLR signaling is required for Salmonella typhimurium virulence. *Cell* **144**, 675–688 (2011).
369. O'Brien, A. D. *et al.* Genetic control of susceptibility to Salmonella typhimurium in mice: role of the LPS gene. *J Immunol* **124**, 20–24 (1980).
370. Royle, M. C. J., Tötemeyer, S., Alldridge, L. C., Maskell, D. J. & Bryant, C. E. Stimulation of Toll-like receptor 4 by lipopolysaccharide during cellular invasion by live Salmonella typhimurium is a critical but not exclusive event leading to macrophage responses. *J Immunol* **170**, 5445–5454 (2003).
371. Fitzgerald, K. A. & Kagan, J. C. Toll-like Receptors and the Control of Immunity. *Cell* **180**, 1044–1066 (2020).
372. Sander, L. E. *et al.* Detection of prokaryotic mRNA signifies microbial viability and promotes immunity. *Nature* **474**, 385–389 (2011).
373. Broz, P. *et al.* Redundant roles for inflammasome receptors NLRP3 and NLRC4 in host defense against Salmonella. *J Exp Med* **207**, 1745–1755 (2010).
374. Sun, Y.-H., Rolán, H. G. & Tsolis, R. M. Injection of flagellin into the host cell cytosol by Salmonella enterica serotype Typhimurium. *J Biol Chem* **282**, 33897–33901 (2007).
375. Gram, A. M. *et al.* Salmonella Flagellin Activates NAIP/NLRC4 and Canonical NLRP3 Inflammasomes in Human Macrophages. *J Immunol* **206**, 631–640 (2021).
376. Miao, E. A. *et al.* Innate immune detection of the type III secretion apparatus through the NLRC4 inflammasome. *Proc Natl Acad Sci U S A* **107**, 3076–3080 (2010).
377. Kofoed, E. M. & Vance, R. E. Innate immune recognition of bacterial ligands by NAIPs determines inflammasome specificity. *Nature* **477**, 592–595 (2011).
378. Zhao, Y. *et al.* The NLRC4 inflammasome receptors for bacterial flagellin and type III secretion apparatus. *Nature* **477**, 596–600 (2011).
379. Li, P. *et al.* Mice deficient in IL-1 beta-converting enzyme are defective in production of mature IL-1 beta and resistant to endotoxic shock. *Cell* **80**, 401–411 (1995).
380. Shi, J. *et al.* Cleavage of GSDMD by inflammatory caspases determines pyroptotic cell death. *Nature* **526**, 660–665 (2015).
381. Egan, M. S. *et al.* Inflammasomes primarily restrict cytosolic Salmonella replication within human macrophages. *Elife* **12**, RP90107 (2025).
382. Xu, L. *et al.* Salmonella Induces the cGAS-STING-Dependent Type I Interferon Response in Murine Macrophages by Triggering mtDNA Release. *mBio* **13**, e03632-21 (2022).

383. Manderson, A. P., Kay, J. G., Hammond, L. A., Brown, D. L. & Stow, J. L. Subcompartments of the macrophage recycling endosome direct the differential secretion of IL-6 and TNFalpha. *J Cell Biol* **178**, 57–69 (2007).
384. Medzhitov, R. & Horng, T. Transcriptional control of the inflammatory response. *Nat Rev Immunol* **9**, 692–703 (2009).
385. Phair, I. R. *et al.* AMPK integrates metabolite and kinase-based immunometabolic control in macrophages. *Mol Metab* 101661 (2022) doi:10.1016/j.molmet.2022.101661.
386. Meares, G. P., Qin, H., Liu, Y., Holdbrooks, A. T. & Benveniste, E. N. AMP-activated protein kinase restricts IFN-γ signaling. *J Immunol* **190**, 372–380 (2013).
387. Mancini, S. J. *et al.* Activation of AMP-activated protein kinase rapidly suppresses multiple pro-inflammatory pathways in adipocytes including IL-1 receptor-associated kinase-4 phosphorylation. *Mol Cell Endocrinol* **440**, 44–56 (2017).
388. Guilliams, M., Bruhns, P., Saeys, Y., Hammad, H. & Lambrecht, B. N. The function of Fcγ receptors in dendritic cells and macrophages. *Nat Rev Immunol* **14**, 94–108 (2014).
389. Jawhara, S., Pluskota, E., Cao, W., Plow, E. F. & Soloviev, D. A. Distinct Effects of Integrins αXβ2 and αMβ2 on Leukocyte Subpopulations during Inflammation and Antimicrobial Responses. *Infect Immun* **85**, e00644-16 (2017).
390. Skjesol, A. *et al.* The TLR4 adaptor TRAM controls the phagocytosis of Gram-negative bacteria by interacting with the Rab11-family interacting protein 2. *PLOS Pathogens* **15**, e1007684 (2019).
391. Schroeder, G. N. & Hilbi, H. Molecular Pathogenesis of Shigella spp.: Controlling Host Cell Signaling, Invasion, and Death by Type III Secretion. *Clin Microbiol Rev* **21**, 134–156 (2008).
392. Szeto, J., Namolovan, A., Osborne, S. E., Coombes, B. K. & Brumell, J. H. Salmonella-containing vacuoles display centrifugal movement associated with cell-to-cell transfer in epithelial cells. *Infect Immun* **77**, 996–1007 (2009).
393. D'Costa, V. M. *et al.* BioID screen of Salmonella type 3 secreted effectors reveals host factors involved in vacuole positioning and stability during infection. *Nat Microbiol* **4**, 2511–2522 (2019).
394. Chakraborty, S., Mizusaki, H. & Kenney, L. J. A FRET-based DNA biosensor tracks OmpR-dependent acidification of Salmonella during macrophage infection. *PLoS Biol* **13**, e1002116 (2015).
395. Xu, Y. *et al.* A Bacterial Effector Reveals the V-ATPase-ATG16L1 Axis that Initiates Xenophagy. *Cell* **178**, 552-566.e20 (2019).
396. Fu, J. *et al.* Mechanisms and regulation of defensins in host defense. *Signal Transduct Target Ther* **8**, 300 (2023).
397. Birmingham, C. L., Smith, A. C., Bakowski, M. A., Yoshimori, T. & Brumell, J. H. Autophagy controls Salmonella infection in response to damage to the Salmonella-containing vacuole. *J Biol Chem* **281**, 11374–11383 (2006).
398. Zhao, Z. *et al.* Autophagosome-independent essential function for the autophagy protein Atg5 in cellular immunity to intracellular pathogens. *Cell Host Microbe* **4**, 458–469 (2008).
399. Liu, F.-T. & Stowell, S. R. The role of galectins in immunity and infection. *Nat Rev Immunol* **23**, 479–494 (2023).
400. Thurston, T. L. M., Wandel, M. P., von Muhlinen, N., Foeglein, Á. & Randow, F. Galectin 8 targets damaged vesicles for autophagy to defend cells against bacterial invasion. *Nature* **482**, 414–418 (2012).
401. Zheng, Y. T. *et al.* The adaptor protein p62/SQSTM1 targets invading bacteria to the autophagy pathway. *J Immunol* **183**, 5909–5916 (2009).
402. Wild, P. *et al.* Phosphorylation of the autophagy receptor optineurin restricts Salmonella growth. *Science* **333**, 228–233 (2011).
403. Jia, J. *et al.* Galectins Control mTOR in Response to Endomembrane Damage. *Molecular Cell* **70**, 120-135.e8 (2018).
404. Perrin, A. J., Jiang, X., Birmingham, C. L., So, N. S. Y. & Brumell, J. H. Recognition of bacteria in the cytosol of Mammalian cells by the ubiquitin system. *Curr Biol* **14**, 806–811 (2004).

405. Fiskin, E., Bionda, T., Dikic, I. & Behrends, C. Global Analysis of Host and Bacterial Ubiquitinome in Response to Salmonella Typhimurium Infection. *Mol Cell* **62**, 967–981 (2016).
406. Tripathi-Giesgen, I., Behrends, C. & Alpi, A. F. The ubiquitin ligation machinery in the defense against bacterial pathogens. *EMBO Rep* **22**, e52864 (2021).
407. Ghosh, S. *et al.* Host AAA-ATPase VCP/p97 lyses ubiquitinated intracellular bacteria as an innate antimicrobial defence. *Nat Microbiol* 1–16 (2025) doi:10.1038/s41564-025-01984-y.
408. Noad, J. *et al.* LUBAC-synthesized linear ubiquitin chains restrict cytosol-invading bacteria by activating autophagy and NF-κB. *Nat Microbiol* **2**, 17063 (2017).
409. van Wijk, S. J. L. *et al.* Linear ubiquitination of cytosolic Salmonella Typhimurium activates NF-κB and restricts bacterial proliferation. *Nat Microbiol* **2**, 17066 (2017).
410. Kim, J., Kundu, M., Viollet, B. & Guan, K.-L. AMPK and mTOR regulate autophagy through direct phosphorylation of Ulk1. *Nature Cell Biology* **13**, 132–141 (2011).
411. Ramírez-Peinado, S. *et al.* Glucose-starved cells do not engage in prosurvival autophagy. *J Biol Chem* **288**, 30387–30398 (2013).
412. Lang, M. J. *et al.* Glucose starvation inhibits autophagy via vacuolar hydrolysis and induces plasma membrane internalization by down-regulating recycling. *J Biol Chem* **289**, 16736–16747 (2014).
413. Nwadike, C., Williamson, L. E., Gallagher, L. E., Guan, J.-L. & Chan, E. Y. W. AMPK Inhibits ULK1-Dependent Autophagosome Formation and Lysosomal Acidification via Distinct Mechanisms. *Mol Cell Biol* **38**, e00023-18 (2018).
414. Martin, K. R., Celano, S. L., Sheldon, R. D., Jones, R. G. & MacKeigan, J. P. Quantitative Analysis of Autophagy in Single Cells: Differential Response to Amino Acid and Glucose Starvation. *bioRxiv* 2023.12.01.569679 (2023) doi:10.1101/2023.12.01.569679.
415. Barnaba, C., Broadbent, D. G., Kaminsky, E. G., Perez, G. I. & Schmidt, J. C. AMPK regulates phagophore-to-autophagosome maturation. *J Cell Biol* **223**, e202309145 (2024).
416. Benito-Cuesta, I., Ordóñez-Gutiérrez, L. & Wandosell, F. AMPK activation does not enhance autophagy in neurons in contrast to MTORC1 inhibition: different impact on β-amyloid clearance. *Autophagy* **17**, 656–671 (2021).
417. Park, J.-M., Lee, D.-H. & Kim, D.-H. Redefining the role of AMPK in autophagy and the energy stress response. *Nat Commun* **14**, 2994 (2023).
418. Shang, L. *et al.* Nutrient starvation elicits an acute autophagic response mediated by Ulk1 dephosphorylation and its subsequent dissociation from AMPK. *Proc Natl Acad Sci U S A* **108**, 4788–4793 (2011).
419. Mack, H. I. D., Zheng, B., Asara, J. M. & Thomas, S. M. AMPK-dependent phosphorylation of ULK1 regulates ATG9 localization. *Autophagy* **8**, 1197–1214 (2012).
420. Longo, M. *et al.* Opposing roles for AMPK in regulating distinct mitophagy pathways. *Mol Cell* **84**, 4350-4367.e9 (2024).
421. Losier, T. T. *et al.* AMPK Promotes Xenophagy through Priming of Autophagic Kinases upon Detection of Bacterial Outer Membrane Vesicles. *Cell Reports* **26**, 2150-2165.e5 (2019).
422. Alsaadi, R. M. *et al.* ULK1-mediated phosphorylation of ATG16L1 promotes xenophagy, but destabilizes the ATG16L1 Crohn's mutant. *EMBO Rep* **20**, e46885 (2019).
423. Manzanillo, P. S. *et al.* The ubiquitin ligase parkin mediates resistance to intracellular pathogens. *Nature* **501**, 512–516 (2013).
424. Strelko, C. L. *et al.* Itaconic Acid Is a Mammalian Metabolite Induced during Macrophage Activation. *J. Am. Chem. Soc.* **133**, 16386–16389 (2011).
425. Michelucci, A. *et al.* Immune-responsive gene 1 protein links metabolism to immunity by catalyzing itaconic acid production. *Proc. Natl. Acad. Sci. U.S.A.* **110**, 7820–7825 (2013).
426. Bambouskova, M. *et al.* Electrophilic properties of itaconate and derivatives regulate the IκBζ–ATF3 inflammatory axis. *Nature* **556**, 501–504 (2018).
427. Mills, E. L. *et al.* Itaconate is an anti-inflammatory metabolite that activates Nrf2 via alkylation of KEAP1. *Nature* **556**, 113–117 (2018).

428. Lampropoulou, V. *et al.* Itaconate Links Inhibition of Succinate Dehydrogenase with Macrophage Metabolic Remodeling and Regulation of Inflammation. *Cell Metab* **24**, 158–166 (2016).
429. Schuster, E.-M. *et al.* TFEB induces mitochondrial itaconate synthesis to suppress bacterial growth in macrophages. *Nat Metab* **4**, 856–866 (2022).
430. Martin, W. R., Frigan, F. & Bergman, E. H. Noninductive metabolism of itaconic acid by Pseudomonas and Salmonella species. *J Bacteriol* **82**, 905–908 (1961).
431. Sasikaran, J., Ziemski, M., Zadora, P. K., Fleig, A. & Berg, I. A. Bacterial itaconate degradation promotes pathogenicity. *Nat Chem Biol* **10**, 371–377 (2014).
432. Rosenberg, G. *et al.* Host succinate is an activation signal for Salmonella virulence during intracellular infection. *Science* **371**, 400–405 (2021).
433. Tannahill, G. M. *et al.* Succinate is an inflammatory signal that induces IL-1β through HIF-1α. *Nature* **496**, 238–242 (2013).
434. Jiang, L. *et al.* Salmonella Typhimurium reprograms macrophage metabolism via T3SS effector SopE2 to promote intracellular replication and virulence. *Nat Commun* **12**, 879 (2021).
435. Tanner, L. B. *et al.* Four Key Steps Control Glycolytic Flux in Mammalian Cells. *cels* **7**, 49-62.e8 (2018).
436. Wang, M. *et al.* Phosphorylation of PFKL regulates metabolic reprogramming in macrophages following pattern recognition receptor activation. *Nat Commun* **15**, 6438 (2024).
437. Wang, X. *et al.* Lactate promotes Salmonella intracellular replication and systemic infection via driving macrophage M2 polarization. *Microbiology Spectrum* **11**, e02253-23 (2023).
438. Qualls, J. E. *et al.* Sustained generation of nitric oxide and control of mycobacterial infection requires argininosuccinate synthase 1. *Cell Host Microbe* **12**, 313–323 (2012).
439. Cleeter, M. W., Cooper, J. M., Darley-Usmar, V. M., Moncada, S. & Schapira, A. H. Reversible inhibition of cytochrome c oxidase, the terminal enzyme of the mitochondrial respiratory chain, by nitric oxide. Implications for neurodegenerative diseases. *FEBS Lett* **345**, 50–54 (1994).
440. Palmieri, E. M. *et al.* Nitric oxide orchestrates metabolic rewiring in M1 macrophages by targeting aconitase 2 and pyruvate dehydrogenase. *Nat Commun* **11**, 698 (2020).
441. Skon-Hegg, C. *et al.* LACC1 Regulates TNF and IL-17 in Mouse Models of Arthritis and Inflammation. *The Journal of Immunology* **202**, 183–193 (2019).
442. Wei, Z., Oh, J., Flavell, R. A. & Crawford, J. M. LACC1 bridges NOS2 and polyamine metabolism in inflammatory macrophages. *Nature* **609**, 348–353 (2022).
443. Hardbower, D. M. *et al.* Ornithine decarboxylase regulates M1 macrophage activation and mucosal inflammation via histone modifications. *Proc Natl Acad Sci U S A* **114**, E751–E760 (2017).
444. Nakamura, A. *et al.* Symbiotic polyamine metabolism regulates epithelial proliferation and macrophage differentiation in the colon. *Nat Commun* **12**, 2105 (2021).
445. Mao, Y., Shi, D., Li, G. & Jiang, P. Citrulline depletion by ASS1 is required for proinflammatory macrophage activation and immune responses. *Mol Cell* **82**, 527-541.e7 (2022).
446. Hooftman, A. *et al.* Macrophage fumarate hydratase restrains mtRNA-mediated interferon production. *Nature* **615**, 490–498 (2023).
447. Herb, M. & Schramm, M. Functions of ROS in Macrophages and Antimicrobial Immunity. *Antioxidants (Basel)* **10**, 313 (2021).
448. West, A. P. *et al.* TLR signalling augments macrophage bactericidal activity through mitochondrial ROS. *Nature* **472**, 476–480 (2011).
449. Herb, M. *et al.* Mitochondrial reactive oxygen species enable proinflammatory signaling through disulfide linkage of NEMO. *Sci Signal* **12**, eaar5926 (2019).
450. Roos, D. *et al.* Hematologically important mutations: X-linked chronic granulomatous disease (fourth update). *Blood Cells Mol Dis* **90**, 102587 (2021).
451. Kim, N.-H. *et al.* The xanthine oxidase-NFAT5 pathway regulates macrophage activation and TLR-induced inflammatory arthritis. *Eur J Immunol* **44**, 2721–2736 (2014).

452. Buchmeier, N. A., Lipps, C. J., So, M. Y. & Heffron, F. Recombination-deficient mutants of Salmonella typhimurium are avirulent and sensitive to the oxidative burst of macrophages. *Mol Microbiol* **7**, 933–936 (1993).
453. Chakraborty, S. *et al.* Glycolytic reprograming in Salmonella counters NOX2-mediated dissipation of ΔpH. *Nat Commun* **11**, 1783 (2020).
454. Fasnacht, M. & Polacek, N. Oxidative Stress in Bacteria and the Central Dogma of Molecular Biology. *Front Mol Biosci* **8**, 671037 (2021).
455. van der Heijden, J., Bosman, E. S., Reynolds, L. A. & Finlay, B. B. Direct measurement of oxidative and nitrosative stress dynamics in Salmonella inside macrophages. *Proc Natl Acad Sci U S A* **112**, 560–565 (2015).
456. Miao, E. A. *et al.* Caspase-1-induced pyroptosis is an innate immune effector mechanism against intracellular bacteria. *Nat Immunol* **11**, 1136–1142 (2010).
457. Broz, P. *et al.* Caspase-11 increases susceptibility to Salmonella infection in the absence of caspase-1. *Nature* **490**, 288–291 (2012).
458. Kayagaki, N. *et al.* NINJ1 mediates plasma membrane rupture during lytic cell death. *Nature* **591**, 131–136 (2021).
459. Fattinger, S. A. *et al.* Gasdermin D is the only Gasdermin that provides protection against acute Salmonella gut infection in mice. *Proceedings of the National Academy of Sciences* **120**, e2315503120 (2023).
460. Monack, D. M., Raupach, B., Hromockyj, A. E. & Falkow, S. Salmonella typhimurium invasion induces apoptosis in infected macrophages. *Proc Natl Acad Sci U S A* **93**, 9833–9838 (1996).
461. Hsu, L.-C. *et al.* The protein kinase PKR is required for macrophage apoptosis after activation of Toll-like receptor 4. *Nature* **428**, 341–345 (2004).
462. He, S. & Wang, X. RIP kinases as modulators of inflammation and immunity. *Nat Immunol* **19**, 912–922 (2018).
463. Robinson, N. *et al.* Type I interferon induces necroptosis in macrophages during infection with Salmonella enterica serovar Typhimurium. *Nat Immunol* **13**, 954–962 (2012).
464. Exton, M. S. Infection-induced anorexia: active host defence strategy. *Appetite* **29**, 369–383 (1997).
465. Yang, Y. *et al.* Yersinia infection induces glucose depletion and AMPK-dependent inhibition of pyroptosis in mice. *Nat Microbiol* **9**, 1–16 (2024).
466. Ilanges, A. *et al.* Brainstem ADCYAP1+ neurons control multiple aspects of sickness behaviour. *Nature* **609**, 761–771 (2022).
467. Jin, H., Li, M., Jeong, E., Castro-Martinez, F. & Zuker, C. S. A body-brain circuit that regulates body inflammatory responses. *Nature* **630**, 695–703 (2024).
468. Rao, S. *et al.* Pathogen-Mediated Inhibition of Anorexia Promotes Host Survival and Transmission. *Cell* (2017) doi:10.1016/J.CELL.2017.01.006.
469. Ganesan, R. *et al.* Salmonella Typhimurium disrupts Sirt1/AMPK checkpoint control of mTOR to impair autophagy. *PLOS Pathogens* **13**, e1006227 (2017).
470. Ma, L. *et al.* FLT4/VEGFR3 activates AMPK to coordinate glycometabolic reprogramming with autophagy and inflammasome activation for bacterial elimination. *Autophagy* **18**, 1385–1400 (2022).
471. Tattoli, I. *et al.* Amino Acid Starvation Induced by Invasive Bacterial Pathogens Triggers an Innate Host Defense Program. *Cell Host & Microbe* **11**, 563–575 (2012).
472. Smiles, W. J. *et al.* New developments in AMPK and mTORC1 cross-talk. *Essays Biochem* **68**, 321–336 (2024).
473. Liu, Y. *et al.* TLR9 and beclin 1 crosstalk regulates muscle AMPK activation in exercise. *Nature* **578**, 605–609 (2020).
474. Smith, T. K. T. *et al.* AMPK-mediated regulation of endogenous cholesterol synthesis does not affect atherosclerosis in a murine Pcsk9-AAV model. *Atherosclerosis* **397**, 117608 (2024).
475. Steinberg, G. R. & Hardie, D. G. New insights into activation and function of the AMPK. *Nat. Rev. Mol. Cell Biol.* **24**, 255–272 (2023).

476. Sharpe, L. J. & Brown, A. J. Controlling Cholesterol Synthesis beyond 3-Hydroxy-3-methylglutaryl-CoA Reductase (HMGCR)*. *Journal of Biological Chemistry* **288**, 18707–18715 (2013).
477. Luo, J., Yang, H. & Song, B.-L. Mechanisms and regulation of cholesterol homeostasis. *Nat Rev Mol Cell Biol* **21**, 225–245 (2020).
478. Lee, M. K. S. *et al.* Defective AMPK regulation of cholesterol metabolism accelerates atherosclerosis by promoting HSPC mobilization and myelopoiesis. *Molecular Metabolism* **61**, 101514 (2022).
479. Yang, Q. *et al.* Prkaa1 Metabolically Regulates Monocyte/Macrophage Recruitment and Viability in Diet-Induced Murine Metabolic Disorders. *Frontiers in Cell and Developmental Biology* **8**, (2021).
480. Loh, K. *et al.* Inhibition of Adenosine Monophosphate-Activated Protein Kinase-3-Hydroxy-3-Methylglutaryl Coenzyme A Reductase Signaling Leads to Hypercholesterolemia and Promotes Hepatic Steatosis and Insulin Resistance. *Hepatology Communications* **3**, 84–98 (2019).
481. Bligh, E. G. & Dyer, W. J. A RAPID METHOD OF TOTAL LIPID EXTRACTION AND PURIFICATION. *Canadian Journal of Biochemistry and Physiology* **37**, 911–917 (1959).
482. Fullerton, M. D., Hakimuddin, F., Bonen, A. & Bakovic, M. The Development of a Metabolic Disease Phenotype in CTP:Phosphoethanolamine Cytidylyltransferase-deficient Mice *. *Journal of Biological Chemistry* **284**, 25704–25713 (2009).
483. Livak, K. J. & Schmittgen, T. D. Analysis of relative gene expression data using real-time quantitative PCR and the 2(T)(-Delta Delta C) method. *Methods* **25**, 402–408 (2001).
484. Guo, W., Jiang, L., Bhasin, S., Khan, S. M. & Swerdlow, R. H. DNA extraction procedures meaningfully influence qPCR-based mtDNA copy number determination. *Mitochondrion* **9**, 261–265 (2009).
485. Schneider, C. A., Rasband, W. S. & Eliceiri, K. W. NIH Image to ImageJ: 25 years of image analysis. *Nat Methods* **9**, 671–675 (2012).
486. Zack, G. W., Rogers, W. E. & Latt, S. A. Automatic measurement of sister chromatid exchange frequency. *J Histochem Cytochem.* **25**, 741–753 (1977).
487. Koelwyn, G. J., Corr, E. M., Erbay, E. & Moore, K. J. Regulation of macrophage immunometabolism in atherosclerosis. *Nat Immunol* **19**, 526–537 (2018).
488. Schultz, J. R. *et al.* Role of LXRs in control of lipogenesis. *Genes Dev* **14**, 2831–2838 (2000).
489. Laufs, U., Descamps, O. S., Catapano, A. L. & Packard, C. J. Understanding IMPROVE-IT and the cardinal role of LDL-C lowering in CVD prevention. *Eur Heart J* **35**, 1996–2000 (2014).
490. Pietras, E. M. *et al.* Functionally Distinct Subsets of Lineage-Biased Multipotent Progenitors Control Blood Production in Normal and Regenerative Conditions. *Cell Stem Cell* **17**, 35–46 (2015).
491. Engelen, S. E., Robinson, A. J. B., Zurke, Y.-X. & Monaco, C. Therapeutic strategies targeting inflammation and immunity in atherosclerosis: how to proceed? *Nat Rev Cardiol* **19**, 522–542 (2022).
492. Bekkering, S. *et al.* Metabolic Induction of Trained Immunity through the Mevalonate Pathway. *Cell* **172**, 135-146.e9 (2018).
493. Khan, O. M. *et al.* Geranylgeranyltransferase type I (GGTase-I) deficiency hyperactivates macrophages and induces erosive arthritis in mice. *J Clin Invest* **121**, 628–639 (2011).
494. Tirosh, I. *et al.* Dissecting the multicellular ecosystem of metastatic melanoma by single-cell RNA-seq. *Science* **352**, 189–196 (2016).
495. Pujadas, G. *et al.* Genetic disruption of the Gipr in Apoe−/− mice promotes atherosclerosis. *Molecular Metabolism* **65**, 101586 (2022).
496. Witkowski, M., Weeks, T. L. & Hazen, S. L. Gut microbiota and cardiovascular disease. *Circ Res* **127**, 553–570 (2020).
497. Karlsson, F. H. *et al.* Symptomatic atherosclerosis is associated with an altered gut metagenome. *Nat Commun* **3**, 1245 (2012).

498. Badimon, L., Luquero, A., Crespo, J., Peña, E. & Borrell-Pages, M. PCSK9 and LRP5 in macrophage lipid internalization and inflammation. *Cardiovasc Res* **117**, 2054–2068 (2021).
499. Ricci, C. *et al.* PCSK9 induces a pro-inflammatory response in macrophages. *Sci Rep* **8**, 2267 (2018).
500. Liu, S. *et al.* Blood flow patterns regulate PCSK9 secretion via MyD88-mediated pro-inflammatory cytokines. *Cardiovascular Research* **116**, 1721–1732 (2020).
501. Tang, Z.-H. *et al.* New role of PCSK9 in atherosclerotic inflammation promotion involving the TLR4/NF-κB pathway. *Atherosclerosis* **262**, 113–122 (2017).
502. Basu, D. *et al.* Novel Reversible Model of Atherosclerosis and Regression Using Oligonucleotide Regulation of the LDL Receptor. *Circulation Research* **122**, 560–567 (2018).
503. Cui, H., Zhu, X., Li, S., Wang, P. & Fang, J. Liver-Targeted Delivery of Oligonucleotides with N-Acetylgalactosamine Conjugation. *ACS Omega* **6**, 16259–16265 (2021).
504. Anitschkow, N. & Chalatow, S. Classics in arteriosclerosis research: On experimental cholesterin steatosis and its significance in the origin of some pathological processes by N. Anitschkow and S. Chalatow, translated by Mary Z. Pelias, 1913. *Arteriosclerosis, Thrombosis, and Vascular Biology* **3**, 178–182 (1983).
505. Ohashi, K. *et al.* Early embryonic lethality caused by targeted disruption of the 3-hydroxy-3-methylglutaryl-CoA reductase gene. *J Biol Chem* **278**, 42936–42941 (2003).
506. Sakai, K. *et al.* Myeloid HMG-CoA (3-Hydroxy-3-Methylglutaryl-Coenzyme A) Reductase Determines Atherosclerosis by Modulating Migration of Macrophages. *Arteriosclerosis, Thrombosis, and Vascular Biology* **38**, 2590–2600 (2018).
507. Araldi, E. *et al.* Lanosterol Modulates TLR4-Mediated Innate Immune Responses in Macrophages. *Cell Reports* **19**, 2743–2755 (2017).
508. Zhang, X. *et al.* Desmosterol suppresses macrophage inflammasome activation and protects against vascular inflammation and atherosclerosis. *Proc. Natl. Acad. Sci. U. S. A.* **118**, e2107682118 (2021).
509. Fu, H. *et al.* The differential statin effect on cytokine production of monocytes or macrophages is mediated by differential geranylgeranylation-dependent Rac1 activation. *Cell Death Dis* **10**, 1–17 (2019).
510. Akula, M. K. *et al.* Control of the innate immune response by the mevalonate pathway. *Nature Immunology* **17**, 922–929 (2016).
511. Yeudall, S. *et al.* Macrophage acetyl-CoA carboxylase regulates acute inflammation through control of glucose and lipid metabolism. *Science Advances* **8**, eabq1984 (2022).
512. Ilyas, I. *et al.* Mouse models of atherosclerosis in translational research. *Trends in Pharmacological Sciences* **43**, 920–939 (2022).
513. Han, Y. *et al.* Effect of metformin on all-cause and cardiovascular mortality in patients with coronary artery diseases: a systematic review and an updated meta-analysis. *Cardiovasc Diabetol* **18**, 96 (2019).
514. Pinkosky, S. L. *et al.* Long-chain fatty acyl-CoA esters regulate metabolism via allosteric control of AMPK beta 1 isoforms. *Nat. Metab.* **2**, 873-+ (2020).
515. He, C., Li, H., Viollet, B., Zou, M.-H. & Xie, Z. AMPK Suppresses Vascular Inflammation In Vivo by Inhibiting Signal Transducer and Activator of Transcription-1. *Diabetes* **64**, 4285–4297 (2015).
516. Singh, S. *et al.* Myeloid Cell-Specific Deletion of AMPKα1 Worsens Ocular Bacterial Infection by Skewing Macrophage Phenotypes. *J Immunol* **213**, 1656–1665 (2024).
517. Liu, W. *et al.* Activation of TGF-β-activated kinase 1 (TAK1) restricts Salmonella Typhimurium growth by inducing AMPK activation and autophagy. *Cell Death Dis* **9**, 1–16 (2018).
518. Kanehisa, M. & Goto, S. KEGG: kyoto encyclopedia of genes and genomes. *Nucleic Acids Res* **28**, 27–30 (2000).
519. Pang, Z. *et al.* MetaboAnalyst 6.0: towards a unified platform for metabolomics data processing, analysis and interpretation. *Nucleic Acids Res* **52**, W398–W406 (2024).
520. Viollet, B. *et al.* The AMP-activated protein kinase α2 catalytic subunit controls whole-body insulin sensitivity. *J Clin Invest* **111**, 91–98 (2003).

521. Boudaba, N. *et al.* AMPK Re-Activation Suppresses Hepatic Steatosis but its Downregulation Does Not Promote Fatty Liver Development. *EBioMedicine* **28**, 194–209 (2018).
522. Clausen, B. E., Burkhardt, C., Reith, W., Renkawitz, R. & Förster, I. Conditional gene targeting in macrophages and granulocytes using LysMcre mice. *Transgenic Res* **8**, 265–277 (1999).
523. Mounier, R. *et al.* AMPKα1 Regulates Macrophage Skewing at the Time of Resolution of Inflammation during Skeletal Muscle Regeneration. *Cell Metabolism* **18**, 251–264 (2013).
524. Bai, A. *et al.* AMPK agonist downregulates innate and adaptive immune responses in TNBS-induced murine acute and relapsing colitis. *Biochem Pharmacol* **80**, 1708–1717 (2010).
525. Lauterbach, M. A. *et al.* Toll-like Receptor Signaling Rewires Macrophage Metabolism and Promotes Histone Acetylation via ATP-Citrate Lyase. *Immunity* **51**, 997-1011.e7 (2019).
526. Xu, W. *et al.* STAT-1 and c-Fos interaction in nitric oxide synthase-2 gene activation. *Am J Physiol Lung Cell Mol Physiol* **285**, L137-148 (2003).
527. Chen, X. *et al.* Intracellular galectin-3 is a lipopolysaccharide sensor that promotes glycolysis through mTORC1 activation. *Nat Commun* **13**, 7578 (2022).
528. Torsilieri, H. M., Upchurch, C. M., Leitinger, N. & Casanova, J. E. Salmonella-induced cholesterol accumulation in infected macrophages suppresses autophagy via mTORC1 activation. *Mol Biol Cell* **36**, ar3 (2025).
529. Hurley, R. L. *et al.* The Ca2+/calmodulin-dependent protein kinase kinases are AMP-activated protein kinase kinases. *J Biol Chem* **280**, 29060–29066 (2005).
530. Grempler, R. *et al.* Discovery and translation of a target engagement marker for AMP-activated protein kinase (AMPK). *PLoS One* **13**, e0197849 (2018).
531. Wang, A. *et al.* Opposing Effects of Fasting Metabolism on Tissue Tolerance in Bacterial and Viral Inflammation. *Cell* **166**, 1512-1525.e12 (2016).
532. Li, J. *et al.* Identification and characterization of human uracil phosphoribosyltransferase (UPRTase). *J Hum Genet* **52**, 415–422 (2007).
533. Pérignon, J. L., Bories, D. M., Houllier, A. M., Thuillier, L. & Cartier, P. H. Metabolism of pyrimidine bases and nucleosides by pyrimidine-nucleoside phosphorylases in cultured human lymphoid cells. *Biochim Biophys Acta* **928**, 130–136 (1987).
534. Guarda, G. *et al.* Type I interferon inhibits interleukin-1 production and inflammasome activation. *Immunity* **34**, 213–223 (2011).
535. Myles, I. A. *et al.* Signaling via the IL-20 receptor inhibits cutaneous production of IL-1β and IL-17A to promote infection with methicillin-resistant Staphylococcus aureus. *Nat Immunol* **14**, 804–811 (2013).
536. Tu, Y. *et al.* TBC1D23 mediates Golgi-specific LKB1 signaling. *Nat Commun* **15**, 1785 (2024).
537. Freemantle, J. B. *et al.* AMPK associates with and causes fragmentation of the Golgi by phosphorylating the guanine nucleotide exchange factor GBF1. *J Cell Sci* **137**, jcs262182 (2024).
538. Miyamoto, T. *et al.* AMP-activated protein kinase phosphorylates Golgi-specific brefeldin A resistance factor 1 at Thr1337 to induce disassembly of Golgi apparatus. *J Biol Chem* **283**, 4430–4438 (2008).
539. Lopes-da-Silva, M. *et al.* A GBF1-Dependent Mechanism for Environmentally Responsive Regulation of ER-Golgi Transport. *Developmental Cell* **49**, 786-801.e6 (2019).
540. Revelo, N. H., Ter Beest, M. & van den Bogaart, G. Membrane trafficking as an active regulator of constitutively secreted cytokines. *J Cell Sci* **133**, jcs234781 (2019).
541. Pilon, G., Dallaire, P. & Marette, A. Inhibition of inducible nitric-oxide synthase by activators of AMP-activated protein kinase: a new mechanism of action of insulin-sensitizing drugs. *J Biol Chem* **279**, 20767–20774 (2004).
542. Zhang, B., Lakshmanan, J., Du, Y., Smith, J. W. & Harbrecht, B. G. Cell-specific regulation of iNOS by AMP-activated protein kinase in primary rat hepatocytes. *Journal of Surgical Research* **221**, 104–112 (2018).
543. Farlik, M. *et al.* Nonconventional initiation complex assembly by STAT and NF-kappaB transcription factors regulates nitric oxide synthase expression. *Immunity* **33**, 25–34 (2010).

544. Di Giorgio, E. *et al.* NRF2 interacts with distal enhancer and inhibits nitric oxide synthase 2 expression in *KRAS*-driven pancreatic cancer cells. *Biochimica et Biophysica Acta (BBA) - Molecular Cell Research* **1871**, 119606 (2024).
545. Joo, M. S. *et al.* AMPK Facilitates Nuclear Accumulation of Nrf2 by Phosphorylating at Serine 550. *Mol Cell Biol* **36**, 1931–1942 (2016).
546. Bai, W. *et al.* S-nitrosylation of AMPKγ impairs coronary collateral circulation and disrupts VSMC reprogramming. *EMBO Rep* **25**, 128–143 (2024).
547. Xie, Z. *et al.* Citrulline regulates macrophage metabolism and inflammation to counter aging in mice. *Sci Adv* **11**, eads4957 (2025).
548. Burkewitz, K. *et al.* Neuronal CRTC-1 governs systemic mitochondrial metabolism and lifespan via a catecholamine signal. *Cell* **160**, 842–855 (2015).
549. Weir, H. J. *et al.* Dietary Restriction and AMPK Increase Lifespan via Mitochondrial Network and Peroxisome Remodeling. *Cell Metabolism* **26**, 884-896.e5 (2017).
550. Bae, H.-B. *et al.* AMP-activated protein kinase enhances the phagocytic ability of macrophages and neutrophils. *FASEB J* **25**, 4358–4368 (2011).
551. Garcia, D. *et al.* Genetic Liver-Specific AMPK Activation Protects against Diet-Induced Obesity and NAFLD. *Cell Rep* **26**, 192-208.e6 (2019).
552. Woods, A. *et al.* Liver-Specific Activation of AMPK Prevents Steatosis on a High-Fructose Diet. *Cell Rep* **18**, 3043–3051 (2017).
553. Penfold, L. *et al.* AMPK activation protects against prostate cancer by inducing a catabolic cellular state. *Cell Reports* **42**, 112396 (2023).
554. Pollard, A. E. *et al.* AMPK activation protects against diet induced obesity through Ucp1-independent thermogenesis in subcutaneous white adipose tissue. *Nat Metab* **1**, 340–349 (2019).
555. Yin, J. *et al.* Hypoxanthine phosphoribosyl transferase 1 metabolizes temozolomide to activate AMPK for driving chemoresistance of glioblastomas. *Nat Commun* **14**, 5913 (2023).
556. Morales, A. J. *et al.* A type I IFN-dependent DNA damage response regulates the genetic program and inflammasome activation in macrophages. *Elife* **6**, e24655 (2017).
557. Swatek, K. N. & Komander, D. Ubiquitin modifications. *Cell Res.* **26**, 399–422 (2016).
558. Ohtake, F. & Tsuchiya, H. The emerging complexity of ubiquitin architecture. *J Biochem* **161**, 125–133 (2017).
559. Timms, R. T. *et al.* A glycine-specific N-degron pathway mediates the quality control of protein N-myristoylation. *Science* **365**, eaaw4912 (2019).
560. Park, S.-J., Shirahige, K., Ohsugi, M. & Nakai, K. DBTMEE: a database of transcriptome in mouse early embryos. *Nucleic Acids Res* **43**, D771–D776 (2015).
561. Crute, B. E., Seefeld, K., Gamble, J., Kemp, B. E. & Witters, L. A. Functional domains of the alpha 1 catalytic subunit of the AMP-activated protein kinase. *J. Biol. Chem.* **273**, 35347–35354 (1998).
562. Towler, D. A., Eubanks, S. R., Towery, D. S., Adams, S. P. & Glaser, L. Amino-terminal processing of proteins by N-myristoylation. Substrate specificity of N-myristoyl transferase. *J. Biol. Chem.* **262**, 1030–1036 (1987).
563. Aksnes, H., Ree, R. & Arnesen, T. Co-translational, Post-translational, and Non-catalytic Roles of N-Terminal Acetyltransferases. *Mol Cell* **73**, 1097–1114 (2019).
564. Ciechanover, A., Heller, H., Elias, S., Haas, A. L. & Hershko, A. ATP-dependent conjugation of reticulocyte proteins with the polypeptide required for protein degradation. *Proc Natl Acad Sci U S A* **77**, 1365–1368 (1980).
565. Petroski, M. D. & Deshaies, R. J. Function and regulation of cullin-RING ubiquitin ligases. *Nat Rev Mol Cell Biol* **6**, 9–20 (2005).
566. Chiang, H. L., Terlecky, S. R., Plant, C. P. & Dice, J. F. A role for a 70-kilodalton heat shock protein in lysosomal degradation of intracellular proteins. *Science* **246**, 382–385 (1989).
567. Dice, J. F. Peptide sequences that target cytosolic proteins for lysosomal proteolysis. *Trends Biochem Sci* **15**, 305–309 (1990).

568. Anguiano, J. *et al.* Chemical modulation of chaperone-mediated autophagy by retinoic acid derivatives. *Nature Chemical Biology* **9**, 374–382 (2013).
569. Li, Y. *et al.* CRL2ZER1/ZYG11B recognizes small N-terminal residues for degradation. *Nat Commun* **13**, 7636 (2022).
570. Yan, X. *et al.* Molecular basis for recognition of Gly/N-degrons by CRL2ZYG11B and CRL2ZER1. *Molecular Cell* **81**, 3262-3274.e3 (2021).
571. Rajala, R. V. *et al.* Phosphorylation of human N-myristoyltransferase by N-myristoylated SRC family tyrosine kinase members. *Biochem Biophys Res Commun* **288**, 233–239 (2001).
572. Hornbeck, P. V. *et al.* PhosphoSitePlus, 2014: mutations, PTMs and recalibrations. *Nucleic Acids Res* **43**, D512-520 (2015).
573. Thinon, E. *et al.* Global profiling of co- and post-translationally N-myristoylated proteomes in human cells. *Nat Commun* **5**, 4919 (2014).
574. Kozak, M. Recognition of AUG and alternative initiator codons is augmented by G in position +4 but is not generally affected by the nucleotides in positions +5 and +6. *EMBO J* **16**, 2482–2492 (1997).
575. Varshavsky, A. N-degron pathways. *Proc Natl Acad Sci U S A* **121**, e2408697121 (2024).
576. Ridker, P. M. *et al.* Antiinflammatory Therapy with Canakinumab for Atherosclerotic Disease. *N Engl J Med* **377**, 1119–1131 (2017).
577. Entenberg, D., Oktay, M. H. & Condeelis, J. S. Intravital imaging to study cancer progression and metastasis. *Nat Rev Cancer* **23**, 25–42 (2023).
578. Smiles, W. J. *et al.* AMPK phosphosite profiling by label-free mass spectrometry reveals a multitude of mTORC1-regulated substrates. *NPJ Metab Health Dis* **3**, 8 (2025).
579. Qin, W. *et al.* Chemoproteomic Profiling of Itaconation by Bioorthogonal Probes in Inflammatory Macrophages. *J Am Chem Soc* **142**, 10894–10898 (2020).
580. Ashraf, N. & Van Nostrand, J. L. Fine-tuning AMPK in physiology and disease using point-mutant mouse models. *Dis Model Mech* **17**, dmm050798 (2024).
581. Fang, Z. & Peltz, G. Twenty-first century mouse genetics is again at an inflection point. *Lab Anim* **54**, 9–15 (2025).
582. Young, N. P., Crowley, D. & Jacks, T. Uncoupling cancer mutations reveals critical timing of p53 loss in sarcomagenesis. *Cancer Res* **71**, 4040–4047 (2011).

Appendix

ELSEVIER LICENSE
TERMS AND CONDITIONS

Apr 14, 2025

This Agreement between Tyler Smith ("You") and Elsevier ("Elsevier") consists of your license details and the terms and conditions provided by Elsevier and Copyright Clearance Center.

License Number	6007731489889
License date	Apr 14, 2025
Licensed Content Publisher	Elsevier
Licensed Content Publication	Atherosclerosis
Licensed Content Title	The value of a negative study
Licensed Content Author	Kevin Jon Williams
Licensed Content Date	Sep 1, 2024
Licensed Content Volume	396
Licensed Content Issue	n/a
Licensed Content Pages	1
Start Page	118530
End Page	0
Type of Use	reuse in a thesis/dissertation
Portion	full article
Circulation	10
Format	electronic
Are you the author of this Elsevier article?	No
Will you be translating?	No
Title of new work	AMPK regulation of myeloid inflammatory responses during acute and chronic disease
Institution name	University of Ottawa

Atherosclerosis 396 (2024) 118530

Contents lists available at ScienceDirect

Atherosclerosis

journal homepage: www.elsevier.com/locate/atherosclerosis

Editorial

The value of a negative study

ARTICLE INFO

Keywords
Atherosclerosis
AMP kinase
Mouse models
Therapy metformin

What role does endogenous cholesterol synthesis play in atherosclerosis? Within the liver, a lot. Within the arterial wall, not much. Feedback inhibition of synthesis [1–3], as well as inhibition of LDL receptor-mediated uptake, allows the cell to tightly control its cholesterol content. Thus, other mechanisms must be at work in the development of cholesterol-overloaded "foam" cells within atheromata. Decades of work have established that the development of atherosclerotic plaques begins with the subendothelial retention of cholesterol-rich apolipoprotein-B (apoB)-containing lipoproteins, chiefly LDL, followed by their modification by local enzymes within the arterial wall [4–7]. These processes lead to particle aggregation and cellular uptake through LDL-receptor-independent pathways [8,9], usually phagocytosis [10] or, for large aggregates, digestive exophagy [11,12].

But could there still be a role for extrahepatic cholesterol biosynthesis in atherogenesis? This question has potential therapeutic implications, given the availability of several classes of pharmacologic agents that directly or perhaps indirectly inhibit cholesterol synthetic enzymes. Statins and bempedoic acid are on this list and in clinical use (bempedoic acid appears to act only in liver, because of its conversion into its active form there). Metformin [13] and other activators of AMP kinase (AMPK) might also be on this list, owing to a specific regulatory pathway in which AMPK phosphorylates HMG-CoA reductase (HMGCR) at Ser872 (Ser871 in mice), thereby inhibiting it. The AMPK-HMGCR pathway makes physiologic sense: AMPK is activated by energy deficiency; biosynthesis of cholesterol and other isoprenoids is energetically costly; and so energy deficiency shuts it off.

In two papers sharing several authors, Lee et al., in 2022 [14], and Smith et al. in this issue of *Atherosclerosis* [15], used elegant methodologies to address this specific action of AMPK, through the use of knock-in (KI) mice in which the genomic codon for the target serine residue on HMGCR has been replaced by a codon for alanine, which AMPK cannot phosphorylate (*Hmgcr KI* mice).

Smith et al. review an extensive, but messy, prior literature on the role of AMPK more generally in atherosclerosis. Pharmacologic and genetic manipulation of AMPK in animal models have shown an atheroprotective role, an atherogenic role, and, in a study by several of these authors [16], no role. My general feeling is whenever an issue attracts widespread attention and investigation, yet still remains unresolved, then either there's nothing there or the experimental systems are not specific enough. Moreover, even a contradictory literature might have an overall bias, as we bear in mind that positive studies are often easier to publish than negative ones (more on this point, below). The real picture might be even more negative.

With this background, examination of one single specific action of AMPK makes a great deal of sense. Of the numerous targets of AMPK, Lee et al. [14] and then Smith et al. [15] zeroed in on HMGCR exclusively. Lee et al.'s animal model for atherosclerosis was the hypercholesterolemic apoE-knockout mouse (*Apoe*$^{-/-}$), which develops hypercholesterolemia and arterial lesions even on ordinary low-fat laboratory food [17,18]. Lee et al. found that, compared with control *Apoe*$^{-/-}$ mice, the *Apoe*$^{-/-}$*/Hmgcr KI* mice showed significantly larger aortic lesion size, along with more plaque-associated macrophages and lipid accumulation. In addition, the *Apoe*$^{-/-}$*/Hmgcr KI* mice had elevated plasma concentrations of total cholesterol, 27-hydroxycholesterol, and what the authors called LDL and VLDL cholesterol, as well as increased circulating Ly6-C^{hi} monocytes and extramedullary myelopoiesis.

But this list of findings highlights at least two known problems with the *Apoe*$^{-/-}$ mouse as a model of atherogenesis. The first problem is its highly abnormal circulating apoB-lipoproteins, which are mainly β-VLDL, a large cholesterol-rich particle devoid of apoE. Would LDL, the main apoB-lipoprotein in humans, also become suppressed by the AMPK-HMGCR pathway? The second problem is abnormalities in the immune system of *Apoe*$^{-/-}$ mice. Would the AMPK-HMGCR pathway suppress Ly6-C^{hi} monocytes and extramedullary myelopoiesis when

DOI of original article: https://doi.org/10.1016/j.atherosclerosis.2024.117608.

https://doi.org/10.1016/j.atherosclerosis.2024.118530
Received 21 June 2024; Accepted 27 June 2024
Available online 28 June 2024

apoE is present?

Smith et al. are to be commended for their diligence in re-testing a role for the AMPK-HMGCR pathway in atherogenesis, this time in a different animal model that expresses apoE and thereby avoids the abnormal apoB-lipoproteins and the abnormalities in immune function seen in apoE knockout mice. The lay-out of their figures is clear, enhanced by the inclusion of symbols for blood, liver, bone marrow, and spleen to aid the reader. One drawback is a large number of statistical comparisons, uncorrected for their multiplicity.

Smith et al. used Bjørklund et al.'s [19] non-genomic system to induce hypercholesterolemia and atherosclerosis in wild-type and *Hmgcr KI* mice by injection of gain-of-function human $PCSK9^{D374Y}$-adeno-associated virus to destroy hepatic LDL receptors, combined with a high-fat, high-cholesterol "fast food" diet.

Smith et al.'s study showed no effect of the *Hmgcr KI* on atherosclerosis. Smith et al.'s results beyond atherosclerosis are extensive, re-testing essentially all of the findings from Lee et al.'s previous work in the apoE-knockout background. In Smith et al.'s apoE-replete model, diet-fed *Hmgcr KI* mice showed the same levels of plasma cholesterol as diet-fed wild-type mice. Moreover, the knock-in had no detectable effects on hematopoiesis or the immune system.

Which results, Lee et al.'s or Smith et al.'s, are more applicable to humans? My guess would be Smith et al.'s negative findings, because nearly all people have apoE. But Lee et al.'s additional findings beyond atherosclerosis development, listed above and in their published article, might be amenable to testing in human volunteers, before and after administration of an AMP kinase activator, such as metformin. As an example, prior literature indicates a modest effect of metformin to lower plasma concentrations of LDLc in people [20]. The reported mechanisms, however, do not involve a direct effect of AMPK on HMGCR [21,22].

As another example, salsalate, an anti-inflammatory agent noted by Lee et al. [14] and others [23] to also activate AMPK, was tested in a prospective randomized clinical trial of obese or overweight statin-treated patients. The primary outcome was progression of noncalcified coronary artery plaque by coronary computed tomography angiography. The trial was "well-conducted, well-powered" [24]. But the trial failed – no benefit in humans [25]. And yet, salsalate lowered white blood cell counts in that trial [25] and decreased atherosclerosis in a subsequent study in mice [26].

"Negative studies, when well-designed and well-powered, were not failures; they were crucial in forcing the field to look elsewhere." [27] Based on the extensive findings now presented by Smith et al. [15], it seems likely that we will be looking at strategies other than activation of the AMPK-HMGCR pathway to reduce atherosclerotic burden. It is a valuable contribution. We will continue to use metformin clinically, but for other reasons.

Declaration of competing interest

Dr Williams reports an ownership interest in Hygieia, Inc.

Acknowledgements

The author acknowledges support from the Ruth and Yonatan Ben-Avraham Fund.

References

[1] R. Schoenheimer, F. Breusch, Synthesis and destruction of cholesterol in the organism, J. Biol. Chem. 103 (1933) 439–448, https://doi.org/10.1016/S0021-9258(18)75823-7.

[2] R.G. Gould, C.B. Taylor, J.S. Hagerman, I. Warner, D.J. Campbell, Cholesterol metabolism. I. Effect of dietary cholesterol on the synthesis of cholesterol in dog tissue in vitro, J. Biol. Chem. 201 (1953) 519–528, https://doi.org/10.1016/S0021-9258(18)66206-4.

[3] M.S. Brown, J.L. Goldstein, Cholesterol feedback: from Schoenheimer's bottle to Scap's MELADL, J. Lipid Res. 50 (2009) S15–S27, https://doi.org/10.1194/jlr.R800054-JLR200.

[4] K.J. Williams, I. Tabas, The response-to-retention hypothesis of early atherogenesis, Arterioscler. Thromb. Vasc. Biol. 15 (1995) 551–561, https://doi.org/10.1161/01.ATV.15.5.551.

[5] J. Borén, K.J. Williams, The central role of arterial retention of cholesterol-rich apoB-containing lipoproteins in the pathogenesis of atherosclerosis: a triumph of simplicity, Curr. Opin. Lipidol. 27 (2016) 473–483, https://doi.org/10.1097/MOL.0000000000000330.

[6] M. Torzewski, Enzymatically modified LDL, atherosclerosis and beyond: paving the way to acceptance, Front Biosci (Landmark Ed) 23 (2018) 1257–1271, https://doi.org/10.2741/4642.

[7] M. Ruuth, S.D. Nguyen, T. Vihervaara, M. Hilvo, T.D. Laajala, P.K. Kondadi, A. Gisterå, H. Lähteenmäki, T. Kittilä, J. Huusko, M. Uusitupa, U. Schwab, M. J. Savolainen, J. Sinisalo, M.-L. Lokki, M.S. Nieminen, A. Jula, M. Perola, S. Ylä-Herttula, L. Rudel, A. Öörni, M. Baumann, A. Baruch, R. Laaksonen, D.F. J. Ketelhuth, T. Aittokallio, M. Jauhiainen, R. Käkelä, J. Borén, K.J. Williams, P. T. Kovanen, K. Öörni, Susceptibility of low-density lipoprotein particles to aggregate depends on particle lipidome, is modifiable, and associates with future cardiovascular deaths, Eur. Heart J. 39 (2018) 2562–2573, https://doi.org/10.1093/eurheartj/ehy319.

[8] S.W. Sakr, R.J. Eddy, H. Barth, F. Wang, S. Greenberg, F.R. Maxfield, I. Tabas, The uptake and degradation of matrix-bound lipoproteins by macrophages require an intact actin cytoskeleton, Rho family GTPases, and myosin ATPase activity, J. Biol. Chem. 276 (2001) 37649–37658, https://doi.org/10.1074/jbc.M105129200.

[9] B.B. Boyanovsky, P. Shridas, M. Simons, D.R. van der Westhuyzen, N.R. Webb, Syndecan-4 mediates macrophage uptake of group V secretory phospholipase A_2-modified low density lipoprotein, J. Lipid Res. 50 (2009) 641–650, https://doi.org/10.1194/jlr.M800450-JLR200.

[10] I. Tabas, Y. Li, R.W. Brocia, S.W. Xu, T.L. Swenson, K.J. Williams, Lipoprotein lipase and sphingomyelinase synergistically enhance the association of atherogenic lipoproteins with smooth muscle cells and extracellular matrix. A possible mechanism for low density lipoprotein and lipoprotein(a) retention and macrophage foam cell formation, J. Biol. Chem. 268 (1993) 20419–20432, https://doi.org/10.1016/S0021-9258(20)80745-5.

[11] I. Grosheva, A.S. Haka, C. Qin, L.M. Pierini, F.R. Maxfield, Aggregated LDL in contact with macrophages induces local increases in free cholesterol levels that regulate local actin polymerization, Arterioscler. Thromb. Vasc. Biol. 29 (2009) 1615–1621, https://doi.org/10.1161/ATVBAHA.109.191882.

[12] N. Steinfeld, C.J. Ma, F.R. Maxfield, Signaling pathways regulating the extracellular digestion of lipoprotein aggregates by macrophages, Mol. Biol. Cell 35 (2024) ar5, https://doi.org/10.1091/mbc.E23-06-0239.

[13] L. He, F.E. Wondisford, Metformin action: concentrations matter, Cell Metabol. 21 (2015) 159–162, https://doi.org/10.1016/j.cmet.2015.01.003.

[14] M.K.S. Lee, O.D. Cooney, X. Lin, S. Nadarajah, D. Dragoljevic, K. Huynh, D.-A. Onda, S. Galic, P.J. Meikle, T. Edlund, M.D. Fullerton, B.E. Kemp, A.J. Murphy, K. Loh, Defective AMPK regulation of cholesterol metabolism accelerates atherosclerosis by promoting HSPC mobilization and myelopoiesis, Mol. Metabol. 61 (2022) 101514, https://doi.org/10.1016/j.molmet.2022.101514.

[15] T.K.T. Smith, P. Ghorbani, N.D. LeBlond, J.R.C. Nunes, C. O'Dwyer, N. Ambursley, C. Fong-McMaster, L. Minarrieta, L.A. Burkovsky, R. El-Hakim, N.A. Trzaskalski, C. A.A. Locatelli, C. Stotts, C. Pember, K.J. Rayner, B.E. Kemp, K. Loh, M.-E. Harper, E.E. Mulvihill, J. St-Pierre, M.D. Fullerton, AMPK-mediated regulation of endogenous cholesterol synthesis does not affect atherosclerosis in a murine *Pcsk9*-AAV model, Atherosclerosis (396) (2024) 117608. In press.

[16] N.D. LeBlond, P. Ghorbani, C. O'Dwyer, N. Ambursley, J.R.C. Nunes, T.K.T. Smith, N.A. Trzaskalski, E.E. Mulvihill, B. Viollet, M. Foretz, M.D. Fullerton, Myeloid deletion and therapeutic activation of AMPK do not alter atherosclerosis in male or female mice, J. Lipid Res. 61 (2020) 1697–1706, https://doi.org/10.1194/jlr.RA120001040.

[17] Y. Nakashima, A.S. Plump, E.W. Raines, J.L. Breslow, R. Ross, ApoE-deficient mice develop lesions of all phases of atherosclerosis throughout the arterial tree, Arterioscler. Thromb. 14 (1994) 133–140, https://doi.org/10.1161/01.atv.14.1.133.

[18] R.L. Reddick, S.H. Zhang, N. Maeda, Atherosclerosis in mice lacking apo E. Evaluation of lesional development and progression, Arterioscler. Thromb. 14 (1994) 141–147, https://doi.org/10.1161/01.atv.14.1.141.

[19] M.M. Bjørklund, A.K. Hollensen, M.K. Hagensen, F. Dagnæs-Hansen, C. Christoffersen, J.G. Mikkelsen, J.F. Bentzon, Induction of atherosclerosis in mice and hamsters without germline genetic engineering, Circ. Res. 114 (2014) 1684–1689, https://doi.org/10.1161/CIRCRESAHA.114.302937.

[20] M.G. Wulffelé, A. Kooy, D. de Zeeuw, C.D. Stehouwer, R.T. Gansevoort, The effect of metformin on blood pressure, plasma cholesterol and triglycerides in type 2 diabetes mellitus: a systematic review, J. Intern. Med. 256 (2004) 1–14, https://doi.org/10.1111/j.1365-2796.2004.01328.x.

[21] T. Xu, S. Brandmaier, A.C. Messias, C. Herder, H.H.M. Draisma, A. Demirkan, Z. Yu, J.S. Ried, T. Haller, M. Heier, M. Campillos, G. Fobo, R. Stark, C. Holzapfel, J. Adam, S. Chi, M. Rotter, T. Panni, A.S. Quante, Y. He, C. Prehn, W. Roemisch-Margl, G. Kastenmüller, G. Willemsen, R. Pool, K. Kasa, K.W. van Dijk, T. Hankemeier, C. Meisinger, B. Thorand, A. Ruepp, M. Hrabé de Angelis, Y. Li, H.-E. Wichmann, B. Stratmann, K. Strauch, A. Metspalu, C. Gieger, K. Suhre, J. Adamski, T. Illig, W. Rathmann, M. Roden, A. Peters, C.M. van Duijn, D. I. Boomsma, T. Meitinger, R. Wang-Sattler, Effects of metformin on metabolite profiles and LDL cholesterol in patients with type 2 diabetes, Diabetes Care 38 (2015) 1858–1867, https://doi.org/10.2337/dc15-0658.

[22] D. Hu, Y. Guo, R. Wu, T. Shao, J. Long, B. Yu, H. Wang, Y. Luo, H. Lu, J. Zhang, Y. E. Chen, D. Peng, New insight into metformin-induced cholesterol-lowering effect. Crosstalk between glucose and cholesterol homeostasis via ChREBP (carbohydrate-responsive element-binding protein)-mediated PCSK9 (proprotein convertase subtilisin/kexin type 9) regulation, Arterioscler. Thromb. Vasc. Biol. 41 (2021) e208–e223, https://doi.org/10.1161/ATVBAHA.120.315708.

[23] S.A. Hawley, M.D. Fullerton, F.A. Ross, J.D. Schertzer, C. Chevtzoff, K.J. Walker, M.W. Peggie, D. Zibrova, K.A. Green, K.J. Mustard, B.E. Kemp, K. Sakamoto, G. R. Steinberg, D.G. Hardie, The ancient drug salicylate directly activates AMP-activated protein kinase, Science 336 (2012) 918–922, https://doi.org/10.1126/science.1215327.

[24] P.M. Ridker, Informative neutral studies matter—why the Targeting Inflammation with Salsalate in Cardiovascular Disease (TINSAL-CVD) Trial deserves our attention, JAMA Cardiol 1 (2016) 423–424, https://doi.org/10.1001/jamacardio.2016.0604.

[25] T.H. Hauser, N. Salastekar, E.J. Schaefer, T. Desai, H.L. Goldfine, K.M. Fowler, G. M. Weber, F. Welty, M. Clouse, S.E. Shoelson, A.B. Goldfine, For the Targeting Inflammation Using Salsalate in Cardiovascular Disease (TINSAL-CVD) Study Team. Effect of targeting inflammation with salsalate: the TINSAL-CVD randomized clinical trial on progression of coronary plaque in overweight and obese patients using statins, JAMA Cardiol 1 (2016) 413–423, https://doi.org/10.1001/jamacardio.2016.0605.

[26] E.A. Day, R.J. Ford, B.K. Smith, V.P. Houde, S. Stypa, S. Rehal, S. Lhotak, B. E. Kemp, B.L. Trigatti, G.H. Werstuck, R.C. Austin, M.D. Fullerton, G.R. Steinberg, Salsalate reduces atherosclerosis through AMPKβ1 in mice, Mol. Metabol. 53 (2021) 101321, https://doi.org/10.1016/j.molmet.2021.101321.

[27] K.J. Williams, Eradicating atherosclerotic events by targeting early subclinical disease: it is time to retire the therapeutic paradigm of too much, too late, Arterioscler. Thromb. Vasc. Biol. 44 (2024) 48–64, https://doi.org/10.1161/ATVBAHA.123.320065.

Kevin Jon Williams
Lewis Katz School of Medicine at Temple University, Philadelphia, PA, USA
E-mail address: kjwilliams@temple.edu.

Tyler Smith

RESEARCH EXPERIENCE SUMMARY

Ph.D. in Biochemistry (anticipated completion: June 2025) 2019 – 2025
University of Ottawa, Ottawa, Canada

- Independently led 3 *in vivo* and *ex vivo* projects that generated one first-authored manuscript and one in preparation for submission.
- Awarded 6 presentation awards at national and international conferences.
- Investigated novel metabolic pathways in myeloid cells during homeostatic and inflammatory conditions using pharmacological activators and genetic approaches.

Skills Flow cytometry; Mouse handling; Primary immune cell isolation; Transcriptomics; RT-qPCR; ELISA; Western blotting; Histology; Immunofluorescence; scRNA seq; R

EDUCATION

Ph.D. in Biochemistry 2019 – present
University of Ottawa, Ottawa, Ontario, Canada
Transferred from Master's degree: December 2020
Expected degree conferral date: June 2025

B.Sc. with Honours in Translational and Molecular Medicine 2015 – 2019
University of Ottawa, Ottawa, Ontario, Canada
cGPA: 9.6/10.0 (3.96/4.0)

PUBLICATIONS – *2 first author, 9 co-author manuscripts*

First Author

1. **Smith TKT**, Ghorbani P, LeBlond ND, Nunes JRC, O'Dwyer C, Ambursley N, Fong-McMaster C, Minarrieta L, Burkovsky LA, El-Hakim R, Trzaskalski N, Locatelli CAA, Stotts C, Pember C, Rayner KJ, Kemp BE, Loh K, Harper ME, Mulvihill EE, St-Pierre J, Fullerton MD (2024). AMPK-mediated regulation of endogenous cholesterol synthesis does not affect atherosclerosis in a murine *Pcsk9*-AAV model. *Atheroscler.* (*IF = 5.3)*. In press.
2. **Smith TKT** and Kahiel Z, Leblond ND, Ghorbani P, Farah E, Al-Awosi R, Côté M, Gadde S, Fullerton MD (2019). Characterization of redox-responsive LXR-activating nanoparticle formulations in primary mouse macrophages. *Molecules (IF = 4.93)*. 24(20): 3751.

First Author Under Review

1. **Smith TKT**, Townsend LK, Smiles WJ, Oakhill JS, Fullerton MD, Steinberg GR (2025). AMPK: orchestrating metabolism in health and disease. *Nat. Metab.* (*IF = 19.2*). Under review.

Contributing Author

1. Nunes JRC, O'Dwyer C, Ghorbani P, **Smith TKT**, Chauhan S, Robert-Gostlin V, Girouard MD, Viollet B, Foretz M, Fullerton MD (2024). Myeloid AMPK signaling restricts fibrosis but is not required for metformin improvements during CDAHFD-induced NASH in mice. *J. Lipid. Res. (IF = 6.50)*. In press.
2. Day EA, Townsend LK, Rehal S, Batchuluun B, Wang D, Morrow MR, Lu R, Lundenberg L, Lu JH, Desjardins EM, **Smith TKT**, Raphenya AR, McArthur AG, Fullerton MD, Steinberg GR (2023). Macrophage AMPKβ1 activation by PF-06409577 reduces the

inflammatory response, cholesterol synthesis and atherosclerosis in mice. *iScience (IF = 6.11).* 26(11): 108269.

3. Ghorbani P, Kim SY, **Smith TKT**, Minarrieta L, Kilgour MK, Ilijevska M, Alecu I, Snider SA, Margison KD, Nunes JRC, Woo D, Pember C, O'Dwyer C, St-Pierre J, Bennett SAL, Nair MG, Fullerton MD (2023). Choline metabolism underpins macrophage IL-4 polarization and RELMα up-regulation in helminth infection. *PLOS Pathog.* (*IF = 7.46)*. 19(9): e1011658.
4. Nunes JRC, **Smith TKT**, Ghorbani P, O'Dwyer C, Trzaskalski NA, Dergham H, Pember C, Kilgour MK, Mulvihill EE, Fullerton MD (2023). Thermoneutral housing does not accelerate metabolic dysfunction-associated fatty liver disease in male or female C57Bl/6J mice fed a Western diet. *Am. J. Physiol. Endocrinol. Metab. (IF = 5.90).* 325(1): E10-E20.
5. Stewart CM, Phan A, Bo Y, Leblond ND, **Smith TKT**, Laroche G, Giguère PM, Fullerton MD, Pelchat M, Kobasa D; Cote M (2021). Ebola virus triggers receptor tyrosine kinase-dependent signaling to promote the delivery of viral particles to entry-conducive intracellular compartments. *PLOS Pathog.* (*IF = 7.46)*. 17(1): Online.
6. Phillips WJ, Baghai T, Ong M, Lo B, Ibrahim AM, **Smith TKT**, Song X (2021). A contemporary report of clinical outcomes in patients with melanoma brain metastases. *Curr. Oncol. (IF = 2.26).* 28(1), 428-439.
7. LeBlond ND, Ghorbani P, O'Dwyer C, Ambursley N, Nunes JRC, **Smith TKT**, Trzaskalski NA, Mulvihill EE, Viollet B, Foretz M, Fullerton MD (2020). Myeloid deletion and therapeutic activation of AMP-activated protein kinase (AMPK) do not alter atherosclerosis in male or female mice. *J. Lipid Res.* (*IF = 5.92*). 61(12): 1697-1706.
8. LeBlond ND, Nunes JRC, **Smith TKT**, Robichaud S, Gadde S, Cote M, Kemp B, Ouimet M, Fullerton MD (2020). Foam cell induction activates AMPK but uncouples its regulation of autophagy and lysosomal homeostasis. *Int. J. Mol. Sci.* (*IF = 6.21*). 21(23): 9033.
9. Steward CM, Dorion SS, Ottenbrite MAF, LeBlond ND, **Smith TKT**, Qiu S, Fullerton MD, Kobasa D, Côté M (2019). A diacylglycerol kinase inhibitor, R-59-022, blocks filovirus internalization in host cells. *Viruses (IF = 5.81)*. 11(3), 206.

SELECTED CONFERENCE PRESENTATIONS – *4 oral and 2 poster awards*

Podium Presentations

1. **Smith TKT**, Kemp BE, Fullerton MD. AMPK activation modulates macrophage metabolism during *Salmonella* Typhimurium infection. Immunometabolism Forum. Dublin, Ireland. Presented and attended virtually. March 14, 2025.
2. **Smith TKT**, Ghorbani P, LeBlond ND, Kemp BE, Fullerton MD. *Immune-dependent AMPK signaling to HMG-CoA reductase protects against atherosclerosis*. 65th Annual Canadian Society for Molecular Biosciences International Conference. Ottawa, Ontario, Canada. May 30-June 2, 2023. #Won oral presentation award.
3. **Smith TKT**, Ghorbani P, LeBlond ND, Kemp BE, Fullerton MD. *Immune-dependent AMPK signaling to HMG-CoA reductase is protective against atherosclerosis*. 2023 Centre for Catalysis Research and Innovation Talk Series. Ottawa, Ontario, Canada. March 9, 2023.
4. **Smith TKT**, Ghorbani P, LeBlond ND, Kemp BE, Fullerton MD. *Immune-dependent AMPK signaling to HMG-CoA reductase protects against atherosclerosis*. 2022 Ottawa Institute of Systems Biology Scientific Conference. Cornwall, Ontario, Canada. May 24-25, 2022. #Won oral presentation award.
5. **Smith TKT**, Ghorbani P, LeBlond ND, Kemp BE, Fullerton MD. *Immune-dependent AMPK signaling to HMG-CoA reductase protects against atherosclerosis*. 34th Ottawa Cardiovascular Research Day. Ottawa, Ontario, Canada. Presented and attended virtually. May 26-27, 2022. #Won oral presentation award.

6. **Smith TKT**, Ghorbani P, LeBlond ND, Kemp BE, Fullerton MD. *Immune-dependent AMPK signaling to HMG-CoA reductase protects against atherosclerosis*. Immunometabolism Forum. Dublin, Ireland. Presented and attended virtually. May 6, 2022.
7. **Smith TKT**, Kemp BE, Fullerton MD. *AMP-activated protein kinase requires myristoylation to regulate cellular metabolism*. 2021 Canadian Student Health Research Forum. Winnipeg, Manitoba, Canada. Attended and presented virtually. June 14-18, 2021.
8. **Smith TKT**, LeBlond ND, Kemp BE, Fullerton MD. AMPK-mediated inhibition of HMG-CoA reductase is protective against atherosclerosis. 2019 Canadian Lipid and Vascular Summit. Banff, AB. #Won oral presentation award.

Poster Presentations

1. **Smith TKT**, Kemp BE, Fullerton MD. *Exploring the role of AMPK in* Salmonella enterica *serovar typhimurium infection.* BMI Departmental Seminar Day. Ottawa, Canada. Apr. 29, 2024. #Won poster presentation award.
2. **Smith TKT**, Kemp BE, Fullerton MD. *Exploring the role of AMPK in bacterial infection*. 12th International Meeting on AMPK. Lorne, Australia. Oct. 1-6, 2023. #Won poster presentation award.
3. **Smith TKT,** Ghorbani P, LeBlond ND, Kemp BE, Fullerton MD. *Immune-dependent AMPK signaling to HMG-CoA reductase protects against atherosclerosis*. 2022 Canadian Vascular and Lipid Summit. Whistler, British Columbia, Canada. Oct. 13-16, 2022.
4. **Smith TKT**, Ghorbani P, LeBlond ND, Kemp BE, Fullerton MD. *Immune-dependent AMPK signaling to HMG-CoA reductase protects against atherosclerosis*. 5th European Workshop on AMPK and AMPK-related kinases. Glasgow, United Kingdom. Sept. 27-29, 2022.
5. **Smith TKT**, Kemp BE, Fullerton MD. *Myristoylation links AMP-activated protein kinase to immunometabolism*. 11th International Meeting on AMPK. Evian-Les-Bains, France. Attended and presented virtually. Sept. 26-30, 2021.

SCHOLARSHIPS (2020 – present) – *represents $287,500 CAD out of $363,500 CAD total*

Ontario Graduate Scholarship – Doctoral 2024
University of Ottawa, Ontario - $15,000 CAD

CIHR Vanier Canada Graduate Scholarship 2021 – 2024
University of Ottawa, Ontario - $150,000 CAD total
- Ranked 7th out of 188 qualifying candidates (top 4%)

CIHR Canada Graduate Scholarship – Doctoral (Declined) 2021
University of Ottawa, Ontario - $105,000 CAD total
- Ranked 24th out of 488 qualifying candidates (top 5%)

CIHR Canada Graduate Scholarship – Master's 2020
University of Ottawa, Ontario - $17,500 CAD

SELECTED AWARDS AND DISTINCTIONS

Syed Sattar Student Award - PhD 2025
University of Ottawa, Ottawa, Ontario, Canada

Faculty of Medicine Graduate Studies Excellence Award – PhD 2024
University of Ottawa, Ottawa, Ontario, Canada

Faculty of Medicine Leadership Award 2023
University of Ottawa, Ottawa, Ontario, Canada

AMPK Meeting Poster Presentation Award 2023
12th International AMPK Meeting, Lorne, Australia

CSMB Conference Oral Presentation Award 2023
65th CSMB International Conference, Ottawa, Ontario, Canada - $500 CAD

2022 OISB Scientific Conference Oral Presentation Award 2022
OISB Scientific Conference, Cornwall, Ontario, Canada

Dr. Yves Marcel Award for Best Basic Science Oral Presentation 2022
34th Ottawa Cardiovascular Research Day, Virtual - $200 CAD

Canadian Vascular and Lipid Summit Oral Presentation Award 2019
Canadian Vascular and Lipid Summit, Banff, Alberta, Canada - $500 CAD

USports Top 8 Academic All-Canadian Nominee 2018
University of Ottawa athlete representative for prestigious national competition

MENTORSHIP

Student Mentorship 2019 – present
Fullerton Laboratory, Faculty of Medicine, Ottawa, Ontario

- Directly mentored 2 Honours students and 2 rotation students (3 months each) one-on-one in all aspects of scientific discovery (cumulative time: 2.5 years).
- Demonstrated wet lab techniques and introduced best practices for data analysis and integrity for an additional 7 undergraduate and 2 Master's students.

Faculty Mentorship – Flow Cytometry 2022-2024
Fullerton Laboratory, Faculty of Medicine, Ottawa, Ontario

- Provided expert guidance to 2 collaborators on experimental setup for their assays.

Departmental Mentorship 2020 – 2023
BMI Graduate Student Association, Faculty of Medicine, Ottawa, Ontario
Co-President 2022 – 2023
Vice President, Internal Affairs 2020 – 2022

- Championed student funding increases and actively advocated for higher stipends at the university and national level, resulting in a $4,000 annual increase in stipend value.
- Communicated student concerns at monthly departmental and faculty meetings.
- Liaised with 2 other student associations to collaborate on key events and address common issues.

Varsity Swim Team Academic Mentor 2017 - 2023
University of Ottawa Gee-Gees, Ottawa, Ontario

- Conducted 5 workshops and 15 annual one-on-one meetings about effective time management and study techniques.

- Achieved an increase of 25% in the number of Academic All-Canadians (8.0 average or higher) after starting in role.

EXTRACURRICULAR INVOLVEMENT

Faculty of Medicine Awards of Excellence Selection Committee 2023-2024
University of Ottawa, Ottawa, Ontario, Canada

Biochemistry Graduate Program Director Selection Committee 2023
University of Ottawa, Ottawa, Ontario, Canada

UOHI Trainee of the Year Selection Committee 2020 – 2024
University of Ottawa Heart Institute, Ottawa, Ontario, Canada

Asst. Dean of Graduate and Postdoctoral Studies Selection Committee 2020
University of Ottawa, Ontario, Canada

Encounters with Canada – Dissection Demonstrator 2019 – 2023
University of Ottawa, Ottawa, Ontario, Canada

University of Ottawa Varsity Athlete 2015 – 2019
University of Ottawa Gee-Gees Swim Team, Ottawa, Ontario, Canada
Team Captain (2017 – 2018)